University of Southampton

Faculty of Physical Sciences and Engineering

Optoelectronics Research Centre

Functionalisation of Optical Fibres by the integration of 2D Transition Metal Dichalcogenide Materials

by

Adam Henry Lewis

Thesis for the degree of Doctor of Philosophy

September 2019

University of Southampton

Abstract

Faculty of Physical Sciences and Engineering

Optoelectronics Research Centre

Thesis for the degree of Doctor of Philosophy

Functionalisation of Optical Fibres by the integration of 2D Transition Metal Dichalcogenide Materials

by

Adam Henry Lewis

In this thesis, the concept of functionalising microstructured optical fibres is proposed using a unique and novel concept of liquid phase deposition of two dimensional materials. Two fields of research have been analysed in this work. Firstly, the concept of thermal poling – whereby centrosymmetric materials with negligible values of second order nonlinearity are heated under the presence of an electrical field to break the centrosymmetry of the structure and generate a non-zero second order nonlinearity (SON) – is analysed. This quadratic nonlinearity can potentially be augmented via the insertion of intrinsically highly nonlinear 2D materials such as Transition Metal Dichalcogenides. Another area of research has been functionalising the hollow regions of antiresonant optical fibres. This is a relatively new design of fibre, whereby light is guided in a hollow core using a guidance mechanism known as inhibited coupling. The hollow regions of an anti-resonant fibre (ARF) offer an excellent template for the deposition of functional materials such as 2D films. When the optical properties of such materials can be modified via external stimuli, it offers a method to modify the transmission capability of the optical fibre. We successfully demonstrate electro-optical control on the devices, showing loss of 3dB in the guidance regions. Following on from these results, other materials were also investigated for their electro-optic properties including ZnSe in its bulk form and compared with the performance of the 2D materials.

Table of Contents

Table of Tables

Table of Figures

Table of Figures

Table of Figures

List of Accompanying Materials

Research Thesis: Declaration of Authorship

Print name:	Adam Lewis
Title of thesis:	Functionalisation of Optical Fibres by the integration of 2D Transition Metal Dichalcogenide Materials

I declare that this thesis and the work presented in it are my own and has been generated by me as the result of my own original research.

I confirm that:

1. This work was done wholly or mainly while in candidature for a research degree at this University;
2. Where any part of this thesis has previously been submitted for a degree or any other qualification at this University or any other institution, this has been clearly stated;
3. Where I have consulted the published work of others, this is always clearly attributed;
4. Where I have quoted from the work of others, the source is always given. With the exception of such quotations, this thesis is entirely my own work;
5. I have acknowledged all main sources of help;
6. Where the thesis is based on work done by myself jointly with others, I have made clear exactly what was done by others and what I have contributed myself;
7. None of this work has been published before submission

Signature: Date: 19/09/2019

Acknowledgements

I would like to highlight the many people who have helped and supported me throughout the time of my PhD. I will begin with my supervisor, Pier Sazio, who has been a constant support and help in all aspects of my PhD – from writing papers, to lab work, to calming me down when I was stressed and picking me up when I results weren't going as well as hoped! I would like to extend this thanks to Francesco De Lucia too, whose help in the lab has been vital, and made me feel so welcome to the group when I first arrived to Southampton. I would also like to thank Dan Hewak and all the Novel Glass Group – Che-Chung Huang, Chris Craig, Edwin Weatherby, Jin Yao, Katrina Morgan, Ioannis Zempekis, Ghadah Al-Zaidy, Nikos Aspiotis, Andrea Ravagli, Bruno Moog, Matt Delaney, Fernando Guzman-Cruz and Ellis Archer – working with you all has been a pleasure and I am grateful to your support in the world of Chalcogenides, I hope success to you all. Other I would like to highlight are Tom Bradley and Gregory Jasion, for your help with working with hollow core fibres, you have both helped me so much, supplying me with sources and helping me wherever possible. I would also like to thank Francesco Poletti and John Hayes for supplying me with the fibres.

Outside of the lab there are also many people who I need to thank. To my longest friends, Jack Delderfield and Thomas Adey, I am so grateful for your support, and your ability to remind me to relax in the evenings and weekends! This thanks also needs to be extended to Charlie Leathem, Chris O'Shea and Kristian Hook. Newer friends made at the ORC also need to be thanked – Josh Pooley, Florian Le Roi, Omar Adnan Abbas, Armen Aghajani, Milos Nedeljkovic and Jon Gorecki. Thank you for making the office a welcoming place!

Of course there are a few special people (and cats) I hold dearly in my heart and who I devote this thesis to. Yanli Qi – thank you so much for supporting and loving me despite the stress I have been in, you make each day worth waking up for. For my siblings, Jack and Tilly, hopefully some of this thesis makes sense to you. But this all pales in comparison to the gratitude I must show to my Mum, Helen. You have always been there for me, through every step and none of this would have been possible without you.

Definitions and Abbreviations

CVD	Chemical Vapour Deposition
ALD	Atomic Layer Deposition
TMDC	Transition Metal Dichalcogenide
h-BN	Hexagonal Boron Nitride
FET	Field Effect Transistor
SHG	Second Harmonic Generation
SH	Second Harmonic
XPS	X-ray Photon Spectroscopy
AFM	Atomic Force Microscopy
CCD	Charge Coupled Device
FWHM	Full Width Half Maximum
STM	Scanning Tunneling Microscope
IPA	Isopropanol
NMP	N-Methyl-2-Pyrrolidone
PMMA	Poly(methyl methacrylate)
LPD	Liquid Phase Deposition
ATTM	Ammonium Tetrathiomolybdate
DMF	Dimethylformamide
SFG	Sum Frequency Generation
DFG	Difference Frequency Generation
NPM	Non-Phase Matched
BPM	Birefringent Phase Matching
PP	Periodic Poling
QPM	Quasi-Phase Matching
UV	Ultra Violet
SON	Second Order Nonlinearity
HV	High Voltage
PBG	Photonic Bandgap
IC	Inhibited Coupling
NCF	Negative Curvature Fibre
NC	Negative Curvature
HC-NCF	Hollow Core Negative Curvature Fibre
ARF	Anti-Resonant Fibre

ARROW	Anti-Resonant Reflecting Optical Waveguide
IR	Infra-Red
SEM	Scanning Electron Microscopy
MMF	Multi-Mode Fibre
OSA	Optical Spectrum Analyser
MFD	Mode Field Diameter
WLS	White Light Source
SMF	Single Mode Fibre
E-Field	Electrical Field
RI	Refractive Index
ATTT	Ammonium Tetrathiotungstate
HPCVD	High Pressure Chemical Vapour Deposition
BSD	Back Scattered Detection

Chapter 1 Introduction

1.1 Overview

Optical fibre communication systems are now a basis of modern life. Constant information data transfer, for personal use, business use and government use relies upon fast, efficient and secure systems. This has required consistent and large amounts of research into how to improve these systems, to keep ahead of the demand for more and more data transfer. This in turn has driven the demand for high performance materials for optoelectronic devices and a remarkable step was made with the discovery of graphene in 2004. This is regarded as the first 2D material to be experimentally produced, as predicted by Feynman's "Plenty of Room at the Bottom" lecture.

Since the exfoliation of graphene, the synthesis of a range of different 2D materials for nanoelectronics and photonics have been produced. These range from Phosphorene, a material of made from single layered phosphorous bonded together by Van Der Waals forces to hexagonal Boron Nitride, a single layer of boron and nitrogen bonded in a manner very similar to the way carbon bonds in graphene. There has also been the creation of the transition metal chalcogenides. These are different from the previous films, whereby the film is constructed from a layer of metal sandwiched between two layers of chalcogen. These metals are commonly found in group six of the periodic table, namely Molybdenum (Mo) and Tungsten (W), bonded with members of group 16 of the periodic table made from Sulphur (S), Selenium (Se) and Tellurium (Te). These materials have been found to have a range of different capabilities, and as such, plenty of research has been devoted to these materials. These will be explained in later chapters of this work.

There has also been a range of different methods of synthesising these films. To categorise them, there are two main groups of methods. The top-down method corresponds to taking a bulk samples of the material and breaking it down into a single layer. This involves the scotch-tape method (which was the way the first graphene samples were made) and exfoliation. The other type of synthesis is via the bottom-up methods. This involves the generation of the films from its constituent precursors. This involves chemical vapour deposition (CVD) and Atomic Layer Deposition (ALD). These will be further developed upon in later chapters.

The integration of these films into modern telecommunications is steadily increasing. Usually this involves the use of 2D materials placed onto planar devices. However, some works have seen the use of these 2D films on optical fibres. This enhances the mode field interaction with the film, and offers a long interaction length with the material. We aim at enhancing this interaction further, by combining functional fibre technologies with 2D materials.

1.2 Motivation and Aims

Current telecommunications systems rely on a mixture of planar and fibre systems. This can generate issues in coupling them together, generating loss. One way to bypass this would be to fully fiberize these systems. However, the most commonly used optical fibres offer little in ways to do this. Common solid core-cladding structured fibres are difficult to functionalise, with polishing the fibre down into a D-shaped fibre the only clear alternative. Otherwise, specialist fibres, such as hollow core fibres would need to be made. These fibres have recently seen huge research effort, with the hollow core negative curvature fibres being a particular fibre type of interest. These have recently been seen a very good alternative for solid core fibres, as their air core allows for quicker transmission of signals and with recent developments showing decreases in loss. Furthermore, their large internal surface area offers a good platform for integrating an optoelectronic film. The same is true for twin-holed fibres, currently used for optical fibre poling.

The aim of this thesis is to outline methods of which fibre functionalisation can be achieved. A literature review will look into various ways this is done, such as the aforementioned D-shaped fibre. The main bulk of the thesis will look into our methods to achieve this. We offer an alternative view on how to achieve the best film integration with a maximum of a mode overlap. To do this, we place the film on the inside of the optical fibre. Different applications have been suggested for this; for optical modulation using negative curvature fibres and second harmonic generation for twin-hole poled fibres. A focus will be placed on synthesis methods, involving both planar and fibre devices. The main technique used was that of liquid phase deposition, with the precursor ammonium tetrathiomolybdate. Our modulation results show potential, with a 3dB depth having been demonstrated. This required an external high voltage of the order of kV. Integrating such devices into current systems may not be easy, so we suggest methods to lower this high voltage.

1.3 Outline

The outline of the thesis is as follows:

The second chapter will look into a background on the materials of interest in this thesis, namely those of MoS_2 and WS_2 in their 2D form. An outline and background history on the capabilities of these films will be given, as well as various characterisation techniques used to test the quality of the films. The future outlook for these films will also be outlined. This will be followed by a deep dive into analysis on how these films have been synthesised, with a range of different techniques investigated.

Chapter 3 will concern work that has been performed with optical fibre poling, which has been enhanced by the integration of a 2D film. This will begin by outlining the background of poled fibres, as well as discuss how integrated films help the quality of the second harmonic generation. This will be followed by an explanation of the work we have performed on the twin hole fibres, integrating 2D films into them. We will then draw conclusions from this, asking whether the additional loss is outweighed by the increase in second order nonlinearity increase.

The next chapter, chapter 4, will focus on work involving negative curvature fibres. This is a relatively unique fibre type, and so the chapter will begin by focussing on the guidance mechanism behind them. Simulations work involving COMSOL Multiphysics will then be discussed, followed by experimental work from this. This will then outline the applications of these fibres, namely optical modulation through absorptive effects, with a conclusion of the fibres' capacity.

The penultimate chapter will look at other materials that have been investigated during the course of this work. These will look into WS_2, another well researched 2D material and ZnSe, a bulk transition metal dichalcogenide (TMDC) material. These have been used for similar reasons to MoS_2, but to differences between them, have not been the focus of this thesis. The reasoning behind this will be outlined in these chapters.

The final chapter will give a look into the future work that could come from this project. Here, ways to improve the previously made devices will be highlighted, with suggestions of theoretical and experimental work that has been performed used to strengthen some of our claims.

Chapter 2 Materials Background

2.1 Outline of materials

2.1.1 Graphene

The field of 2D materials has long being theorised, however, it was only in 2004 with the exfoliation of graphene from graphite that it was proven experimentally [1]. It would be impossible to write this thesis without a brief analysis of graphene, and how it has changed the outlook for optoelectronics.

Graphite is a well known material, commonly used in pencil lead. It is formed by stacked layers of carbon atoms, which naturally bond into a honeycomb lattice as seen in Figure 2.1a [2]. The isolation of a single layer of graphite generates a material known as graphene. Amazingly, this material is chemically stable in its monolayer form, and since it was experimentally exfoliated by Novoselev et al. in 2004, it has opened up new areas of research into 2D materials [1].

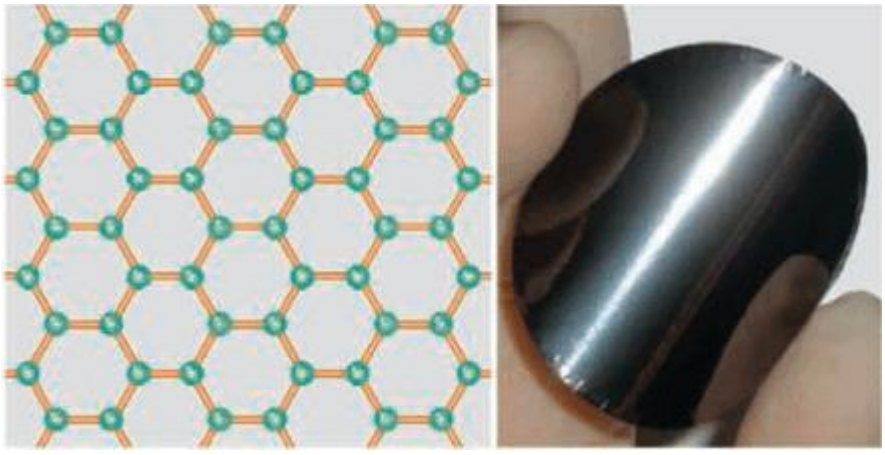

Figure 2.1: LHS: The atomic image of the honeycomb lattice of graphene. The green dots correspond to carbon atoms, and the yellow lines are the sp^2 hybridized bonds between them. RHS: Graphene paper, a conductive, thermally stable and flexible material. From ref. [2].

What has driven this intense research has been the remarkable properties of graphene. The original paper describing the exfoliation of graphene goes onto outline the materials potential as an electronically active material. The electrical field effect was observed in few layered graphene, which had a thickness of less than 10nm. The paper also quotes high mobility values, reaching 10,000 $cm^2/V.s$ [1]. The material was therefore touted as an interesting route forward for metallic transistors, however further applications have been considered. The paper finishes with the

sentence "… nontransistor applications of this atomically thin material ultimately may prove to be most exciting."

This was indeed proven to be correct. Modern graphene technologies are now beginning to move from the laboratory and into industry, as well as research into graphene applications now beginning to be seen not only in scientific journals, but also in the mainstream media [3],[4]. Furthermore, a wealth of research into other fields regarding graphene, such as material synthesis [5], graphene composites [6] and other 2D films have been investigated [7]-[12], leading to current results showing the production of conductive, pristine graphene paper as seen in Figure 2.1b [2].

This can be observed in papers relating to exfoliation and CVD techniques for graphene. The original method to create graphene was done by a rather crude method known as the scotch tape method. This is a rather simplistic approach to graphene creation, whereby the film is extracted from its bulk counterpart, graphite, by applying adhesive tape to the bulk material and "ripping" a layer off. This method is grouped into the category of the 'top-down' approach. Other such methodologies include Lithium intercalation [13], sonication of bulk material in a solvent [14], and ball-milling [15]. These are cost-effective methods to generate sheets of graphene on an industrial scale. Regular papers are published on such films, as the flakes generated are excellent for scientific purposes as they are almost purely single crystalline.

Other methodologies of graphene creation also exist. This category includes synthesis of graphene flake through methods such as Chemical Vapour Deposition. For graphene synthesis, this commonly uses the breakdown of organic gas, CH_4, onto assembled substrates of either Copper, Cu, or Nickel, Ni, under vacuum and high heat [16],[17], an example of which is seen in Figure 2.2. A metal is used as the bonding sites offered by the metal lattice is well matched to that of crystalline graphene. Many reports have attested to the use of this technique, as highly crystalline and large scale graphene films can be formed. However, the synthesis process is more complicated than exfoliation methods, and many papers are still being generated on the best 'recipe' to create such samples. Furthermore, great lengths must be taken to ensure a high quality film has been created, such as pristine and clean growth conditions, and pretreatment techniques such as Plasma Etching [18]. These deposition techniques will be further remarked upon in the next chapter.

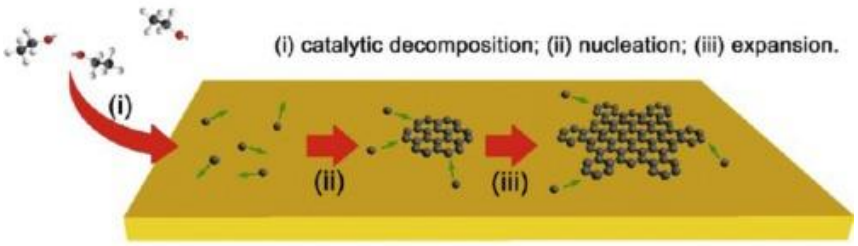

Figure 2.2: An outline of the CVD process for the formation of graphene onto a metallic substrate. The three steps are undergone under high temperature and under vacuum. The atmosphere of the chamber is inert gas to remove the likelihood of contamination. From ref. [16].

Graphene has also been exploited for its optical properties. Remarkably, graphene has been observed to have a theoretical constant of absorption of light, at 2.3% [19]. This is due to graphene's unique structure, as a 2D material without a band-gap. This percentage increase by the number of layers of graphene present. Furthermore, this means that graphene is visible to the naked eye, despite being only a single layer thick!

Further works have analysed the third order optical nonlinear response of graphene [20]. As a centrosymmetric material, graphene has no discernible second order nonlinearity, however it can give rise to third harmonic generation. Other nonlinear effects such as four-wave-mixing have also been experimentally proven [21]. The results show the material has a good third order nonlinear susceptibility, a measure of the third order nonlinear strength, which is comparable to other nonlinear materials such as carbon nanotubes. Combined with monolayer graphene's small absorption, graphene is thus a material of interest for nonlinear optical devices.

The third order nonlinearity of graphene has been exploited in fibre-based systems. A wealth of research has seen graphene used as a saturable absorber [22],[23]. This is a device placed within a fibre laser cavity to generate pulses, which become transparent under high optical intensity due to electrons becoming excited from the valence band to the conduction band. However, the relaxation time for these materials is extremely fast, allowing for the valence band to be refilled before the next pulse. To achieve this with graphene, high power laser experiments have been used on graphene integrated systems, with the semiconductor placed onto the end face of the fibre, or even onto D-shaped fibres [24]. Graphene excels as a cheap alternative to SESAMs, with high stability and a remarkable damage threshold.

Other fibre based systems involving graphene is in the field of sensing. Here, graphene is deposited within the vicinity of an optical fibre – usually one that has active cladding guidance, such as a tapered microfiber [25] or D shaped fibre [26]. Using different methods, notable changes to the

guidance properties of the fibre occur due to the local environment. One example uses a microfiber placed so that evanescent light interacts with graphene, seen in Figure 2.3. The graphene undergoes a refractive index change when placed in a NH_3 environment, due to absorption of the molecule. The output of the MZI therefore observes a change as the refractive index alters the guidance properties. For increasing NH_3 absorption, the spectral output decreases.

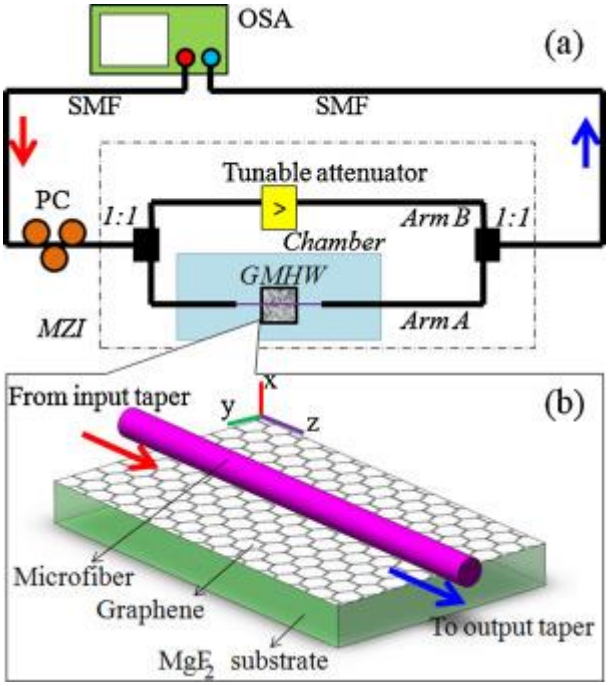

Figure 2.3: A sensing device manufactured using a microfibre in contact with a graphene sheet. When placed into the chamber, the presence of NH_3 changes the refractive index of graphene, leading to a change in the guidance properties of the fibre. The interference change is measured by an OSA, and can give a measure of the concentration of the NH_3, by noting the change in the output spectra. From ref. [25].

However, graphene does have its drawbacks. Due to its bandgap-less nature, it would be hard to integrate into semiconductor based transistor systems. Post processing of the graphene itself could lead to such a device being created [27], however since the isolation of graphene, alternative 2D materials have been investigated. These include the transition metal dichalcogenides [8],[9], phosphorene [11], germanene [12] and hexagonal Boron Nitride (h-BN) [7] amongst others.

2.1.2 2D Transition Metal Dichalcogenides

Building upon the work carried out on graphene, other 2D materials have been analysed. One family of materials of real interest are the TMDCs. Figure 2.4 shows the structure of the 2D layered material featuring layers of transition metal (M), usually Mo/W, sandwiched between layers of chalcogen (X), usually S/Se, denoted in the form of MX_2. There are a few major differences between graphene and MX_2. Intrinsically, the notable difference is that TMDCs have an optical bandgap

larger than 0 [28]. This opens up the materials for applications that graphene cannot easily address, such as transistors [28]. This section gives an in depth discussion on the capabilities of TMDC films, with MoS_2 used as the canonical TMDC used in the arguments.

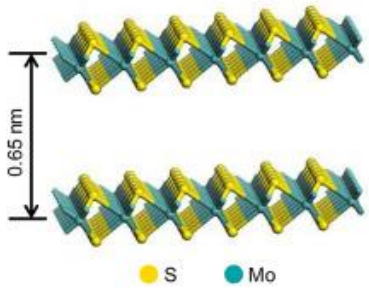

Figure 2.4: The atomic structure of MoS_2. This structural shape is much the same for other MX_2 2D materials, with S being replaceable by Se/Te and Mo replaced with W, for example. From ref. [29].

For current to flow, the conduction band within the material must be (partially) occupied. For metals, the conduction band and the valence band intertwine, meaning current flows readily. However, for semiconductors, there is a gap between them where no electron states can exist. This is known as the bandgap, as explained in Figure 2.5 [30]. To move from the valence band to the conduction band, electrons must be supplied an amount of energy more than or equal to the bandgap. By altering the value of the bandgap, various properties within the material such as its absorption can be changed. For TMDC materials, such as MoS_2, the bandgap has been observed to increase when the number of layers of the material decreases [8]. Furthermore, a sharp change is seen from moving from bilayer film to a monolayer film. This is due to the change from an indirect bandgap (bilayer) to a direct bandgap (monolayer). Figure 2.6 describes this [8], where the transition region between the two bands is able to be excited directly, without the need of additional crystal momentum to shift the electron from the highest point of the valence band to the location of the lowest point of the conduction band. For MoS_2, the alteration of the bandgap is significant, changing from 1.29eV for bulk material to 1.9eV for monolayered film. Mak et al. were the first group to experimentally characterise these changes, using photoluminescence studies on exfoliated films [8].

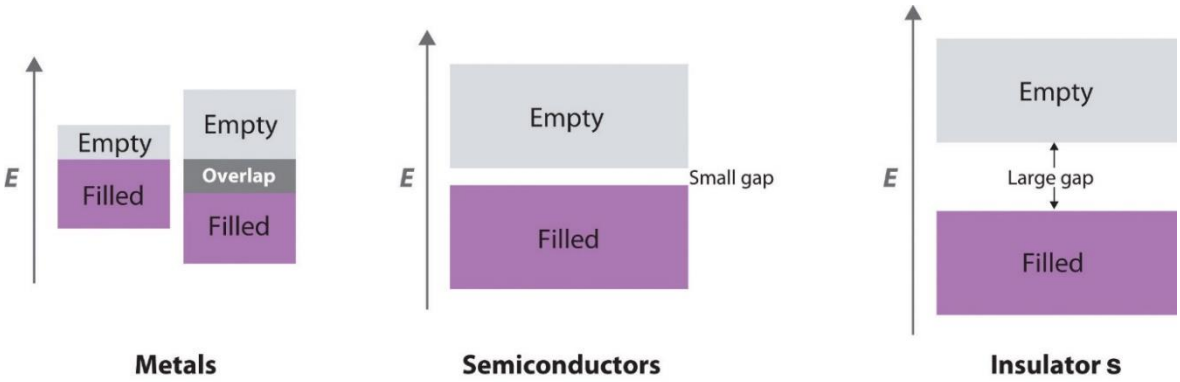

Figure 2.5: The valance (dark purple) and conduction (grey) band occupation for different genres of material. The small gap for the semiconductors is known as the bandgap. From ref. [30].

The presence of a bandgap within MoS_2 and other TMDC films has led to many applications that pure graphene is unable to perform. One of these is the field effect transistor (FET) which is a semiconductor device that allows current to flow between two terminals known as the source and drain. To do this, the electrical properties of the semiconductor material between them are altered by an external electric field, known as the gate. Simple MoS_2 transistors have already been demonstrated. A key paper on this is from Radisavljevic et al. whose work was the first published room temperature MoS_2 FET [28]. The device which can be seen in Figure 2.7 produced mobility values which could be suitable for commercial applications, at around 200 $cm^2V^{-1}s^{-1}$. The switching capability was performed at low voltages. To do this, pristine MoS_2 sheets were created using the aforementioned scotch tape method, followed by the deposition of HfO_2 gate insulating layer onto the 2D layers. With ever increasing research into silicon miniaturization, TMDC materials offer a potentially very useful method for augmenting these incumbent technologies.

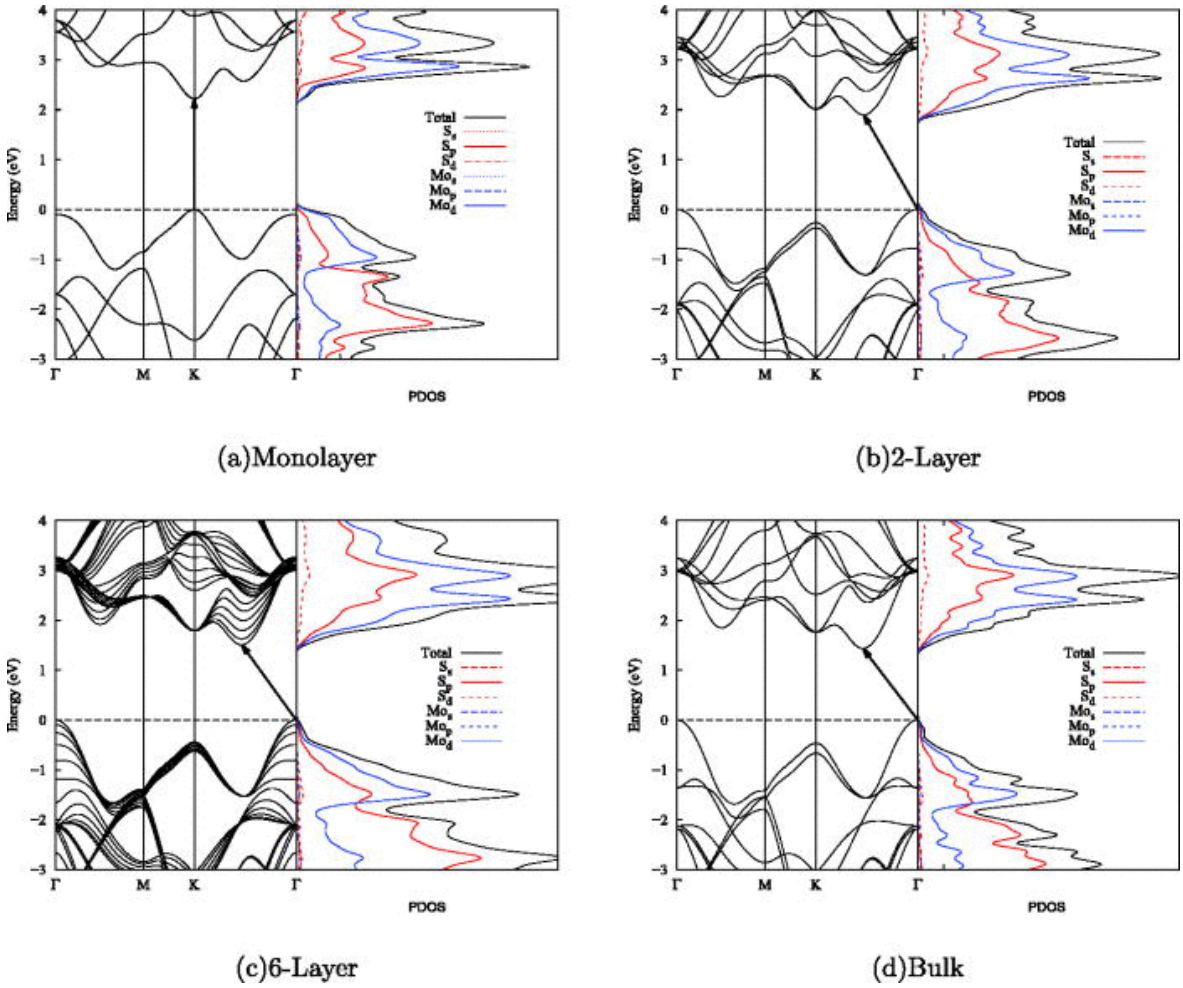

Figure 2.6: The bands that form the bandgap for different number of layer of MoS_2. For monolayer material, the peak in the valence band is located at the same location as the lowest point of the conduction band, hence is a direct bandgap material. From bi-layer to bulk material, these two points do not line up, so require extra crystal momentum to transfer to the location of the lowest conduction band. This is known as an indirect semiconductor. Taken from Ref [8].

This is further enhanced by looking at the optical qualities of TMDC films. Much has been discussed in regards to MoS_2's bandgap, but it is interesting to note how this affects its refractive index and absorption coefficient. Unlike graphene, MoS_2's absorption quality is a function of wavelength. This is well highlighted in work from Yim et al. who used ellipsometry to measure the n and k values of MoS_2 [31] as shown in Figure 2.8. The two peak absorptions are related to MoS_2 exciton absorption bands. Furthermore, the two properties were seen to be highly dependent on the film thickness, meaning control on the two quantities can be given by selecting the amount of deposited layers. Note also how the absorbance ($\alpha = 4\pi k/\lambda$) shows low absorption at low energies. This implies MoS_2 would be an almost lossless transmitter at infrared wavelengths.

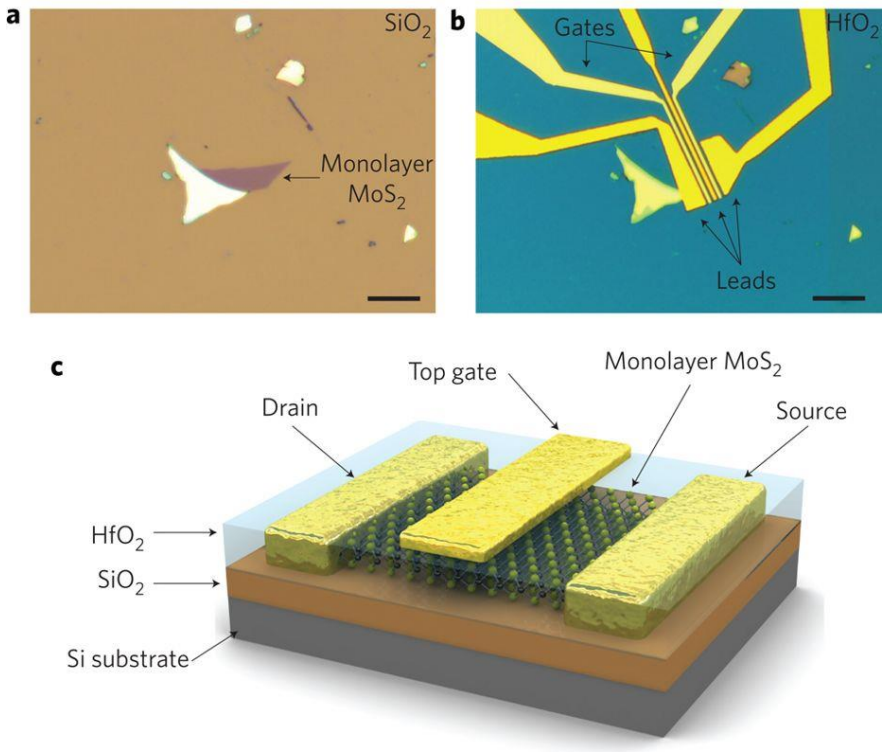

Figure 2.7: The FET created using an exfoliated monolayer of MoS_2. From ref. [28].

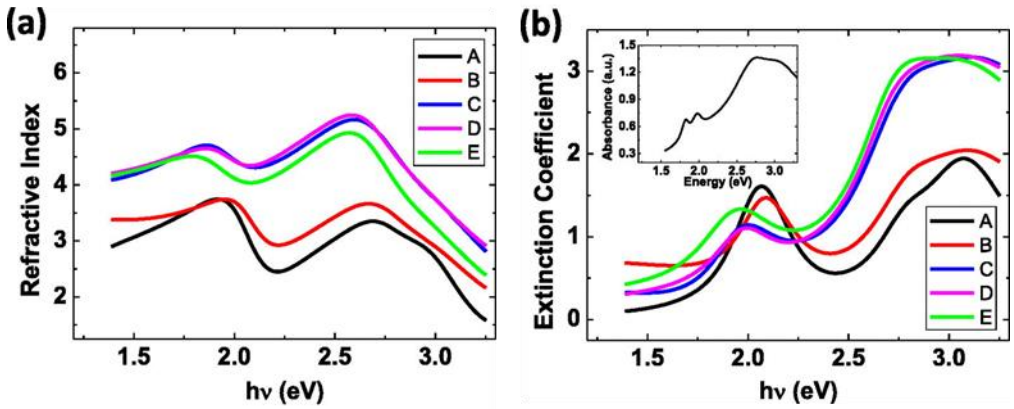

Figure 2.8: The optical constants of MoS_2 for different layer numbers of MoS_2. A corresponds to tri-layer MoS_2 material, with B,C,D,E increasing in multilayer thickness. The thickness of the samples was measured by spectroscopic ellipsometry - A had a thickness of around 1.99nm, B a thickness of 3.01nm, C had a thickness of 5.53nm, D had a thickness of 9.83nm and E a thickness of 19.88nm. From ref. [31].

There is also interest in analysing MoS_2 and its tungsten analogue for their optical nonlinearity properties. There have been numerous studies on the use of MoS_2 for third order effects [32]-[34], as discussed with graphene. However, due to the materials crystal structure it also has a second order nonlinearity value greater than 0. This is known as a non-centrosymmetric material, as it lacks a centre of inversion symmetry as described in Figure 2.9 [34]. This allows MoS_2 to give rise to

effects such as second harmonic generation (SHG) [35]. This is necessary for many optical systems, such as UV lasers to generate short wavelength light.

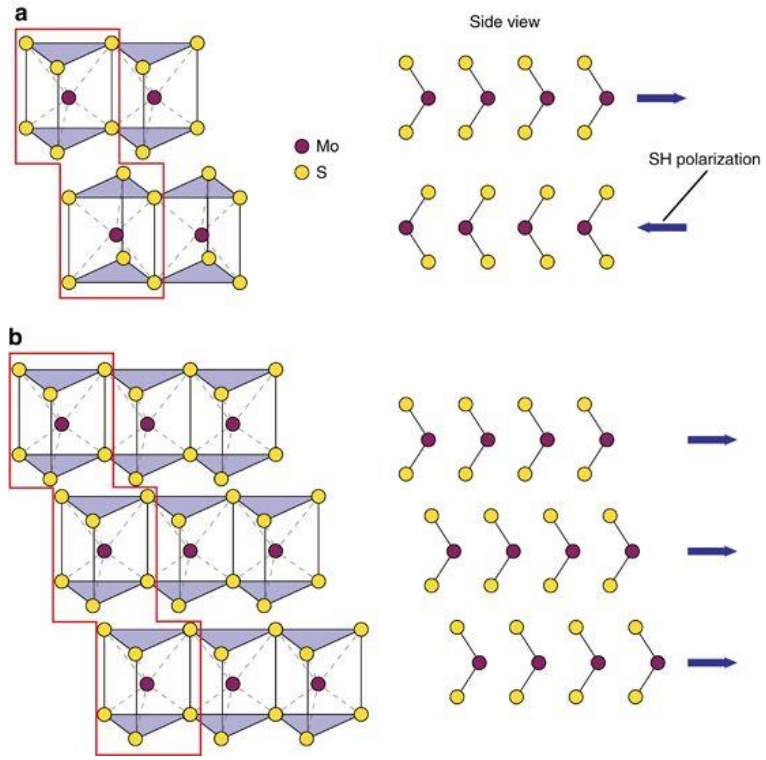

Figure 2.9: The structure of MoS_2 in bilayer and tri-layer form. The alignment of the sulphur atoms in the bi-layer film causes the material to have a centre of inversion symmetry. This is different for the tri-layer film, where this symmetry does not exist. This allows for second optical nonlinearity effects to occur. From ref. [34].

Further analysis of MoS_2 and other TMDC films has also seen external control on the optical properties of the material using an electrical field [36]. By applying extra charge carriers into a film, the refractive index and absorption coefficient are affected. This has highlighted MoS_2 and the TMDC films for possible optical modulation processes [36][37][38]. As a figure of merit for the capability of the modulation, the change of the refractive index per volt, $\Delta n/\Delta V$, has been calculated for two of the key TMDC films, MoS_2 and WS_2. From ref [38] MoS_2, the $\Delta n/\Delta V$ is found to be 0.01dB/V. The value of the $\Delta n/\Delta V$ for WS_2 is calculated to be 0.012dB/V, for a refractive index change of 0.83dB under the application of 67V [36]. It would therefore seem that the two films react with similar capabilities, but Yu et al. [36] show in their paper that WS_2 is the film with the highest modulation but unfortunately do not quantify it.

Like graphene, TMDCs have also found uses as saturable absorbers in laser systems [39]. Through the same techniques, such as D-shaped fibres and placing MoS_2/WS_2 onto the endface of a fibre, pulsing can be generated in the laser, both of Q-switching [40] and the mode-locking regime [41]. Once again, a high amount of power needs to be applied to the additional material.

The synthesis of TMDCs also is much like that of graphene. Both bottom up methods and top down methods exist. The top down methods include Lithium intercalation [42], sonication [43] as well as the scotch tape method [28]. This is complemented by the bottom up methods, including CVD, but also including ALD and liquid precursor techniques. This allows for TMDCs to be deposited upon CMOS surfaces that are then able to be used in device applications. This is very beneficial, as the transfer of films can leave them damaged.

For the majority of this discussion, MoS_2 has been used as a reference material. However, the field of monolayer TMDCs includes more materials such as WS_2 and $MoSe_2$. The characteristics of these materials are worth investigating. Although the properties of the materials act in a similar method, the intrinsic values between them are different. Values such as their bandgap, second order nonlinear coefficient and mobility all differ from material to material. This makes choosing the correct material for the correct application important. An analysis of these material's characteristics is shown in Table 2.1. This means that a range of different applications of TMDC materials can be used, with further control on such qualities given by being selective on the number of layers deposited.

Material	**Single Layer Bandgap (e) (eV)**	**Bulk Bandgap (e) (eV)**	**Single Layer Bandgap (DFT) (eV)**	**Bulk bandgap (DFT) (eV)**
MoS_2	1.89	1.23	2.38	1.23
$MoSe_2$	1.57	1.09	2.03	1.09
WS_2	1.98	1.35	2.51	1.32
WSe_2	1.54	1.2	2.11	1.21

Table 2.1: The bandgap values for four well known TMDC films, in both their monolayer and bulk values. The experimental values are highlighted as (e) [44] and theoretical values taken by the DFT calculation and labelled as (DFT), calculated via DFT, are supplied [45].

The synthesis methods to generate the TMDCs are also very similar. However, in general, the selenide composites require a lesser temperature to achieve synthesis of high quality films. When trying to synthesize such materials is it important to note the conditions involved. For the selenide TMDCs, a constant flow of toxic H_2Se is needed, something that raises concern for safety. Optimizing the synthesis conditions required for each application is key when considering which TMDC to use for what purpose. Due to the clear benefits TMDC materials offer, it is this form of monolayer material that will form the bulk of the experimental work in this thesis.

2.1.3 Characterisation of Materials

As research into the capabilities of 2D TMDC materials has advanced, so have the methods by which to measure the quality and uniformity of such films. These range from optical methods, such as Raman spectroscopy [46] and X-Ray photon spectroscopy (XPS) [47] to mechanical techniques, such as atomic force microscopy (AFM) [48]. Each method is able to analyse different qualities of the film, such as the number of layers, the crystal quality and even atomic ratios.

The phenomena each technique exploits to characterise also differs. We will begin by discussing the technique known as Raman spectroscopy, and how it can be used to analyse films. Raman spectroscopy works by focussing laser light onto a target. This supplies energy to electrons within atoms, exciting them to states known as virtual levels [49]. To relax down to the ground state, the electrons elastically relax, releasing photons of the same energy as the initial excitation. This is the case for elastic scatter, and is known as Rayleigh scattering. However, a small portion of the excited electrons relax down to the ground state through an intermediary higher energy state. This is known as inelastic scattering, and releases a photon of energy different to the case of elastic scattering. This difference is measured, and the differences in the wavelength values is plotted, generating the Raman shift spectra. The outputted light is usually refocussed onto a CCD camera which is able to give a measure of the intensity of the emitted light, as well as a measure of the Raman shift. Each bond produces a characteristic Raman peak that can be deconvolved for material analysis.

For 2D TMDC materials, there are two well recognised Raman peaks. These are known as the A_{1g} and E^1_{2g} bands, corresponding to in-plane and out-of-plane resonances, as seen in Figure 2.10a. For monolayer material, the response is shown in the red 1L trace in Figure 2.10b. Raman spectroscopy becomes a useful tool for TMDC materials as the separation of these two peaks changes when films of different thicknesses are analysed. This effect takes its origin from coulomb shielding effects on the atoms, as well as interlayer interactions. A study by Li et al. analysed how this response reacts, showing that the larger the difference in the two Raman peaks, the more layers of material is present [46]. For 532nm laser light, typical Raman spectra for MoS_2 shown in Figure 2.10b.

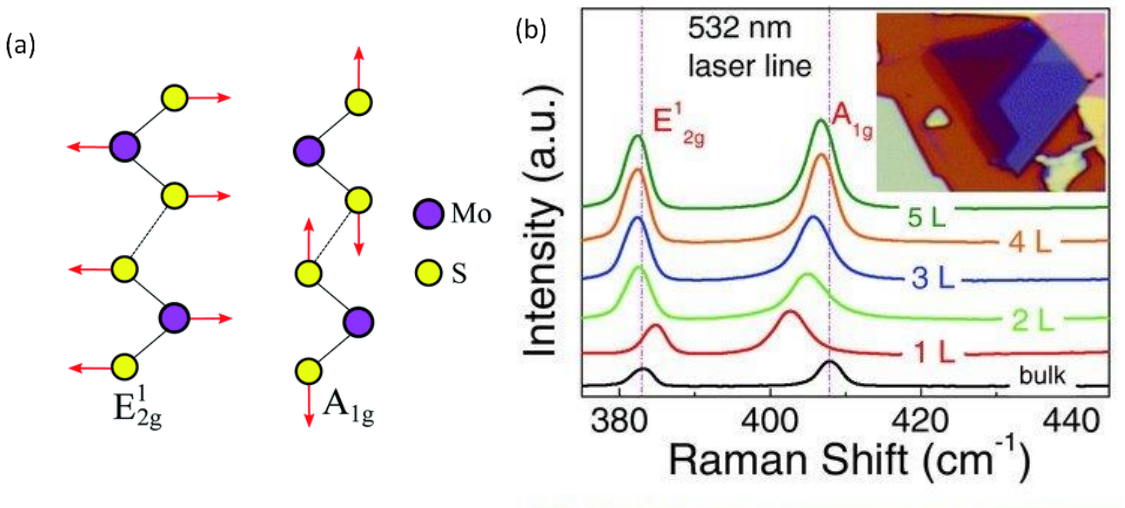

Figure 2.10: (a) The vibrations between the molecules that form the two notable Raman shift peaks, from ref. [50]. (b) The Raman traces of MoS_2 for different layered material. The peak positions change, causing the separation between them to also to change. From this difference, the number of layers present in a sample can be deciphered. From ref. [46].

When analysing such spectra, there are also other characteristic aspects that can be used to learn more about the sample. The full-width half-maximum (FWHM) of the two peaks can give a measure of the crystalline quality of the film. For many exfoliated samples, the characteristic peaks are very sharp, with FWHMs of around 4-6cm^{-1}. Many CVD grown TMDCs are known to have wider Raman peaks, with many papers reporting that higher temperature depositions have thinner FWHM, implying higher temperatures produces more crystalline samples. Furthermore, knowledge can be gained by analysing the relative intensities of the peaks. It has been noted by work from Chakraborty et al. that with more excess charge applied to a MoS_2 crystal, the intensity of the E^1_{2g} increases in comparison to the A_{1g}. The FWHM of the A_{1g} peak also increased [51]. Exfoliated samples are well known to be very crystalline and it is for this reason that exfoliated films are widely regarded in 2D TMDC based literature.

Raman spectroscopy offers itself as an exceptionally useful technique that is non-destructive. Raman scans can be completed at low power, allowing for the film to remain undamaged. This allows for the film to then be used for application purposes, or even for in-situ characterisations. Furthermore, the usage of the method does not require the material to be on the surface of the investigated substrate. The focus of the spectroscope allows for the user to align the beam on parts of the deposition that may be blocked off from other (surface) methods. This makes Raman a quick and relatively easy technique to gauge the quality of deposited TMDC films.

Photoluminescence is another technique much investigated for TMDC characterisation. It is an optical technique, much like that of Raman spectroscopy. An incident laser beam is focussed onto the sample, with the optical response being that of photoluminescence. Here, the incident light excites electrons/holes to cross the optical bandgap and recombine. This releases energy in the form of photons [52], corresponding in wavelength to the value of the bandgap. It is well recorded in the literature that the bandgap of TMDCs varies with the number of layers deposited. This will therefore alter the peak positions of the photoluminescence trace allow us to characterise the number of layers present. A good example in Figure 2.11 shows how the bandgap of MoS_2 changes when the number of layers is different. As can be seen, the value decreases, which can be analysed with PL results.

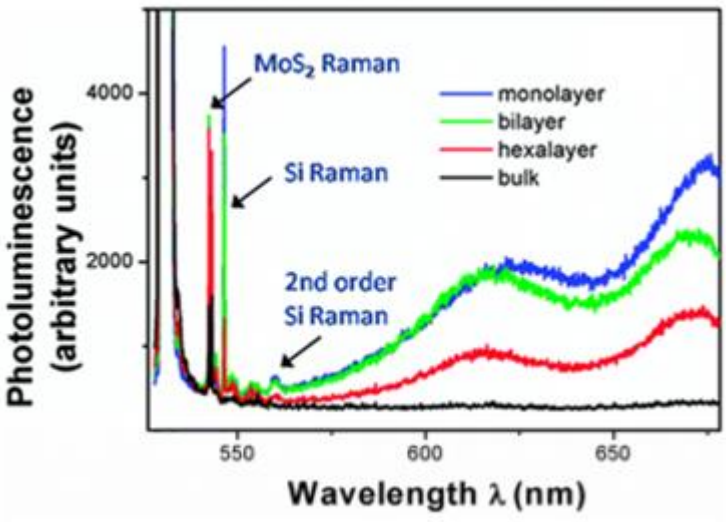

Figure 2.11: The PL intensities for different layered films. From Ref [53].

Usually, this work is able to be performed in the same sort of set up as Raman spectral studies. Analogous to Raman, this method does not require for the surface of the material to be the surface analysed, and it is a non-destructive technique. Overall, Raman and PL spectroscopy are able to produce high accuracy measurements as to the number of layers present in a TMDC sample.

Another technique commonly applied is Atomic Force Microscopy. Here a cantilever is used to scan over the surface of a material, and measure the repulsive (although sometimes attractive) force of atoms. Many AFM measurements are focussed on characterising the exact height of a TMDC film. To do this, a scan is performed over a longer length scale (over a few microns) moving from the sample onto the substrate. The height can then be measured by analysing the movement of the cantilever [54]. This technique can be used to measure the height of the deposited layers, as well as confirm the crystallinity of the material. This can produce images as seen in Figure 2.12, which shows an AFM trace shown along the yellow line [48]. Here, an exfoliated triangular sample is shown, with multiple layers showing how the film has a ‘step’ when moving along the trace. The

result of this clarifies the number of layer deposited and the uniformity of the sample. Some aspects of AFM studies can be destructive of the sample and requires a flat surface with the film presented to the cantilever. For high precision experiments, scanning tunnel microscopy can be used to achieve atomic resolution. This is able to build up a map of how individual atoms are located in the material. This produces images shown in Figure 2.13, taken from Lu *et al.*, where a map of the sample is created [55].

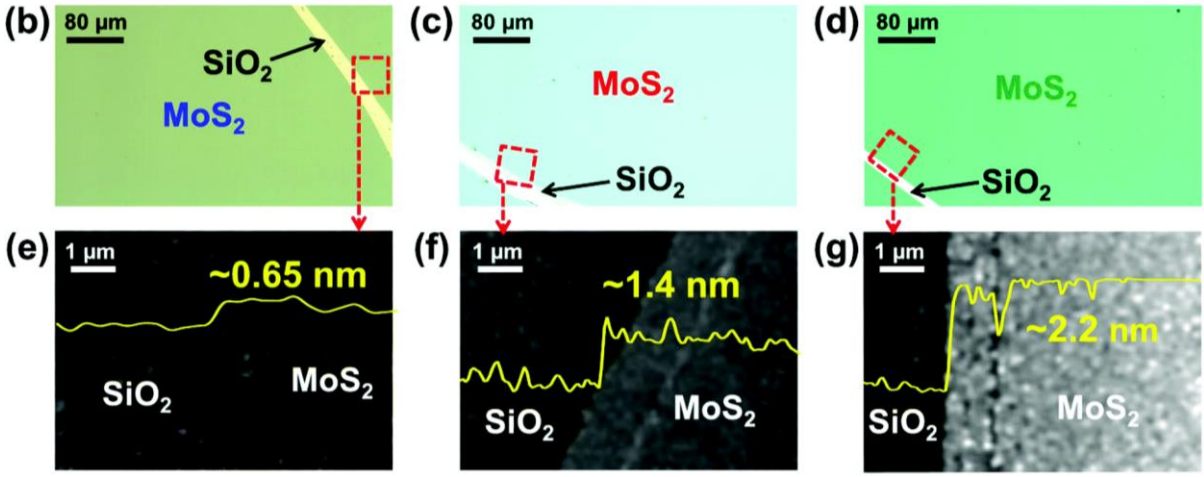

Figure 2.12: AFM images for MoS_2 film of different thicknesses. This is a key method of analysing the thickness of a sample, as well as characterising the uniformity of a sample. From ref. [52].

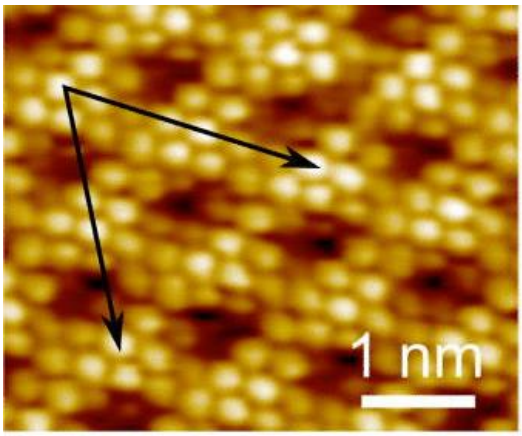

Figure 2.13: STM images of an MoS_2 sample. The bright region where the arrows originate correspond to sulphur atoms, with the arrows showing the direction of the nearest neighbour sulphur atoms in the (100) and (010) crystal lattice. The hexagonal structure of the crystal can clearly be shown with a lattice constant of 0.315nm. This can be a very precise method of analysing the crystal quality of a film. From ref. [55].

The previous characterisation techniques focus on how many layers are deposited and on the uniformity of the film. X-ray photoelectron spectroscopy differs in that it measures the ratio between the constituent atoms of a material, as well as giving a measure of the presence of any impurities. It works by concentrating X-rays onto the surface of a film, which is supplies enough

energy to eject the electron from the nucleus it is bonded to. The kinetic energy of these electrons is measured. Each energy corresponds to the presence of a unique atom, allowing for the number of these bonds to be deciphered by analysing the intensity of each energy peak [56]. By taking a ratio of the intensity of each peak, the ratio of Metal to Chalcogen can be deciphered. This gives a good indication of quality of the deposited material, as this method is able to detect defects within the material, and is able to confirm the purity of the sample. The technique in itself is non-destructive, but for the best analysis, the sample needs to be coated with a carbon coating. This coating is not necessarily easy to remove, meaning the sample is unable to perform in future experiments. It also suffers from a poor penetration depth, so cannot accurately measure bulk films.

The characterisation techniques allow for us to learn a lot about the film quality. When all the techniques are used for a single sample, much can be learned, both about the deposition quality as well as the applications that different samples could be used for.

2.2 Materials Synthesis

Another factor driving the field of 2D materials is the synthesis of reproducible, uniform and high quality flakes. Since the generation of graphene, there have been a wealth of works on how best to create 2D material. The definition of the best material is also in contention. Some applications require large area films, with less effort noted on the quality of the deposition, whereas other applications require small scale 2D films, but rely on high crystallinity and uniformity. In general, highly-crystalline purely-monolayer films are the most sought after. This is because these films produce the highest values of bandgap, second order optical nonlinearity and carrier mobility [57][58]. In this section, various different deposition methods of 2D materials will be discussed, analysing the benefits and detriments of each method.

It is formally considered that there are two fields of deposition techniques. These are known as the bottom-up and top-down methods. The top-down method can be described as taking a bulk material, and through various techniques, removing multiple layers of material. The process can then be repeated until the film is in its monolayer form. The first exfoliation of graphene used this technique, using the scotch-tape method [1]. The bottom-up approach differs by the reaction of precursor materials onto a substrate, usually a metal or glass. This involves techniques such as CVD.

2.2.1 Exfoliation

2.2.1.1 Exfoliation Techniques

The nominal exfoliation technique is the well known scotch tape method. This was the first technique to isolate monolayer graphene. The method involves using adhesive tape on a bulk sample of layered material, which can be performed in ambient conditions. The weak Van der Waals forces holding the graphene together are broken by the force applied to the ripping motion for the tape. The process can be repeated multiple times, until only a single layer of material remains. However, it is only able to produce small scale. Furthermore, the uniformity of such samples can be an issue, with images such as Figure 2.14 showing a deposition of graphene with multiple layer differences on a small (micron) scale. Note also various cracks and folds within the film. If such a film were to be used for optical purpose, these effects would induce heavy loss due to scattering. This limits the applications of the exfoliated films.

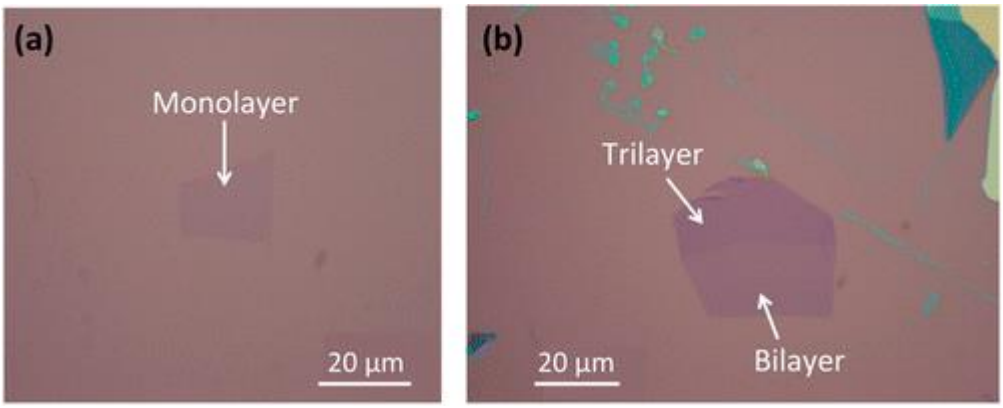

Figure 2.14: An exfoliated sample of graphene. Note the inconistencies of the film over small length scales as seen in (b). This is an issue of exfoliated samples, as non-consistent film is created. From ref. [59].

However, monolayer material produced via the mechanical exfoliation process have their root from highly crystalline bulk material. When a layer is isolated, it still maintains the high crystallinity. Due to this, many laboratory experiments still use the scotch tape technique, as it allows for ideal performance films for small scale experiments, such as transistors, to be tested. Small scale devices tested with supreme crystallinity allow for future devices (of larger scale) to be constructed with full knowledge of the capabilities of the material.

Other techniques to exfoliate a film via the top-down method include the use of a liquid solvent host to split the film apart. This is known as the liquid exfoliation technique. Here, bulk crystals of layered material are placed inside of a solvent host, commonly IPA or NMP [60]. The solution is then placed in a sonicator – an instrument where a substance is subject to sound waves. The agitation of the crystals mixed with bubbles forming between the layers of the material leads to the

dispersion of layers from the bulk sample. By pouring the sample onto a substrate, and allowing the liquid to evaporate, high crystallinity material remains. However, this relatively simple technique is not without its issues. The deposited crystal films are usually of small size, with few monolayer samples produced throughout the process. The material is therefore has very inconsistent thickness. However, much like the scotch tape method, the applications for such a technique are plenty. Other liquid exfoliation techniques are also known, with the ultra-sonication method being the easiest to use.

Lithium intercalation exfoliation is one of these. For this technique, bulk layered material is augmented by the insertion of Li^+ ions between the layers. The intercalation then splits the layer by the introduction of a thermal shock, or though ultra-sonication of the sample. The produced layers suffer from the many problems outlined in the liquid exfoliation method, with poor uniformity and small size. However, they also offer the same benefit of high crystallinity. One example of lithium intercalation used for device generation is from Zhao *et al.* who used graphene oxide as an intercalant of MoS_2 [61]. The graphene 'wrapped' around the MoS_2 to generate a heterojunction. This was then deposited onto a mirror and placed on the inside of a laser cavity to produce pulsing.

2.2.1.2 Exfoliation Technique Applications

As stated, a major benefit of exfoliation techniques of bulk samples down to few-layer samples is the superb crystallinity of the produced films. This offers a wide range of applications that can be tested in the laboratory to measure the feasibility of few layered films. One key area of this is in the creation of FET-based structures which require small gaps between contact electrodes, a prime example of which is the previously highlighted work from Radisavljevic et al. who used scotch tape exfoliated MoS_2 to create the device seen in Figure 2.6 [28]. Further applications include those of biological anti-microbiotics and catalysis. However, for commercialisation of such materials, many devices require large area films of high uniformity and stability. Other methods of material creation have therefore been analysed.

2.2.2 Chemical Vapour Deposition

2.2.2.1 Chemical Vapour Deposition Techniques

CVD is possibly the most regularly used bottom-up technique used for the growth of 2D materials. Precursor material is controllably flown into a chamber into which a substrate is held and heated via a furnace to allow growth of the film. Through control of the temperature of the furnace, the rate of precursor flow and the pressure of the chamber, monolayer material can be achieved, on centimetre scale. CVD offers high uniformity, with very few impurities on the sample. The

crystallinity can also be controlled by adjusting the aforementioned parameters, as well as by pre-treatment or by changing the substrate.

The CVD growth of graphene is performed by the decomposition of methane gas, CH_4, onto a substrate. There are a multitude of works refining this technique, by altering the chamber conditions as mentioned in the previous paragraph. Graphene has been observed to grow well on metallic substrates, as these act as catalysts, by increasing the rate of dehydrogenation of the precursor and enabling a surface for the growth of graphene clusters [62]. This lowers the synthesis temperature from around 1100-1600°C to around 1000°C. However, many electronic applications require the use of nonconductive host materials. Graphene therefore needs to undergo a lift off process, to place the 2D film onto a more device compatible substrate. This is performed by the spin coating of the sample with PMMA, and the removal of the metallic substrate via an acid bath. This can be potentially damaging to the graphene, causing folds or cracks within the graphene structure. However, TMDC materials do not need a catalyst to achieve low temperature growth, allowing as-grown material to be used for devices.

TMDC films come with a wide range of different precursor materials. A selection of these is presented in Table 2.2. Two significant methods apply here. This influences whether the CVD process is a one-step or a two-step procedure. This revolves around the oxidation of the original precursor. Some works react $MoCl_5$ straight with S, to generate MoS_2 in a single step [65]. Others will focus on the sulphurization of MoO_3.

One key factor for CVD growth of 2D films is the temperature at which deposition occurs. A lot of papers have analysed this, noting Raman responses and XPS measurements to see the crystal quality produced. In general, temperature appears to be a key factor. Higher temperatures tend towards higher quality films [63] hence the high values of temperature seen in Table 2.2. However, there are many papers which focus on lowering the temperature for deposition of 2D materials, by changing the precursor such as Ref [64]. This allows for different substrates, such as plastic substrates as noted in Ref [64], which are prone to damage at high temperature, to be used.

Reference	Precursors	Substrate	Temperature (°C)	Film created	Quality	Application
[62]	$MoCl_5$ + Sulphur powder	Si/SiO_2	850	MoS_2	High Crystalline mono/bi-layers	
[64]	$Mo(Co)_6$ and H_2S	Polyimide	200	MoS_2		Gas sensor on plastic
[65]	MoO_3 + S	Si/SiO_2	650	MoS_2	Monolayer film found	
[66]	MoO_3 + S	Si/SiO_2	625	MoS_2		Sensing of NO_2/NH_3
[67]	MoO_3 + Sulphur powder	Sapphire	900	MoS_2		Sensing
[68]	Mo sputtered film + Sulphur	Si/SiO_2	600	MoS_2		
[69]	$Mo(CO)_6$ and DMDS under H_2	Si/SiO_2	550 (26hr)	MoS_2		
[70]	MoO_3 + S powder PTAS Seeding promoter	Si/SiO_2	650	MoS_2		FETs
[71]	MoO_3 + S powder	Sapphire	650	MoS_2		Heterojunctions for Solar Cells
[72]	MoO_3 + S powder	Sapphire	700	MoS_2		Electroluminescence
[73]	MoO_3 + H_2S	Si/SiO_2	600	MoS_2	Monolayer high uniformity	
[74]	MoO_3 + S	GaN	800	MoS_2	Monolayer triangular structure	Photodetection

Table 2.2: A range of CVD methods to create MoS_2 films, from many different sources and for different applications.

This allows for flexible MoS_2 to be grown, opening new opportunities for MoS_2 applications, such as wearable technologies.

At the cost of crystallinity, the large surface area single crystal films produced by CVD, for all its issues, are regarded as the state of the art for few layered material devices. The ability to grow highly uniform, large area monolayer material is hugely beneficial for research purposes as will be explained in the next section.

2.2.2.2 CVD Applications

Large area films are key for the future of 2D materials. Industrial-scale processes for large scale films which have high uniformity, cost effectiveness and few defects are significant. This is a key reason as to why the CVD processes are so heavily researched. Various applications for large-scale films have been suggested, including areas such as sensing and photodetection that require uniform deposition [64][74]. Research is still ongoing into how to scale up these processes as to date only inch scale wafers of high quality have been synthesised. This is mainly constrained by the limit on the temperature uniformity of furnaces.

2.2.3 Atomic Layer Deposition

2.2.3.1 Atomic Layer Deposition Techniques

Another method to synthesis thin films by the bottom up method is known as atomic layer deposition. Much like CVD, it involves the reaction of precursor material on the surface of a substrate inside a furnace chamber. Historically, this technique has been used for the deposition of oxide films. The difference between CVD and ALD is the pulsing mechanism of ALD. This affects the measure of control upon the quality of the deposition. CVD requires a continuous flow of precursor over the substrate, whereas ALD usually occurs in a few stages. These stages are well described in Figure 2.15. First, a pulse of the first precursor is allowed into the chamber. This settles onto the surface of the substrates, with any excess material disposed of via a purging pulse of inert gas, usually either Ar or N_2. The secondary precursor is then flowed into the chamber, with this precursor reacting with the first one. Waste precursor is purged out of the chamber by a second inert gas flow. This process is repeated as many times as needed by the user, until a conformal film is produced.

Many papers have reported upon this, using a variety of precursors. Many of these are the same as the precursors used in CVD. Table 2.3 provides some examples texts, with the pulse times used in the deposition also supplied. The quality of the deposition is also outlined in the table, as well as the temperature required for deposition. Note how the deposition temperatures in comparison to

CVD are much lower. The substrates and precursors selected are almost identical to those of CVD. In comparison to other ALD papers, there are notable differences in the number of pulses and pulse durations to achieve monolayer film, for example those of the $MoCl_5$ precursors used in Table 2.3. This inconsistency shows the research yet to be completed on ALD techniques.

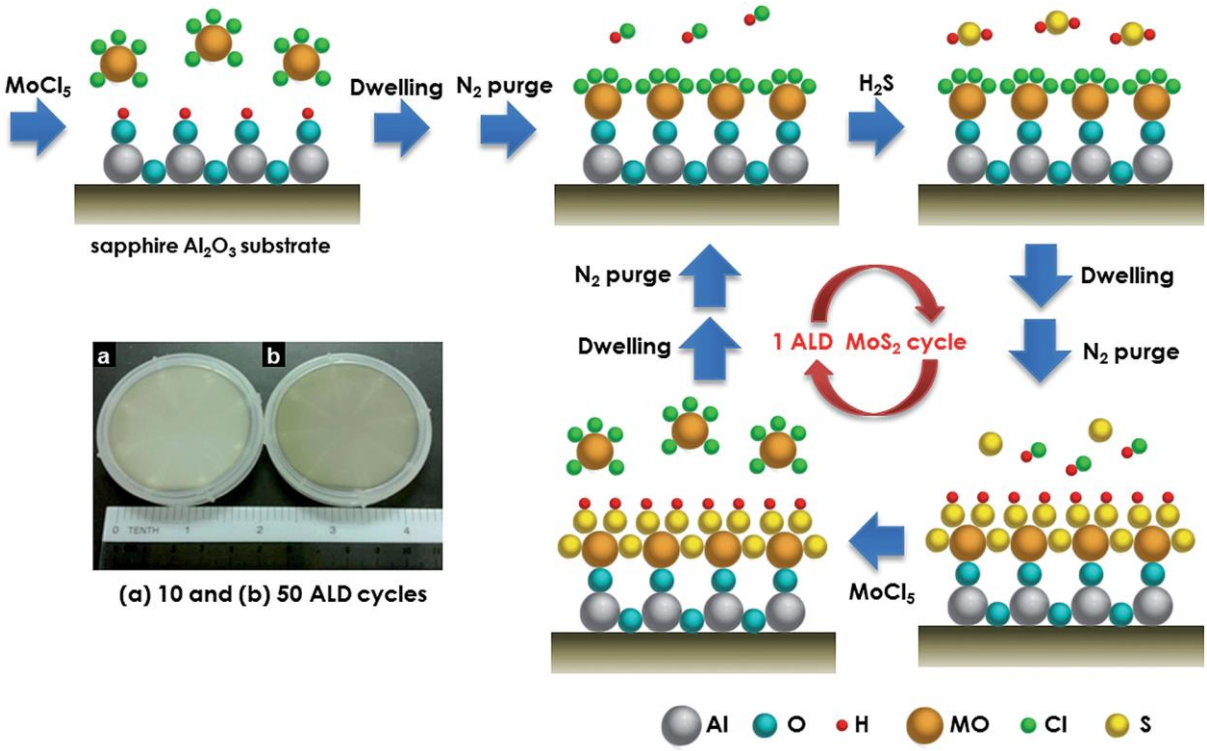

Figure 2.15: A demonstration of how the ALD method works for thin film deposition. This example uses a reaction between $MoCl_5$ and H_2S. From ref. [75].

However, ALD is not without its issues. The amount of waste precursor generates a poor cost efficiency for generation of such films. Much like CVD techniques, the size of the deposition is limited by the size of the furnace, although longer samples would require longer pulse times. However, the lower synthesis temperature needed for deposition allows for different substrates, such as plastics to be used for precursors that would be damaged if a CVD method was used.

2.2.4 Liquid Phase Deposition

2.2.4.1 Liquid Phase Deposition Techniques

Finally, one other highly regarded deposition technique is through what is termed the LPD method. Unlike previous TMDC bottom up methods, this revolves around the thermal decomposition of a single precursor, usually ammonium tetrathiotungstate/tetrathiomolybdate. The method also significantly differs by the way that the precursor is placed onto the substrate.

Reference Number	**Precursors**	**Pulse processes**	**Substrate**	**Number of Cycles**	**Temperature (°C)**	**Film Created**	**Quality**
[75]	$MoCl_5$ + H_2S	5s $MoCl_5$/5s dwell/30s N_2 purge/H_2S 0.1s/5s dwell/20s N2 purge	Sapphire	5 cycles for monolayer	300 (800 sulphur anneal)	MoS_2	5 cycles early stage island growth/10 cycles to produce continuous films, but 2 layer.
[76]	$Mo(CO)_6$ + H_2S	Precursor Pulse=20s/10s purge Ar/Reactant Pulse 10s/10s purge	SiO_2	100	175-225	MoS_2	6nm thickness
[77]	$Mo(CO)_6$ + $CH_3S_2CH_3$	$MoCO_6$ 4s/30s purge/DMDS 1.5s/Purge 10s	Au on Si	-	100	MoS_2	Amorphous
[78]	$MoCl_5$ + H_2S	4s $MoCl_5$/5s Ar purge/3s H_2S/5s Ar Purge	Si/SiO_2	120	500 trilayer/700Bilayer/900 monolayer	MoS_2	High quality
[79]	Benzene + H_2/Ar Plasma	0.2s Benzene/6s N_2 purge/9s Plasma/3s N_2 purge	Cu	10	400	Graphene	
[80]	$WH_2(iPrCp)_2$+O_2 plasma				300	WO_3	

Reference Number	**Precursors**	**Pulse processes**	**Substrate**	**Number of Cycles**	**Temperature (°C)**	**Film Created**	**Quality**
[81]	$Mo(thd)_3$ + H_2S	0.5 $Mo(thd)_3$/1s N_2 purge/2s H_2s/1s N_2 purge	Si or Soda Lime Glass	2000	300	MoS_2	
[82]	MoF_6 and H_2S	MoF_6 1s/5s N_2 purge/1s H_2S/5s N_2 purge	Si	100-1000	200 followed by 350 H_2 anneal	MoS_2	
[83]	$MoCl_5$ + H_2S	1s $MoCl_5$/30s N_2 purge/1s H_2S/30s N_2 purge	Si/SiO_2	1000	400	MoS_2	
[84]	WF_6 + H_2S	10s WF_6/10s H_2 plasma/60s H_2S - 20s chamber evac between pulses	Al_2O_3	65	300	WS_2	

Table 2.3: A range of ALD methods to create MoS_2 films, from many different sources and for different applications.

Rather than a flow of precursor into a chamber as described previously, here the substrate is pretreated with a solution in which the precursor has been dissolved. This is usually achieved by processes called dip coating [85] and spin coating [86] that are able to produced thin and uniform liquid coatings of the substrate surface. The treated substrate is then placed into a furnace, usually under vacuum and additional gas flow, and the dissolved precursor thermally decomposes into few layered TMDC material. By control of the amount of precursor material dissolved in the solvent, few layer MoS_2 can be produced. Due to the low temperature deposition and versatility of the deposition method, the liquid phase deposition technique is a key part of this thesis. The liquid host allows for the precursor material to easily coat the inner regions of small hollow regions of, for example, a fibre.

This technique began gaining favour in the thin film community after a paper by Liu et al. created few layer MoS_2 using ammonium tetrathiomolybdate (ATTM) as a precursor [85]. The precursor was dissolved into Dimethylformamide (DMF) in a 1.5wt% concentration. A substrate, Si/SiO_2 was then dipped into the solution, and slowly drawn out of the liquid, leaving a thin layer of solution on top of the substrate. The host solvent was then evaporated from the substrate by a hot plate, at a temperature of 80°C. This was lower than the decomposition temperature of ATTM leaving the precursor unaffected. The substrate was then placed inside of a vacuum furnace, and allowed to decompose at 500°C, under a flow of hydrogen. The addition of hydrogen to the process allowed the decomposition to occur at a lower temperature. This is because the conversion from $(NH_4)_2MoS_4$ to MoS_2 could be performed in a single step, as demonstrated by Equation 2.3, rather than a two step method seen in Equation 2.1 and Equation 2.2.

$$(NH_4)_2MoS_4 = 2NH_3 + H_2S + MoS_3 \qquad \text{Equation 2.1}$$

$$MoS_3 = MoS_2 + S \qquad \text{Equation 2.2}$$

$$(NH_4)_2MoS_4 + H_2 = 2NH_3 + 2H_2S + MoS_2 \qquad \text{Equation 2.3}$$

This lowered the necessary temperature from around 800°C to 450°C. A second anneal in a sulphur environment was then performed at 1000°C. The created film can be seen in Figure 2.16, showing relatively uniform trilayer film with occasional areas of bilayer reported. An investigation was performed on the quality of the MoS_2 both with and without the high temperature anneal. Overall,

the crystal quality, photoluminescence and FET behaviour of the MoS_2 greatly improved after the second anneal, however, the uniformity was produced in the initial anneal.

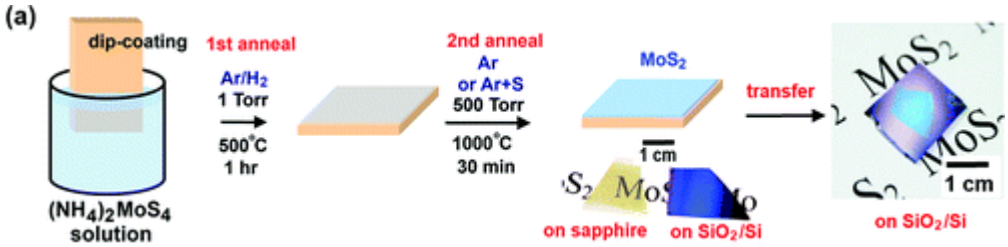

Figure 2.16: The liquid phase deposition method described for the deposition of MoS_2 using ammonium tetrathiomolybdate. The results of the deposition are shown on the last image, showing centimeter scale depositon of bilayer/trilayer film. From ref. [85].

This highlighted the liquid phase deposition method as a low temperature synthesis technique. It was able to work on a variety of substrates, with the thin liquid coating achieved through two main methods. These are spin coating – where a drop of liquid is placed onto the surface of the substrate and formed into a thin layer via centripetal force – and dip coating – whereby the substrate is placed into the solvent solution and removed under constant slow speed. However, certain issues remained in the deposition. One was the uniformity of the film, which was improved by work by Yang *et al* [86]. They changed the host solvent solution in which the precursor material was dissolved. A solution of 4.5ml of DMF, 4.5ml of butylamine and 1ml of amino-ethanol was used, to help disperse the precursor, as well as help adhesion of the liquid to the substrates surface. Amino-ethanol was especially good at improving the adhesive quality, as it is a heavily viscous solvent. This enabled the substrate to be spin coated, with high uniformity and larger area substrates of 2 inches to be used, in comparison with the dip-coating procedure by Liu that used who used centimetre scale wafers. Furthermore, the addition of the amine-based solvents increased the controllability of the formation of layered material by altering the concentration of the precursor in the solvent solution.

2.2.4.2 Liquid Phase Deposition Applications

The applications of the LPD method are much alike to previous CVD and ALD works. Both Liu and Yang are able to produce functional FET structures with their respective MoS_2 films. Unique benefits of containing the deposition in a liquid host has seen this process used for more niche applications. These involve a roll-to-roll process as seen in Figure 2.17. Here, the precursor material is able to be used as a spray to coat the substrate, allowing for large areas to be coated over time [87]. This was shown to coat substrates of over 50cm with remarkable uniformity. Such a roll-to-roll process could lead to huge benefits in reducing costs in MoS_2 production. The work described in this thesis uses another major benefit of the liquid phase host solvent to allow capillary action to coat the inner

regions of optical fibres with the precursor material. As far as the author is aware, this will be the first time the methodology has been used for this purpose and offers a unique approach for TMDC deposition.

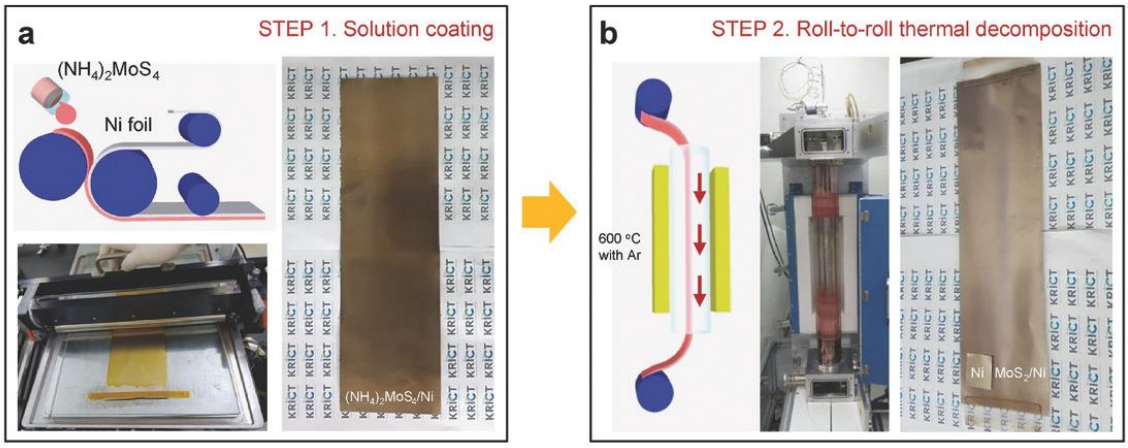

Figure 2.17: A roll to roll process to create large scale MoS_2, using the deposition of ammonium tetrathiomolybdate over scales of tens of centimetres. From ref. [87].

2.3 Overview

The field of 2D materials is still nascent, as the application space they can be used for has not been fully explored. Graphene, for example, has been suggested for a variety of different applications, with some of those beginning to move from the laboratory to solve real world problems. The same is true of the TMDC materials. Their impressive optoelectronic and mechanical properties, combined with their ability to be placed onto flexible substrates means there has been many works looking into producing 'wearable' technology, amongst other things such as biosensing, solar cells and logic gates.

Furthermore, a variety of different 2D films have been looked over in the writing of this thesis, such as hexagonal boron nitride, germanene and black phosphorus, each with different capabilities and different properties, for example their electronic bandgaps, means a wide range of devices are yet to be explored. All this is helping to further drive the miniaturization of current technologies, to appease greater demand in an ever-more connected world.

The synthesis methods discussed are also increasingly being refined, allowing lower temperature and better quality films to be produced. By reducing the cost efficiency of such materials, industry is soon to be unable to ignore their properties.

Finally, new applications using novel concepts are continuing to be explored. This forms the basis of the following thesis.

Chapter 3 Thermal Poling

3.1 Thermal Poling Background

Optical fibres act as a basis for many telecommunications systems, offering low loss and superfast transmission of data through glassy materials [88]. For the large majority of optical fibres, the guidance of the light is performed through a mechanism known as total internal reflection. This can be understood as reflection of light between a material of higher refractive index to a material of lower refractive index. At most angles of incidence, the light would be refracted and incur a path change. However, as demonstrated in Figure 3.1 at a certain angle, known as the critical angle, no throughput of the light is observed. This is mathematically calculated from Equation 3.1. At all values larger than the critical angle, the light begins to reflect back into the higher index material, becoming confined to the higher index region.

$$\sin(\theta_C) = \frac{n_2}{n_1} \qquad \text{Equation 3.1}$$

This is demonstrated in Figure 3.1. For fibre optics, this effect is performed by coating a cylindrical high index material, n_1, with a lower index material, n_2. These are respectively termed the core and the cladding. To ensure the fibre is able to accept a wide range of input, it is important for the critical angle to be small, hence two materials of very similar refractive index are used, commonly the same material, silica. The core silica is purposefully doped with ions to increase the refractive index by a small measure. Due to the mechanical strength, cost efficiency and mature technologies of optical fibres, they are key components of telecommunications systems.

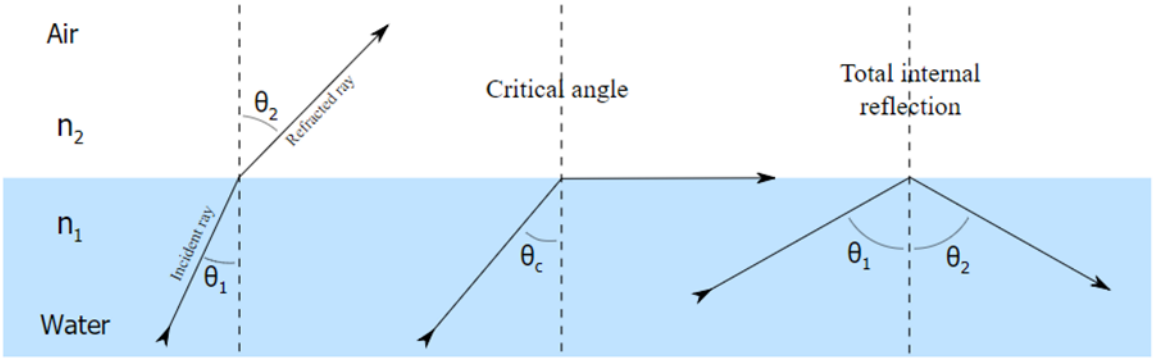

Figure 3.1: A visual representation of how light rays are perturbed when travelling from a material of higher refractive index, n_1, to one of lower refractive index, n_2. For small angles, the light is refracted at the surface. However, at the critical angle, the light will become confined to the surface boundary. At angles above this angle, the ray is reflected. This is known as total internal reflection. From Ref [89].

The use of optical fibres for telecommunications is mainly focussed at around the 1550nm mark. This is for a variety of reasons. One key is the low intrinsic loss inherent to the host silica glass in the core material. This is well highlighted in Figure 3.2, showing an overall decrease in the loss with increasing wavelength, a process dominated by Rayleigh scattering. However, at the 1.4μm region, a large increase in the loss is seen due to absorption from the OH^- bonds. Dispersion is also a material parameter of interest. Here, light of different wavelengths travelling at different speeds within a material, due to the refractive index being a function of the wavelength. This can be detrimental for phenomena such as laser pulses, which begin to lengthen (or shorten) due to dispersive effects. If such pulses began to lengthen to the point that pulses began to overlap, the data could become corrupted, thus compromising the performance of communications systems.

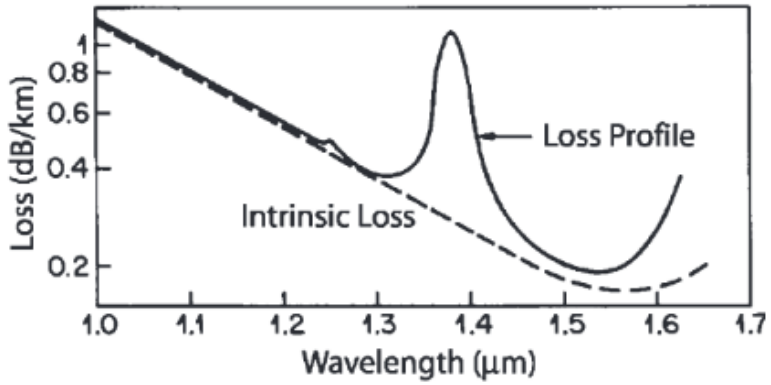

Figure 3.2: A description of how the loss of how optical fibres is affected by the wavelength. The dashed line corresponds to Rayleigh scattering (~$1/\lambda^4$). The large increase at around 1.4um corresponds to an OH bond absorbance. From Ref [88].

Another material effect is optical nonlinearity which gives rise to many phenomena. When considering light of frequency ω propagating through a medium, it induces electrical dipoles in the atoms [90]. For low intensity light, these dipoles usually vibrate at the same frequency, whereby the polarisation, **P**(ω), reacts linearly as $\mathbf{P}(\omega) = \epsilon_0 \chi^{(1)}(\omega)$. The corresponding $\chi^{(1)}$ produces a measure of the absorption of the material and is a linear property. This is for small intensity light, whereby higher order terms effectively equate to zero. The full Taylor expansion of the polarisation must be considered when discussing high powered light, as highlighted by Equation 3.2. Here, the high nonlinear order susceptibilities, $\chi^{(2)}$ and $\chi^{(3)}$ are integral as the value of the electrical field is large enough to produce a notable effect on the polarisation [91].

$$\boldsymbol{P}(\omega) = \epsilon_0(\chi^{(1)}\boldsymbol{E} + \chi^{(2)}\boldsymbol{E^2} + \chi^{(3)}\boldsymbol{E^3} + \cdots) \qquad \text{Equation 3.2}$$

This change in the polarisation can produce some interesting effects in the medium. Considering that the polarisation change is now nonlinear, the response of the medium is to emit light of a

different frequency to the input. This can lead to a large range of effects, summarized by Table 3.1 [91].

Input Frequency	Perturbation	Output Frequency	Effect
ω_1	$P(2\omega_1) \propto \chi^{(2)}E_1^2$	$\omega_2 = 2\omega_1$	SHG
ω_1, ω_2	$P(\omega_1 + \omega_2) \propto \chi^{(2)}E_1E_2$	$\omega_3 = \omega_1 + \omega_2$	SFG
ω_1, ω_2	$P(\omega_1 - \omega_2) \propto \chi^{(2)}E_1E^*_2$	$\omega_3 = \omega_1 - \omega_2$	DFG

Table 3.1: Second order nonlinear effects which cause an alteration to the output frequency of light once leaving a medium.

These are known as SHG –second harmonic generation, SFG – sum frequency generation and DFG – difference frequency generation. Many materials have negligible values of $\chi^{(2)}$, due to their crystal structure being centrosymmetric. However, all materials have a value of $\chi^{(3)}$. 3rd order effects include third harmonic generation, the Kerr effect and saturable absorption.

Luckily for data communications systems, the value of the nonlinearity is also low, as silica is a centrosymmetric structure, hence has no discernible second order nonlinearity. The third order nonlinearity also does not produce much effect, especially under low power transmission. However, for many devices, a high nonlinearity value is sought. For many systems, this is performed by the transfer from a weakly nonlinear fibre into a highly nonlinear planar device [92]. Materials such a lithium niobate have a high intrinsic second order nonlinearity value, as well as being easy to structure the quadratic nonlinearity thanks to the ferroelectric properties of the material [93]. However, it is impossible to form these materials into optical fibres.

It is worth focussing on SHG as an effect in the context of this thesis. SHG is a sum frequency generation effect whereby two photons of the same frequency $\omega_1 = \omega_2 = \omega$ interact with a host material and generate a single photon, of frequency 2ω [88], and is outlined in Figure 3.3. This effect can be used in laser systems to generate new output wavelengths [94]. Other applications of the phenomenon can be seen in biomedical applications, in a technique known as second harmonic microscopy [95].

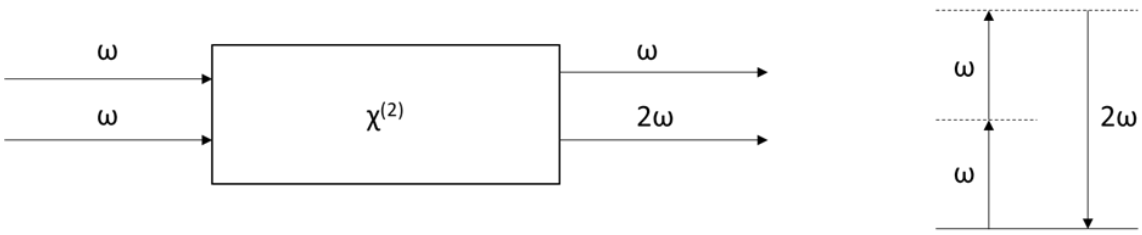

Figure 3.3: A schematic of how second harmonic generation can occur in a medium with a non zero second order nonlinear material, with the corresponding energy level diagram of the SHG effect.

3.1.1 Theory of Thermal Poling

The translation from fibre based systems to planar systems can come at a cost of high loss and difficulty in alignment. Therefore all-optical-fibre based, high second order nonlinearity structures are widely researched. One such technique to achieve this is known as thermal poling. The concept relies on the breaking of the centrosymmetry of the material. To do this, charge impurities of the fibre are allowed to migrate within the material, through the application of a high electric field under high temperatures where the impurity charges become mobile. The electrical field is left on during the cooling down process, fixing the charges into position in the fibre. After removing the externally applied electric field, a layer of negatively charged region is created inside the glass and a "frozen-in" electric field is permanently created a few microns of distance from the anodic surface. The second order nonlinearity is created inside the glass due to a third order optical rectification process. To characterise the effectiveness of the poling, the second harmonic signal can measured, with the key parameter to measure the strength of the nonlinearity being it's $\chi^{(2)}$ value. This is calculated from Equation 3.3 [96], where ω is the fundamental frequency, d is the nonlinear coefficient, L is the length of the device, ε_0 is the dielectric constant, c_0 is the speed of light in a vacuum, and ρ is an enhancement factor regarding multimodal nature of the source. The refractive indices, n_ω^* and $n_{2\omega}^*$ correspond to the effective values at the fundamental and second harmonic respectively. A_{OVL} is the area of the overlap integral of the two interacting fields, and $\Delta\beta$ is the wavevector mismatch.

$$d^2 = \frac{c_0^3 \varepsilon_0 n_\omega^{*2} n_{2\omega}^*}{8\omega^2} \frac{A_{OVL} \Delta\beta^2}{sin^2\left(\frac{\Delta\beta L}{2}\right)\rho} \frac{P_{2\omega}}{P_\omega^2} \qquad \text{Equation 3.3}$$

The final terms, $P_{2\omega}$and P_ω^2, is a ratio of the output power of the second harmonic wave (2ω) and the input power of the fundamental wave (ω). To calculate the $\chi^{(2)}$ from d, the value of the nonlinear coefficient is multiplied by the factor ρ.

However, there is an intrinsic issue when analysing the propagation of the pump and the newly generated second harmonic signal. It is well known that the speed of light, v, in a medium is equal

to the speed of light, c, divided by the refractive index of the material, n. The value of this refractive index is known to be a function of the wavelength, n = n(λ), so therefore light of different wavelengths will travel through a medium at different speeds. When the two signals are in synchronisation with one another, they interfere constructively – producing SH signal. However with SHG, this can lead to the pump signal and SH signal beginning to travel out of synchronisation with each other. At sufficient lengths, this can lead to destructive interference. This is known as phase mismatch and can be severely detrimental to a SH device, causing a lack of build up of SH signal, producing the trace seen in Figure 3.4 labelled NPM.

Fortunately, there are ways to prevent this, known as phase matching. There are two well recognised methods to achieve this. Birefringent phase matching (BPM) is one of these, whereby a crystal which is birefringent – i.e. has different refractive index depending upon the orientation of the crystal lattice – propagates the pump and second harmonic signal in different polarisations to achieve phase matching.

Another phase matching technique is to produce a medium whereby the domains of the material switch after certain lengths, such as periodically poled $LiNbO_3$ [97]. Here, the domains of the crystal are switched as the SH begins to interact destructively. The domains are switched so that the SH now begins to act constructively, producing an overall large SH output. However, for amorphous silica fibre, BPM and periodic poling (PP) via domain inversion are inapplicable, so an alternative Quasi-Phase Matching (QPM) technique is used instead.

3.1.1.1 Quasi-Phase Matching

For optical fibres, the concept of periodical poling is complicated as domains are not present so instead a technique of UV erasure is used, whereby as soon as destructive interference begins to occur, a change is made to the material to prevent it becoming a problem. However, due to the inability to change the orientations of the domains, instead the second order nonlinearity is (periodically) erased completely. This causes no further SH signal to be generated, leading to no further depletion of the signal via phase mismatch, as seen in Figure 3.4. In the case of thermally poled fibres, this can be achieved by the application of localised heat onto the sample, or better still, the UV erasure of the nonlinearity. Here, UV light is focussed onto the core region of the fibre, supplying enough localised energy to excite electrons which will travel through the thermally poled field and annihilate it [98]. If the UV light is directed onto the sample for sufficient time, the SON will be completely erased. Regions of destructive interference are eliminated, leaving only regions of positive second harmonic generation. To calculate the size of these gratings, Equation 3.5 must be satisfied [99]. For efficient phasematching, the mismatch frequency ΔK is set to zero. Here, the grating period is Λ_{QPM}, λ is the fundamental wavelength, and the effective refractive indices are

$n_{eff}^{2\omega}$ and n_{eff}^{ω} for the second harmonic frequency and the fundamental frequency respectively. The optimisation of these gratings is key, as over short scales the second order nonlinearity can be low.

$$\Delta K = \frac{4\pi}{\lambda} n_{eff}^{2\omega} - 2\frac{2\pi}{\lambda} n_{eff}^{\omega} - \frac{2\pi}{\Lambda_{QPM}} = 0 \qquad \text{Equation 3.4}$$

$$\Lambda_{QPM} = \frac{\lambda}{2(n_{eff}^{2\omega} - n_{eff}^{\omega})} \qquad \text{Equation 3.5}$$

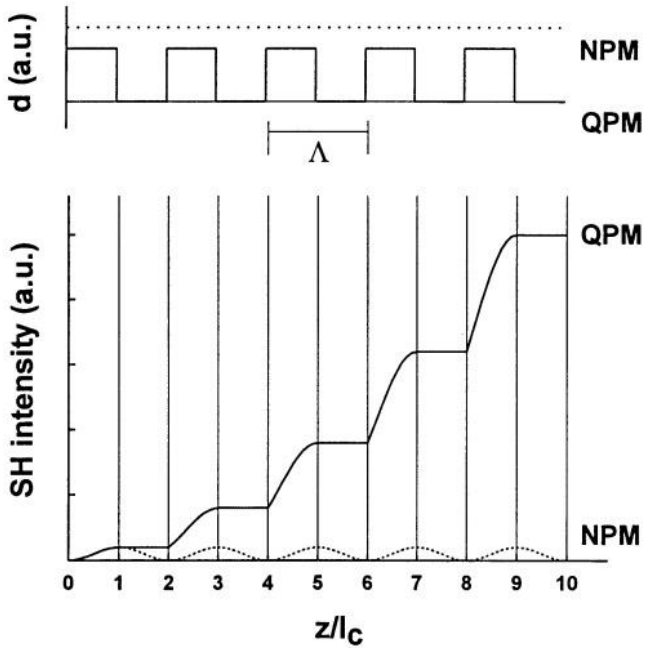

Figure 3.4: A representation of how quasi-phase matching affects the relative intensity of the SH light. For non-phase-matched material, the nonlinear coefficient, d, remains constant along the length of the functionalised surface, leading to a sinusoidal pattern as seen in NPM. However, by erasing the value of d at certain regions, the SH trace begins to build up, due to the absence of destructive interference. From Ref [100].

It is therefore clear that by poling a large length of material, high efficiency of SHG can be achieved in some samples. Optical fibres are able to offer this as an alternative to planar samples, as their high length and flexibility allow for ease of use. The history behind optical fibre poling will be discussed in the next section, with the methodology of how to achieve acceptable nonlinearity values analysed. However, there is a practical limit to the highest achievable values of $\chi^{(2)}$. To achieve high values, large electrical fields need to be applied to the fibre. This is both unsafe and potentially damaging to the glass. The latter is true of using high temperatures for poling. It would therefore seem that new ideas must be applied to thermal poling of optical fibres to achieve better results, which forms the basis of this chapter of this thesis.

3.1.2 History of Thermal Poling

It was well known that the presence of a high electrical field had an effect on the optical properties of silica glass, specifically the second order nonlinearity, with poor efficiency for early poling experiments [101]. The application of heat to the sample changed this, beginning the concept known as thermal poling. The first experiments into the poling of silica glass were performed on silica substrates [96], in a setup shown in Figure 3.5. Here, a large electrical field, 5 x 10^4 V/cm, was applied to the glass, whilst being maintained at a temperature of 250-325^{o}C. It was found to be a repeatable process, with the generated nonlinearity able to be removed through the re-application of heat. Further, the reheated samples were seen to observe nonlinear effects once poling had been re-performed – showing no hysteresis. Via the testing of multiple substrates, it was observed that the sample with fewest charge impurities showed the lowest SHG signal. It was therefore proposed that the poling process was achieved via two mechanisms [102] – either Al impurities within the glass are becoming para-magnetically destabilised or that the charge impurities with in the fibre are becoming fixed in position, generating a large fixed electrical field within the fibre. It would later be confirmed that the second mechanism was correct.

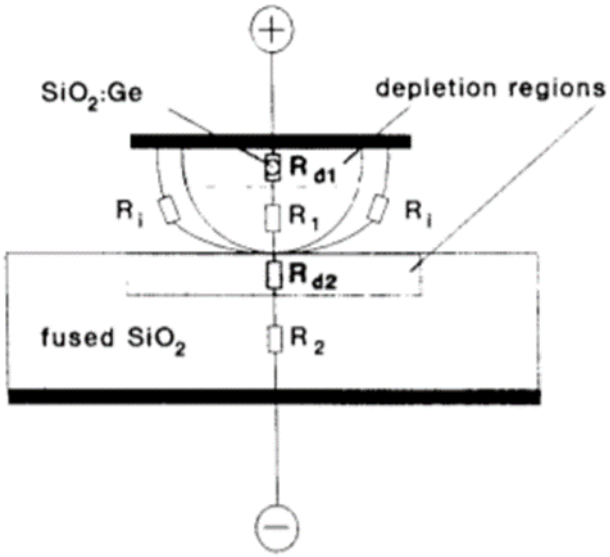

Figure 3.5: The schematic used by Kazansky *et al.* to pole a D-shaped optical fibre. The resistance values of the schematic are shown, with the path of least resistance being the central path – through the fibre. The depletion regions are also shown. Importantly, this region encompasses the core of the fibre. From Ref [96].

Later works showed the translation from planar substrates onto optical fibers. Kazansky *et al.* produced SHG results in a D-shaped optical fiber, using the setup seen in Figure 3.5 [96]. In this schematic, a depletion region of the fibre is shown. This region is considered the area in a glass sample where the charge has migrated from, leaving behind “purer” glass. It can be discovered

experimentally through a process known as decorative etching, where the silica is dipped into a low concentration solution of HF. The HF reacts at a higher rate with unpoled glass than poled glass. This creates an optically visible division between the two areas within the optical fibre [103]. In Kazansky's experiments, poling was carried out at 280^{o}C at an applied voltage of 4.3kV. In initial tests, pumping through non-phased matched fibre generated green second harmonic light, observable by the naked eye. The produced second order nonlinearity measured 0.3pm/V.

To further improve the results of the poling process, the anatomy of the fibre was changed to allow for higher interaction between the electrical field and the core of the fibre [104]. This was performed by altering the internal structure of the fibre to contain two hollow regions in the cladding of the fibre, into which aluminium wires could be inserted. A voltage of 800V was applied to the contacts within the fibre, generating an electrical field of 8 x 10^5 V/cm. They estimated a second order nonlinearity of 0.84 pm/V and the addition of the holes to the fibre did not seem to affect the loss properties of the fibre, as the light was well confined to the core. To reduce the loss of the fibre, the removal of the metallic contacts is necessary. This is easily performed with wires, however the insertion of the wires (of small thickness) is extremely time consuming and bending of the wire often occurs. This severely limits the length of the poling sample. One major benefit of thermal poling optical fibres are the long length scales which are able to be produced. By using wires, this benefit is bypassed. In this paper, the length was only 3.3cm [104].

Later works on thermal poling focussed on different electrode configurations. Margulis *et al.* showed evidence that the use of a cathode in the thermal poling system was not needed to achieve high quality second order nonlinearity [105]. Here, AuSn electrodes were placed in the twin holes of the fibre [106]. These were both connected to a singular electrical source – the anode. The poling process was then performed, with the depletion regions both appearing around both electrodes. It was thus discovered that the fibre could be poled without a cathode [105]. By using a single anode which used air to supply negative charge to act as an electrical ground, electrical breakdown within the fibre could be strongly suppressed. This can lead to many benefits, such as placing the holes of the fibre closer to the core, as well as using a larger voltage in the experiment.

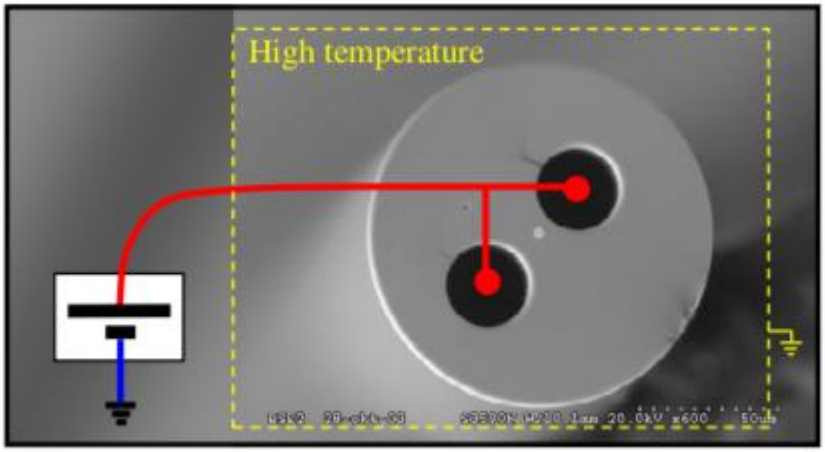

Figure 3.6: The double anode poling configuration for Margulis et al.'s experiments. Here, air was used to ground the device, with two floating anodes placed in the inner holes of the optical silica fibre. From Ref [105].

New methodologies of poling, to try and make poling a more accessible process for industrial applications have also been investigated. Fokine *et al.* investigated the use of liquid electrodes, namely BiSn – which are in a liquid state at high temperature [107]. By the application of pressure, the electrodes would flow far into the fibre allowing metre lengths to be filled. It is known that the insertion of metallic electrodes into the system can be detrimental with regards to optical loss. For the removal of the BiSn electrodes, high temperatures would be needed – which would allow the migrated charge to return to its isotropic positions. Our group therefore began to look into different metallic electrodes to be used for thermal poling.

A combination of Margulis' work and the use of liquid metals as electrodes was reported in work by De Lucia *et al.* who formed a technique for poling labelled induction poling [99] as outlined in Figure 3.7. Here, the short inductor (blue) fibre was equipped with manually inserted metallic wires, whereas the long induced fibre (red) was integrated with BiSn electrodes using pressurization. However, interestingly only the inductor fibre (blue) was connected to the high voltage power supply. It was found that during the poling process, the red fibre began to form a depletion region when close enough to the blue fibre. Remarkably, it was noted that the induced electrical field was present all along the length of the fibre, not just the region adjacent to the blue inductor fibre. The concept of induction poling could be transferred inside a single fibre, with both holes filled. Here, only a single embedded electrode would be placed into contact with the HV electrical supply, yet both metal filled holes would form a depletion region. This work helped show easier methodologies of thermal poling. It is important to note that small $\chi^{(2)}$ value observed with this experiment was due to the low impurity concentration of the optical fibre used rather than the induction poling process curtailing the $\chi^{(2)}$ of the fibre.

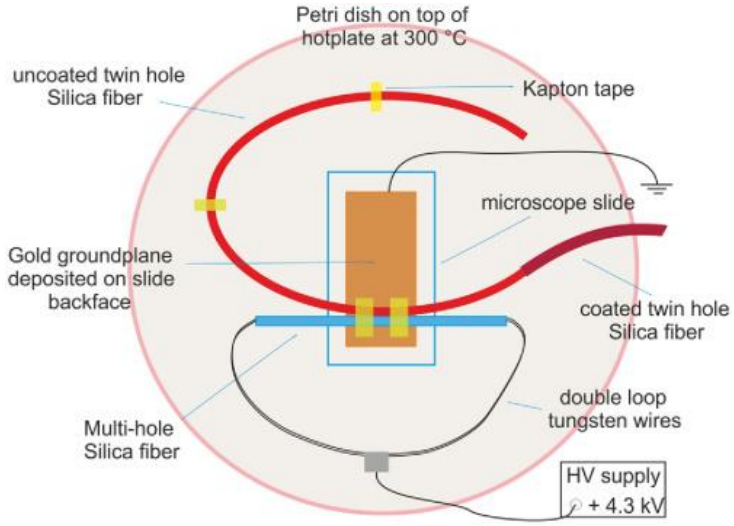

Figure 3.7: The setup used in induction poling experiments [99]. The voltage is supplied only to the short twin hole fibre seen in the blue coating. This is place in the vicinity of the red coated fibre, which has been filled with a metallic liquid. These are not contact with any power supply. Even with this lack of contact, the red induced fibre has successfully shown a depletion region.

A further work from De Lucia *et al.* looked into different liquid electrodes to be used in the poling process [108]. Issues with using Mercury or Gallium as the electrodes are their toxicity, as well as the transmission losses due to the presence of residues left through the removal process. Besides Mercury and Gallium, novel solutions for the filling of the twin holes such as tap water and hydrochloric acid were also tested as embedded electrodes, resulting in the formation of depletion regions.

3.1.3 Limitations of Thermal Poling

Of the references mentioned in section 2.1.2, the maximum achieved second order nonlinearity in optical fibres measures at a value of 0.12pm/V [108] due to the glass quality, and the use of Mercury as an anode. De Lucia also argues in ref [99] that there is an upper limit to the rectification of the electrical field in a silica optical fibre, $\chi^{(2)} \approx 3\chi^{(3)}E_{rec}$ to produce a high $\chi^{(2)}$, at about 1pm/V. It is argued that the maximum electrical field that can be applied is curtailed by silica's dielectric field strength. For example, by increasing the electrical field strength, the risk of damaging the fibre due to an electrical breakdown rises. It is also argued that the $\chi^{(3)}$ of the glass is an intrinsic value which is not easily changed. Fundamentally, due to the poling process revolving around the movement of dopant atoms, it has also been observed theoretically that for increased dopant concentration, a plateau is reached for the generated $\chi^{(2)}$ [109]. Therefore novel techniques to improve the capabilities of thermally poled fibres are investigated.

3.2 Synthesis of Thermal Poling Samples

Methods to increase the $\chi^{(2)}$ but not alter the glass quality are therefore sought out. Here, the concept of the insertion of an intrinsically high $\chi^{(2)}$ material, deposited in such a way that material is present in such a manner that phase matching of SHG is conserved, i.e. regions of oriented deposition followed by regions left bare, could be periodically patterned inside a fibre structure to improve its second order quadratic nonlinearity was initially proposed by F. De Lucia. However, the deposition technique would be very hard to implement. To pattern the composite structure, the concept of poling the device and gratings writing was suggested as an alternative "synthetic" approach to the creation of second order nonlinearity via equation $\chi^{(2)} \approx 3\chi^{(3)}E_{rec}$. To lower the impact the additional material has on the overall optical loss of the fibre, a thin material with low intrinsic loss was required, which led to the investigation into the area of 2D materials. Graphene, the most well characterised of these, is known to have a high $\chi^{(3)}$, however it's deposition requires a metallic substrate. However, the TMDC 2D materials have been reported to have intrinsically high $\chi^{(3)}$ values when synthesised in their few-layer. This is highlighted in work showing the use of MoS_2 as a saturable absorber [39].

To test this as a possibility, some preliminary numerical simulations have been realized in COMSOL to test the possibility of exploiting 2D materials inside twin hole silica fibres. The geometry investigated were those of an asymmetric fibre that were produced at the University of Southampton. The core was composed of silica doped with germania, with a refractive index of 1.456 and a diameter of 4μm. The centre of the hollow regions of the fibre were placed at a position 18μm and 28μm from the core with an equal diameter of 30μm. The cladding layer was chosen as pure silica, with a refractive index of 1.444.

The MoS_2 was located in the hollow regions of the fibre, with a thickness of 50nm. Experimentally, the aim was to produce thin layer films, of 1-3 layers of roughly 3nm thickness, but this was not computationally plausible due to calculation time required, so as a compromise, a thicker film of 50nm was integrated. Light was guided down the fibre at 1550nm, producing the results seen in Figure 3.8. The modal images show strong guidance in the core region (Figure 3.8a) and comparatively weak guidance in MoS_2 (Figure 3.8b) integrated regions. In the line plot (Figure 3.8c), there are two peaks occurring at the edge of the MoS_2 region, implying we have evanescent guidance in this region. It would therefore suggest small amounts of interaction between the mode and the TMDC material. If the nonlinear coefficient of the film were to be exploited by this overlap, it could be possible to add further nonlinearity to a twin-hole fibre. This is possibly enough nonlinearity to generate more signal than previously achievable, whilst inserting as little loss as possible to the system.

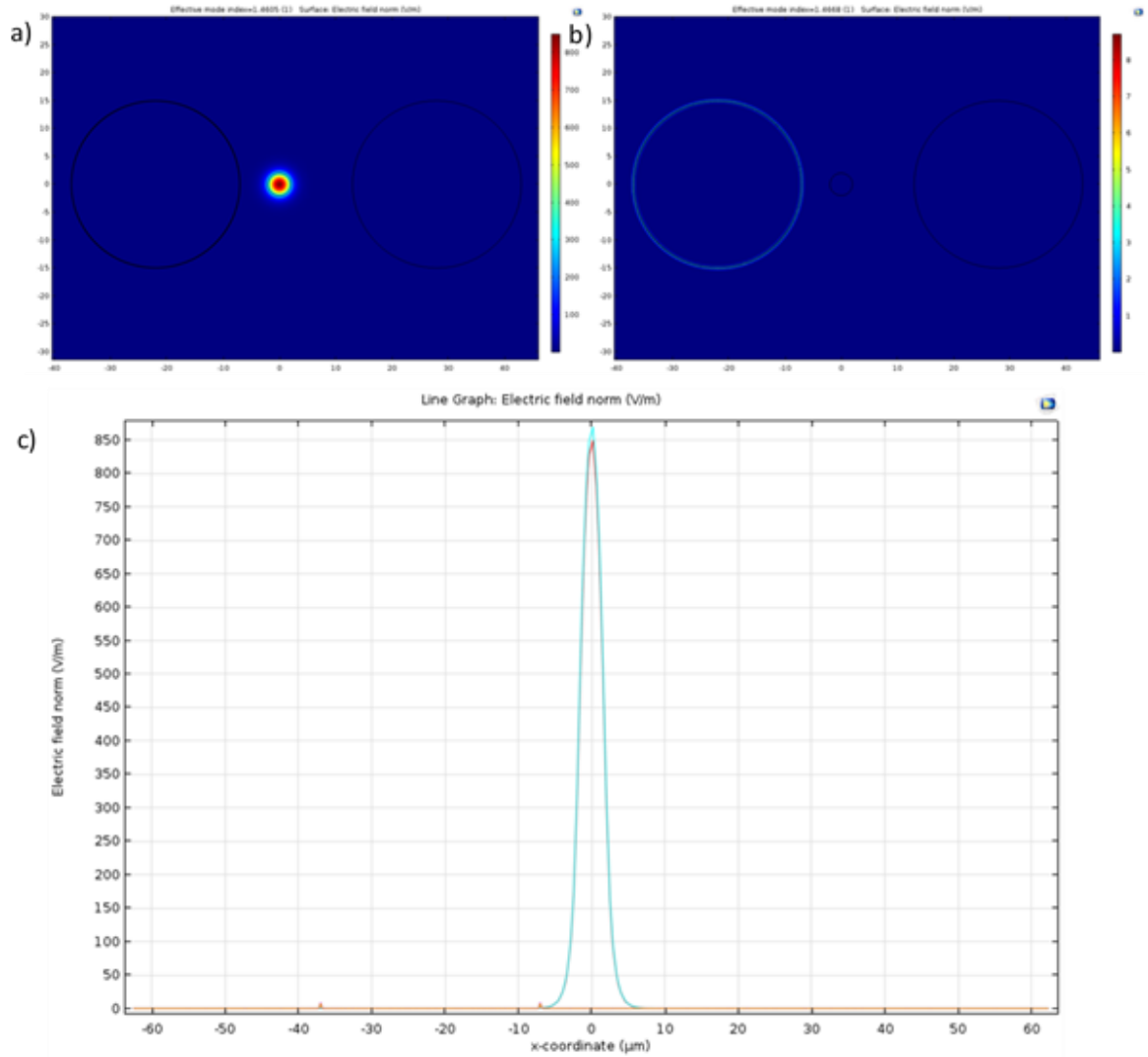

Figure 3.8: The results of a theoretical model to demonstrate how the guidance of the mode is affect by the insertion of MoS_2 into a twin hole fibre. The top images show the modal images at different effective index values, with the outcome plotted as a line graph along the x axis, in the bottom graph.

3.2.1 Creating MoS_2 Twin Holed Fibres

To create a MoS_2 integrated fibre, it was important to note the key points to analyse. To ensure the highest second order nonlinearity is achieved, a low number of layers – ideally monolayer – material is needed with high crystallinity. It is also important to keep the synthesis method of relatively low temperature so as to not damage the fibre. To integrate a long length of material is also important. After a literature review, it appeared that an ALD method would be the best method to begin with. ALD offers a low temperature deposition process capable of achieving monolayer deposition via control of the pulsing of precursor material, as explained further in chapter 2. It's capability for low temperature deposition, as well as its high crystal quality, offers an interesting method of deposition.

3.2.2 ALD Techniques

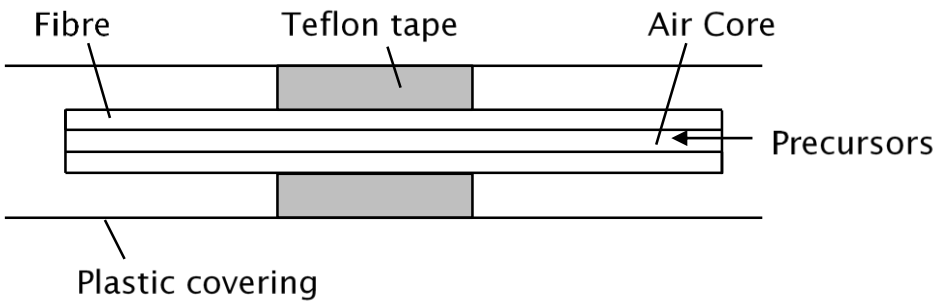

Figure 3.9: A brief description of how the initial 500um ALD experiments were performed. The capillary fibre was inserted into a plastic tube, blocked off via Teflon tape. Any processed precursor would therefore be deposited on the inner regions of the fibre.

Our experiments began with the deposition of MoO_3 on the inner core of a 500µm hollow core fibre, of 4cm length. This fibre type was chosen as it offered a large internal surface to perform preliminary tests for deposition. For this, a reaction between $MoCl_5$ and distilled water was performed. As $MoCl_5$ is an oxidant, the reaction could be performed at room temperature. To ensure flow was maintained purely on the inside of the fibre, the outside diameter of the fibre was blocked off by Teflon tape. The process was purged with a 100sccm Ar flow, to ensure an inert atmosphere and to also act as the carrying and purging gas for both H_2O and $MoCl_5$. This is outlined in Figure 3.9. The pulse conditions were as follows; a 3 minutes flow of H_2O, purged by 2 minutes of purging gas, then 5 minutes of $MoCl_5$ followed by a 2 minute purge.

The second step of the ALD process could then be performed. This was completed by placing the fibre into a tube furnace and was annealed under a H_2S environment. A flow of 30 sccm of H_2S and 120 sccm of Ar were used in the anneal. This converted the MoO_3 into MoS_2 with the only waste material being H_2O. The fibre was heated to 450^oC, and allowed to dwell for 15 minutes, before ramping the furnace to 900^oC and annealing for 2 hours. To confirm the deposition had been successful, Raman spectroscopy was used for as it is an excellent method to characterise deposition, with two typical traces from the first samples shown in Figure 3.10. For MoS_2, a key parameter in the analysis of a deposited film is the separation of two key Raman peaks, as they act as an indication of the number of layers of film deposited. An important factor of note is the major differences between the Raman peaks in Figure 3.10, whereby the focus of the laser is only displaced by a few centimetres. Furthermore, there are notable peaks seen at the 800cm^{-1} and 480cm^{-1} mark, implying the presence of MoO_3. From the separation of the two peaks, it was clear that bulk material had been formed. Figure 3.10a has a separation of 24.9cm^{-1} and Figure 3.10 has

a separation of 26.2cm^{-1}. There was also a clear issue with the uniformity, which meant that methods must be used to refine the deposition.

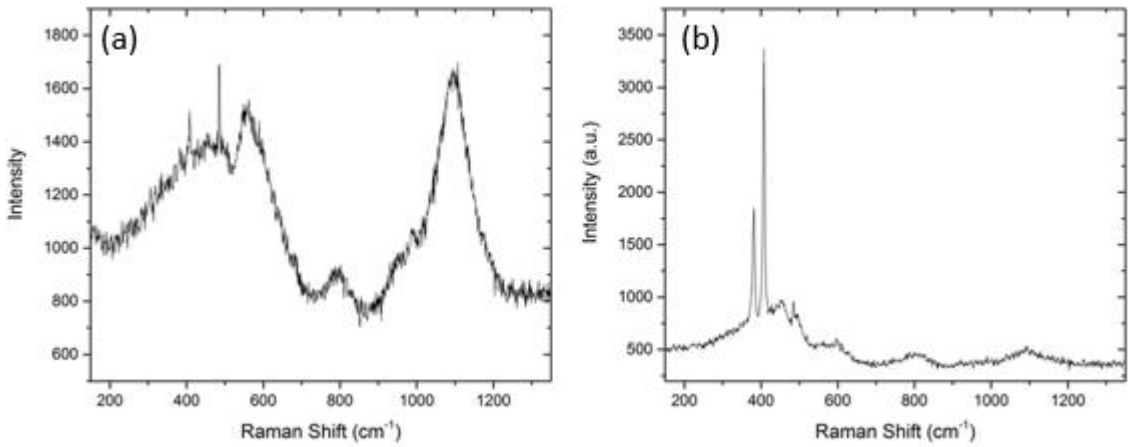

Figure 3.10: Two Raman spectra from the initial ALD MoO_3 after being converted into MoS_2 deposition. Two Raman signals are taken at different parts of the fibre. Fig. 3.9a shows an noisy trace, with poor signal appearing from the two MoS_2 Raman peaks, with other peaks found at 800cm^{-1} and 1100cm^{-1} implying contamination. Fig. 3.9b in contrast, shows two sharp Raman peaks from the MoS_2. However, the contamination is still visible in the trace. The separations imply bulk material is present.

The issues in the uniformity, allied with the bulk nature of the deposition meant that a few modifications were made to the process. One simple technique was to alter the pulse times of the precursors into the deposition chamber. For lower pulse times, if less MoO_3 is deposited we would expect less MoS_2 to be present at the end of the anneal and hence fewer layers. The results of this can be seen in Figure 3.11a, where the pulse times have all been decreased. The deposition was a 45 seconds of flow of H_2O, with a 60 second purge of Ar, then 75 seconds of $MoCl_5$ and finalised with a 60 second purge. The other change was in the pre-treatment of the fibre. Previously, the only pretreatment the fibre went through was an Ar purge. We changed this by adding a piranha solution etching step. Piranha solution is solution made from H_2SO_4 and H_2O_2. It is known to be aggressive on glass, and is able to clean the surface of substrates. It also produces a hydrophilic surface, meaning that it is able to promote reactions involving water as the H_2O was readily accepted onto the fibres surface. The experiment was repeated with these process changes, and the Raman spectroscopy taken. This is shown in Figure 3.11. However, the deposition made very little change to the peak separation, with the pretreated sample having a peak separation of 26cm^{-1} and the sample that did not go through the piranha etch having a separation of 24.7cm^{-1}. Also visible is the 480cm^{-1} peak, implying the presence of MoO_3. Overall, both changes did not have much effect on the quality of the deposition.

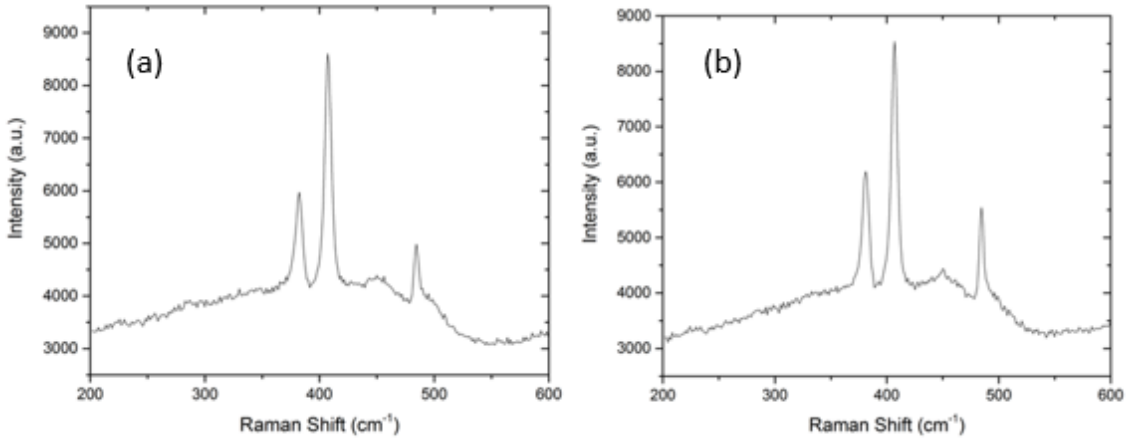

Figure 3.11: Two Raman results from the decreased pulse times for ALD deposited MoO_3 after conversion to MoS_2 at different points along the fibre. Once again, bulk MoS_2 is present. Furthermore, peaks at 500cm^{-1} suggest the presence of a contaminant material. A shorter wavenumber range has been analysed under Raman to enhance the investigation of the two resonant Raman peaks.

Other issues were evident such as the crude setup for these experiments that would be detrimental in smaller diameter and longer length fibres. It was clear that the Teflon tape used would not be easy for creating a perfect seal in later experiments which would use a fibre with a total outer diameter of 127µm. Furthermore, the structural integrity of the fibre becomes problematic under high temperatures of 900°C that was necessary for the complete conversion of MoO_3. It was noted that the fibre began to become brittle at around the 700°C mark. We therefore began to try different deposition methods for our fibre samples.

3.2.3 Exfoliation Techniques

After the failures of the ALD technique for the deposition of thin layer MoS_2 films, we decided to move towards deposition processes based on exfoliated MoS_2 to the deposition using exfoliated MoS_2. The benefits of exfoliated films such as the perfect crystallinity of the deposition have been explained in previous chapters, but there were fears that the lack of uniformity of the sample, which could cause scattering. However, by being in a liquid host solvent, it would allow simple penetration into the fibre. This would allow for the possibility of filling long lengths of fibre. Furthermore, the low temperatures needed to remove the host solvent would cause little damage to the fibre.

To test this method, two procedures were used. The first used a bespoke, in-house manufactured solution of MoS_2 flakes. This was created by the sonication of bulk molybdenite – a common ore of MoS_2 layered material - in solvents. Two different host solutions were used in this experiment. The first was a solution of MoS_2 placed in 100% isopropanol (IPA), and the second of MoS_2 placed in a

30/70 split of IPA/water respectively. The weight concentrations of the solutions were kept the same, at a 0.25% concentration. The solutions were sonicated at 60°C for 3 hours. The resulting solution of IPA/water is shown in Figure 3.12, with a significant difference in the colour of the solution in comparison to plain water. The pure IPA solution also showed this colour change.

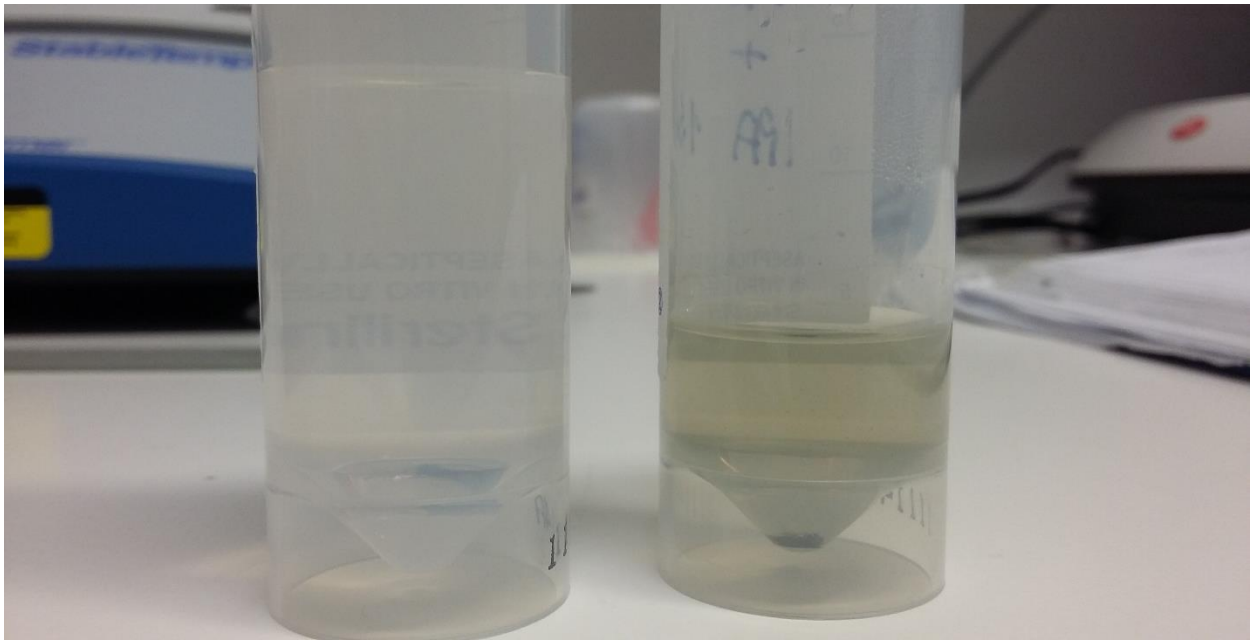

Figure 3.12: A liquid exfoliated sample of MoS_2 in a mixture of IPA/Water in comparison to a sample container with just water. Note the significant colour change due to the dispersion of the MoS_2 thin films.

The two liquids were then used to fill 50µm capillary core fibres. This could easily be performed by capillarity. Once filled, the fibres were placed onto a hot plate, and allowed to cool to a moderate temperature of 100°C, just above IPA's boiling temperature of 82°C. This value was chosen as previous tests at 200°C had seen the liquid begin to boil, expelling the host solvent, but also the molybdenum disulphide. The lower temperature test caused the host solvent for both samples begin to gradually evaporate, hopefully depositing flakes of MoS_2. These were tested under Raman spectroscopy.

The results of this can be seen in Figure 3.13. Here, we see an image of the outcome of the deposition. The material begins to form together into bulk material at the meniscus of the host solvent. When a Raman scan is performed on this bulk object, the resultant trace shows the two resonant peaks, but of poor separation. Further, the remaining parts of the fibre show no deposition at all. For the IPA only solution, no MoS_2 presence was found. This was a concern, as the deposition was poor.

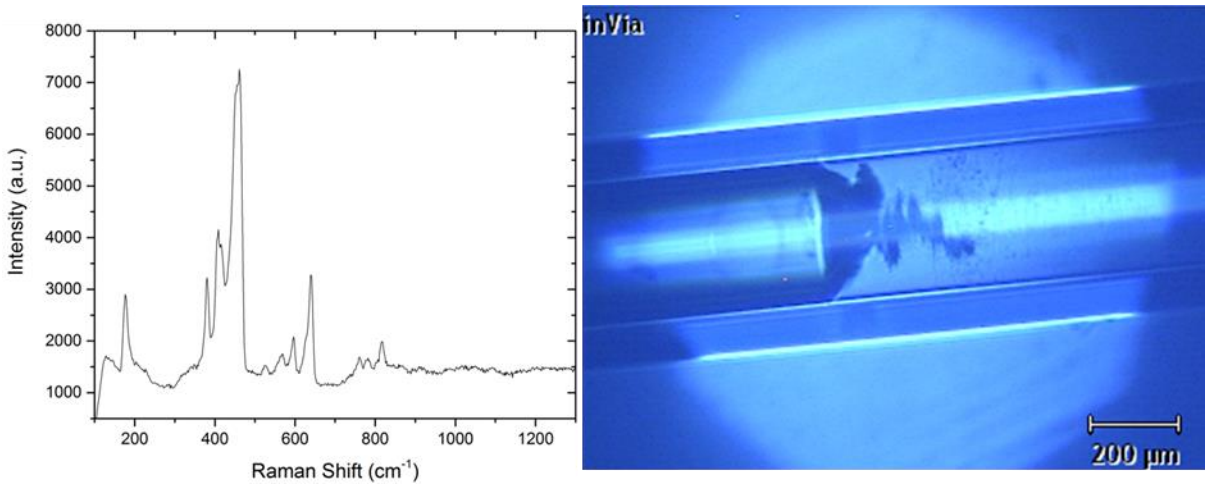

Figure 3.13: A Raman spectra of an exfoliated MoS_2 sample using a 633nm excitation laser. This generates second order peaks, hence the difference to previous spectra. This trace was obtained from focussing the Raman laser onto a flake of MoS_2 as seen in the image on the right. However, along the rest of the fibre, the Raman trace is devoid of any MoS_2 response.

In attempts to improve the custom made solutions, different sonication conditions and concentrations were selected, but to no avail. The clumping issue kept re-occurring. Instead, a commercially available solution was acquired (graphenesupermarket.com). This solution was made up from pristine MoS_2 flakes in an ethanol/water solution. The depositions were reattempted using the previous experimental conditions. However, despite using a variety of different methods to ensure the solution was well dissipated within the fibre, such as sonication of the fibre and the splicing of both ends of the fibre, the same issues remained, just as in in Figure 3.13.

3.2.4 Liquid Phase Deposition Techniques

The next method of deposition was that of liquid phase deposition. This procedure had many benefits over ALD. Deposition could occur from a single precursor and control on the number of layers was found to be related to the concentration of the precursor solution. Furthermore, the liquid was found to flow smoothly into the fibre via capillarity. This had two major benefits. First, it would create an even coating along the fibre meaning uniformity at the end faces would be less of an issue. Second, it would be able to fill small hole sizes simply and easily with long lengths achievable – limited only by the size of the furnace.

The precursor solution first used was from work by Liu *et al.* A single precursor, $(NH_4)_2MoS_4$ was found to thermally decompose to MoS_2 at a low temperature of 450^{o}C under a H_2 flow. Liu *et al.* used DMF as a host solvent for their samples with 1.5 wt%, using the dip coating method to coat their silica substrates [85]. For our first experiments using this process, 50µm hollow core fibres were used. The solution was created using ATTM in pure DMF, sonicated for 30 mins at 60^{o}C. It was

allowed to flow into the fibre by placing an end face into the solution. It would propagate into the fibre via capillarity. It was then placed onto a hotplate in air for 10 minutes, at 90°C, to remove the host solvent, followed by a low pressure furnace, to anneal at 450°C. Two typical Raman traces can be seen due to this solution in Figure 3.14. The two peaks have separations of 23.6cm^{-1} and 22.3cm^{-1} implying bilayer to trilayer film. For preliminary experiments, 5cm long fibres were used – with all 5cms filled before the annealing stage.

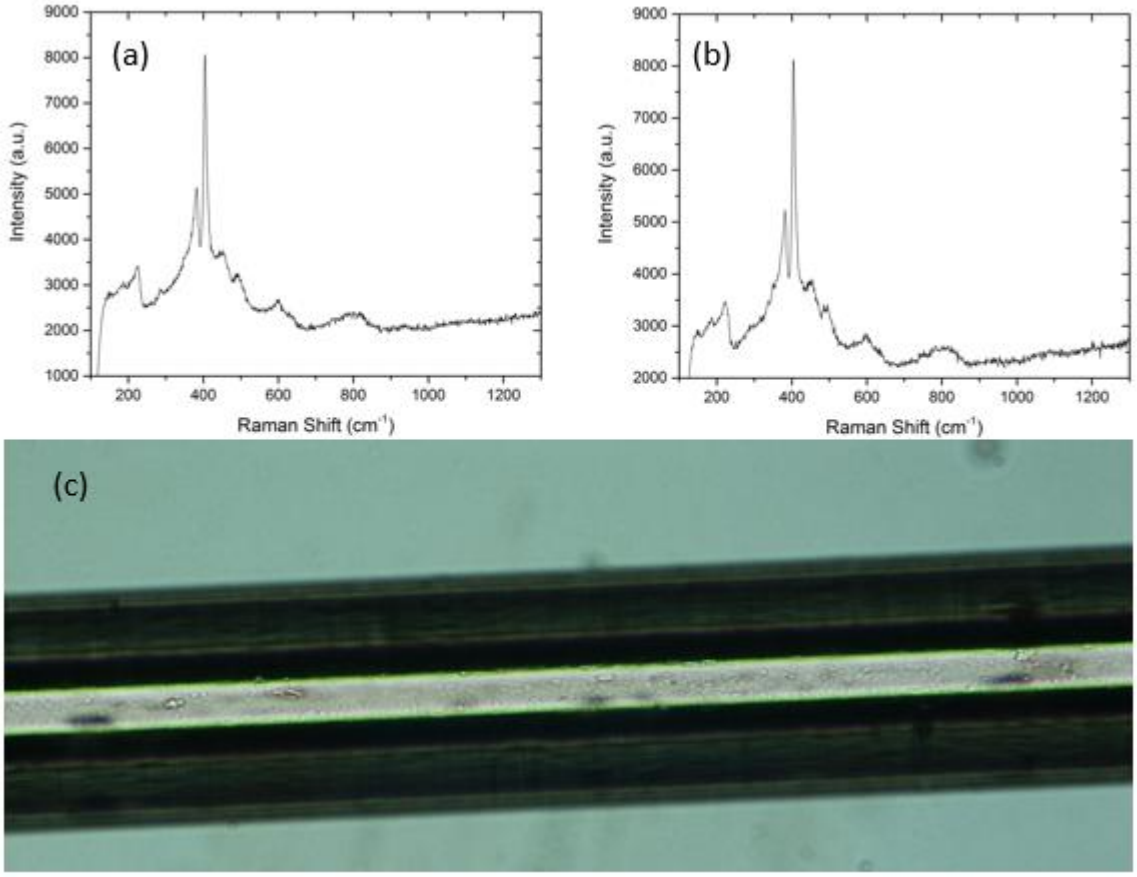

Figure 3.14: Raman spectra of MoS_2 deposited via a liquid phase deposition technique, using ATTM dissolved in DMF. Two typical Raman responses are shown (a) and (b), with peak separations implying bi-layer to tri-layer film. (c) shows An image is also provided of the deposition inside the 50um hollow core fibre. As can be seen, dark patches are present, implying the coverage of the film is not ideal. Improvements were therefore made.

A paper by Yang *et al.* suggested improvements to the deposition quality of the MoS_2 through an alteration in the host solvent [86]. In the paper, the solvent solution was changed replacing the initial purely DMF solution with a solution of DMF and Aminoethanol. It was found that the Aminoethanol promoted growth on the substrates, by forming bonds with the substrate which were easily broken. The process was improved by adding butylamine to the solution. This appeared to help the growth of the MoS_2, and allowed for self-limiting synthesis to occur.

The solution used in the following experiments was therefore changed to align with this work. An initial test analysed how the two key factors affected the deposition, the temperature and the concentration. A 0.5wt%, 1.0wt% and 1.5wt% solution of $(NH_4)_2MoS_4$ mixed with DMF, Butylamine and Aminoethanol in a 4.5/4.5/1 ml ratio was made. The solution was flowed into the fibre by capillarity and annealed under the same process conditions, but with differing temperatures of 450°C, 500°C and 550°C. The results of the Raman analysis is exhibited in Table 3.2, showing the average separations for and their standard deviations. The averages show a film of around 3 layer thickness for deposition temperatures of 550°C. These show standard deviations of around 1.5cm^{-1} corresponding to possible bilayer film. The 500°C anneals suggest relatively bulk film, however, the deviation could show bilayer film. However, this is unlikely, as the large deviation implies a very non-uniform film. A typical Raman peak is shown in Figure 3.15. Two supplementary Raman images are also shown, to show which Raman traces have been rejected from our calculations. One of these is from the 450°C anneal for 0.5% which displayed poor deposition with no discernible distinctive Raman peaks. For increasing concentration, we find that not much change occurs. It seems that temperature is the most important factor in deposition quality. A limit of 550°C was chosen as the quality of the silica fibre was key, as at around 600°C the fibre began to suffer and became brittle. Our next step was to transfer this work into twin hole fibre structures.

Concentration	**Anneal Temperature**	**Averages**	**STD DEV**
0.5pc	450	NULL	Null
	500	25.95	3.15
	550	21.73	1.31
1pc	450	NULL	NULL
	500	26.07	4.61
	550	20.76	1.32
1.5pc	450	25.29	2.69
	500	24.77	3.43
	550	21.16	1.57

Table 3.2: Data investigating the effect of temperature and concentration of precursor on the deposited quality of MoS_2. Temperature control on the deposition appeared to be the key quantity in fibre based experiments.

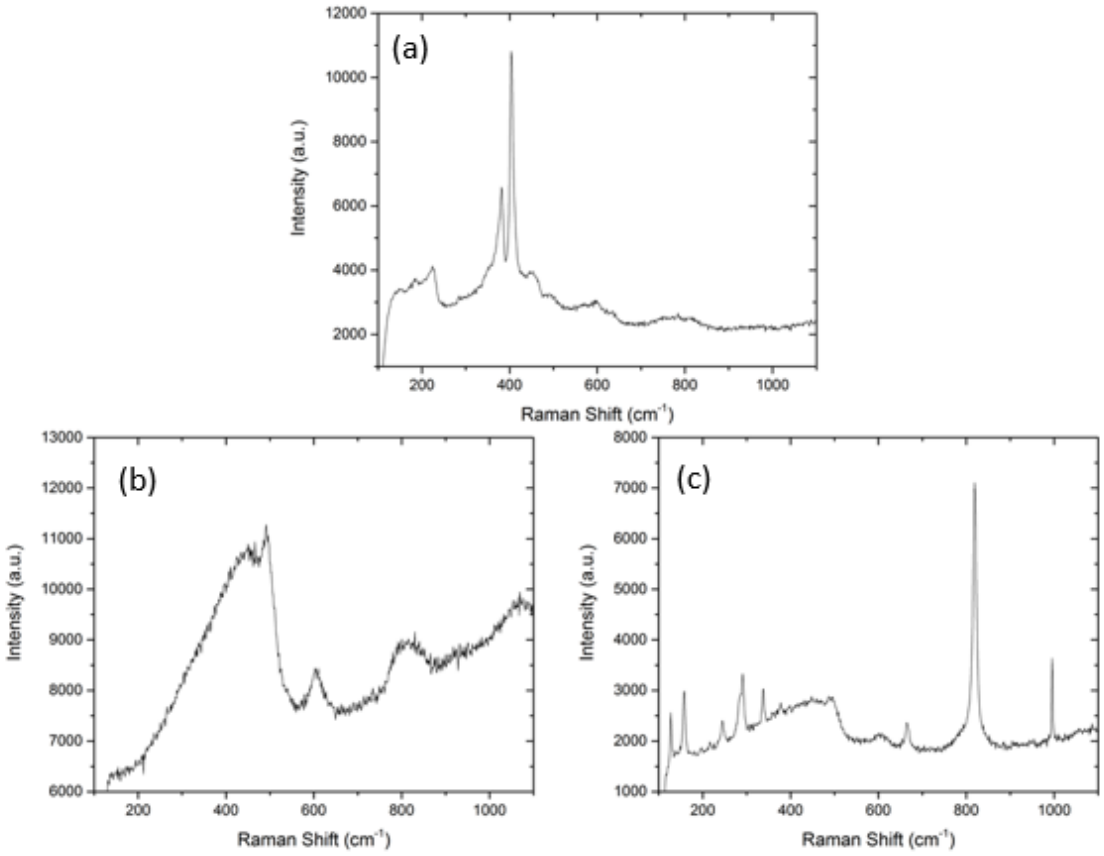

Figure 3.15: a) A typical Raman spectra for a MoS_2 film deposited via liquid phase deposition. The deposition conditions were a 550°C anneal, using a 1.5wt% solution. The separation is of 22.2cm^{-1} suggesting bi-layer film. Two further images, (b) and (c) are provided that do not show good Raman response and these outliers have therefore been removed from the standard deviation calculation. These correspond to a 500°C anneal with a 1.5wt% solution and 450°C anneal with a 0.5wt% solution.

The knowledge from capillary fibres was then transferred into twin hole fibre structures, with solid cores but hollow circular regions placed either side of the core. The deposition process discussed in the previous section was then performed on these fibre samples. The only difference to previous attempts to fill the fibre is that the time taken to fill long lengths of the fibre was longer due to the reduced hole size. The fibre itself also had the same tolerance to temperature, and the low temperature of annealing meant the fibre was not harmed.

Before the poling process took place, we analysed the fibre under Raman spectroscopy. Under the Raman investigation, the length of the deposition reached around 35cm, with different samples showing the relative uniformity of deposition. Raman spectroscopy would allow for the fibre to be re-used for applications processes. For the twin hole fibres, both hollow regions of the fibre were integrated with MoS_2, with Raman confirming that film had been deposited in both hollow regions.

The next process was to pole the fibre. This part was undertaken by a member of our group, Francesco De Lucia. His work over the last few years has focussed on improvements to the poling process. For these fibres, liquid metal electrodes were used, in this case mercury.

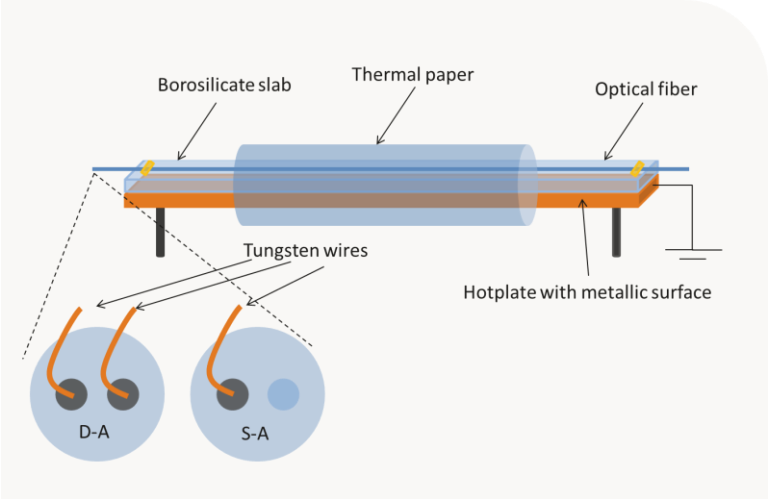

Figure 3.16: The set up used for the poling of the twin holed fibre device. The holes of the fibre were integrated with an electrode, and place onto a metallic surface onto which a high voltage could be applied. From Ref [113].

This was used as it was a liquid at room temperature, meaning that it could easily fill the fibre and act as an electrode, but also be removed at the end of the process at room temperature, using the same pressurization system created for filling them. This procedure should remove additional optical loss seen in other research papers, which leave the solid electrode within the fibre leading to high loss [111]. Here, only one hole of the fibre was filled with mercury. To do this, one hole was filled for a few millimetres with epoxy glue in a process known as selective filling [112] – blocking the channel off as seen in Figure 3.17. Mercury could then be flowed into the fibre via pressurization system applying 200psi to a mercury vial, with the only route for the pressure to escape being via the fibre. Contact was made to the mercury electrode through the insertion of thin tungsten wires into the hollow region of the fibre. Once connected to a high voltage power supply, the fibre could be poled in single anode configuration. The process was completed under a high temperature of 250^{o}C, with an applied voltage of 6kV. The temperature was applied for 30 minutes before the voltage was turned on, and kept at a high value for 2 hours, before the temperature was turned off. The heat was allowed to dissipate, and after an additional hour the voltage was switched off. Once at room temperature, the pressurization system could flow gas through the fibre to remove the mercury. This was necessary to remove the anode, as this could incur heavy optical loss if left in the fibre.

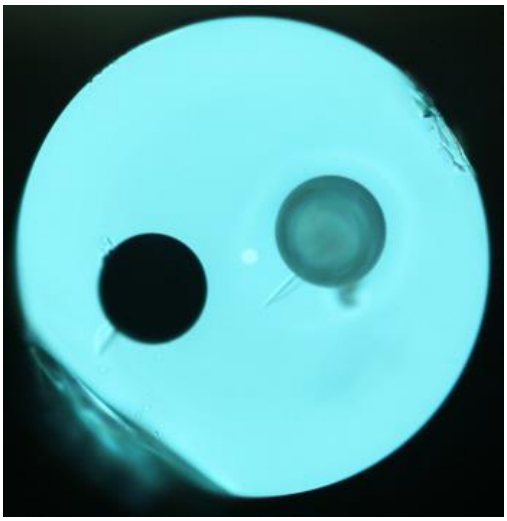

Figure 3.17: A twin holed fibre with one hole filled with epoxy glue. This would block this channel for filling with MoS_2 precursor solutions and the Hg electrodes. The fibre has a diameter of 250µm with the hole sizes being of 30µm diameter. The offset of the hollow regions are 5µm and 11µm from the core of the fibre.

To clarify if the poling process had been successful, the fibre was decoratively etched. This is achieved by placing the fibre into a 58% HF solution for one minute. Although this does not give a measure of the produced second order nonlinearity, it is able to tell us whether the fibre has been successfully poled. This can be seen by the depletion regions, as seen in Figure 3.18. The clear depletion region seen around the hole around the on the right is clearly the fibre where the mercury anode has been placed, but note how there seems to be a second depletion region in the second hole. This implies that the MoS_2 has acted as an 'induced' anode [9]. It is almost as if it has produced its own depletion region. This was totally unexpected. This was also replicated in a three-hole structure. This implies that the induced anode can induce a further anode. Three clear depletion regions can be observed. As a further benefit for using the three holed fibre structure, it would also allow us to see how the deposition is affected by the size of the hole – and if there was a limit to the size the MoS_2 precursor solution would be able to penetrate. As can be seen from Figure 3.18, the induced ring around the central hole suggests that MoS_2 was present. It would therefore seem that the deposition process works well in small diameter conditions.

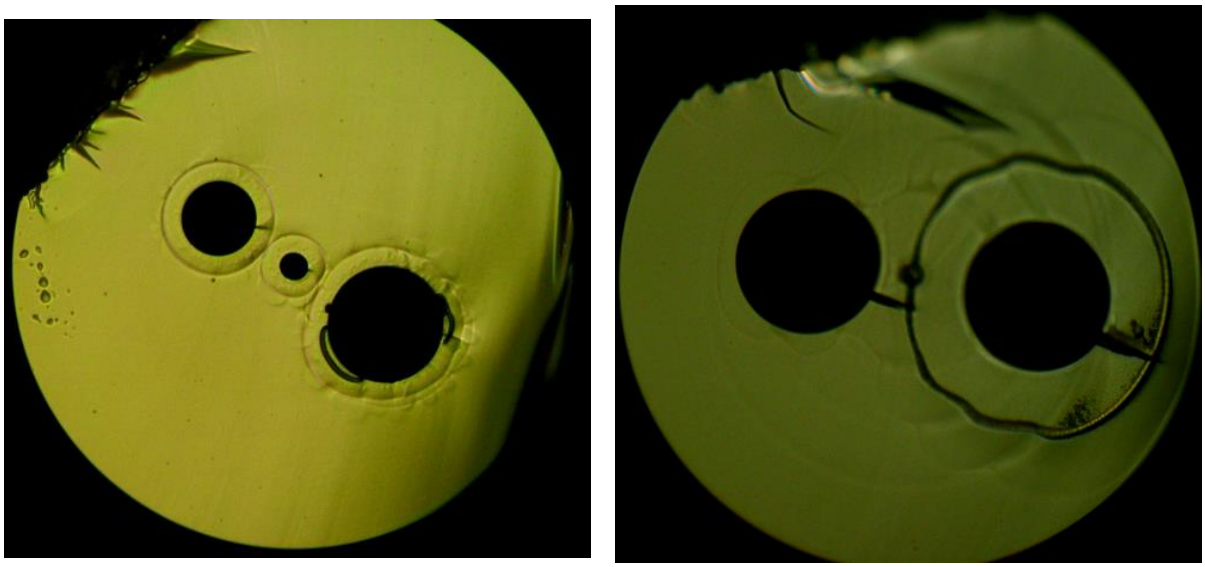

Figure 3.18: The results of decorative etching on two poled fibres in which MoS_2 deposition has been performed in all hollow regions. The three holed fibre has a total diameter of 250µm, with the three holes being of 45µm, 30µm and 10µm. The twin holed fibre has the same measurements as that from Figure 3.17. For both fibres, the anode has been placed into the hole on the right hand side. For the three holed fibre, the induced anode in the 'core' hole seems to have induced on the left hand side.

However, the samples produced in Figure 3.18 were not usable for device applications. The three holed fibre – although a great example to show that thermal poling has succeeded – does not guide light and would be unable to undergo the quasi-phasematching necessary to produce a waveguiding device with a strong signal.

The depositions were therefore re-created in different twin-hole fibre structures created at the University of Southampton silica fibre group. The holes in the fibre were made by a water drilling process, generating holes of 20µm size in positions equidistant from the core, 10µm away. Using the same deposition process of a liquid phase deposition with a 1wt% solution, the deposition was performed under 100sccm of 6% H_2/Ar at an annealing temperature of 500^{o}C. The poling process was repeated under the conditions of a temperature of 250^{o}C, an applied voltage of 6kV and a poling duration of 2hrs. Once again, a single anode poling process was used, with both hollow regions of the fibre integrated with MoS_2. Raman spectroscopy was used to confirm the presence of an MoS_2 film, showing good deposition over a 20cm region within the fibre. Further Raman analysis showed regions of poor deposition combined with regions of no deposition. After this investigation, the fibre was cleaved into two different samples, one with good deposition – labelled MoS_2-01 – and one with poor/no deposition – labelled MoS_2-02. Importantly, the two fibres were of equal length of 20cm. Due to the samples both being poled at the exact same time, a comparison between the quality of the MoS_2 deposition will be seen once the SHG is measured. The fibre had

buffer fibre, a SM980 from Thor labs of 30cm of length spliced to each end of the fibre, and could then be placed into the QPM set up.

Figure 3.19: A brief schematic of the final device, with SMF980 spliced (dashed lines) either side of the poled fibre after the gratings writing process.

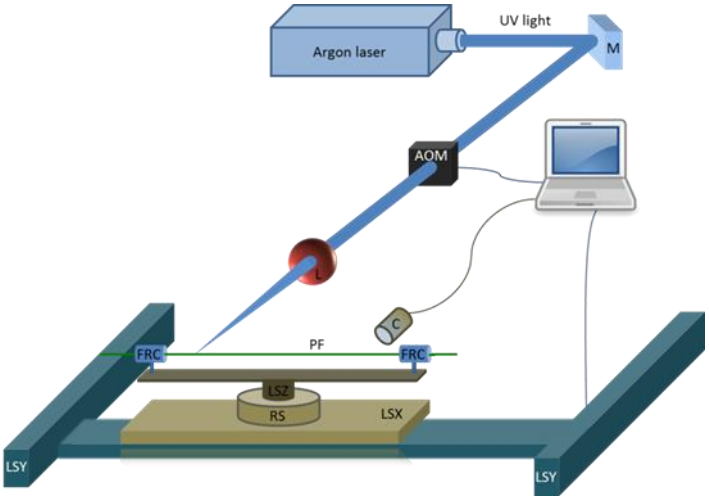

Figure 3.20: The optical set up used to write the UV gratings into the poled fibre device. An acousto-optic modulator (AOM) is synchronised with the movement of the linear stage (LSX) to allow for UV light to write in gratings to the poled fibre (PF). From ref [113].

For the QPM set up, a UV laser of wavelength 244nm, with a fluence of 14J/cm^2 was focussed into a circular beam measuring 10µm by 10µm of radius onto the sample, generating gratings optimised for a pump beam of 1550nm. This should allow for SHG generation of 775nm light. An optical setup such as that seen in Figure 3.20 was used to produce these $\chi^{(2)}$ gratings. The gratings were optimised using the refractive index of the core glass when applied to Equation 3.5, as had been performed on previous poling experiments. It is unclear at this stage of the device as to how to include the SHG generated from the MoS_2 into the grating writing equation, so for now the grating was optimised purely from the glass.

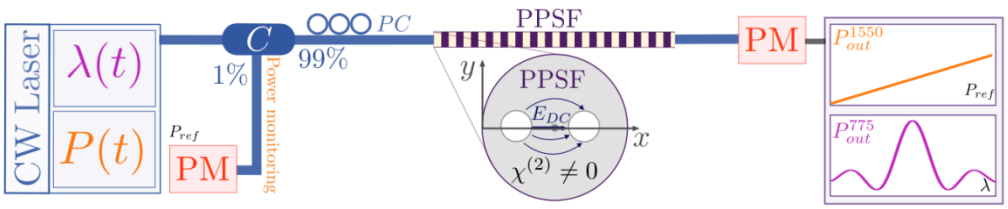

Figure 3.21: A schematic of the characterisation set up for the periodically poled fibre (PPSF). The input from a CW Laser (Agilent, model 8164B, linewidth ≈ 100kHz) and output of the device is measured. P corresponds to the power of the Laser, and λ for its wavelength. C is the coupler in the system, which allows for power monitoring of the laser with PM being the power meters used for measuring the fundamental and second harmonic power. From ref [113].

To then finalise the quality of the created $\chi^{(2)}$, the fibre was placed into a narrowband 1550nm characterisation laser system of Opera Photonics, at the University of Brussels to launch light down the poled fibre. The optical set up is shown in Figure 3.21, with the power detector at the output measuring only the power of the SHG light. The strength of the second harmonic was measured and shown in Table 3.3. Furthermore, the loss of the fibre was measured, including the loss from the splicing, as seen in Figure 3.19, the MoS_2 and the loss from the coupling. The result from this was input into Equation 3.3 to estimate the second order nonlinear susceptibility.

Device name	**Measured $\chi^{(2)}$ (pm/V)**	**Loss (dB/cm)**
MoS_2-01	0.0474 ± $1x10^{-4}$	0.021
MoS_2-02	0.0095 ± $1x10^{-4}$	0.017
Reference fibre	0.0426 ± $1x10^{-4}$	0.013

Table 3.3: Results from the poling process on three fibres with the same poling and QPM conditions. The MoS_2 fibres are integrated with 2D film, with the -01 sample being of good quality deposition and the -02 sample of poor deposition.

A non-functionalised reference fibre free of any MoS_2 was also supplied, in which the same poling procedure had been applied and the same treatment after poling. Two results are shown from the same optical fibre, with the MoS_2-01 sample showing excellent deposition of MoS_2 (as measured by Raman) and the MoS_2-02 fibre showing poor deposition. From the results, it can be seen that an almost 10% increase in the $\chi^{(2)}$ had been generated in the MoS_2-01 fibre by the insertion of a 2D film in comparison to the reference fibre. As an extra benefit, the loss did not increase much further, indicating that the fibre still performs as well as non-integrated structures. In contrast, the fibre with poor deposition of MoS_2 produces very little SH light, suggesting that the quality of the deposition is paramount to the working of the integrated film. This is likely due to the regions of poor deposition likely having more layers. This in turn would likely produce more scattering points,

and higher intrinsic loss. The generated second harmonic is therefore likely to be lost and unmeasured, producing the small $\chi^{(2)}$ in Table 3.3.

3.3 Concluding Remarks on Functionalised Thermally Poled Fibres

The first attempt of integration of MoS_2 into twin holed fibre structures has seen an increase in the generated second order nonlinearity of the devices created. This has been measured to be around 10% higher $\chi^{(2)}$. Furthermore, a large section of this work was focussed on the deposition process used to synthesis such films, with the liquid phase deposition approach showing large success, with the functionality of the method being a large factor for its use – as well as its proven ability to deposit quality and uniform films. However, there are a few issues with the device generated, with factors such as the QPM and additional loss to the fibre being a hindering factor. Various methods to improve upon this are to be outlined in the future works section of this thesis.

Chapter 4 Anti-resonant Hollow Core Fibre Optical Modulators

4.1 Anti-resonant Hollow Core Fibres

4.1.1 History of Anti-Resonant Hollow Core Fibres

The most common optical fibres used today are known as step index fibres, which transmit light through a phenomenon known as total internal reflection [88]. They have a cylindrical solid core of a higher refractive index, surrounded by a cladding of lower refractive index. This is a mature technology which has been refined over decades of research, to create fibres which form the basis of modern telecommunications systems. One major benefit of these fibres is the small measure of loss produced, meaning large distances can be covered with little data degradation. However, recent fibre structures have seen optical guidance through hollow air cores, with potentially lower loss capabilities [114]. Here, the cladding material has a higher refractive index, meaning the mechanism by which guidance is achieved is different. This will be discussed later in this section. These hollow core fibres begin to show many benefits to step index fibres. For example, by guiding through air, the speed of the light is not inhibited by the refractive index of the glass, therefore we see faster transmission. Further, for high powered light guidance, the core material can begin to be damaged. This does not occur in the air core. A description of hollow core fibres will be discussed in this section.

The first hollow core fibre to be developed is that of the photonic bandgap (PBG) fibre [115]. These are made of hollow glass tubes in a periodic lattice, an example of which is seen in Figure 4.1 [115]. Their lattice structure produces an optical bandgap effect, where light in the core region cannot be guided in the cladding region, causing the propagating mode to be confined in the core. This is usually enabled by producing a defect in the core, breaking the lattice - such as an increased central hole size. Due to the guidance mechanism, this means the propagating light is confined to a short wavelength range, as otherwise the light guides in the cladding. Control on the size of the spectral width is created by altering the ratio between the diameter of the air hole, D, and the distance between the air core, Λ. The effect of this is seen in Figure 4.1c [116]. The shaded regions are those where a mode is able to exist in the cladding, with the white regions being that of the bandgap. It is worth noting that for smaller D/Λ ratios, the bandwidth of the fibre becomes smaller, as the bandgap decreases. Small transmission windows in hollow fibres are of interest to the community of high powered laser physics, as pulses are usually of precise wavelengths.

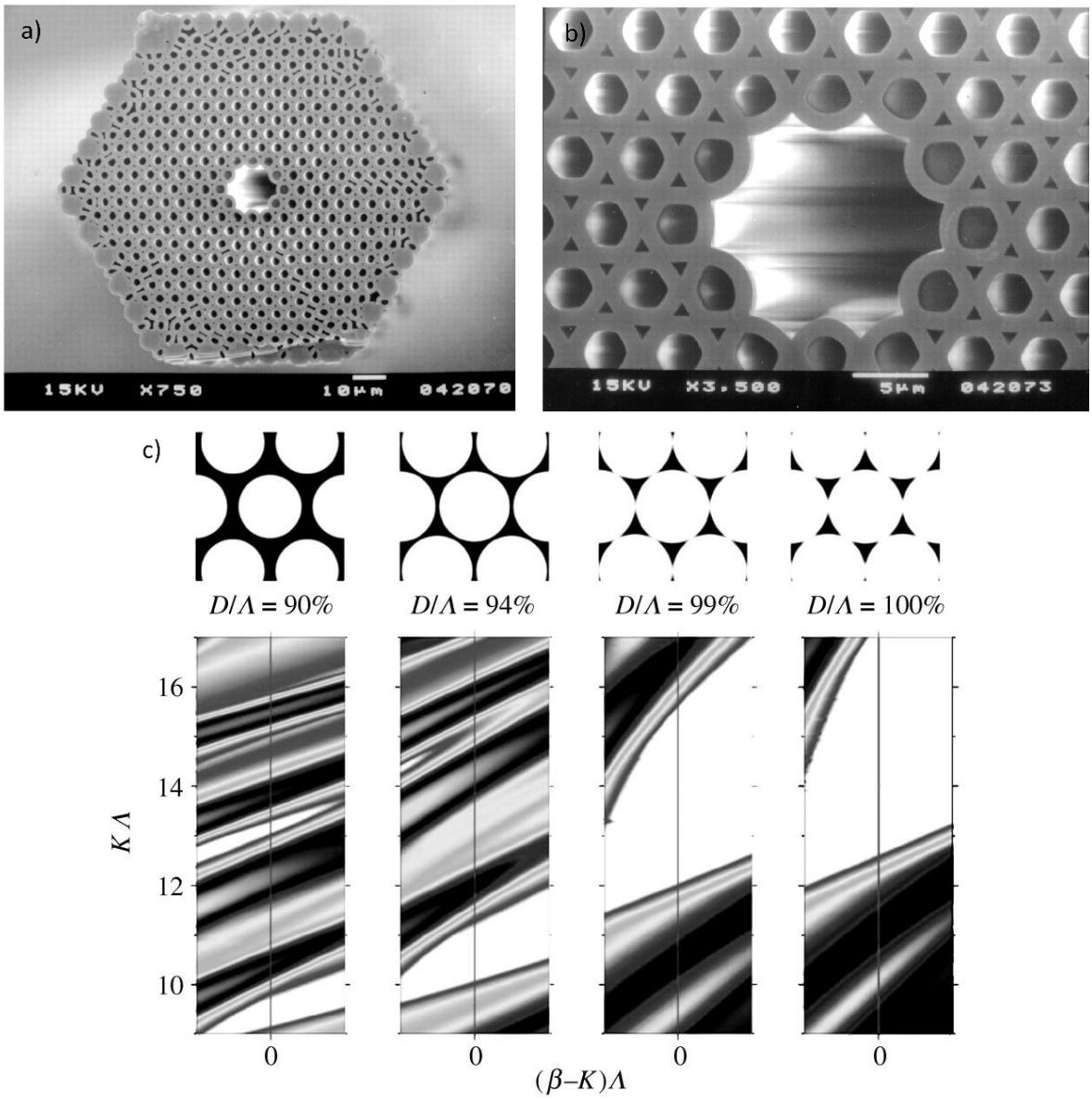

Figure 4.1: A hollow core photonic bandgap guidance fibre, created through the periodic lattice of small silica tubes arranged in a honeycomb lattice. The bottom part of the figure shows how the bandgap is affected by the ratio of the diameter of the hollow regions to the distance between the hollow cores. From ref. [116].

Further works into hollow core optical fibres began on Kagome lattice fibres in 2002. These fibres were created with repetitive structures, but guided with a large bandwidth meaning their guidance mechanism could not be explained by PBG theory [117]. The structure of a Kagome fibre can be seen in Figure 4.2, with thin glass struts forming triangular shaped patterns of a periodic nature. The transmission spectra is also shown in Figure 4.2c, with a low loss over the aforementioned large bandwidth. The guidance mechanism of Kagome fibres was solved in work by Couny *et al.* The explanation behind their guidance properties stems from the idea of Inhibited Coupling (IC) [118]. Here, a large mismatch between the core modes and cladding modes causes the light to be confined

in the air core. Modes contained within the cladding region begin to dissipate due to material absorption over long lengths, causing only the core guided modes to be obtained at the output for long fibre lengths. This guidance mechanism formed the basis of a new structure of hollow core optical fibres, named Negative Curvature Fibres (NCFs).

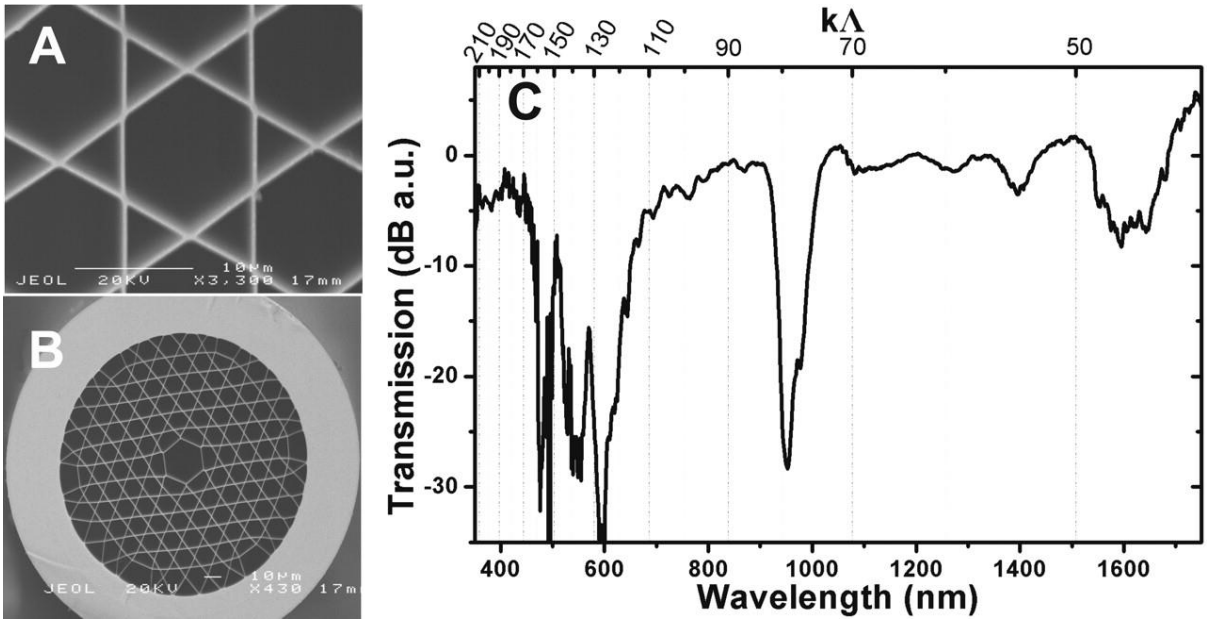

Figure 4.2: A Kagome lattice hollow core fibre showing the triangular struts made of silica. Shown also is the transmission spectra of the fibre, showing a wide bandwidth not usually associated with the photonic bandgap guidance mechanism. From ref [118].

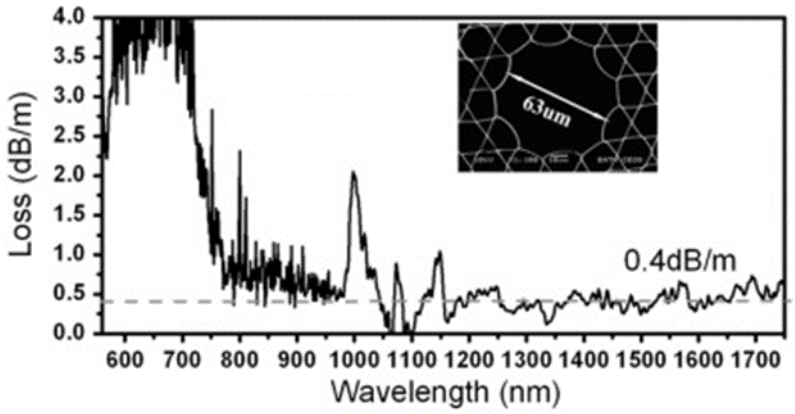

Figure 4.3: The guidance spectra of a Kagome lattice with a negative curvature core, showing little loss at 0.4dB/m in the NIR region. From ref [119].

Through analysis methods to decrease the loss of Kagome lattice fibres, the cores boundary shape was constructed to be of a negative curvature. This was found to reduce the attenuation of the fibre to as low as 0.4dB/m as shown in Figure 4.3, with later works showing the internal structure could be refined further to contain circular tubes on the cladding edge of a fibre [120][121][122], as observed in Figure 4.4a. This was known as a Negative Curvature Fibre. It was able to achieve high quality guidance, forming spectral bands defined by the thickness of the internal tubes. A

typical guidance spectra is represented in Figure 4.4b, with regions of resonance seen producing high loss, and regions of anti-resonance showing little loss [120]. The microstructure was also much easier to produce, saving time and costs, thus showing potential commercial manufacturing viability.

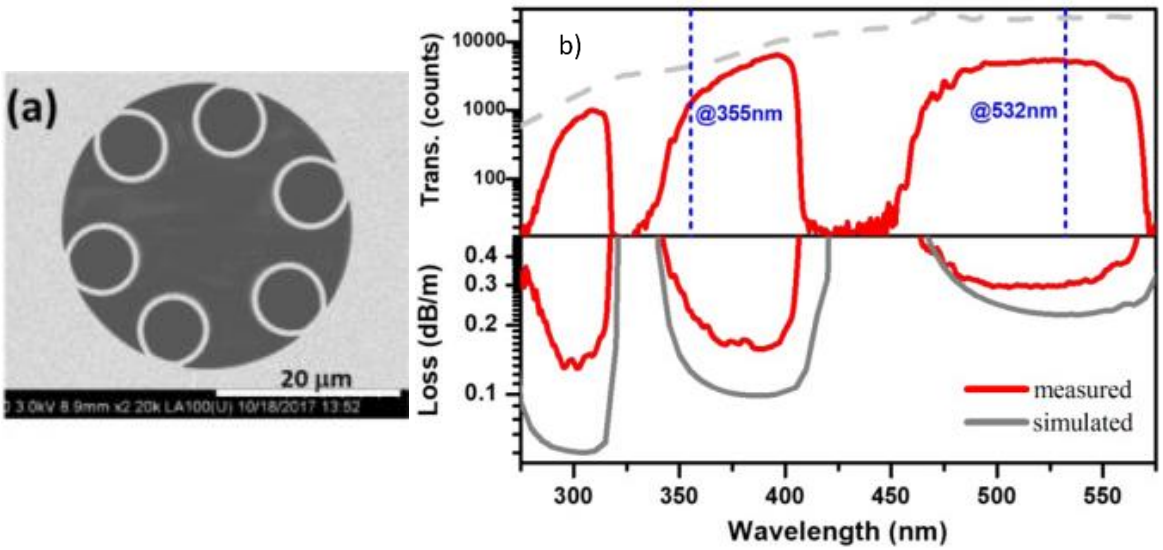

Figure 4.4: An image of a hollow core negative curvature fibre with six internal rings. The anti-resonant transmission spectra is also shown, showing regions of good guidance between regions of poor guidance. Low loss is seen in these transmission windows. From ref [120].

4.1.2 Manufacture and Working Mechanism of ARFs

It is worth mentioning at this point how such fibres are created. Following on from the techniques used to create photonic bandgap fibres [123], the process is refined to allow for pressurised gas to enter the preform, to control the size of the created NC cladding region [124]. The basis of the production of such intricate cladding structures revolves around the stack and draw technique. The microstructured fibres, comprising of air and fused silica and are typically manufactured using a macroscopic fibre preform up to one metre in length. This incorporates the desired transverse glass lattice pattern, typically using capillary fibre tubes stacked onto one another forming the desired cladding shape. These are then drawn on a glass drawing tower into the microscopic scale fibres that, due to the remarkable thermomechanical properties of pure silica, almost perfectly preserve the intended cross-sectional lattice design. By adjusting drawing parameters such as feed rate, tractor speed and drawing tower furnace temperature, the fibre dimensions are set according to a simplified mass conservation law, $A_p v_p = A_f v_f$ where A_p and A_f are the cross-sectional area of the preform and fibre respectively while v_p is the preform feed rate and v_f the fibre drawing speed. The tower furnace temperature is maintained between the glass softening and melting temperature of around 2100 ^{o}C. The very wide viscosity range of pure silica is exploited to ensure precise control

of the microstructured fibre dimensions and uniformity, with online measurement tools such as laser interferometry of the outside diameter enabling automatic instrumentation feedback.

For the production of defects, capillaries of different shapes or sizes are added. For PBG fibres, this can be a time consuming process, with much care needed due to their intricate structures. The fibre is slowly drawn, decreasing the diameter of the overall structure by roughly a factor of 10. This can then be placed into a solid cladding structure and is drawn again, creating the fibre structures seen in the previous figures. By applying external pressure to the structure via inert gas, the shape of the preform is maintained.

A NCFs guidance mechanism was thought to be formed from a type of inhibited coupling, also known as anti-resonance. This produced the ARROW model, as highlighted by Yu and Knight [124], whereby each region of the fibre is considered as a cavity in of itself. This produces a mismatch between the core and cladding modes, confining propagating light to the air core. A theoretical calculation for the resonant wavelengths, λ_R, can be performed via Equation 4.1 [124].

$$\lambda_R = \frac{2d\sqrt{n_2^2 - 1}}{m} \qquad \text{Equation 4.1}$$

Where d is the thickness of the glass strut, n_2 is the refractive index of the glass and m is an integer.

These wavelengths are where light is guided purely in the cladding. Theory states that it should be only at single wavelengths where no transmission is found, but for experimentally produced fibres, a bandwidth of wavelengths is produced due to issues such as non-uniform cladding structures, with the shape, thickness or diameter being inconsistent.

The relatively easy manufacturing method has led to a variety of different internal structures. These are highlighted in Figure 4.5 [120], [125]-[129]. As can be seen, a variety of different numbers of tubular rings can be chosen, to alter the shape of the mode and the loss associated with it. There is also a difference in the shape of the internal rings. Elliptical ringed structures have been investigated by Chaudhuri *et al.* in attempts to lower the loss at a guidance wavelength of 1060nm as shown in Figure 4.5b. There has also been the investigation of including more boundaries into the cladding structure. This includes the use of 'conjoined-tubes' or nested rings in the structure as shown in Figure 4.5c and 4.5d respectively. This was observed to lower the loss of the fibre in comparison to non-nested ring structures. The working theory behind this is that more glass/air boundaries can aid the confinement of light to the core [130] and that by nesting these rings, the size of the core is not affected, meaning the loss occurring due to bend loss is not infringed [127].

4.1.3 Examples of ARFs

The reduction of loss occurring through either bend loss, material absorption or coupling into cladding regions, has been a key parameter to improve in fibre manufacturing. To date, the lowest published loss achieved in a NCF is 2dB km^{-1} at a wavelength of 1514nm from work by Gao *et al.* with the created fibre in Figure 4.5c [126]. The authors attribute this capability due to the introduction of additional interfaces. This low loss, with a relatively simple fabrication method offer HC-NCFs as a possible alternative for next generation telecommunications systems.

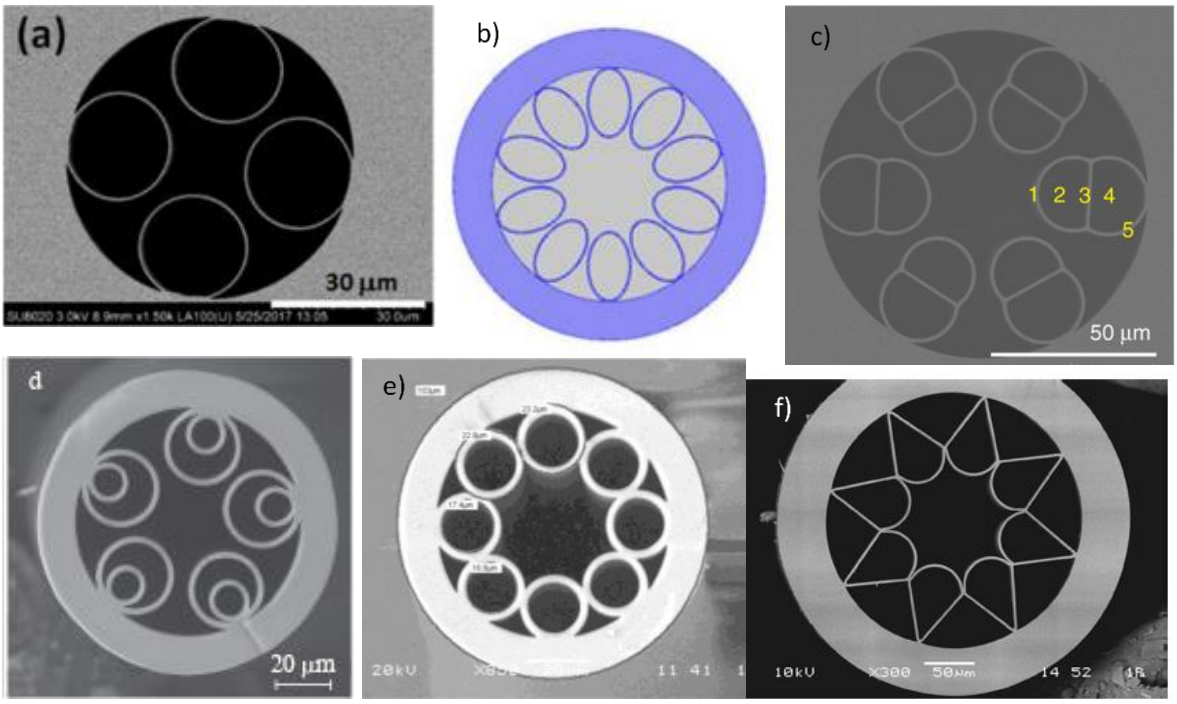

Figure 4.5: A variety of different hollow core negative curvature fibre structures. (a) shows an experimentally produced 4 ringed structure able to guide in the UV region. [120] (b) shows a theoretical construct with elliptical rings, in an effort to reduce fibre loss. [125] (c) shows a dual cladding structure, to further reduce the loss. [126] (d) shows a nested model shape, experimentally produced. [127] (e) shows a 8 ringed structure with the cladding rings in contact with one another. [128] (f) shows an ice-cream cone lattice, used for mid-IR guidance. [129]

As outlined in Figure 4.5e, the tubular structure shows regions whereby the cladding rings have been moulded to touch one another [128]. In an investigation by Kolyadin *et al.* the touching of the rings seems to generate additional loss, due to the point of contact beginning to act as "optical resonators", and draws a theoretical model to show how they impact the loss in a fibre [131]. Another internal structure can be seen in Figure 4.5f with an 'ice-cream cone' structure with negative curvature interfaces. This fibre was used for mid-IR applications and was able to detect the IR absorption of gases in its transmission spectra [129].

The benefits of the use of NCFs are much like those of PBG fibres. Their air cores allow for high powered light transmission while circumventing unwanted parasitic effects associated with solid core guidance as their hollow cores guidance mean little interaction due to material nonlinearities. Furthermore, anti-resonant fibres have been seen to be used for more active approaches. By internally filling the fibre with a gas, the transmission spectra is seen to undergo changes, supplying evidence of the gases presence. The internal structure of such fibres also allows for transmission in the mid infrared regions, meaning the unique absorption regions of liquids as such can be analysed [132]. This has led to such fibres being potentially used as a sensing device, with various papers reporting upon this. Alternatively, the introduction of nonlinear gases such as hydrogen caused stimulated Raman scattering, to alter the guided wavelength from 1064nm to 1907nm [133]. By the correct construction of the fibre cladding, both wavelengths were capable of low loss guidance. The NCF structure offers large surface area, allowing for the functionalisation of the surfaces.

4.1.4 Composite Material ARFs

The integration of a secondary material into the inner cladding of the fibre could also offer an active method of guidance control of such fibres. Our group showed this, in a seminal work by Belardi *et al*. showing how the deposition of silicon into the cladding regions of the fibre can alter the spectral properties of guidance [134]. A theoretical model was also proposed in this work, showing that the addition of a composite material could be considered as a culmination of the glass host material and the silicon addition, as explained by Figure 4.6. By taking a weighted average of the refractive index of the material, the change in the position of the anti-resonant regions could be predicted. The fibre was then reproduced experimentally, through the thermal decomposition of silane gas on the inner regions of the fibre. Here, around 50nm of material was deposited, with confirmation of this shown via Raman scattering and SEM images, shown also in Figure 4.7. A conformal film was produced, with little discrepancy in the quality of the deposition. When observing the optical spectrum, the theoretical prediction was confirmed, with a shift in the transmission windows presence. However, the thick silicon layer introduced a large amount of loss into the system, even over a short (30cm) deposition length. However, this laid the ground work for looking into how an additional material could integrate into an optical fibre.

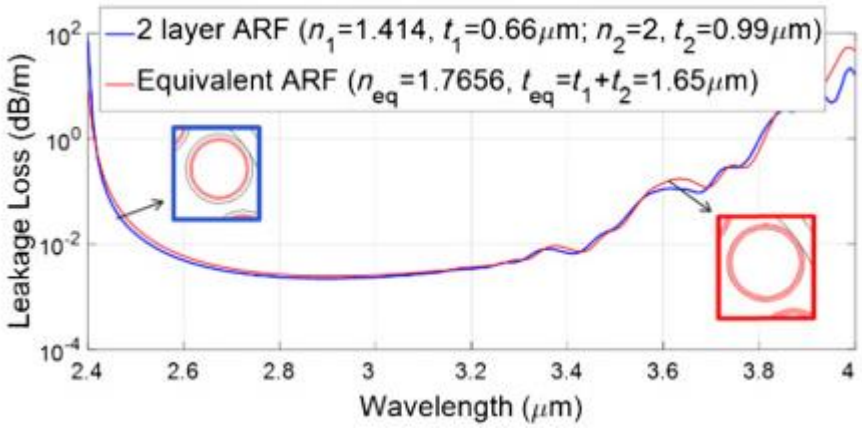

Figure 4.6: A theoretical outlook on how the dual material cladding can be considered, as either two distinct material surfaces, or a weighted average. As can be seen, the two traces correlated well with each other. From ref [134].

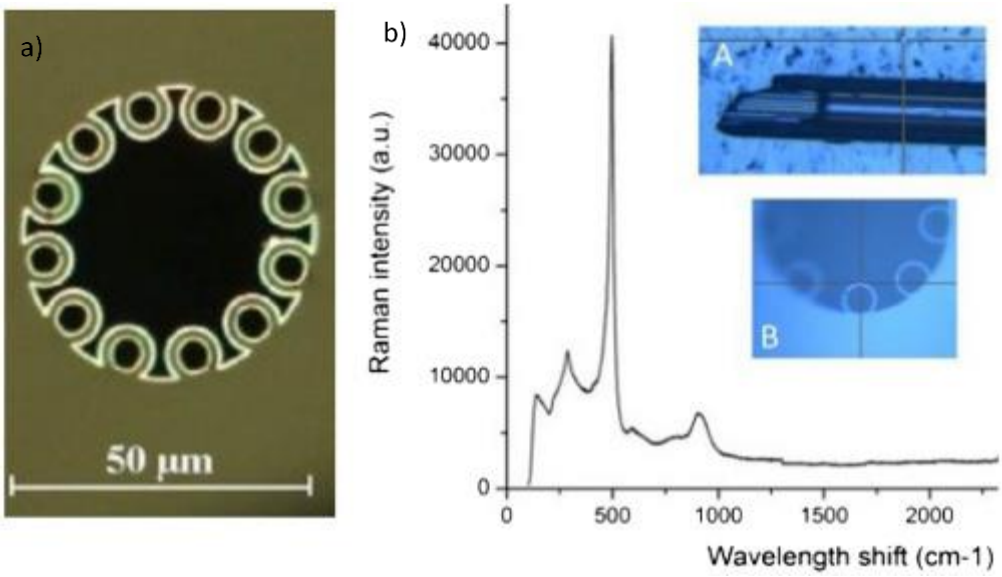

Figure 4.7: An experimentally produced silicon deposited NCHCF with a roughly 50nm deposited film. The Raman spectra of the fibre is also produced, with a sharp peak at 500cm^{-1} signifying the presence of Silicon. From ref [134].

We then began to propose how MoS_2 could be integrated into a NCF. It has been seen that MoS_2 has been observed to change its optical properties in the presence of an electrical field. The issue with the silicon deposition was the amount of loss introduced into the system and the danger of silane gas, which is known to be extremely reactive with air. By deposition of a much thinner layer of material, it may be possible to achieve spectral control on the fibre, with the addition of little loss.

We aim to produce an electro-optical modulator inside of an optical fibre. This should negate the need for an optical fibre to convert from a fibre system to a planar based optical system, which can generate additional loss due to inefficient coupling. Our focus was on the manufacture of high

quality film on the inner regions of an ARF. We began by modelling the system to see what would be achievable in terms of modulation depth and help characterise the additional loss a composite film would add.

4.2 Modelling of Hollow Core Fibres

4.2.1 Negative Curvature Fibres

4.2.1.1 Modelling of Template Negative Curvature Fibres

To begin the modelling process, we first looked into programs that would allow us to do such. A well known program is that of COMSOL, a finite element solver that allows us to build the structure of fibre and analyse its mode guidance. A mesh is generated and calculations are performed at each point of the mesh. For optical fibres, the mode analysis module is used, to produce an intensity image of how the majority of the power is located when propagating in a fibre. This is able to find the fundamental mode by analysing around the effective mode index of the core, n_{eff}. This is the value of the refractive index of the core which takes into account the surrounding cladding refractive index.

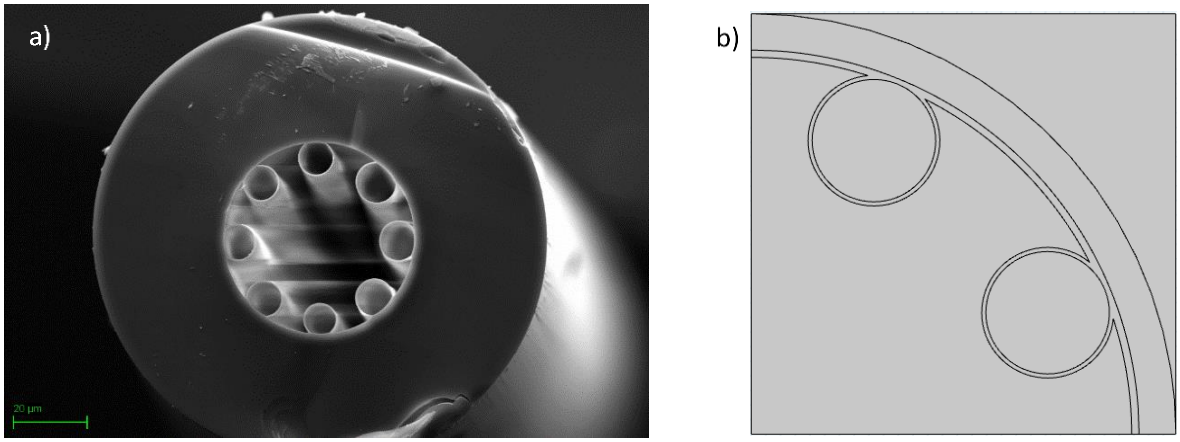

Figure 4.8: a) A 8-ring hollow core fibre structure made of borosilicate created at the University of Southampton. A thickness of 0.282um of the struts is measured from the SEM images. b) shows the fibre reconstructed in COMSOL, showing only a quarter of the fibre to allow for easier computational work.

A borosilicate 8 ring structure was analysed under SEM imaging to characterise the shape of the fibre and parameters such as the cladding ring diameter and strut thickness. The fibre chosen was the template fibre from ref [134], and had previous been experimentally chosen to host silicon deposition. Such a fibre was then reconstructed in COMSOL as seen in Figure 4.8b. Due to the symmetric nature of the fibre, only a quarter of the fibre was generated in the model saving

computation time. This had the following parameters: A core radius of 16.8um, with internal cladding rings of 4.475um radius. The inner rings had a thickness of 0.28um. The material, borosilicate, had a refractive index of 1.473.

To test this fibre, the mode was analysed around an effective refractive index of 1 (the index of air). Experimentally, the fibre had been observed to guide at 1550nm. This wavelength was therefore chosen to analyse the functionality of the fibre. COMSOL generated 6 modal images at around the effective refractive index as observed in Figure 4.9. Here 6 different mode images are shown, with the fundamental mode being the most significant of these. Also supplied in Figure 4.9b-f are the higher order modes investigated. These are necessary to observe to ensure that the subsequent analysis of the mode images is correct.

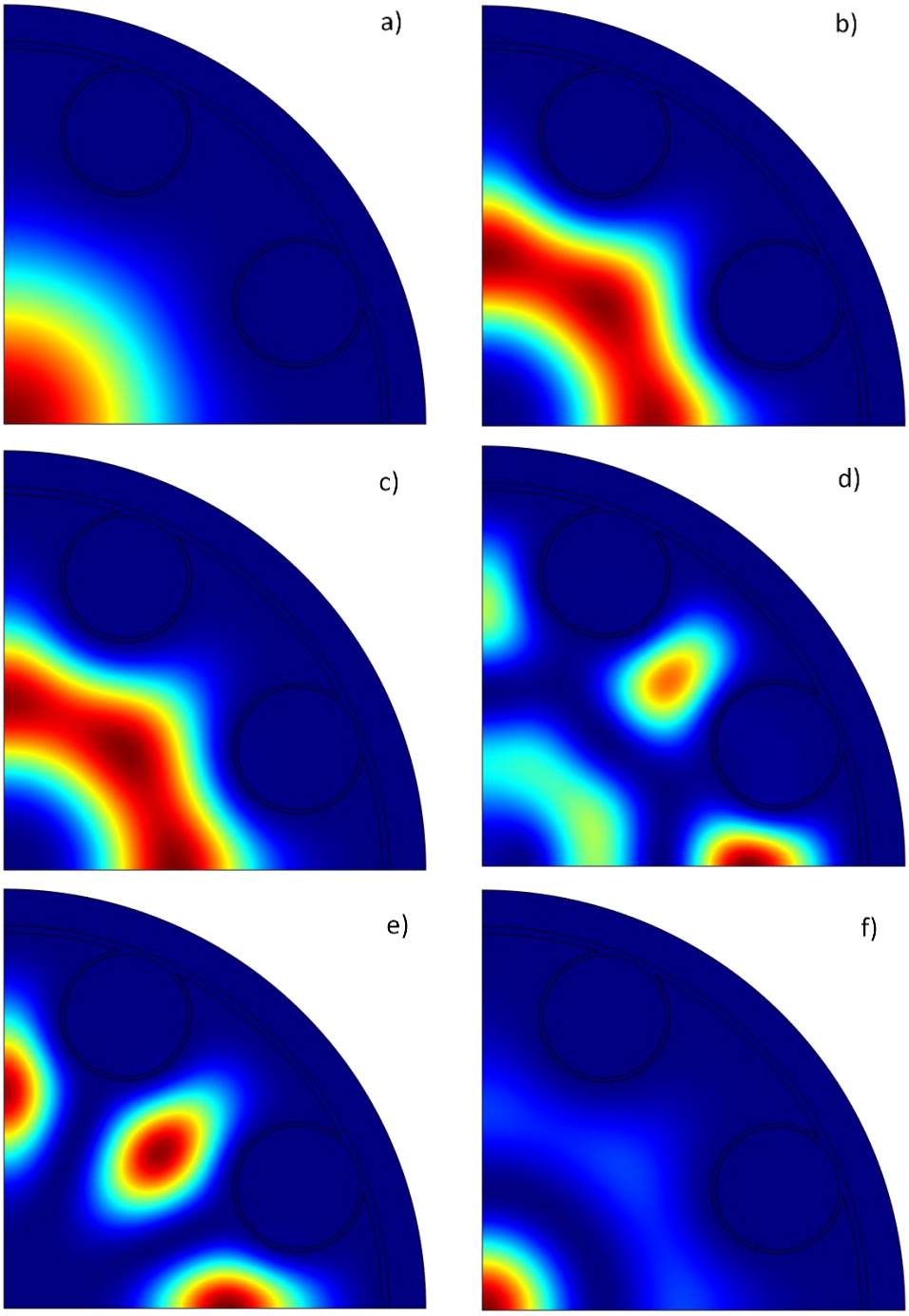

Figure 4.9: 6 mode images of how the 8-ringed structure reacts under 1550nm excitation. Figure 4.9a shows the fundamental mode, with the highest fractional power present in the core with figure 4.9b-f showing higher order modes

From these images, it is clear which mode is the fundamental modes, seen in Figure 4.9a. When numerically analysing these modes, the fundamental mode is the mode with the highest total intensity in the core region in comparison to the cladding region. This ratio was key in creating a parameter sweep of the wavelength.

To observe the guidance quality of the fibre as a function of the wavelength, the model was adapted into a MATLAB script. This script was able to run the model and extract the key results of the scan. Key amongst these was the fractional power, as this power would be able to tell us two significant factors. It would suggest which of the six resultant modes of the model was the fundamental mode, as well as the measure of the quality of the guidance. The MATLAB script was created to obtain the mode from the simulation and search through the results to find the mode with the highest integral power. This would be the fundamental mode. The model could then be run over a variety of wavelengths to construct Figure 4.12a which shows how the fibre reacts. As can be seen, a resonant window is observed at 600nm. Furthermore, this fractional power could be placed into Equation 4.2 to obtain the loss at each wavelength [126].

$$Loss\ (dB/m) = \frac{40\pi}{\ln(10)} \frac{Im(n_{eff})}{\lambda} \qquad \text{Equation 4.2}$$

This could also be performed in the MATLAB script, and produced the results seen in Figure 4.10.

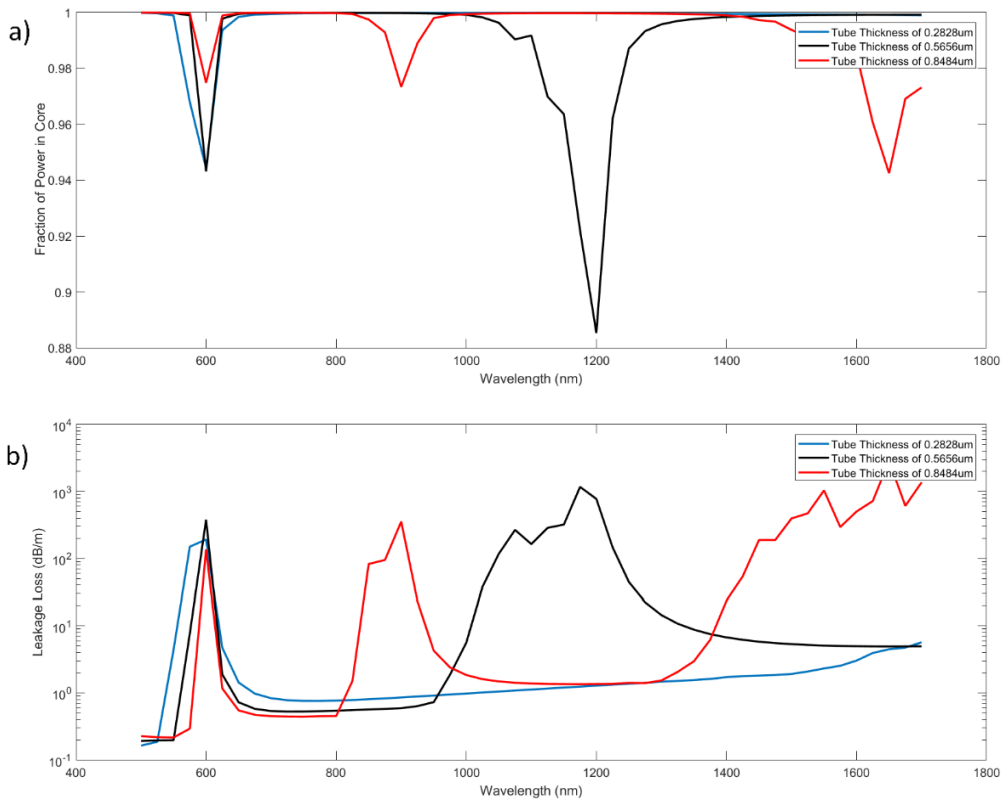

Figure 4.10: Simulated results of how the optical fibres transmission spectra changes with increasing tube thickness. The fractional power in the core is shown in figure a, with the corresponding leakage loss shown in figure b.

Now that a functional anti-resonant fibre model had been formed, we began to investigate the effects of the thickness of the glass cladding regions on the mode shape. It was clear to see that by increasing the thickness, the fibre would achieve both resonant and anti-resonant guidance, as

observed in Figure 4.10. There was a clear dependence on the thickness of the glass struts, with a ratio of integer values as seen in Equation 4.1. This suggested the created model worked as an anti-resonant hollow core fibre.

4.2.1.2 Integration of TMDC films into the Negative Curvature Fibre

The next step for the theoretical model was to introduce MoS_2 films into the generated structure. To do this, a deposition was applied to hollow regions of the inner rings of the cladding, to keep the computation time of the model to a reasonable value. The modelled deposition can be observed in Figure 4.11. We then performed analysis of the film, using film thicknesses of 3nm, 5nm and 10nm with the results demonstrated in Figure 4.12. These were selected due to computational constraints placed on the finite element solver – COMSOL was unable to render results for sub 3nm depositions without the program crashing. For the deposition of MoS_2, the material properties of MoS_2 were selected as having a constant refractive index of 4.29 and an absorption coefficient of zero.

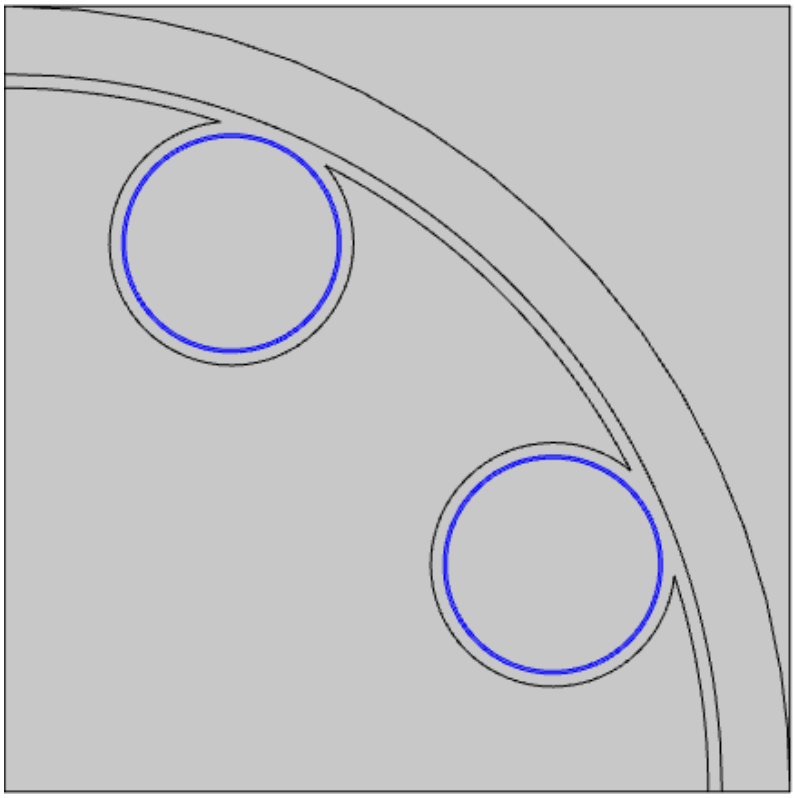

Figure 4.11: A demonstration of where in the optical fibre structure MoS_2 film has been deposited. This is highlighted by the blue region, in this image of around 100nm for pictoral purposes. In the simulations, the thickness of the film was much smaller.

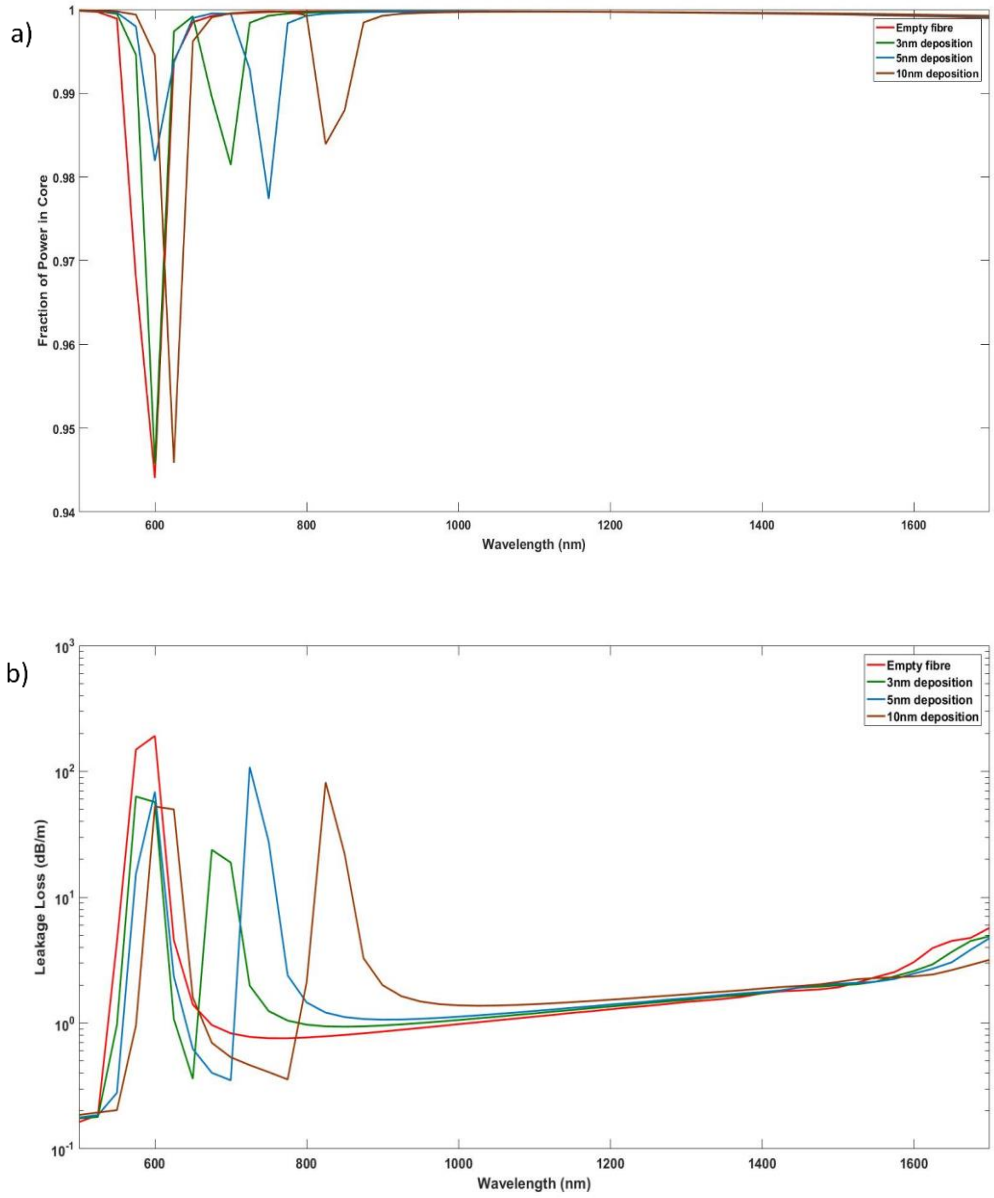

Figure 4.12: Simulated results of how the optical fibres transmission spectra changes with the implementation of MoS_2 into the cladding regions of the 8-ringed HCF structure. Different thicknesses of MoS_2 of 3nm, 5nm and 10nm are produced. The fractional power in the core is shown in figure a, with the corresponding leakage loss shown in figure b.

The effect of the introduction of the TMDC film is twofold. The first, and most obvious difference, is the appearance of a secondary peak in the trace for the introduction of another layer. It appears as if a new resonance condition is created using the film as the boundary. To test this, the refractive index of MoS_2 and the thickness of the TMDC film was placed into Equation 4.1. All three film depositions produced low λ_R values of 83nm (for a 10nm deposition), 42nm (for a 5nm deposition) and 25nm (for a 3nm deposition). These do not correspond to the secondary anti-resonant windows seen in the simulations of Figure 4.12, and are far below the lowest wavelengths measured in our

study as such small wavelengths would have been very computationally intense to test. The presence of these secondary peaks is therefore more likely to occur due to the large refractive index change between the borosilicate and the MoS_2 and possible guidance in the MoS_2 region.

The other change the additional film brings is a slight change in the first resonance window. We appear to find a shift towards longer wavelengths.

4.2.1.3 Concept of Modulation in the Negative Curvature Fibre

The simulation then turned towards looking into the potential capabilities of a modulation device using these films. From our work [36], WS_2 was seen to observe the larger refractive index change when exposed to an electrical field. The model was therefore modified to work for WS_2, by changing the refractive index of the 'deposited' material to 4.80. As per results from Yu *et al.*, we find that for an applied voltage of 67V, the gating effect causes this refractive index to decrease to 3.97. This was also simulated, with the two results compared.

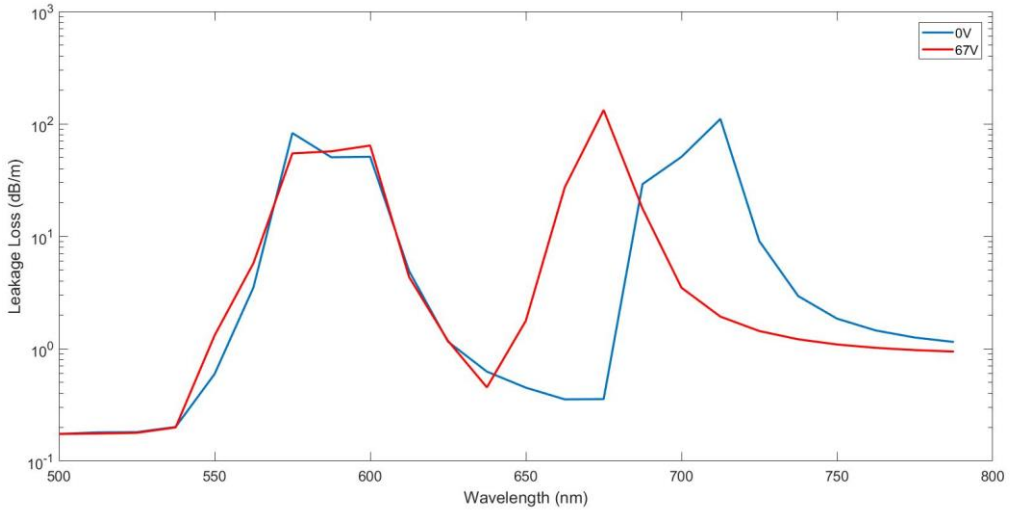

Figure 4.13: The results of the modulation of WS_2 in a 8-ringed NCF structure, showing a shift in the second resonant window at 725nm changing to a peak at 675nm.

As can be seen in Figure 4.13, the change in the refractive index leads to a manipulation in the location of the secondary resonance peak. We see a shift in the peak values loss changing from 725nm for 0V, to 675nm for the applied field. At the 725nm mark, we find that the application of the voltage leads to a loss difference over two orders of magnitude. At the 675nm mark, this is improved further with three orders of magnitudes difference in the loss. This would suggest such a fibre would perform exceptionally.

4.2.2 Anti-Resonant Fibre

4.2.2.1 Modelling of the Template Anti-Resonant Fibre

However, the limited availability of the 8-ring structure meant an alternative fibre structure needed to be used experimentally. Our focus turned to a silica based fibre, which was modelled. This structure was re-created in COMSOL, and can be seen in the inset of Figure 4.14a. This was a triangular ringed structure with touching cladding regions, which although is not an ideal internal design - as the contact between the sides can be inhibiting to the loss and bend loss - the fibre guided well in two regions of interest, at around 600-800nm and from 1200-1600nm. Our new device sought to exploit the semiconductor nature of the MoS_2. The first antiresonant window corresponded well to MoS_2's electronic bandgap region, and the second window showed low loss at telecommunications wavelengths. In constructing the COMSOL model, the size of the triangular structures is relatively accurate, but differs in that the fibre structure used in the experiments has irregularities due to the drawing step, whereas the models triangular structures are all identical. Discrepancies in the size of these shapes can lead to widening of anti-resonant windows.

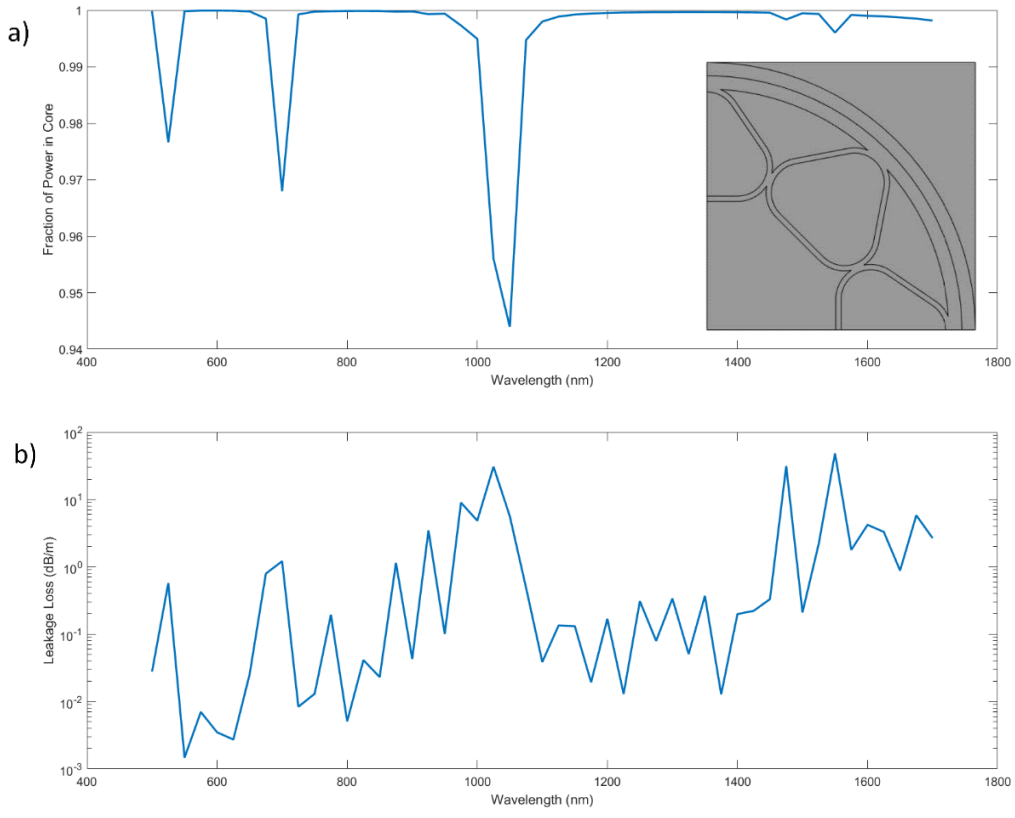

Figure 4.14: The simulated fractional power and leakage loss spectra of the B0461Y fibre used for the rest of the experiments.

The model was then simulated at an effective mode index of 1. As can be seen in Figure 4.15a, at a wavelength of 1550nm, single mode guidance is present. As for Figure 4.9, the higher order modes

are supplied and show different types of guidance capability of the fibre structure. For a bare fibre which looks as shown in the inset of Figure 4.14a, the loss as a function of wavelength can be seen in Figure 4.14b. Unfortunately, the leakage loss images is noisy, with anti-resonant windows visible, but hard to decipher and correctly characterise. This is due to the model being too 'perfect'. The guidance breaks down most likely due to the touching of the cladding struts.

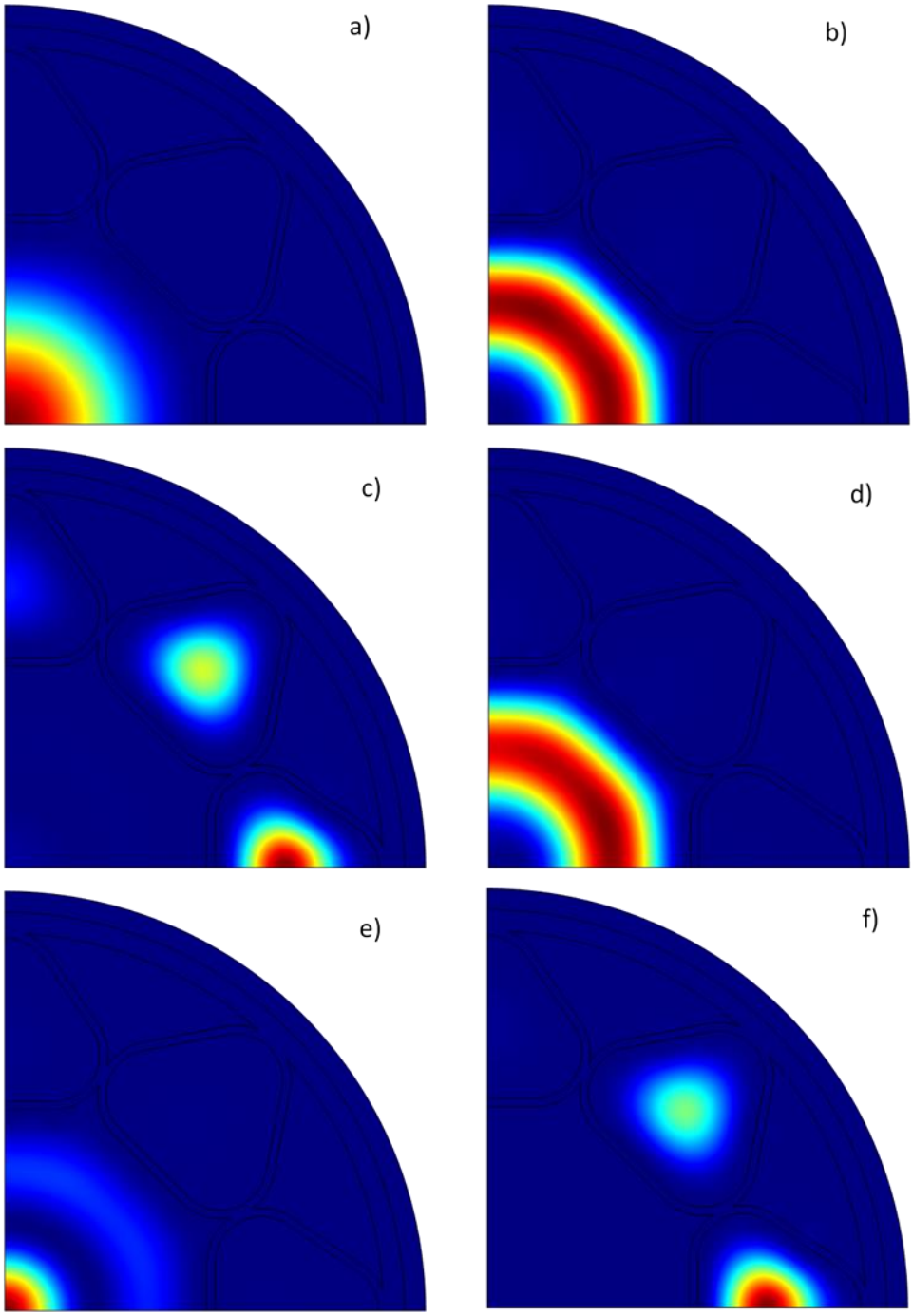

Figure 4.15: Resulting mode images of the B0461Y fibre in its base state, with no composite film. Figure 4.15a demonstrates the fundamental mode, showing little overlap into the cladding region.

4.2.2.2 Integration of TMDC Films into the Anti-Resonant Fibre

However, it is clear from the fractional power graphs that changes in the spectra could be found with the insertion of a secondary film. This was recreated much as the same as the 8 ringed structure discussed previously. Using the same parameters for MoS_2s optical properties, the model was ran in a cladding only deposition schematic. Due to the increase in the surface area of the model, computational power was further reduced, and so larger deposited films, so 10nm, 15nm and 25nm MoS_2 thin films were investigated.

The fractional power in the core was compared to that of an empty fibre. There are a few clear differences between the three traces in Figure 4.16. We clearly see a shift in the guidance windows, with the windows red shifting. Further, the loss of the system also is much larger overall. From these traces, it is clear that the film is beginning to interact with the light. If we can control the film, we can control the guidance properties of the system. There seems to be a few key characteristics of the film that the modelling overlooks, especially when comparing our model with experimental data. It is worth reminding ourselves of the issues with the model.

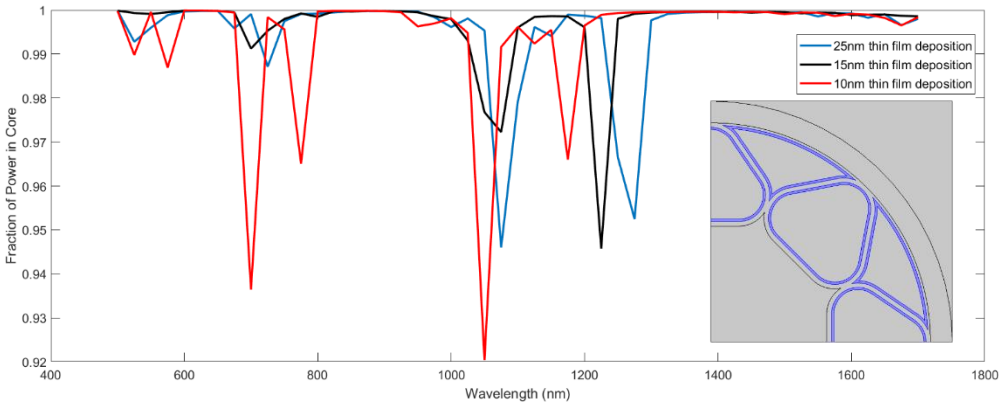

Figure 4.16: Simulated results of the B0461Y fibre integrated with MoS_2 of differing film thicknesses. The inset shows the structure of the fibre, with the blue sections showing the regions where MoS_2 has been deposited. This referred to as a cladding only deposition.

4.2.3 Limitations of the Theoretical Model

There are a few caveats in the model that are worth explaining. The first one is to do with the optical absorption of MoS_2. In the model, both values for V=0 and V_{max}, the absorption coefficient is considered as 0. The various papers record this value as around 0.4 x 10^6 cm^{-1} at the wavelength of the bandgap for single layer MoS_2 which would be important in noting the overall loss due to absorption of the system. Furthermore, the absorption coefficient is a function of the wavelength. The value of 0 was chosen as at near-IR wavelengths, the value is sufficiently small to be considered as zero. This renders the loss values of our simulations to be incorrect.

The other issue is with the refractive index dependence on the wavelength, which also has been ignored on in the model. This is due to consistent refractive index values being difficult to find within the literature. Many papers report on the wavelength dependence, but do not give values that reach the near-IR region. The refractive index was therefore changed to be present for the highest refractive index differences. This occurs at around the 1.8eV range (corresponding to around 700nm). This region therefore became of intense interest in the relevance of the model – i.e. the results near IR regions are likely to be less accurate.

When analysing the papers on how the gating of MoS_2 occurs, it is worth noting the mechanism by which modulation occurs. There is a clear wavelength dependence in these papers due to the bandgap being of significance. This would be difficult to place into the COMSOL dynamic. There are possible effects such as the doping of the charge carrier which cannot be solved in the mode analysis software.

Interestingly, we do not see the mode guided inside the MoS_2 region at the anti-resonant peaks. The high index change from MoS_2 (n=4.2) to silica (n=1.47) is a large difference, with the possibility of light being guided in the large index region. This is one of the faults we thought the modelling would highlight. Further, the shape of the cladding in the model is different to that of the experimental fibre, and therefore the deposition is different. In this case, we see more deposition than expected, which could alter the overall effect of the modulation.

Furthermore, the model does not let us see other values of significance for the optical fibre. We have already discussing the intrinsic loss of the MoS_2, but the model does not take into account the prospect of scattering occurring in the film. Unless the film production is perfect, it would be expected for scattering to occur, which would add high loss to the system, as well as possible alter the electro-optical properties. The model also does not account for bend loss in the system, which could see the film being to interact with the light in a TIR-type guidance. Once again, the bend loss may also be heavily affected by scattering.

However, the results of the theoretical system seem to be positive, with large modulation observed in the perfect system. The next step was to perform a deposition inside of the fibre, and analyse it's guidance properties.

4.3 Synthesis of Functional Anti-Resonant Fibre Optical Modulators

4.3.1 Experimental Integration of MoS_2 into Anti-Resonant Fibres

To create the MoS_2 integrated NCF structures, we borrowed the same technique used to deposit films in our twin-holed step index fibres that were used for poling. The fibre used in these experiments was that of the silica ARF seen in the second set of simulations results from the previous sections. Its draw code was labelled as B0461Y, and will it be referred to as such. A silica fibre would fare much better under higher heat than the borosilicate 8 ringed ARFs also simulated. Here, a liquid phase deposition was used, with the precursor Ammonium Tetrathiomolybdate dissolved into a solvent mix of butylamine/dimethylformamide/aminoethanol, using the same 1wt% solution [86].

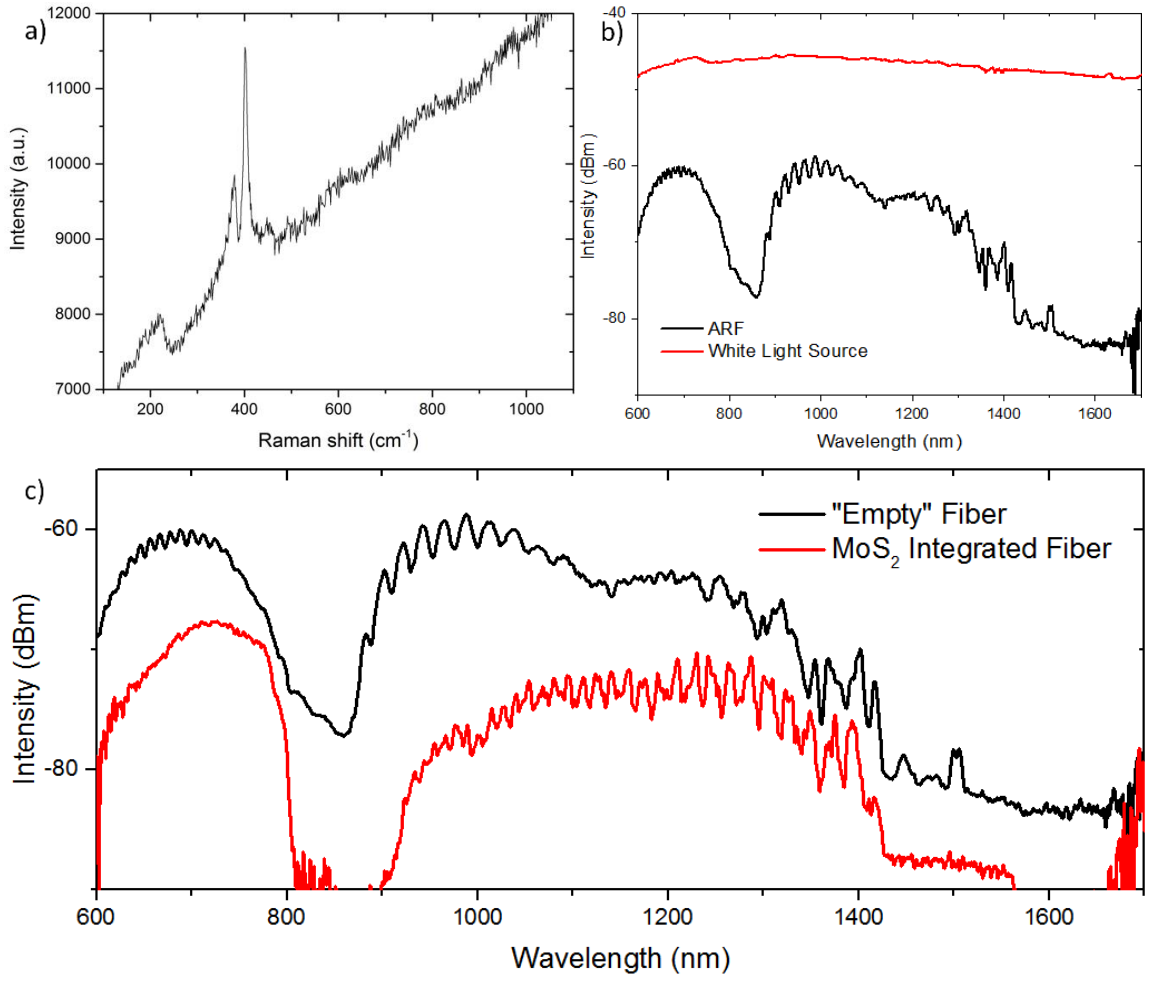

Figure 4.17: a) shows a Raman spectra for a MoS_2 film deposited inside of a B0461Y fibre, at an annealing temperature of 500°C. (b) show the guidance spectra of a hollow B0461Y fibre, compared to that of the WLS guided through a MMF. (c) Shows how the MoS_2 deposited fibre differs from that of an un-functionalised fibre. We see increased loss in the fibre, with multimodal interference reduced in the first resonant window.

This was allowed to flow into all regions of the fibre by capillarity, and followed by an 80°C air anneal on a hotplate. The fibre was then transferred to a tube furnace in which a 500°C anneal under 6% H_2/Ar was performed. The deposition was allowed to fill for around 30cm, and was analysed with Raman spectroscopy. An example trace can be seen in Figure 4.17a.

4.3.2 Characterisation of the fibre device

4.3.2.1 Optical Characterisation

Work on optical characterisation was also performed on the functionalised NCFs. Once Raman spectroscopy had been performed to confirm the deposition of MoS_2, the guidance spectra of the fibre was investigated. To do this, the fibre was butt-coupled to a multimode fibre at the input, with the output connected by a bare fibre adaptor to an OSA (Yokogawa AQ6370). Butt-coupling is an easy process to allow for guidance from one fibre to another, by placing the two fibres in close proximity, and aligning them through the use of an x-y-z stage. To obtain high quality butt-coupling, the mode field diameters (MFD) of the two fibres need to be well matched. For a NCF structure, the size of the MFD is roughly 0.7*D where D is the diameter for the core. A sufficiently large launch fibre was therefore selected for the first experiments. A white light source (WLS) was connected to a commonly used Thorlabs multimode fibre (MMF), which in turn was placed in the x-y-z stage to align with the NCF. This setup is shown in Figure 4.18. Once the alignment was found to produce the highest output, a trace was taken, with the results compared to an empty fibre in Figure 4.17c. It is important that the output was set to a maximum, as this would likely be the condition whereby the light is excited in the fundamental mode. As the majority of the power is contained in the core of the fibre in this mode, and has little overlap with the cladding, it is integral to analyse this mode. However, due to the short length of fibre used, it is expected for higher order modes to be present in the spectra.

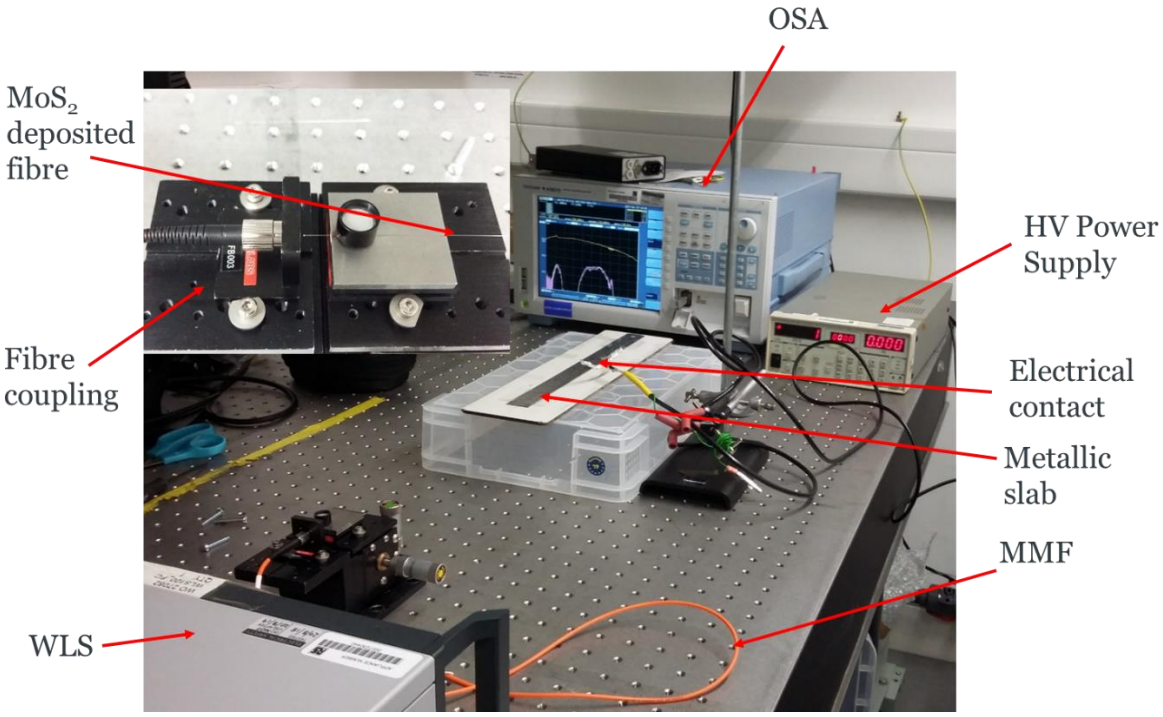

Figure 4.18: Optical set up for the modulation experiments. A white light source was connected to a MMF which was butt coupled to the anti-resonant device. This butt coupling can be seen in the inset. The fibre was then placed onto a metallic slab, and terminated at an OSA. The metallic slab was connected to a HV power supply, and contacted by a thin tungsten wire.

There are a few clear differences between the two traces. Most notable is the increased loss from the MoS_2 integrated fibre. This is likely to occur for a variety of reasons, such as the intrinsic loss of MoS_2, scattering from the film and the coupling process. Methods to improve the transmission properties were analysed. One key area for improvement is in the coupling process, as butt coupling is a fairly crude technique. An improvement could be to involve the use of different fibre types for the butt-coupling, so a comparison between a MMF and a SMF input fibre was made. Alternatively, the fibre could be spliced to the multimode fibre. However, the splice would be an intricate process, and require significant testing to achieve the perfect conditions, to not cause damage to the internal structure of the HCF, as well as not cause damage on the MoS_2. Furthermore, effects such as Fresnel reflections would be present, generating additional loss. A test was performed by using a SMF as the input and compared to the trace generated from a MMF. This produced the result seen in Figure 4.19. The result seemed to produce little effect in comparison to coupling with a multimode fibre, and produced less throughput of the signal. Also present in the figure is the use of a commercially available single mode fibre as the butt-coupled source. From this, the multimode fibre appears as the best option for guidance. The SM fibre was therefore removed.

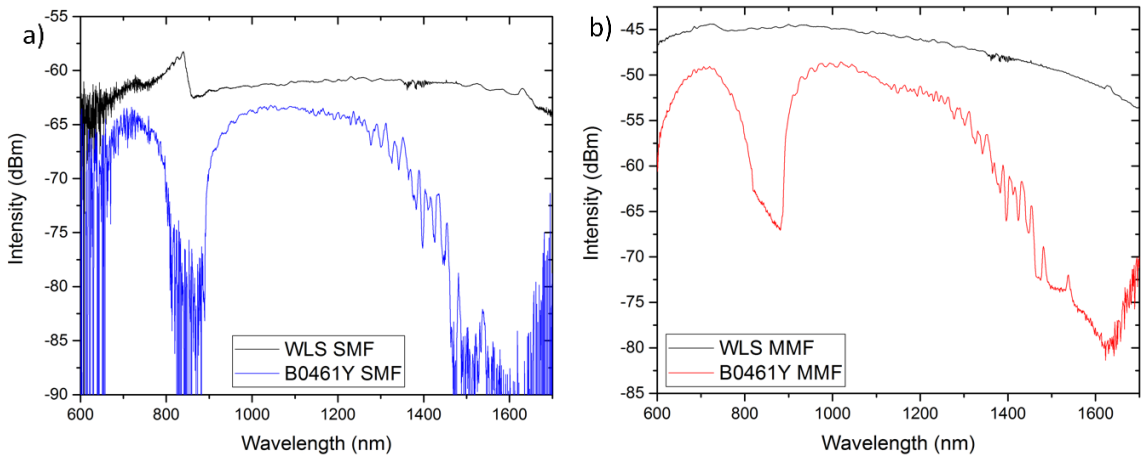

Figure 4.19: A review on how the guidance properties of the WLS are affected by the coupling fibre used in the experiments. A SMF and MMF coupling are compared, with the subsequent loss spectra of the empty B0461Y fibre also provided.

4.3.2.2 Comparison with the Theoretical Model

It is worth mentioning the clear and obvious differences between the created model on COMSOL and the experimental results obtained with deposition in the B0461Y fibre, most notable is the lack of appearance of the secondary peak obtained in the model, which had been considered to correspond to the presence of the MoS_2. Instead, the reaction of the fibre to the integrated film is a shift in the resonance window as per Figure 4.17c. The disappearance of this peak is a concern. As per our simulated results from Figure 4.13, the modulation of the device relies upon this presence, and subsequent shifting, of the secondary peak due to the refractive index change. The device may therefore have to rely on different phenomenon, such as electro-absorptive effect, to function well. It therefore may not reach the predicted two orders of magnitude change in the leakage loss.

Furthermore, the modelled change loss of the fibre was predicted to be quite small, (Figure 4.12b) however in the experimental fibre this loss change is quite dramatic, appearing to be around 10dB in some regions of Figure 4.17c. The location of the anti-resonant wavelengths is also different, but this is likely due to the inconsistency of the fibre draw.

4.3.2.3 Electrical Field Experiments

4.3.2.3.1 Single Anode Experiments

To attempt to modulate the spectra, we began producing experiments focussed on modulating the fibre. Through our modelling and literature review, we expected a small voltage of around 10V to be able to produce notable results. However, works from the literature were able to make direct

electrical contact with the film i.e. a well-defined charge reservoir. For our fibre based process, unless we wanted to cause damage to the fibre or make contact at the end faces of the fibre - which would incur high loss - we would not be able to make contact with the film. We therefore sought to use larger voltages, in the 100V range, to see if we could incur modulation – by placing the MoS_2 within the electrical field, grounded by air.. This would be expected to work much akin to the single anode poling first demonstrated by Margulis et al. [105] who used a single anode within an optical fibre. The ground of the device was achieved via the surrounding air which would be able to supply the sufficient negative charge without any physical contact needed to the anode. . Here, the edge of the fibre would act as the ground plane of the structure. This setup is shown in Figure 4.18 with the inset of Figure 4.18 showing the butt coupling of the fibre. The electrical field would penetrate through the silica host material, of roughly 30um thickness, and be able to interact with the MoS_2 deposited inside. However, this shielding effect from the silica would mean an increased E field would be necessary.

The fibre was kept in contact with the slab by applying tension to the fibre and using a small amount of kapton tape to tie it down. This would also remove the possibility of fibre movement altering the outputted optical trace and additional loss from the bending of the fibre. To protect from the high voltage, the set up was contained within a plastic cover, to ensure safety for the user. The voltage was applied to the fibre. At 100V, no change was observed, however, by steadily increasing the voltage, at around 500V some modification to the output spectra began to appear. At twice this voltage, 1000V, we began to see a more noticeable drop in the intensity of the trace, especially in the first resonance window visible to the OSA. This was further improved at 1500V. These spectra are observed in Figure 4.20, with a grounded trace (V=0) also shown to compare. This was observed at around 1dB modulation, at around 775nm. This was a very important result, but did not agree well with the model produced in section 5.2.1.3, as here only a drop in the intensity of the guided light is a notable difference in the traces. There is little change in the position of the anti-resonant peak. It would therefore suggest that the only effect of the electrical field is the alteration of the MoS_2's absorption coefficient rather than refractive index.

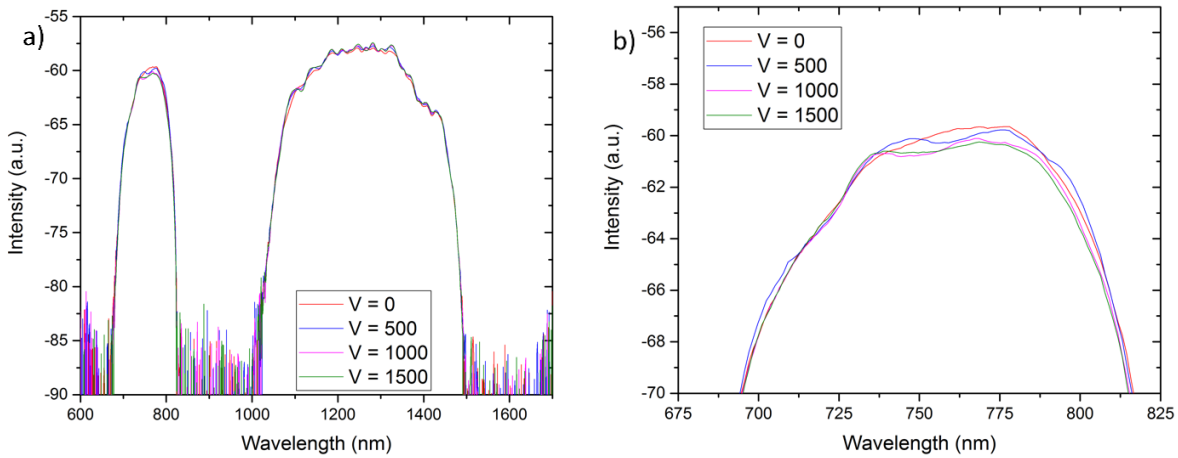

Figure 4.20: MoS_2 integrated fibre under an electrical field in a single anode configuration. This was the first test performed on our MoS_2 integrated fibres, and produced a modulation of 1dB when the slab was charged to 1500V.

To confirm the result of the experiment was due to modulation of the MoS_2, we performed the experiment on a bare (empty) fibre sample. The sample was treated much like the MoS_2 sample, with the coating fully removed. The experimental results are shown in Figure 4.21. As can be seen, at V=0 and V=1.5kV, the traces align almost perfectly. Very little modulation or change in the spectra occurs, with the tiny manipulations in the trace likely due to subtle vibrations in the fibre or inconsistencies in the light source. This would suggest that the MoS_2 is vital for modulation. There is also some feature changes in the spectra of note. The anti-resonant regions guide well in the un-functionalised fibre, mainly due to its short length meaning higher order modes propagate well. In the MoS_2 integrated sample, these regions (800-1000nm and 1500-1700nm) guide poorly – almost as if the higher order modes have been cut out. It is interesting to consider how this happens. It is likely that this is caused by a mixture of effects, from the material absorption of the MoS_2 and also the higher order modes being unable to guide inside the silica cladding due to being blocked by the integrated MoS_2.

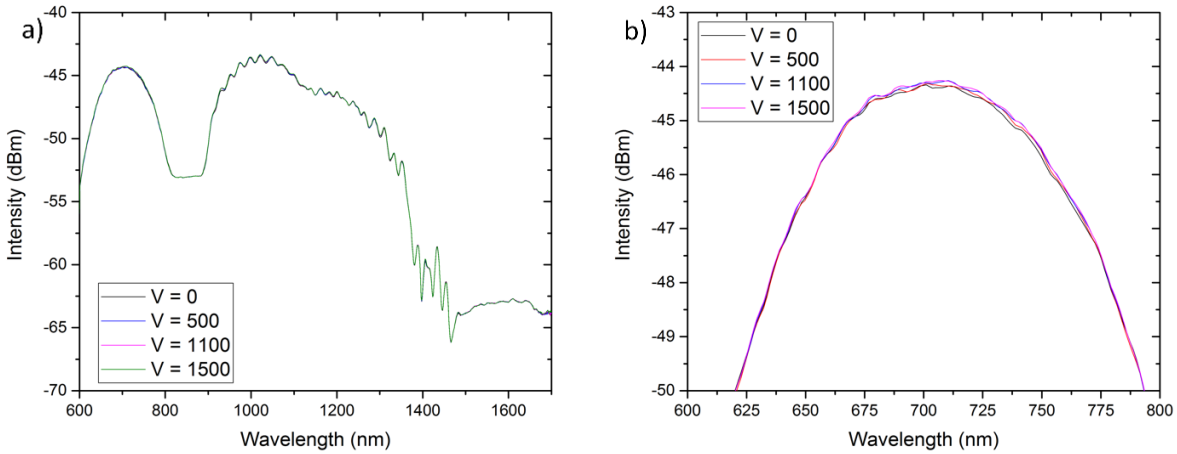

Figure 4.21: The spectra of an empty (non-functionalised) B0461Y fibre under the effect of an electrical field in a single anode configuration. No change can be seen in any wavelength region.

However, the result is impressive. Through an external electrical field, and by using the surrounding air as a ground, the interaction between MoS_2 and guided light can be manipulated. Our next aim was to improve on this 1dB modulation. To do this, a longer deposition was attempted, this time at around 40cm. This was analysed under Raman, and showed the following consistency, over a length of 387mm as seen in Figure 4.22. The optical testing of this showed the trace seen in Figure 4.23. This shows a modulation of around 3.52dB at 744nm. This is close to the modulation depth needed to fulfil modern telecommunications systems, as 3dB corresponds to 50% of the intensity lost. This fibre sample produced our best result to date. However, there were too many concerns over how the process occurs. We were unsure if some sort of charging effect seen at the 500V mark was a concern. This is highlighted in Figure 4.25, where the V=0 trace is lower in intensity than the 500V

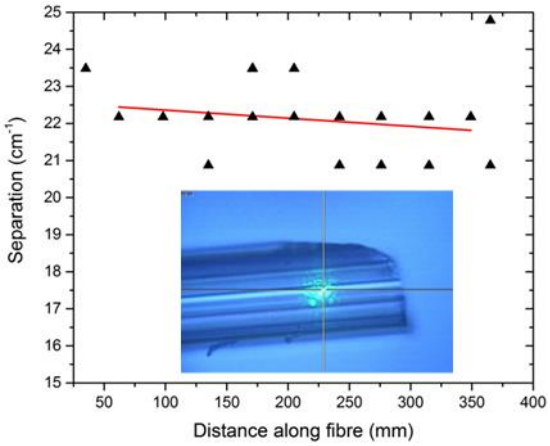

Figure 4.22: Raman separation of scans of the inner region of the anti-resonant hollow core fibre functionalised with MoS_2. The inset shows how the Raman scans were performed, with the 532nm Raman beam focussed through the silica glass host onto the MoS_2 film.

trace. The reason we considered for this is that there was some sort of capacitive effect occurring within the fibre. This may affect the modulation speed obtained in the fibre.

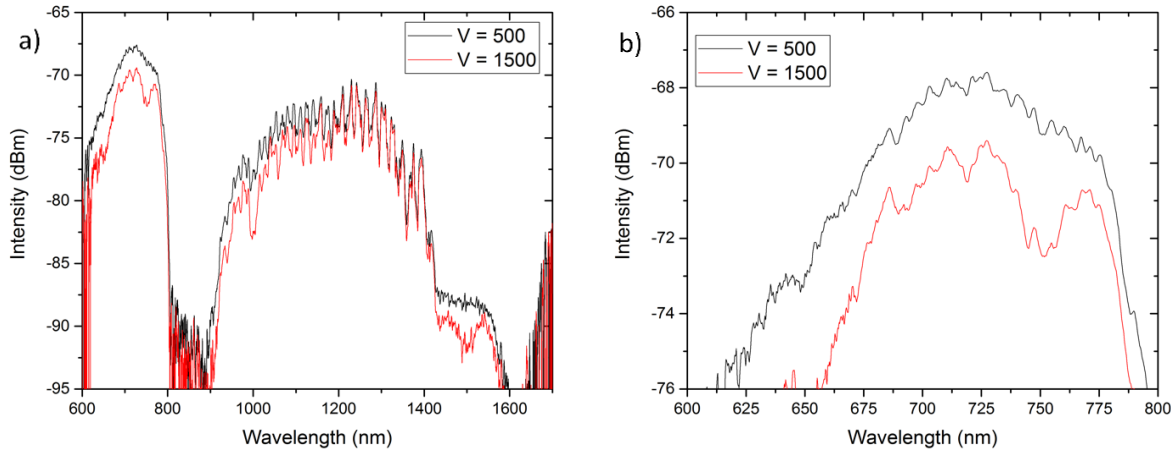

Figure 4.23: MoS_2 integrated B0461Y fibre with the best recorded modulation in these experiments. A single anode configuration was used, and produced a modulation of 3.52dB at a wavelength of 744nm.

4.3.2.3.2 Double Electrode Experiments

After the success of these experiments, a method to characterise the strength of the electrical field and apply direction to the field was created. Here, a second metallic slab was placed in the setup, placed a short distance from the original slab. The functionalised optical fibre was placed in between them. In this experiment, one slab acted as the anode plane, but the new slab acted as a ground plane, as such was connected to an electrode grounded by the HV power supply. This can be seen in a brief schematic in Figure 4.24. The two slab were placed approximately 2mm apart, and the voltage was switched on. The results of this can be seen in Figure 4.25. This is the same fibre used in the previous test in Figure 4.23. A peak voltage of 1500V was achieved, but care must be taken when increasing the voltage. This is due to arcing becoming an issue. Essentially, the electrical breakdown of air had occurred, allowing electrical charge to conduct through the air from slab to slab. Due to worries about if this could lead to damage to the fibre, care must be taken when selecting the high voltages.

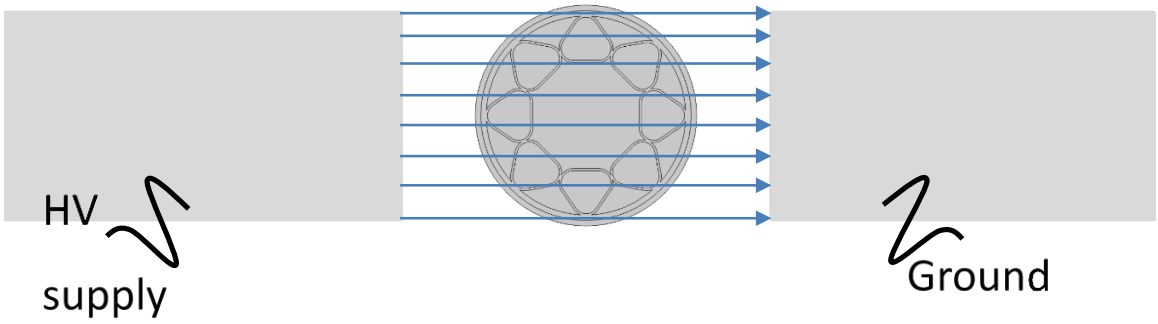

Figure 4.24: A schematic to show how the direction of the electrical field (blue lines) was considered to look when in the double anode configuration. The fibre was placed between two metallic slabs, one connected to the HV supply, and the other directly earthed.

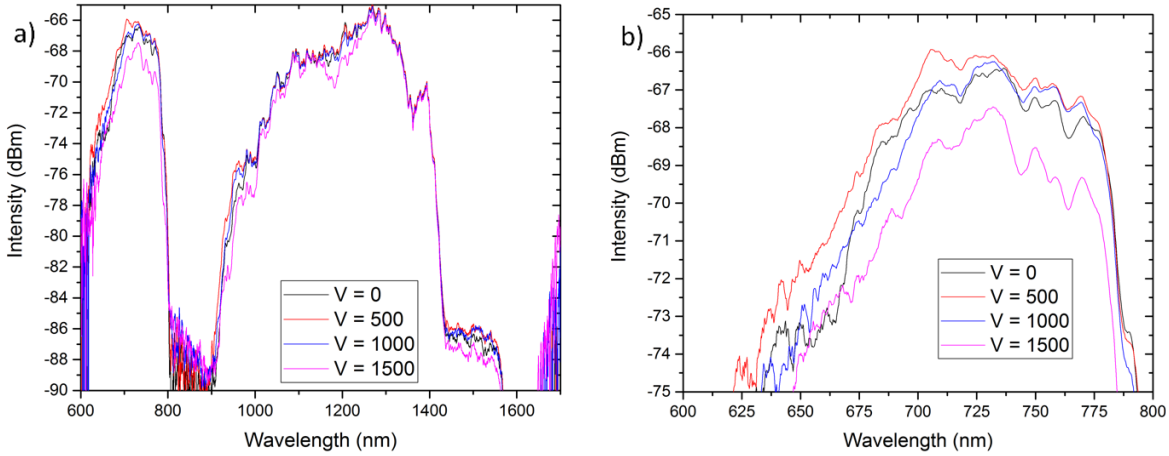

Figure 4.25: Results from a double electrode experiment on a B0461Y MoS_2 integrated fibre. At 1500V, an electrical field of 750 x10^3 V/m was generated, producing a modulation of 3.26 dB at a wavelength of 682nm. The voltage was not raised above 1500V due to arcing becoming an issue.

The results are also less impressive than hoped for. By having more control on the direction of the electrical field, it was also thought that the field would become more localised, increasing its overall value. However, this did not seem to be the case. The same sample was compared for both a single slab and double slab configuration, and as can be seen, the modulation seen in the single slab experiment produces better results.

Initial fears were that this results arose from the fact that the fibre may have not been placed expertly between the two slabs. The fibre was therefore stuck to the edge of the slab through two methods. In the first, a polymer coating of methyl methacrylate (PMMA) was used to bond the fibre to the slab. This could be removed with acetone once the experiment had been completed. The second option was to use small sections of tape onto the edge of the slab, to hold the fibre in place. Although this method would be more time consuming due to the intricacy of placing the tape on, the ease of removal meant it was a useful tool for practise. After a few tests, it was found that the

PMMA method was inferior. The removal using acetone was successful, but required a bit of force to remove the fibre from the slab, causing one or two breakages of the fibre. Furthermore, the removal of the PMMA was incomplete, and led to further removal steps needed, such as the stripping of the fibre with a metallic blade. The tape method was therefore chosen for the majority of experiments, as less breakages were caused.

Two different configurations were selected for the experiments. The fibre was taped onto the anode for one experiment, then repeated with the fibre taped to the ground slab. This was to test the consistency of the electrical field. Theoretically, the results of the experiment should be the same, due to the E field being uniform over the whole separation of the slabs. However, clarity was wanted and tests were run. From Figure 4.26, it can be seen that the traces react in the same manner regardless of whether the fibre is placed on the anode or the ground electrode.

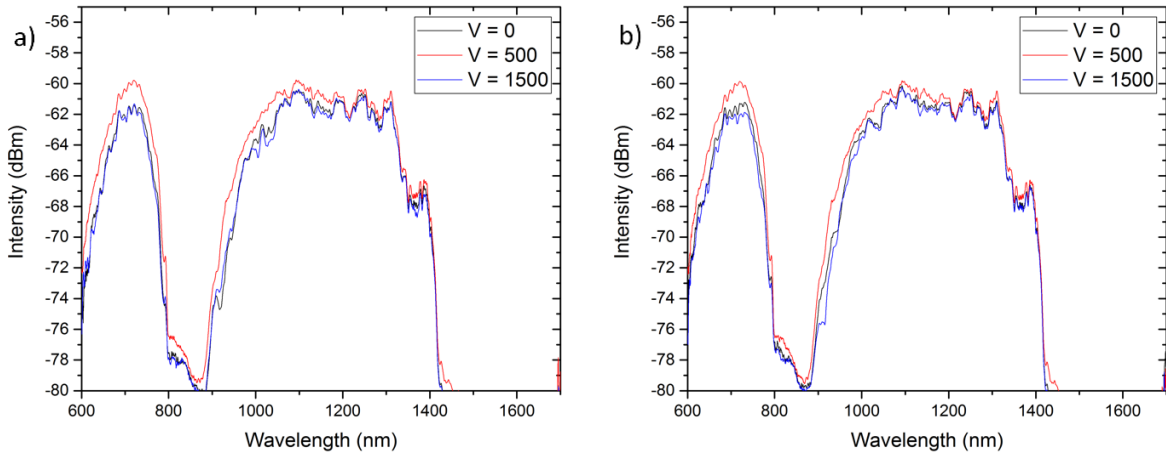

Figure 4.26: Results from a double anode experiment, whereby the fibre is placed on the ground in one experiment and placed on the anode in the other experiment. As can be seen, the graphs are almost identical suggesting it is irrelevant as to which metallic slab the fibre is placed on.

However, the strength of the field could easily be calculated, by simply dividing the distance between the slabs by the applied voltage. This produced electrical field strengths at a maximum of 750×10^3 V/m. This is an order of magnitude less than the electrical fields applied in literature papers such as reports from Newaz *et al*. with an electrical field of 8.3×10^6 V/m **Error! Reference source ot found.** and a field of Vella *et al.* of 40×10^6 V/m **Error! Reference source not found.**. However, almost direct contact is made between the voltage and the field, whereas our fibre device has a barrier of silica, lowering the effect of our applied field.

Due to the weaknesses and potential danger (of arcing) seen in these experiments, future experiments were performed on single anode setups.

4.3.2.4 Selectively Filled Fibres

4.3.2.4.1 Creation and Characterisation of Selectively Filled Fibres

To add further control on the properties of the waveguide, different arrangements of deposition were attempted. For the previous experiments, deposition of MoS_2 occurs in all hollow regions of the fibre. By altering this, and depositing in only the cladding regions such as the simulated model has been performed, the guidance properties and modulation capability are likely to change. To perform this, the technique of selective filling was borrowed from the work performed in Chapter 3. By allowing epoxy glue to fill the channels in the fibre, a cleave was able to be performed to allow deposition in only certain regions [112]. Due to the difference in the size and shape of the hollow regions, different filling rates of the glue would occur in different regions. The glue would also not react with the host solvent and would remain in the fibre throughout the process. The progress of the epoxy filling could be seen via a microscope, and produced a cross sectional image as seen in Figure 4.27. The core remains hollow, with the epoxy causing diffraction in the cladding regions, appearing a green/pink colour.

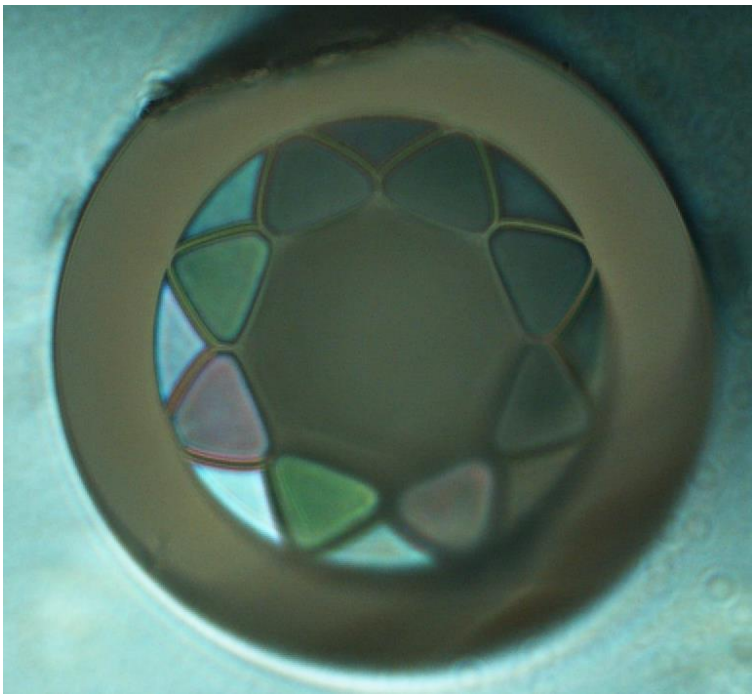

Figure 4.27: A showing of selective filling of the fibre. In this instance, the whole fibre was filled with epoxy glue, and cleaved at the point whereby the core was unfilled, but the cladding filled. The epoxy glue can be seen as the green/pink tinge.

The fibres could then be annealed following the processes outlined earlier in this chapter. To prevent the epoxy glue causing damage to the fibre via expansion under heat, the glue was cleaved

out of the fibre after the air anneal (at 80°C). This prevented any excess liquid penetrating into an unfilled hollow region. After Raman characterisation, the fibres were placed into the optical set up of Figure 4.18 with the metallic slab and HV supply removed to analyse their guidance properties. The results of this can be seen in Figure 4.28a. There are a few notable differences between the three traces. The loss of the fibres are significantly different, with the core only deposition spectra showing large amounts of loss. This is most likely due to this fibre configuration having the largest mode field interaction with the MoS_2. We see the cladding only deposition sample showing the least loss, due to the opposite effect. The mode would need to leak into the silica cladding region of the fibre before being able to be absorbed by the composite film. Also supplied is the WLS spectra of each trace, showing how the small variations in the traces mean that each of the spectra can be compared well to each other.

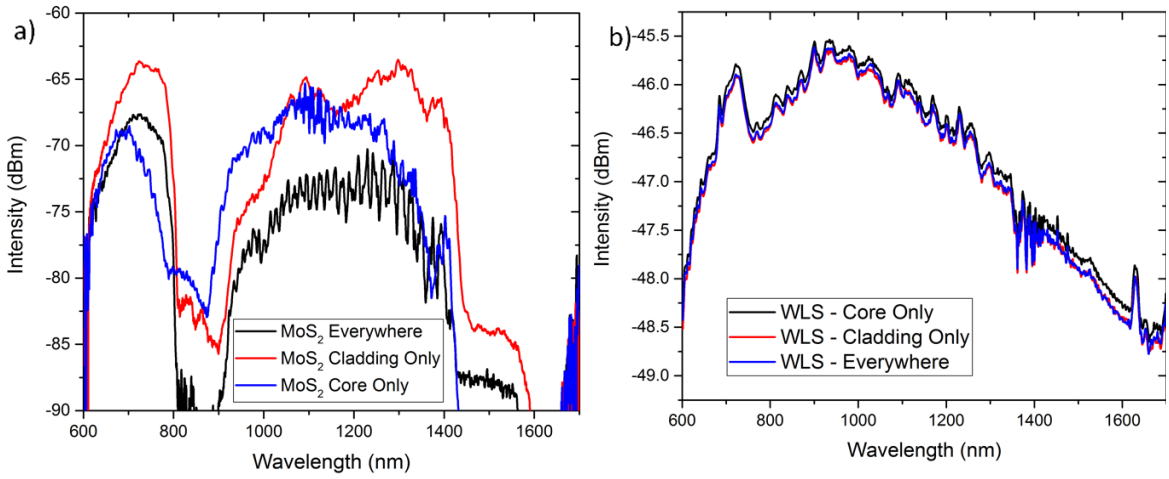

Figure 4.28: Traces to show how different configurations of the fibre react. The WLS spectra are also shown, to ensure that the three lines are aligned well. In the first anti-resonant region, the cladding only deposition produces the least loss, followed by the everywhere deposition, and then the core only deposition.

When considering why the everywhere deposition is less lossy than the core only deposition, we have to consider the guidance mechanism. Our theory is that due to the confinement of the mode to the core is dependent on the number of interfaces of the cladding. Unfortunately, this could not be simulated for small thickness films due to the high computational power required. For deposition everywhere, this would produce 3 interfaces on the core-cladding boundary, hence increasing the confinement. This limits the amount of film interaction present. The three configurations were also tested in a single anode setup for the modulation properties to be tested.

4.3.2.4.2 Electrical Field Experiments with Selectively Filled Fibres

The fibres were placed into the optical set up as observed in Figure 4.18. The samples were placed under a high voltage of 1500V, with their peak modulations recorded. The three examples are shown in Figure 4.29-32, with the core deposition sample showing a peak modulation of 1.6dB at a wavelength of 660nm and the cladding deposition has peak absorption of 1.65dB at a wavelength of 661nm and 1.82dB at a wavelength of 960nm in the near IR range. However, these are dwarfed by the MoS_2 in which deposition had occurred in all hollow regions, with a peak modulation of 651.8nm, with a peak modulation of 4.5dB. Due to the success of the single anode modulation samples, this configuration was maintained for the test on differently functionalised fibres. From the figures, it is evidently clear that the deposition without selective filling shows the highest modulation. The core only sample and the cladding only deposition show little modulation, averaging around 0.6dB in the cladding only sample and around 0.2dB in the core only sample in the 600-800nm region. However, this is much less than that of the everywhere deposition fibre, showing a modulation averaging around 2.2dB.

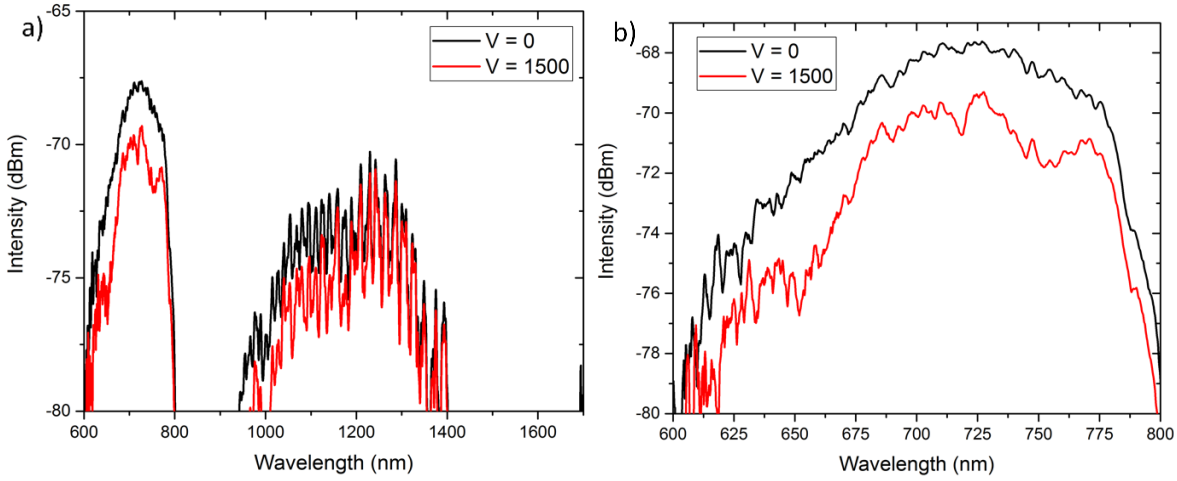

Figure 4.29: Reaction of the fibre in single anode configuration with a large electrical field applied. Here, the maximum modulation strength is of 4.5dB at a wavelength of 651.8nm was recorded.

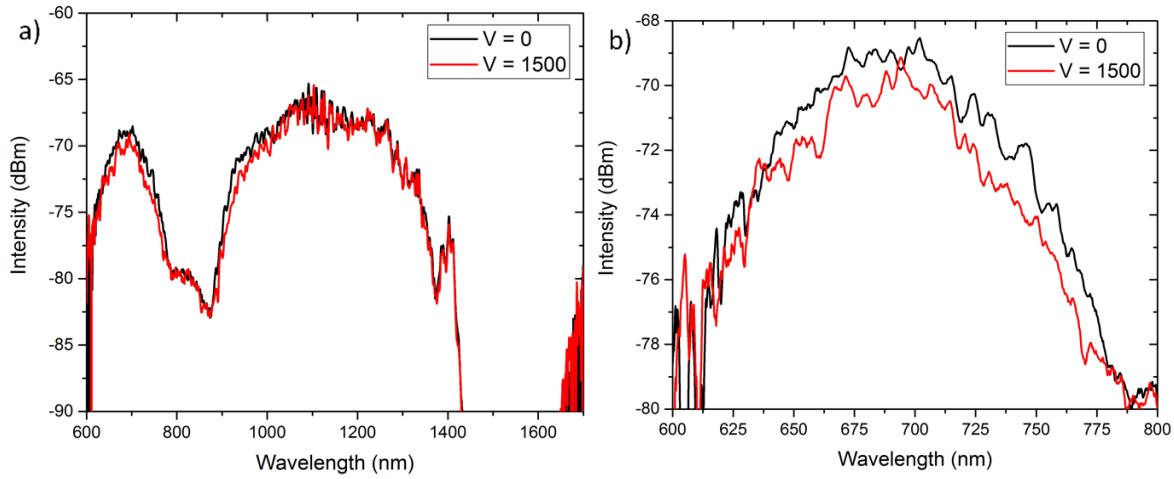

Figure 4.30: Reaction of the optical fibre where deposition had occurred only in the hollow core region of the fibre after a selective filling process. A maximum modulation of 1.6dB at a wavelength of 660nm was found.

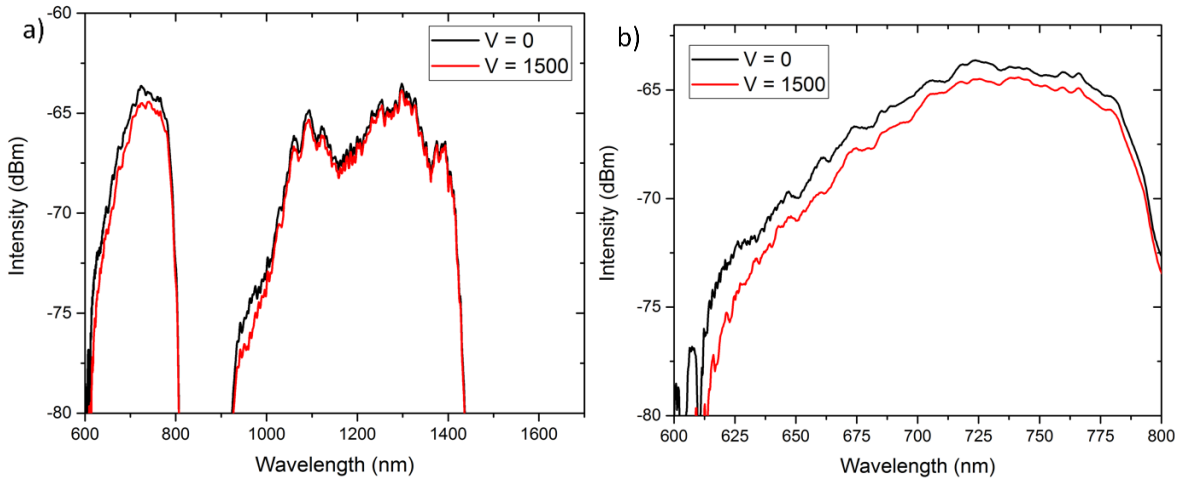

Figure 4.31: Reaction of the optical fibre where deposition had occurred only in the hollow cladding regions of the fibre after a selective filling process. A maximum modulation of 1.82dB at a wavelength of 960nm was found.

4.3.2.5 Modal Analysis of Fibre Devices under Electrical Fields

Furthermore, we were unsure how the modal propagation of the light is affected. As we are using a multimode fibre as an input, we cannot be sure if we are just cutting out higher order modes (which would decrease the obtained intensity of the spectra) when the MoS_2 is under the influence of the field, or if we are affecting the fundamental modes propagation. We therefore analysed to modal contribution. Due to the large amount of power guided in the fundamental mode, it was considered that the loss of power in the modulation was due to an increased film/light interaction, with the fundamental mode 'leaking' onto the composite material.

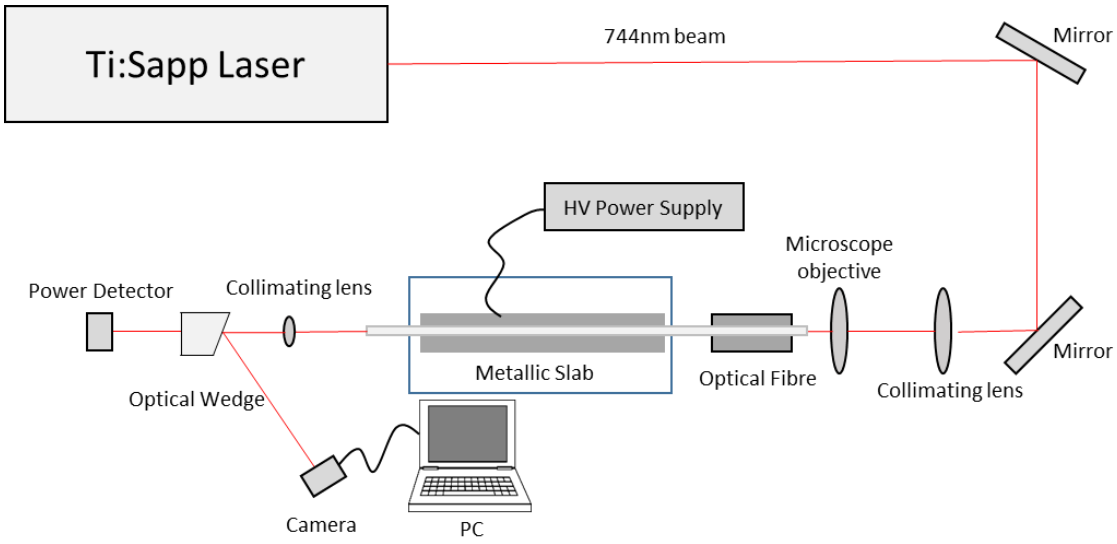

Figure 4.32: Optical setup for the modal analysis of the fundamental mode depletion with the application of an electric field. Rather than a white light source, the input is a Ti:Sapp laser which is coupled into the fibre via free space coupling. The same modulation setup as per previous experiments was used, with the output changed from an OSA to a power detector and camera setup.

The higher order modes carry less power through the transmission, and due to their guidance nature are likely to be interacting with the cladding before the electrical field is turned on. It would be of interest to observe if this is indeed the case, so a mode imaging set up was created.

For this, the set up outlined in Figure 4.32 was created. A tuneable Ti:Sapp laser was directed and focussed into a 50um spot at the input face of the MoS_2 integrated fibre. The fibre was then placed on the metallic slab as per previous experiments, and focussed into a power detector and camera at the output. We then began to study the mode as the voltage was applied. To begin with, the fibre was aligned via an X-Y-Z stage to achieve single mode guidance. This produced the image seen in Figure 4.33a. As can be seen, the majority of the power is located in the core area, with a circular shape suggesting the fundamental mode has been obtained. The electrical field was then steadily applied at 100V increments. Upon reaching around 700V, we began to see a change in the overall shape of the mode, whereby the outer regions of the mode begin to constrict, producing a more circular mode pattern. This is manipulated further with higher voltages. At around 1200V, the majority of the power begins to disappear, with the central intensity being quite low as seen in Figure 4.33c. By 1500V, the fundamental mode has almost completely dissipated, leaving weak signs of a higher order mode as per Figure 4.33d. This mode is most likely to have been propagating in the cladding. Upon the decreasing of the voltage, the shape begins to rematerialize. At 0V, the initial shape returns, with high intensity found at the centre of the fundamental mode. This is confirmed by analysis of the power recorded at the output. Here, the light was placed in a wedge,

meaning around 5% of the light was reflected onto the camera and the rest of the incident power recorded on a power detector. The power was recorded over a 1 minute interval, recording a value every 15 seconds. The recorded power also shows a drop from 1.688 to 1.052 as seen in Table 4.1. This corresponds to around 2.05dB, by placing it into Equation 4.3.

$$dB = 10\ log_{10}(\frac{P_1}{P_2}) \qquad \text{Equation 4.3}$$

Voltage	Avg. Power. (mW)	Standard Deviation
0	1.688	0.016
500	1.712	0.04874423
1000	1.264	0.023323808
1500	1.052	0.037094474
0	1.404	0.034409301

Table 4.1: Power values for the MoS_2 integrated B0461Y fibre with increasing applied voltage to the metallic slab. A modulation of 2.05dB is created, from the average power dropping from 1.688 to 1.052.

Once the electrical field turns off, after a recovery time of around 5 minutes, the initial power is recovered. To confirm these qualities, the empty fibre is recorded in the same experiment. The initial mode shape of the mode was a mess, with multimode guidance occurring. To remove this, the fibre had a bend placed into it, removing the higher order modes, but also affecting the power propagating in the fundamental modes. This explains why the power levels in this experiment are lower than expected. This recovered a mode which looks like that in Figure 4.34. Here, we see a roughly circular mode, with the highest intensity recorded in the central region. Upon the application of the field, we see no change in the modes guidance. This is also confirmed by the power levels remaining the same, as observed in Table 4.2.

Voltage	Avg. Power (mW)	Standard Deviation
0	2.46	0.022803509
500	2.512	0.023151674
1000	2.41	0.133716117
1500	2.518	0.073593478
0	2.514	0.05425864

Table 4.2: Power change in the unfunctionalised (empty) optical fibre placed in the presence of the electrical field. Here, no modulation is seen, with the average power recorded over a 1 minute interval remaining almost constant.

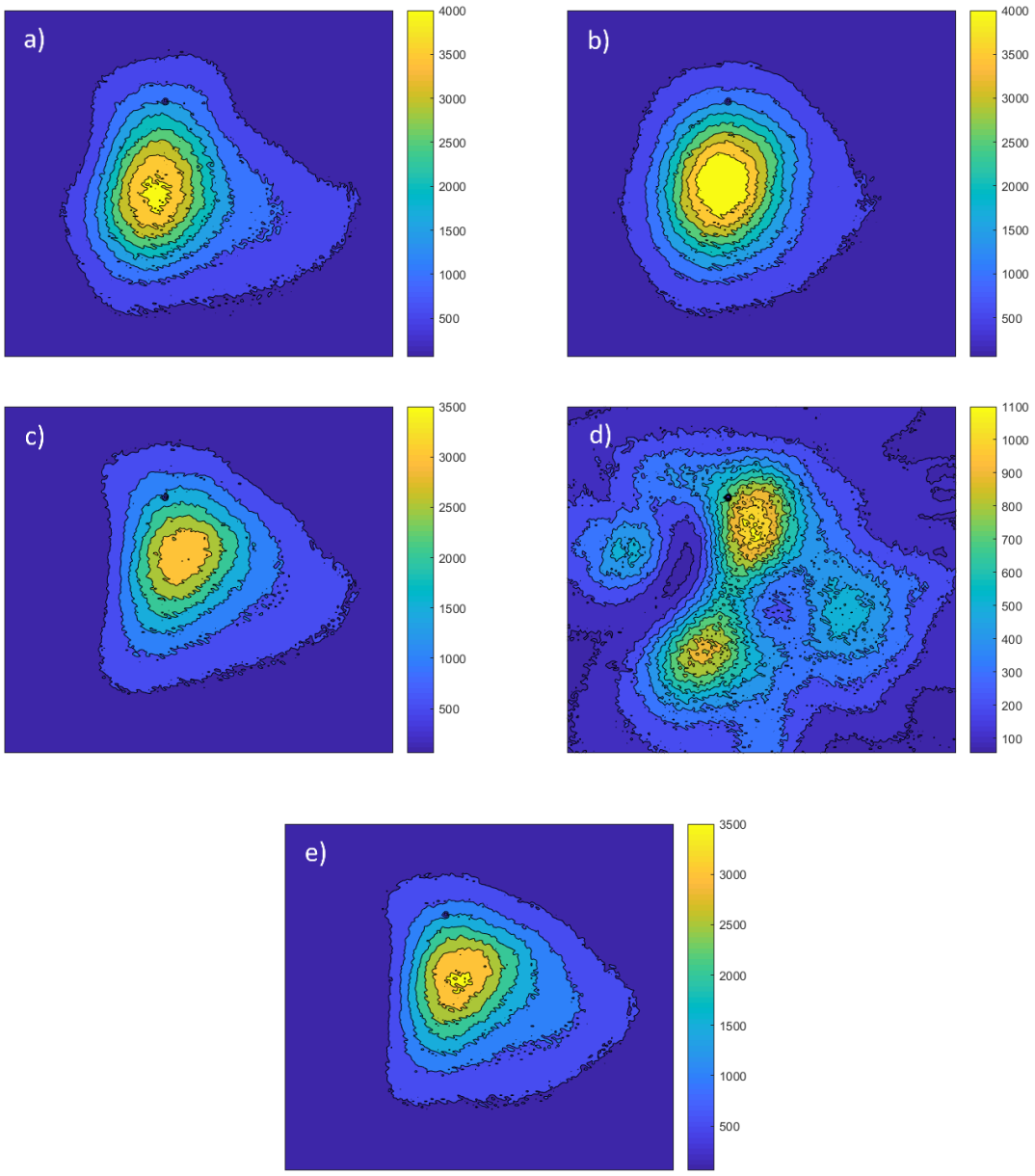

Figure 4.33: Mode imaging of the fibre of a MoS_2 fibre with increasing voltage applied to the single anode.

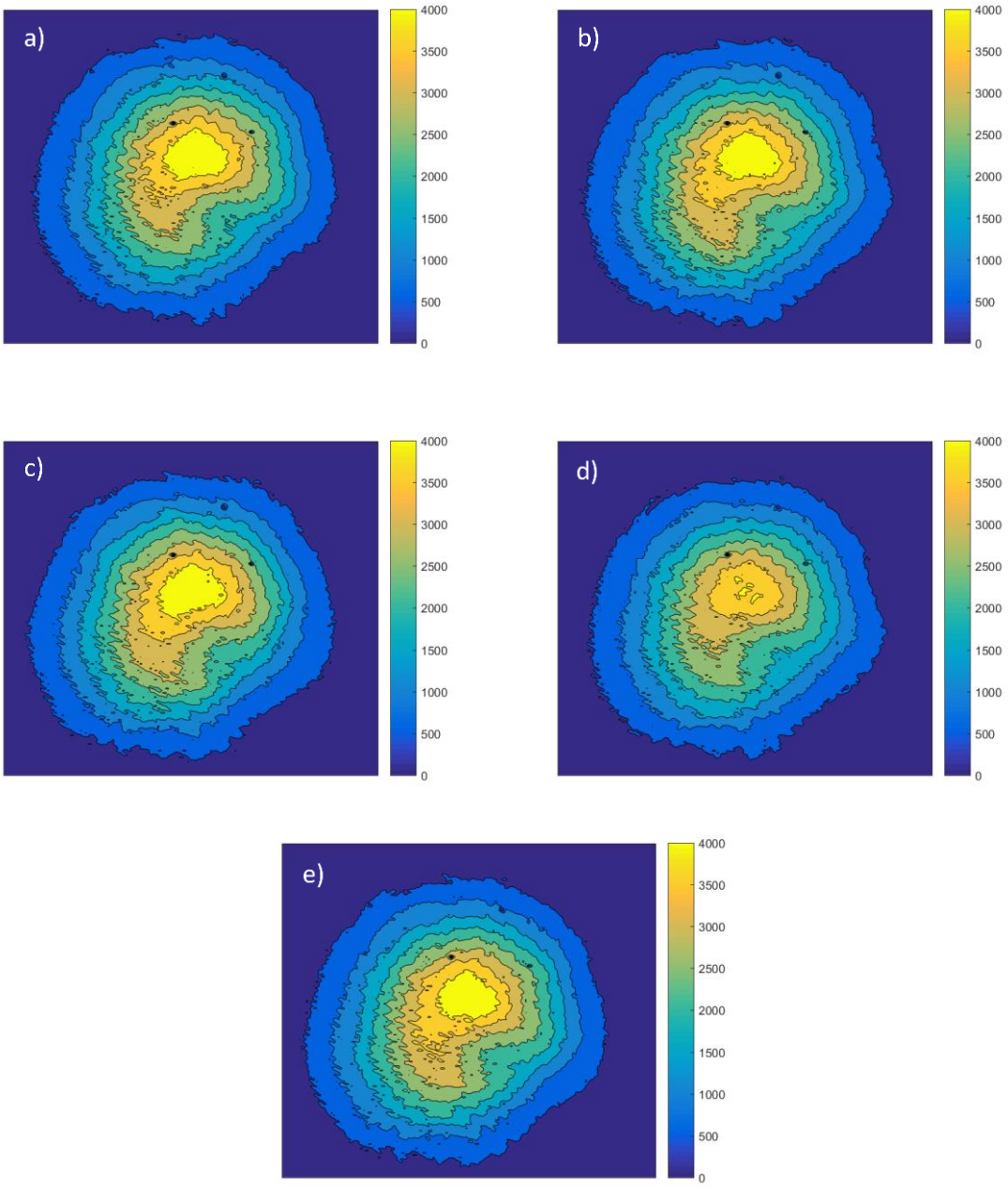

Figure 4.34: Mode imaging of an empty fibre when the voltage increases. As can be seen, the mode images change very little, implying that the applied E field has little effect.

The reasoning for the mode shape changes and the power changes are likely due to the presence of MoS_2. Initial fears were that there was some sort of movement of the fibre, which was causing it to produce more loss as the butt coupling alignment was potentially changed to become out of focus. To analyse this, modal analysis was performed with the camera. The original fundamental mode was captured as seen in Figure 4.35a. The metallic slab was then placed to 1000V, producing the modal image seen in Figure 4.35b, where the fundamental mode has been lost and only higher order modes remain. The alignment of the fibre was then changed, in an attempt to recover the original fundamental mode, however, this did not appear to be possible. Instead, the image

showing the largest intensity is shown in Figure 4.35c, with the same higher order mode pattern. The voltage was then switched off, returning the mode to its fundamental shape. Due to the inability of the fundamental mode to be recovered at 1000V, it would imply that the effect we are seeing is purely due to the manipulation of the MoS_2 film, rather than a movement in the fibre. This is clarified by the recovery of the fundamental mode when the applied field is turned off.

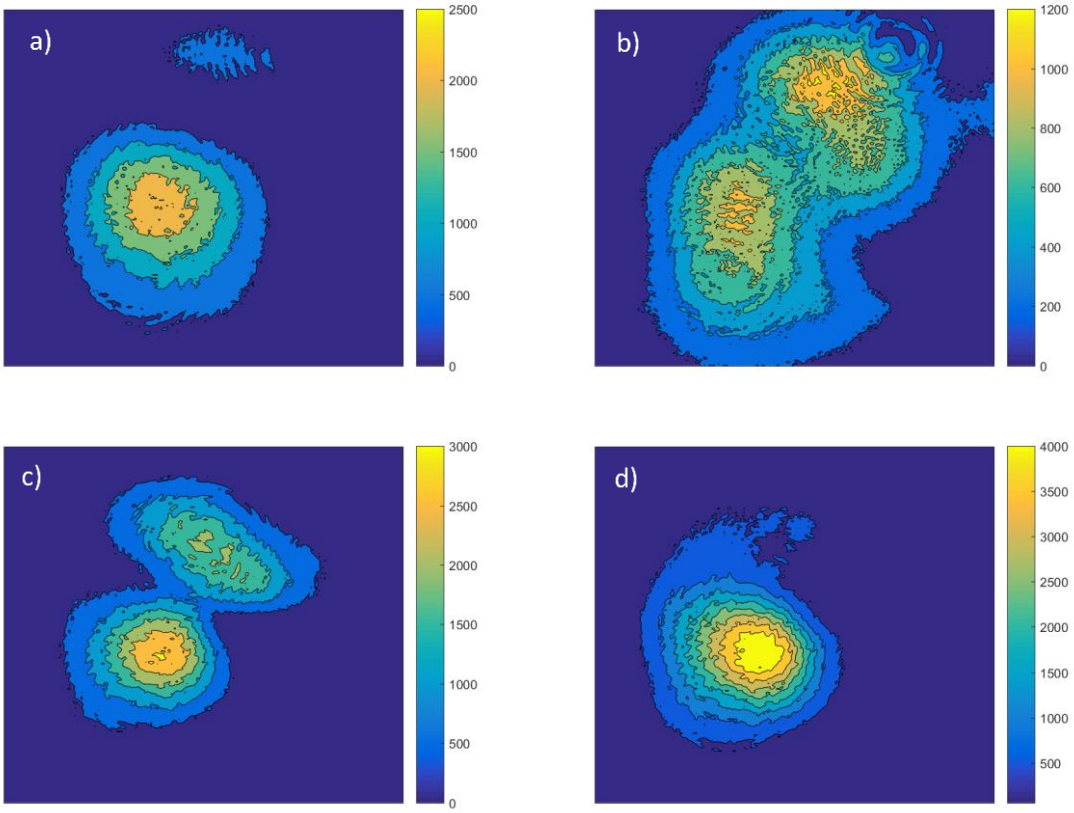

Figure 4.35: Mode images of an experiment to show how realignment of the mode affects the guidance. a) shows the original fundamental mode at 0V. b) shows the result of the application of a 1000V field. The fibre is then realigned with the x-y-z stage to attempt to regain fundamental mode guidance whilst still at 1000V. However, the highest intensity image to be found was that as shown in c). The electric field was then turned off producing d), with the mode returning to it's fundamental shape, only with higher intensity than that shown in a).

4.3.2.6 Alternating Electrical Field Experiments

The final experiment to be performed on these fibre structures was to test these fibres under an alternating field. For this, a function generator was connected to a high power voltage amplifier, which acted as our electrical field source. The function generator was capable of applying 1.5V to the amplifier, which was able to multiply this value by 1000. The rest of the set up remained the same, however the laser source was changed to a 633nm HeNe laser. Once again, the fibre was

butt coupled to the source via a multimode fibre. The output was connected to a power detector, which in turn was connected to an oscilloscope.

It would be important to see how quickly the modulation can occur, as in real world systems, the processing of data occurs over very small time scales, hence a quick On/off ratio necessary. Previous without fibres, we have seen a recovery time is necessary, as the fibre seems to suffer from some sort of capacitive or hysteresis nature. However, we have seen success in using both positive and negative biases in producing modulation.

A preliminary experiment was performed, producing the traces shown in Figure 4.36. Here, we can see how various factors affect the quality of the modulation. Three key parameters were chosen to be investigated. These are the frequency on the input signal, the amplitude of the peak to peak voltage, V_{pp}, and the offset voltage, V_{off}. The first trace to be investigated is shown in Figure 4.36a, where the input frequency was selected as 3Hz, a $400V_{pp}$ and $0V_{off}$. The graph shows a double frequency response, whereby for each wavelength of input signal, two modulations are observed. Interestingly, the two modulation responses are slightly different, with the first response not returning to the minimum guidance intensity. The reasoning behind this is currently unclear.

For the optical modulator, we expected a FET-like response. Here, in the nonlinear region of the FET, a double frequency modulation is observed. When this is moved to the linear region, we would expect single modulation response. This can be observed in our result in Figure 4.36b. Here, the offset voltage was increased to 235V, with the same frequency and same V_{pp}. As can be seen, for each wavelength of input signal, a single modulation response is shown. To learn more about the modulation ability, the V_{pp} was also increased. This can be observed in Figure 4.36c, with a double frequency response shown as the V_{off} was set back to 0. Interestingly, for large modulation, the width of the output signal is strongly decreased. Furthermore, the modulation returns to the minimum intensity for all the traces.

Finally, the frequency of the input signal is changed. For Figure 4.36, a frequency of 10Hz was chosen, whilst for Figure 4.36e a frequency of 15Hz was selected. Once again, a $800V_{pp}$ and a $0V_{off}$ was chosen. Looking at the results from this, it is visible that the fibre begins to suffer at larger frequencies. It is much like the output signal in Figure 4.36a, the modulation fails to return to the minimum intensity. This is likely due to the fibre being unable to remove the excess charge in the fibres before the polarisation of the input voltage switches. It therefore struggles to return to low intensities. This is strongly evident for the 15Hz trace. Here, the modulation capability is heavily decreased. More experiments to further investigate the modulation fibre device are needed to clarify the points made in this section.

4.4 Concluding remarks on Functionalised Negative Curvature Fibres

Using the 2D film MoS_2 and incorporating it into the inner regions of a hollow core anti-resonant fibre, it has been shown to be able to sufficiently gate to produce modulation of to date a maximum of 4.5dB for a maximum input voltage of 1500V at 744nm. When comparing this modulation capability with that of the previously mentioned references which also use TMDC films, we find a $\Delta n/\Delta V$ of 0.003dB/V. This is an order of magnitude below the literature values of 0.01dB/V, which is likely to occur due to the electrical field having to penetrate the silica host material before being able to affect the film. The insertion loss of MoS_2 for such a fibre has an average at a value of around 7.5dB in this region.

For a nascent technology, as the idea of film insertion for this application in hollow core fibres is still highly novel, the results are promising. By analysing further designs of the optical fibre and different methods of applying the electrical field to the functionalised film, we aim to improve the figure of merit of the device to align more with the literature. By then exploiting the length of the fibre device, it is foreseen that a modulator with high modulation depth can be achieved. Further work will also focus on further clarifying the characterisation and mechanisms behind the introduction of this loss.

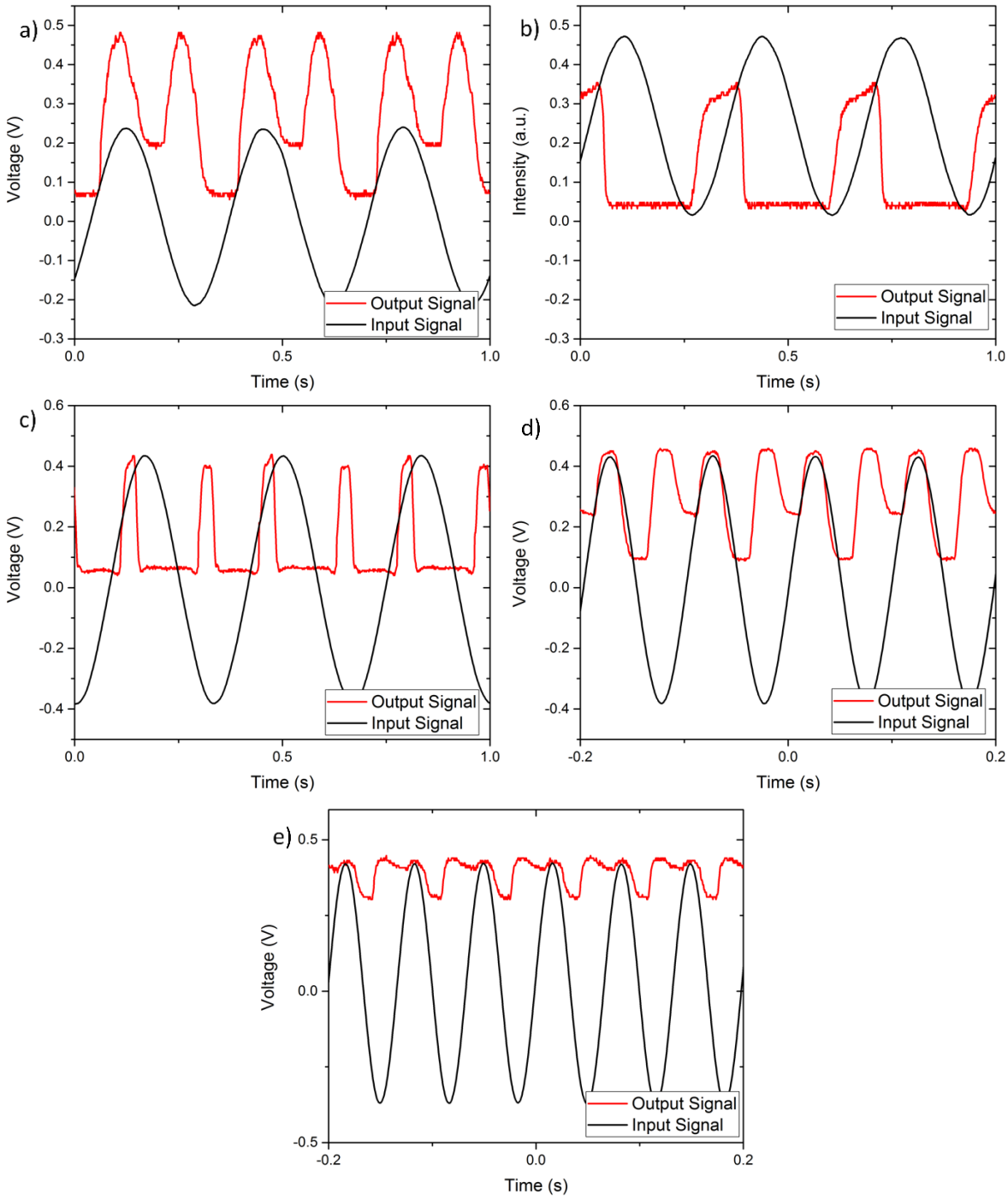

Figure 4.36: MoS_2 fibre with sine wave high voltage input. The Y-axis (voltage) is reduced by a factor of 100.

Chapter 5 Additional Films

5.1 Overview

The focus of this thesis so far has been on the integration of the TMDC thin film MoS_2. To offer a comparison to MoS_2, and broaden the scope of this work, as well as possibly obtain better modulation/SON results, different films were used to functionalise optical fibres and were optically characterised under the experimental conditions previously discussed. These films are thin films of WS_2, also a TMDC film with a structural composition very similarly to MoS_2 and the bulk semiconductor Zinc Selenide, ZnSe. These films offer different comparisons to MoS_2. WS_2, although very similar, has been shown to have better modulation capability and a large SON [36],[136]. However, its deposition conditions have been less widely researched. ZnSe offers a completely different approach due to the large relative thickness of the film, which could heavily effect the mode overlap. These films have relatively low temperature deposition conditions [137][138], and have subsequently been deposited into the hollow regions of optical fibres to observe the effect, with the deposition and optical characterisation of said films discussed in this section.

To begin, a further description of the properties of WS_2 will be discussed, going into deeper analysis than Chapter 2, followed by the results and discussions from the optical experiments. A description of ZnSe will also be outlined, with its unique properties and current applications space presented, finally discussing the optical experiments undergone with these films. An overall conclusion will finish this section.

5.2 Tungsten Disulphide

Tungsten Disulphide, WS_2, is a TMDC material which has been found to be chemically stable in its 2D form. Like many other 2D TMDCs, it is composed of a layer of metal atoms - in this case tungsten – sandwiched between layers of chalcogenides – here, sulphur. It has been found to have properties that have aroused scientific interest, such as an optical bandgap of 2.05eV in its monolayer form [139], an electron mobility of 83cm^2/Vs (at room temp) [140] and a refractive index variable with the wavelength [141], but is generally higher than the RI value of MoS_2 especially beyond 800nm as seen in Figure 5.1. This has therefore seen WS_2 being used in many transistor applications, with performance qualities on par with MoS_2 [142], as well as more niche applications such as photocatalytic hydrogen evolution [143]. Its optical applications include the exploitation of its third order nonlinearity for saturable absorption in laser systems for both Q-switching and modelocking

[144]. It has seen a multitude of research onto the generation of said films, with deposition methods such as exfoliation [145] and CVD used to create high quality flakes [146].

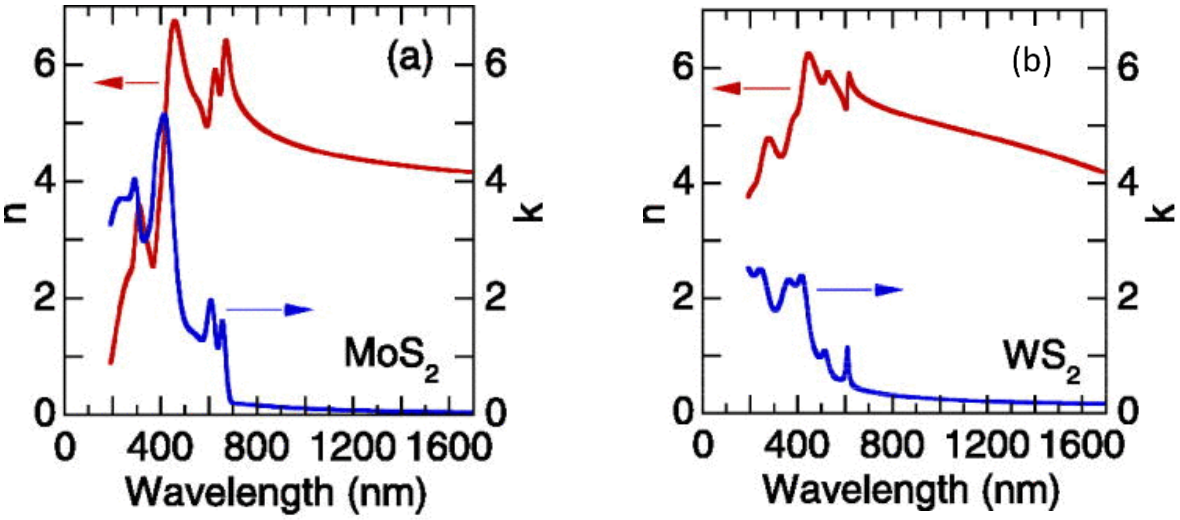

Figure 5.1: Refractive index and absorption coefficient analysis of MoS_2 (a) and WS_2 (b) using ellipsometry. From Ref [141].

When observing the CVD techniques, there is a wide range of precursors available for deposition. These range from WO_3 [147] to more complicated structures such as $W(CO)_6$ [148], with deposition temperatures of 825°C and 800°C respectively for literature content. These are reacted with sulphur power, under a hydrogen flow [147],[149].As a contrast to MoS_2, it generally requires a larger temperature for deposition – hence its general underuse in scientific literature [16].

Inevitably, due to the many similarities between the films, WS_2 and MoS_2 are often compared in their characteristic values. A variety of comparison papers have been seen in the literature, however for this thesis a focus will be placed on the characteristics the films will be used for – their second order nonlinearity, gating ability and optical constants such as RI, absorption coefficient and bandgap.

Second order nonlinearity:

Due to its crystal structure, odd-layered WS_2 is known to be non-centrosymmetric and therefore has a non-zero $\chi^{(2)}$ value. When analysing its $\chi^{(2)}$ value, the literature reports it as 460 pm V^{-1} [136], a value the same order of magnitude to that of MoS_2, which has a reported value of 100pm V^{-1} [110] . However, the difference in the absorption coefficients could lead to a fibre producing less insertion loss.

Gating ability:

A key paper on this topic is noted in the giant gating tunability of TMDCs [36]. In this paper, both MoS_2 and WS_2 underwent the same treatment to alter their optical properties through the introduction of an electrical field to the material. The change in the refractive index could then be calculated by registering the reflectivity and transmission properties of the film, and the change in these values when a field is applied. The focus of the paper is on the WS_2 sample, which was seen to observe larger changes in its RI, in comparison to MoS_2. This is shown in Figure 5.2 whereby a WS_2 device was investigated with a maximum voltage of 67V. It shows a decrease in both the refractive index and absorption coefficient with the applied voltage. Overall, this paper showed a change of a refractive index value of 4.8 to 3.97 at around the *A* exciton, with the WS_2 film producing the best results, with the authors claiming that the large tunability is due to the larger excitonic absorption of WS_2.

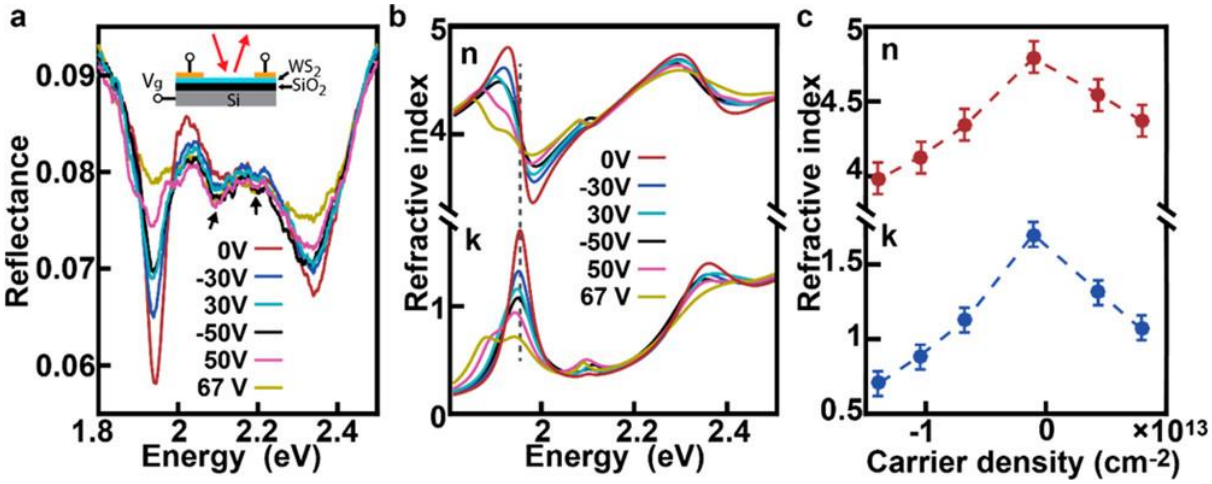

Figure 5.2: Electro-optic and Electro-absorptive effect witnessed in monolayer WS_2, with an inset of the device shown in (a). The change of reflectance is shown, with the corresponding RI and absorption changes shown. The carrier density change is also shown. Image from Ref [36].

Optical Bandgap:

The optical bandgap of WS_2 in its monolayer form has been calculated to be 2.1 eV [5], 0.2 eV larger than that of MoS_2. This has seen WS_2 used for applications such as transistors [142], and has been suggested to be a better alternative to MoS_2 [142]. Due to WS_2s reduced effective mass, it shows a higher charge mobility rate, generating experimental results as strong as MoS_2.

Conclusions

It would therefore appear from our literature searches that WS_2 offers high capabilities than MoS_2 for many applications. However, the scientific community has seen a plethora of works involving the growth and functionality of MoS_2 instead. There are a variety of reasons for this, including the higher temperatures for deposition and poor evaporation rate of tungsten precursors leading to

large scale film manufacture becoming problematic. WS_2 would be interesting as a comparison to MoS_2 for the work described in this thesis – and could possibly improve on the work first proposed with MoS_2 films.

5.2.1 Tungsten Disulphide Deposition

The WS_2 films were integrated into both poling and optical modulation fibres. To achieve this, much like the molybdenum film, a deposition method whereby a precursor could be dissolved into a solvent host was found. Here, the precursor named ammonium tetrathiotungstate (ATTT), a precursor similar to ATTM was used. Unlike our original work on MoS_2, ALD techniques were not considered for this work, due to the high annealing temperatures required. Ammonium tetrathiotungstate allowed for WS_2 deposition at temperatures around 500°C meaning deposition could occur without damage occurring in the fibre. Deposition trials began on 50µm capillary fibre, using the same solvent solution of 1ml Aminoethanol, 4.5ml of DMF and 4.5ml of Butylamine. 1g of precursor was used, making the solution a 1%wt solution. An image of the solution can be seen in Figure 5.4, showing a bright yellow colour once the precursor was fully dissolved. The precursor would flow into the capillary fibre, and once filled was heated on a hotplate at 90°C for 10 minutes in air. The fibre was then annealed under a 6%H_2 flow at 500°C. From a literature search, the precursor needed a slightly higher deposition temperature to fully decompose into WS_2, however this would cause damage to the fibre, hence a reasonably low of 500°C temperature was selected. The fibre was then tested under Raman spectroscopy to confirm the deposition and its quality. A resultant trace is shown in Figure 5.3b. Here, the two resonant peaks are shown, at corresponding values of 351cm^{-1} and 412cm^{-1} – the resonant peaks for WS_2 film, with a ratio of around 1.2 suggesting the presence of bilayer film [151]. Although the film was present, the fibre was inconsistent along the length. It appeared that the deposition could be improved. This was further analysed by another member of our group, Omar Adnan Abbas, who looked further into the solvent chemistry. The DMF solvent was found to not be effective with ATTT, and was replaced with NMP. Due to the nature of NMP, it is considerably more dangerous and hence is not regularly used within materials literature. However, the improvements found on the film deposition quality in his planar samples, meant it was trailed in a twin holed fibre. The concentration of the precursor was also altered. Due to the difference in the two precursors, (ATTM and ATTT) a larger concentration of ATTT in the solution was performed. This time, 2.5g of precursor was placed into a solvent solution of 4.5ml NMP, 4.5ml Butylamine and 1ml Aminoethanol. The resulting deposition was analysed under Raman spectroscopy, showing an example trace in Figure 5.5. This was analysed against length, and found to be improved as per Figure 5.6.

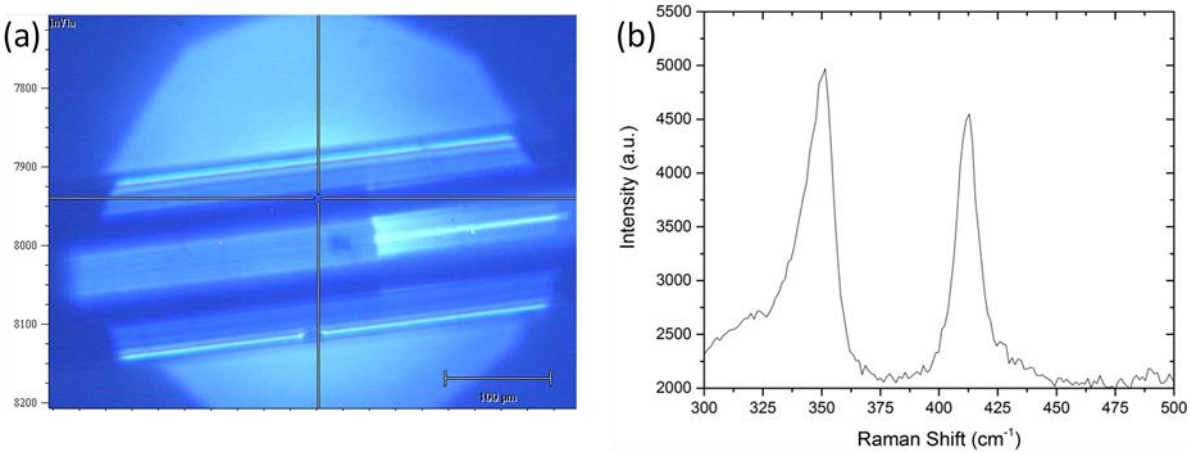

Figure 5.3: A Raman image of the WS_2 deposition using DMF as a host solvent. An image of where in the fibre is focussed is also shown in (a). The two resonant Raman seen in (b) peaks correspond well to WS_2, with the 1.2 ratio corresponding to bilayer material.

Figure 5.4: Images of the precursor solution in three host solvent solutions of DMF/Aminoethanol/Butylamine, NMP/Aminoethanol/butylamine and DMSO. Each has the same wt% at 1%.

5.2.2 Tungsten Disulphide for Poling Applications

The fibre could then be placed in the same setup as the poled MoS_2 sample. It was poled in the set up seen in Figure 3.16 with the same single anode configuration, as both hollow regions of the fibre had been functionalised. The fibre was then quasi-phase-matched via the UV laser, producing

gratings within the fibre. Like the MoS_2 deposition, two fibres from the same source are presented, with the -01 sample showing high quality deposition after Raman, and the -02 fibre showing poor deposition, with the results shown in Table 5.1. After characterisation with the laser system shown in Figure 3.21. the high quality sample was shown to produce a $\chi^{(2)}$ of 0.0471, which when compared to the MoS_2 poled sample ($\chi^{(2)}$ of 0.0473) has a tiny difference. The loss of the fibre is also slightly more, showing a high loss of 2.62dB and 4.48dB, which is almost double the loss from the MoS_2 integrated fibre. This is likely due to the lesser quality of the deposition. Theoretically this does not agree with the expectation, as the literature should state that the WS_2 film has a higher $\chi^{(2)}$. However, once again we find an increase in the $\chi^{(2)}$ in respect to the reference fibre, of almost 10%.

Device name	**Measured $\chi^{(2)}$ (pm/V)**	**Loss (dB/cm)**
WS_2-01	0.0471 ± $1x10^{-4}$	0.033
WS_2-02	0.0115 ± $1x10^{-4}$	0.056
Reference fibre	0.0426 ± $1x10^{-4}$	0.013

Table 5.1: Response of the WS_2 integrated fibres after thermal poling. The measured values show the deposition of WS_2 with good quality deposition shows an increased $\chi^{(2)}$

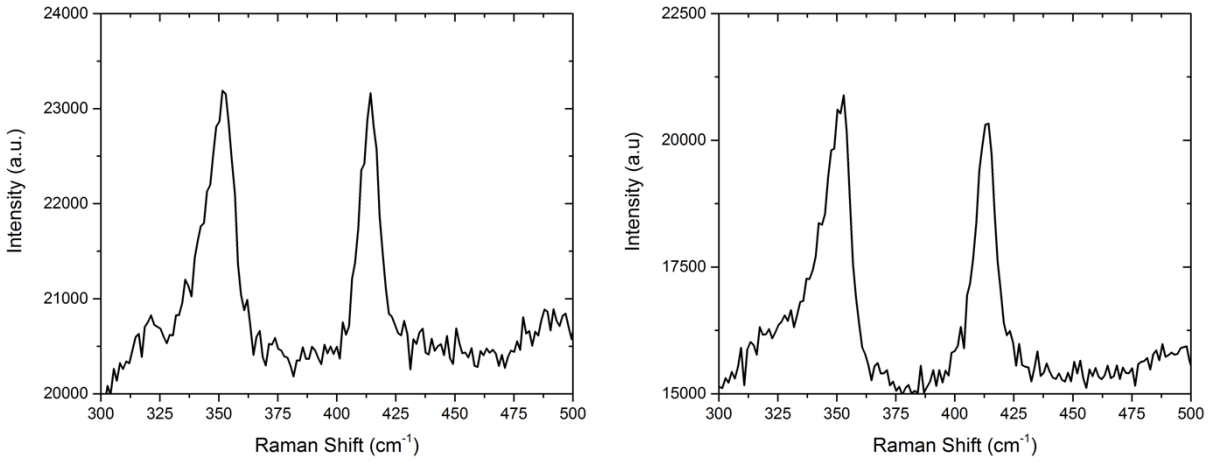

Figure 5.5: Raman images from the good quality deposition, showing two clear resonant peaks of almost equal intensities and a ratio of 1.2, corresponding to monolayer and bilayer material.

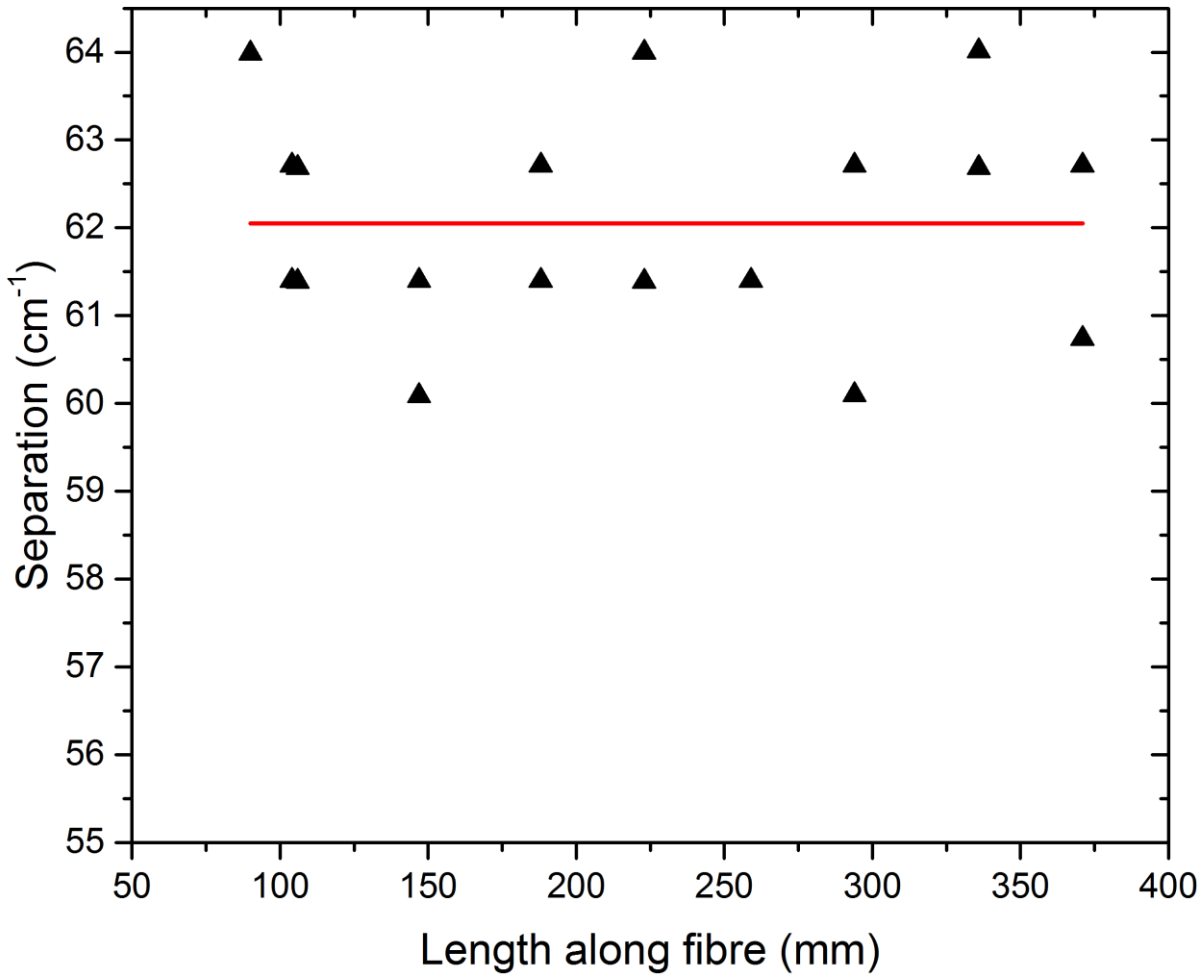

Figure 5.6: Raman scans against length along the fibre, showing almost consistent average values over a length of 300mm.

5.2.3 Tungsten Disulphide Integrated Fibres for Optical Modulation

The WS_2 films were also transferred into our experimental set ups for optical modulation. Due to the similarities between the MoS_2 and WS_2 films, we expected the film to function in the same manner, with similar electrical field requirements. However, as per the literature, the results of the modulation were expected to be better. We began our investigations with a theoretical view on the capabilities of the film.

To model the system, a borosilicate HCNCF fibre was recreated in COMSOL. A WS_2 film was integrated into the fibre, producing the images shown in Figure 5.7. A WS_2 film was selected due to the potential decrease in the loss of the device, as well as the greater gating potential of the film in comparison to MoS_2.

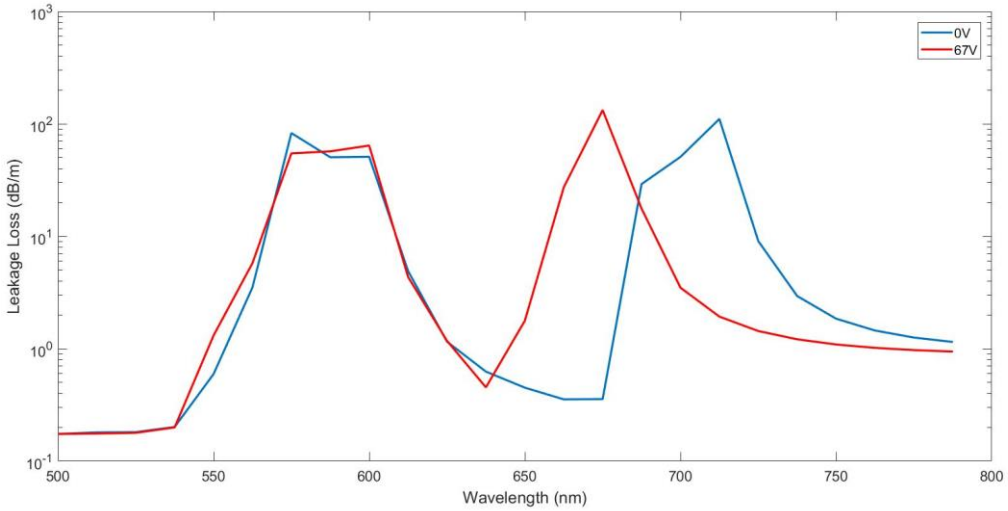

Figure 5.7: Theoretical results from the WS_2 integration and refractive index change due to an applied voltage.

The tungsten disulphide film was also translated into the negative fibre structure, to attempt to modulate the device. It was expected due to works from the literature that the WS_2 film would produce a larger modulation than our best result from a MoS_2 integrated sample – peaking at 3.52dB. Due to the nature of the film, it is expected that the film would react well at smaller voltages hence improving the likelihood the technology could be transferred to industrial applications. After the Raman characterisation work performed in 5.2.1, the best solvent solution and concentration for deposition was found. This was then performed in the fibre sample, with the peak temperature of annealing of 500°C was selected. It was characterised under Raman spectroscopy, producing an example Raman trace as shown in Figure 5.5.

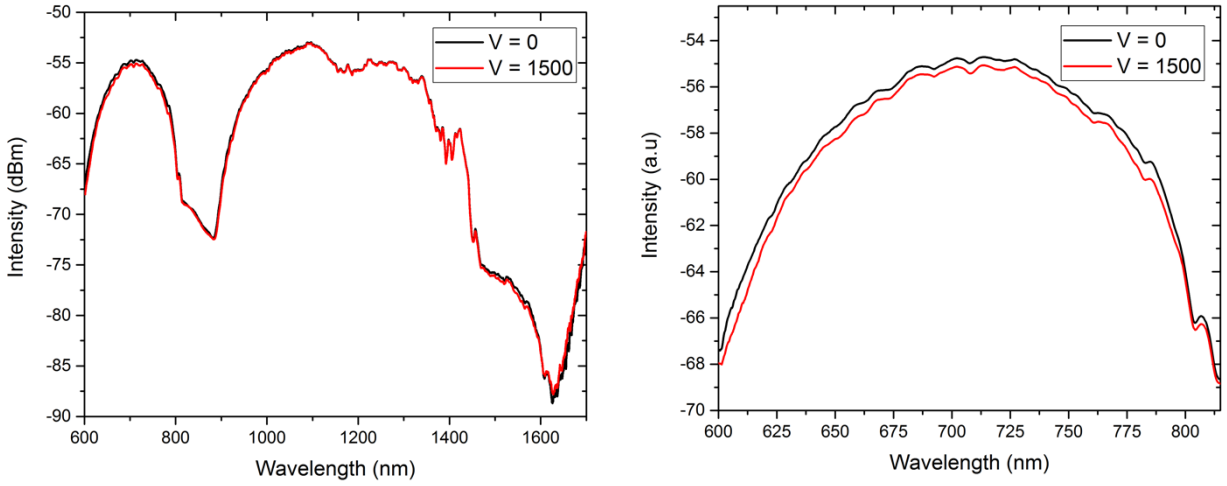

Figure 5.8: Integration of WS_2 into B0461Y fibres, showing the guidance capability at ground voltage and at 1500V. In this case, WS_2 was deposited in all hollow regions of the fibre. It shows a maximum modulation of 0.6dB.

It was also optically characterised by butt coupling it to a WLS via the MMF. The spectrum was collected by an OSA for a zero voltage trace, and is shown in Figure 5.8. It was compared to a MoS_2 and non-functionalised fibre. However when comparing the three traces, it must be kept in mind that the coupling into the fibre is slightly different for each trace, meaning a +/-1dB change could be possible between the spectra. Overall, we see much higher loss in the WS_2 functionalised fibre, likely due to the issues with the WS_2 deposition.

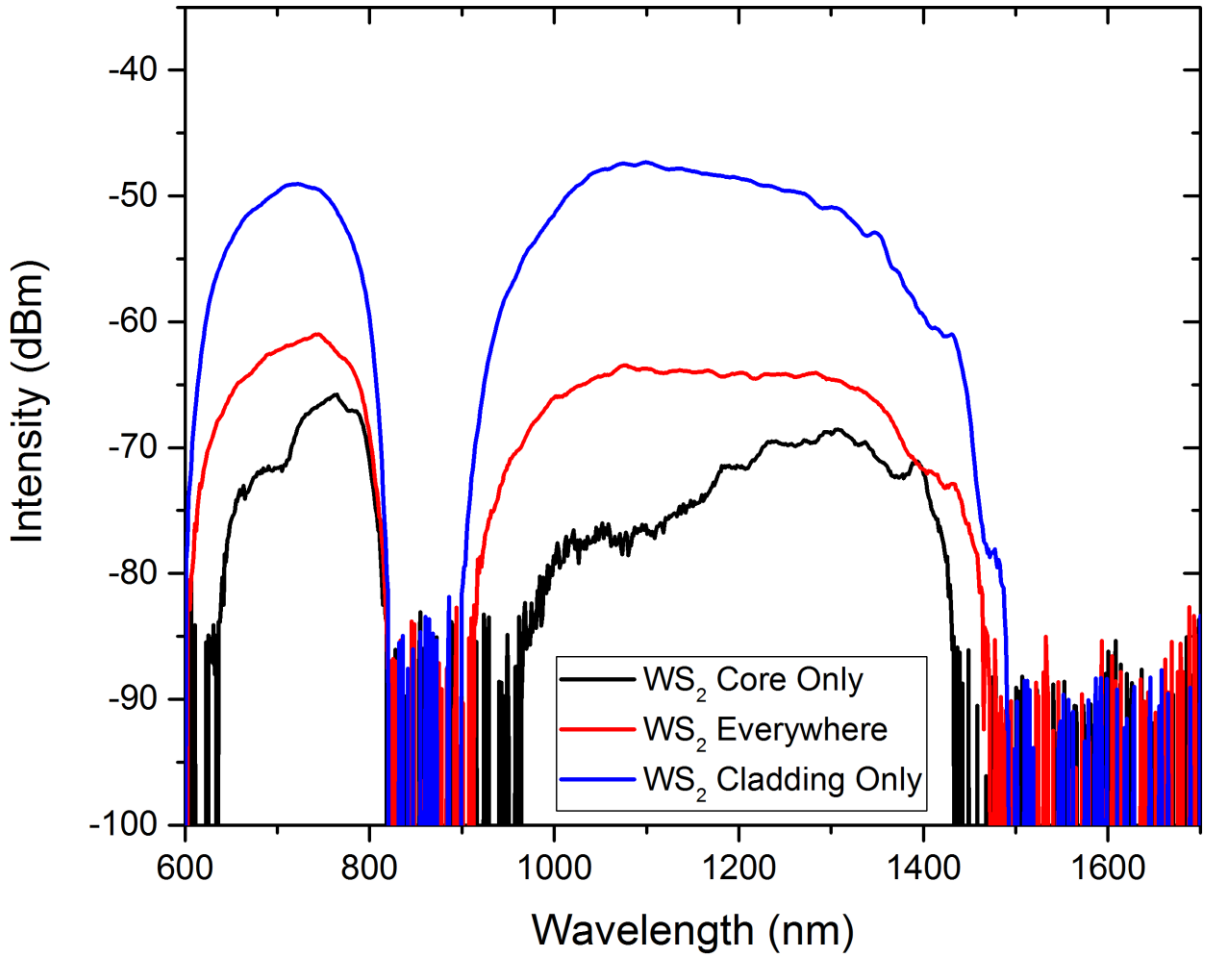

Figure 5.9: Intensity measurements of three different depositions of WS_2 into the B0461Y fibre. In all cases, the fibres were of equal length (90cm) and their depositions had been performed under the same synthesis conditions. As can be seen, the interaction of the film with the guided light is changed with different deposition regions.

The WS_2 fibre were also functionalised in core-only and cladding-only configurations by selective filling methods, as well as deposition in all hollow regions. A comparison between the three was performed, showing the spectra show in Figure 5.9. It follows the same results as MoS_2, showing the core only sample showing the most loss, and the cladding only sample showing the least loss, due to the amount of film interaction and confinement properties of the mode. Each fibre was then tested under the electrical field experiments using the setup demonstrated in Figure 4.32.

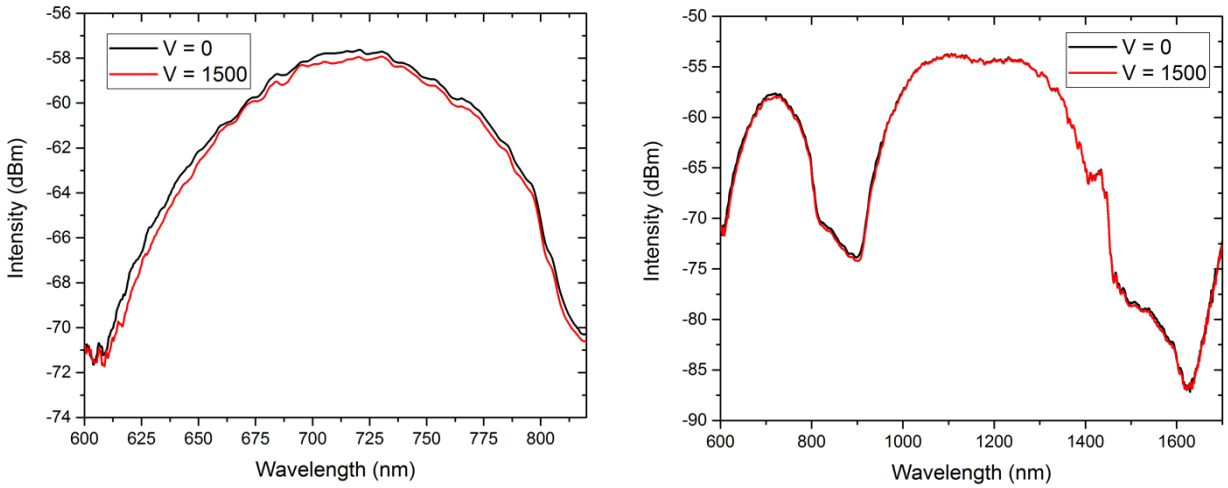

Figure 5.10: Results from the integration of WS_2 into the cladding region of the B0461Y fibre, at the ground and at 1500V. A maximum modulation of 1.01dB is observed.

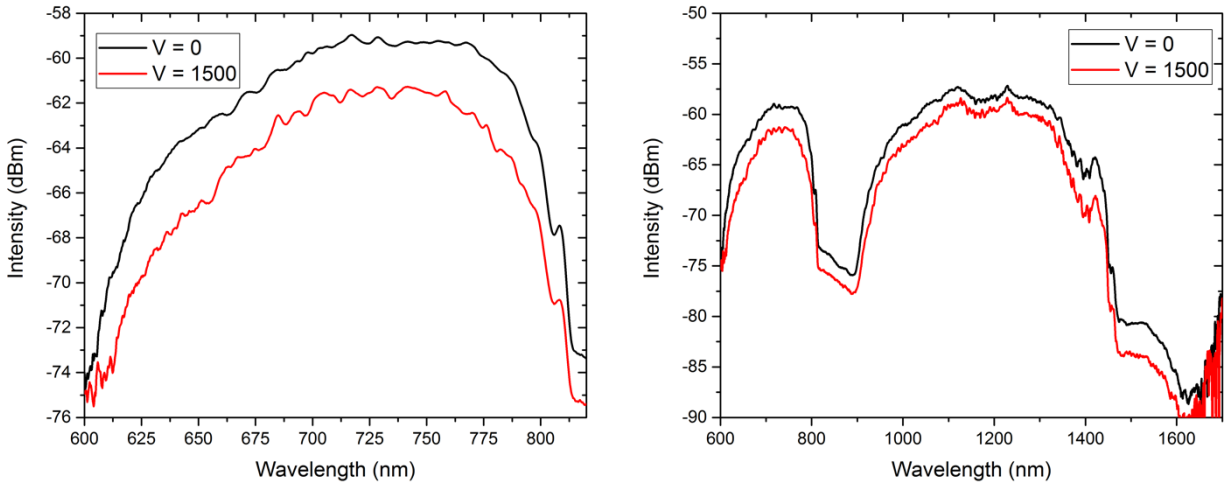

Figure 5.11: Results from the integration of WS_2 into the core region of the B0461Y fibre, at the ground and at 1500V. A maximum modulation of 3.67dB is observed.

All three configurations of fibre were placed onto the metallic slab in a single anode set up. In Figure 5.8,Figure 5.10Figure 5.11 the results of this are shown, observing roughly the same trend than for the MoS_2 fibres. The WS_2 everywhere fibre interacts the well, producing a modulation of 0.60 dB at 655nm, with a smaller average modulation in the first resonant regions of 0.46 dB as seen in Figure 5.8. The cladding only sample reacts with a maximum modulation of 1.01dB at 628nm, with an average modulation of 0.37dB in the first resonance window shown in Figure 5.10. In contrast, these are outperformed by the core only sample, which produces a peak modulation of 3.67dB at 656nm, with an average modulation of 2.79dB as shown in Figure 5.11. Importantly, when compared with MoS_2, the value of the core only deposition compares well, but is not remarkably stronger than the MoS_2 everywhere sample which measures at 1.6dB. However, the core only deposition produces higher loss.

5.2.4 Concluding Remarks on WS_2 integrated fibres

Overall, we see that the use of WS_2 in optical modulation and second harmonic generation experiments leads to results very comparable to that of MoS_2. Due to the more complicated deposition technique, and especially the use of potentially toxic NMP, the MoS_2 functionalised fibres are considered as the more viable technology. Due to the similarities between the two films, this was expected. As a completely different approach, the bulk film ZnSe was also investigated.

5.3 Zinc Selenide

As an alternative approach to the integration of composite films, a large thickness film – Zinc Selenide - was selected to integrate into a fibre. Zinc Selenide is a TMDC material formed of layers of Zinc bonded to Selenium atoms, forming the crystal shown in Figure 5.12 [152]. It has been shown to show a very large optical bandgap, measuring at a value of 2.67eV [153]. Early research works have analysed the refractive index and absorption coefficient, and its dependence on the wavelength, with the spectra shown in Figure 5.13. ZnSe has also been observed to produce second harmonic generation, with a d_{eff} value measuring 27 pm/V at 1.06um [154][155]. Unfortunately, due to the thickness of the film and its high refractive index – measured to be 2.4 at a wavelength of 1064nm from the graph in Figure 5.13 – the film was not chosen to be deposited on the hollow regions of a twin hole fibre for poling. Because of the proximity of the film to the core, it is likely that too much of the propagating mode would be dragged into the ZnSe region, producing too much loss and coupling issues. However, ZnSe has been seen to observe gating, due to its semi-conductor nature allowing for free charge carriers. It has therefore been used for deposition within an anti-resonant fibre structure.

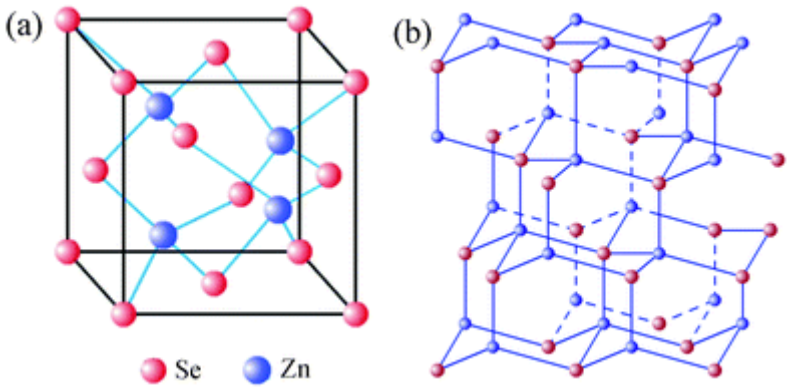

Figure 5.12: The crystal structure of ZnSe. From Ref [152].

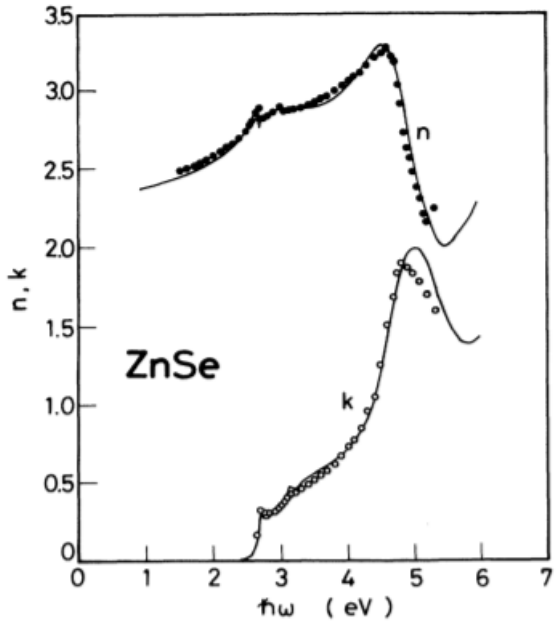

Figure 5.13: The effects of the refractive index and the absorption coefficient change of ZnSe with increasing wavelength of analysis. From Ref [153].

Upon analysing the deposition techniques of ZnSe wide range of deposition methods, such as RF sputtering of thin films [137] and chemical bath deposition [156]. Further depositions have included the technique of high pressure CVD (HPCVD) for ZnSe growth, using dimethylzinc and dimethylselenide as precursors [138]. This method produced thin films into the hollow regions of a capillary core fibre. The large pressure allowed for low temperatures of 450^{o}C to be used in the deposition process leaving little damage to the fibre [138]. However, these precursors are known to be potentially dangerous, with the authors noting the pyrophoric nature of the DMZn precursor raising safety concerns, hence only low flows of gas was used, causing the process to be slow. The high pressure required can also lead to internal cracks in the fibre.

It would be of interest to see how a thicker film interacts with the light in our negative curvature fibre structure. It would be expected that for much larger film thicknesses, especially of films of naturally high refractive index, that there would be a large film/light interaction. This produces both positive and negative aspects for our modulation work. A high interaction could cause extremely high loss, as the guidance mechanism of anti-resonance will begin to break down, leading to poor propagation qualities. However, the large interaction would mean that for only minor changes in the films optical properties could have significant implications to the modulation capability of the composite fibre structure. It is also worth considering the thickness of the film when calculating the electrical field applied to the fibre. Due to this large thickness, cladding regions may begin to ‘shield’ the ZnSe deposition in the core. The possibility of this will be explored in this chapter.

5.3.1 Zinc Selenide Integrated Fibres for Optical Modulation

To begin, a description of the deposition of the ZnSe into the B0461Y fibre is discusses. This work was carried out with colleagues at the Pennsylvania State University (USA). It uses the precursors dimethylselenide (DmSe) and dimethylzinc (DmZn). They are in a gaseous form, and are carried into the deposition chamber by the carrier gas H_2. The concentration of the precursors were 0.015% DmSe and 0.07% DmZn. The process was completed inside of a furnace, using the fibres itself as the deposition chamber. A schematic set up from Penn State University can be seen in Figure 5.14.

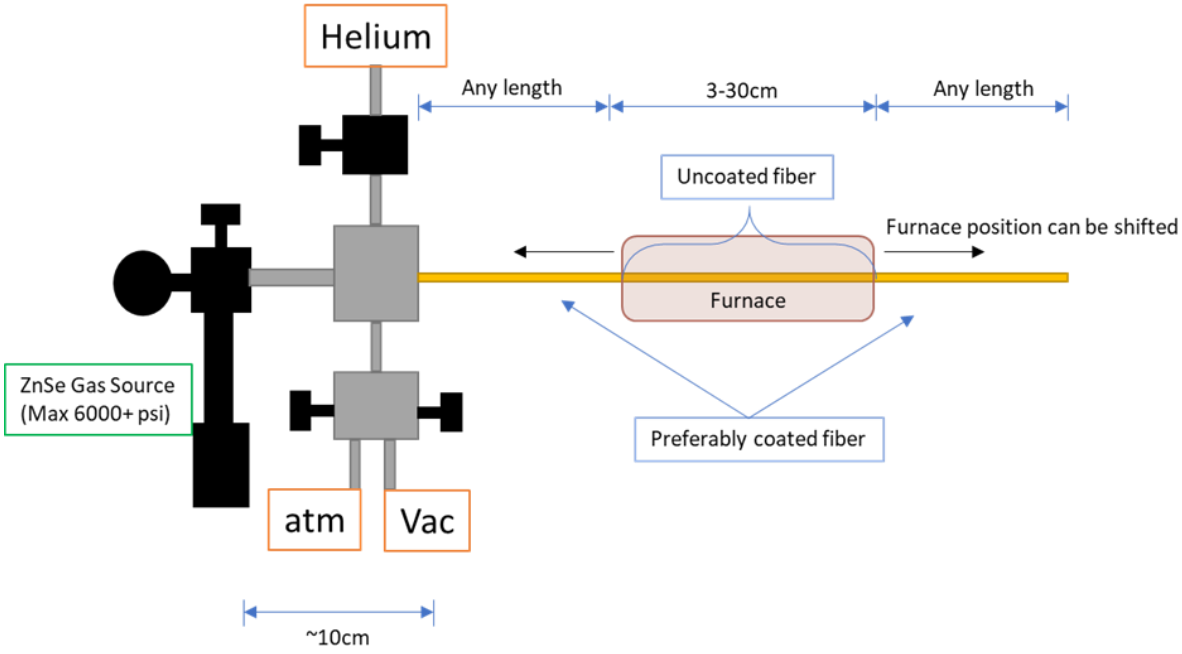

Figure 5.14: The deposition setup used at Penn State University, for the deposition of ZnSe into hollow core optical fibres.

The produced film, due to its large thickness, could be readily seen when analysing the fibre side on. A photograph is shown in Figure 5.18 of the film, showing a bright yellow deposition on the inside of the fibre. We performed a Raman study on the ZnSe film to confirm the deposition – producing the Raman spectra shown in Figure 5.15. However, it is hard to decipher from such spectra the thickness of the deposited film. The method to analyse this was the use of a SEM. Unfortunately, after the sample had expired, it was broken into smaller pieces and coated with a thin (12nm) Au coating, allowing for the electrons to conduct along the sample. When measured, the thickness of the deposition measures 100nm, a significant increase on the potentially trilayer (1.8nm) MoS_2 samples. SEM images of different depositions are shown, with some samples such as Figure 5.16a showing a conformal coating of the inner regions of the fibre, well highlighted from the BSD of the SEM. This was measured during the SEM. From previous results, we know the thickness of the glass struts in an empty fibre is 800nm. In the image seen in Figure 5.16a, we find

a thickness of the strut after ZnSE deposition to be 1000nm. This suggests a 100nm film has been deposited into the fibre, a significant change from the predicted 1.8nm of MoS_2 deposition.

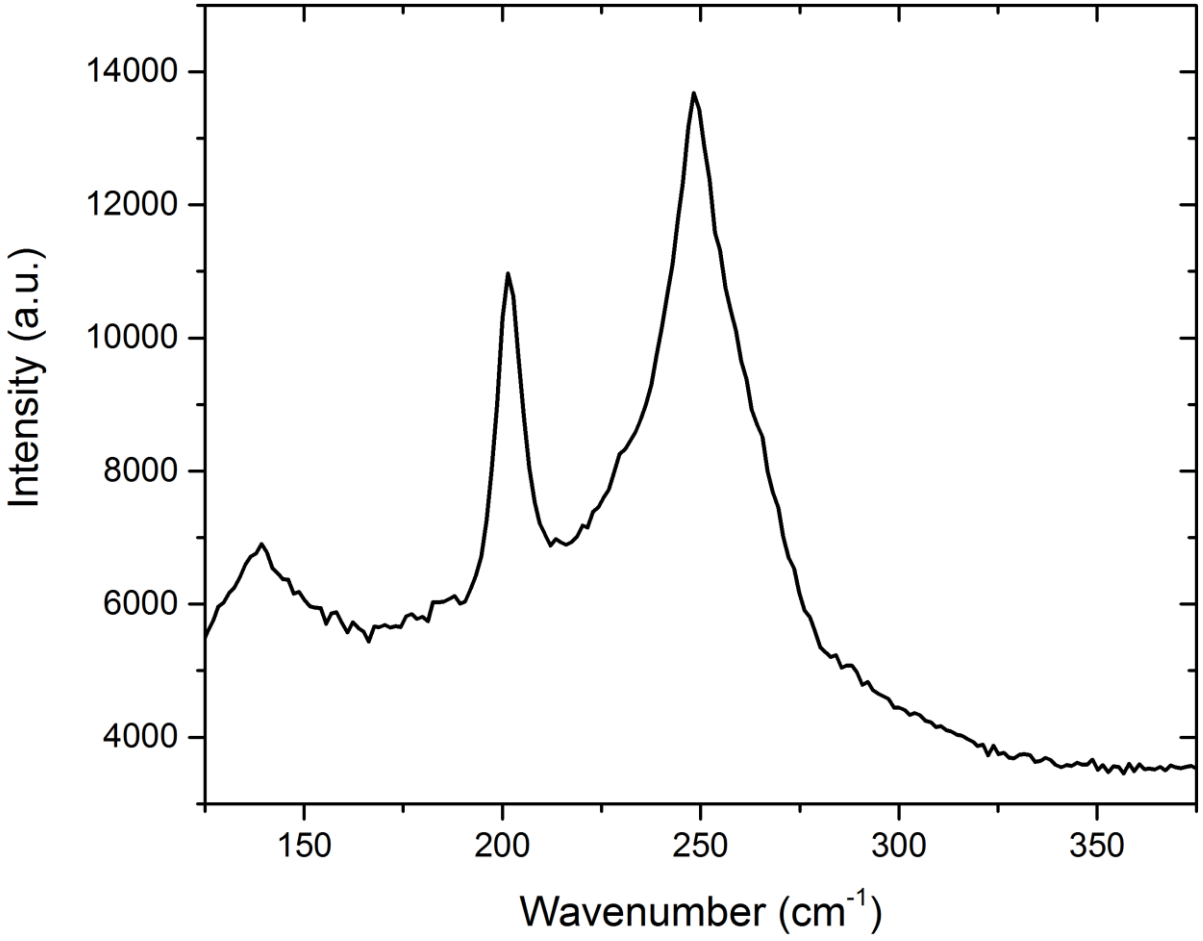

Figure 5.15: A Raman image of a ZnSe integrated B0461Y optical fibre.

However, images such as Figure 5.17b show flakes coming from the fibre, suggesting poor deposition quality. It is also clear from the SEM images that the internal structure struggles under high pressure. Figure 5.17 shows huge distortion to the optical fibre structure – reiterated by the optical microscope image provided in Figure 5.18. However, it is difficult to know how the internal structure of the fibre has been damaged without breaking into the fibre. This could lead to huge scatter loss in the fibre if used in an optical set up – which shall be discussed next.

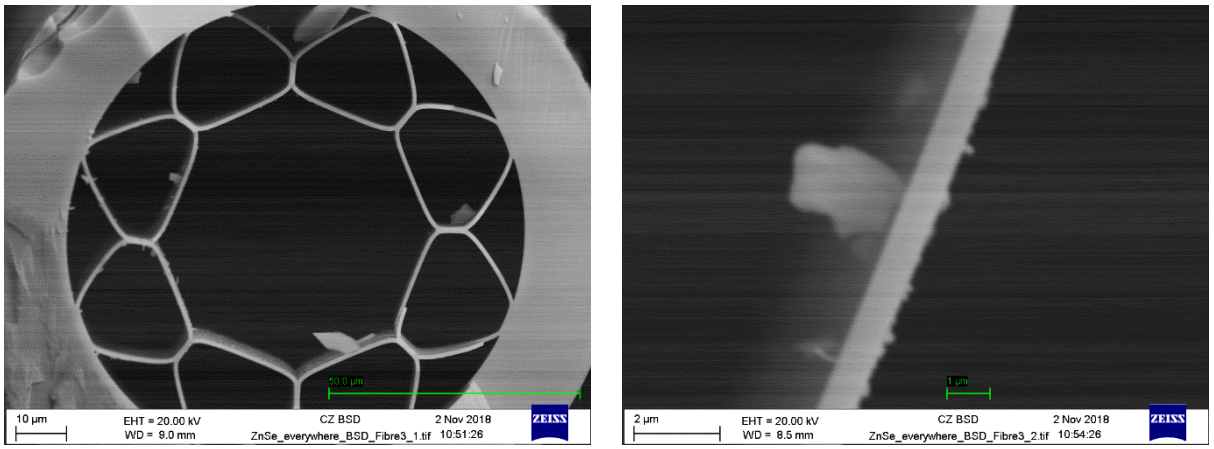

Figure 5.16: A SEM image of a B0461Y fibre which had been integrated with ZnSe. This fibre shows stability, and a relatively conformal film thickness.

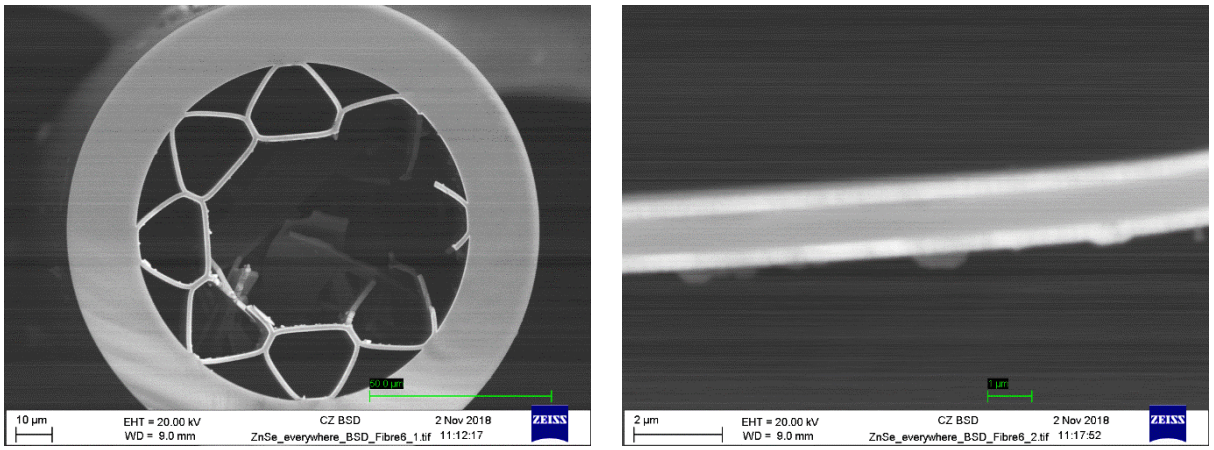

Figure 5.17: A SEM of a second ZnSe deposition in the B0461Y fibre. Here, it is clear too much pressure has been applied to the fibre, causing internal damage to the fibre structure. It also appears to have formed flakes.

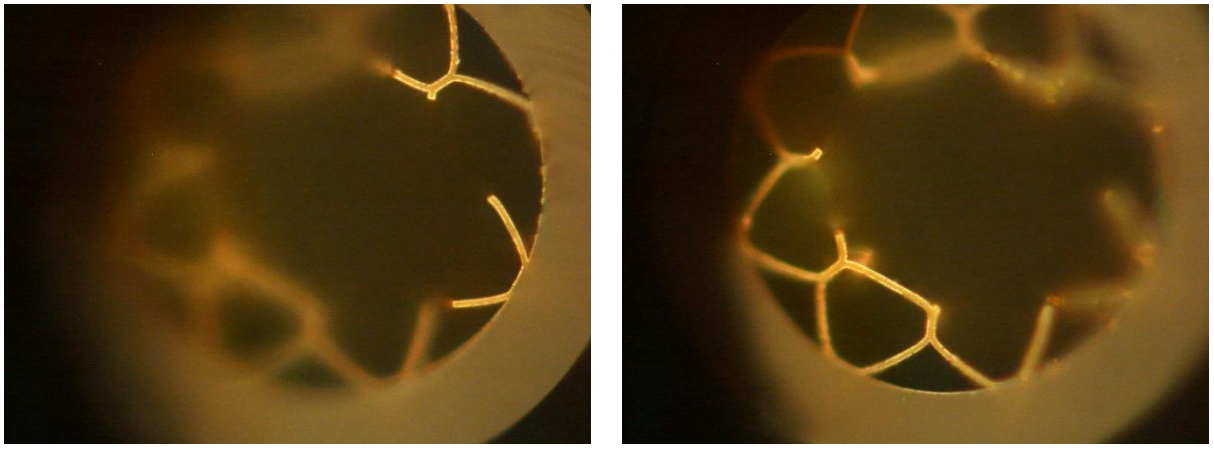

Figure 5.18: An optical microscope image of the SEM image above. The yellow tinge to the image is due to the ZnSe.

The ZnSe fibres were then placed in the optical set up in single anode configuration used in chapter 3 and characterised with a WLS. As can be seen, the trace shows very large optical loss, with some aspects of the trace being very difficult for the OSA to register. It is hard to decipher from this trace the anti-resonant regions as seen in the bare fibre. However, this does suggest a high film-light interaction, which would suggest that a large modulation could be performed if a voltage is applied [157].

The setup was therefore updated to include the metallic slab and the high voltage power supply. Once aligned with the WLS, a high voltage of 1500V was applied, as performed in previous experiments. The resulting spectra are shown in Figure 5.19. As can be seen, there is very little variation between the two traces, implying that the voltage had very little effect on the guidance of the fibre. The theory as to why this has happened is likely due to the difficulty of penetrating the thick silica cladding, as well as ZnSe film, which also is of quite high thickness and high relative electric permittivity. It would be expected that only the outer regions of the ZnSe is interacting with the guided light. It would therefore be likely that only the inner regions of the ZnSe is affected by the voltage – and this electrically shield those inner regions. Therefore no electro-optic or electro-absorptive effects could be observed.

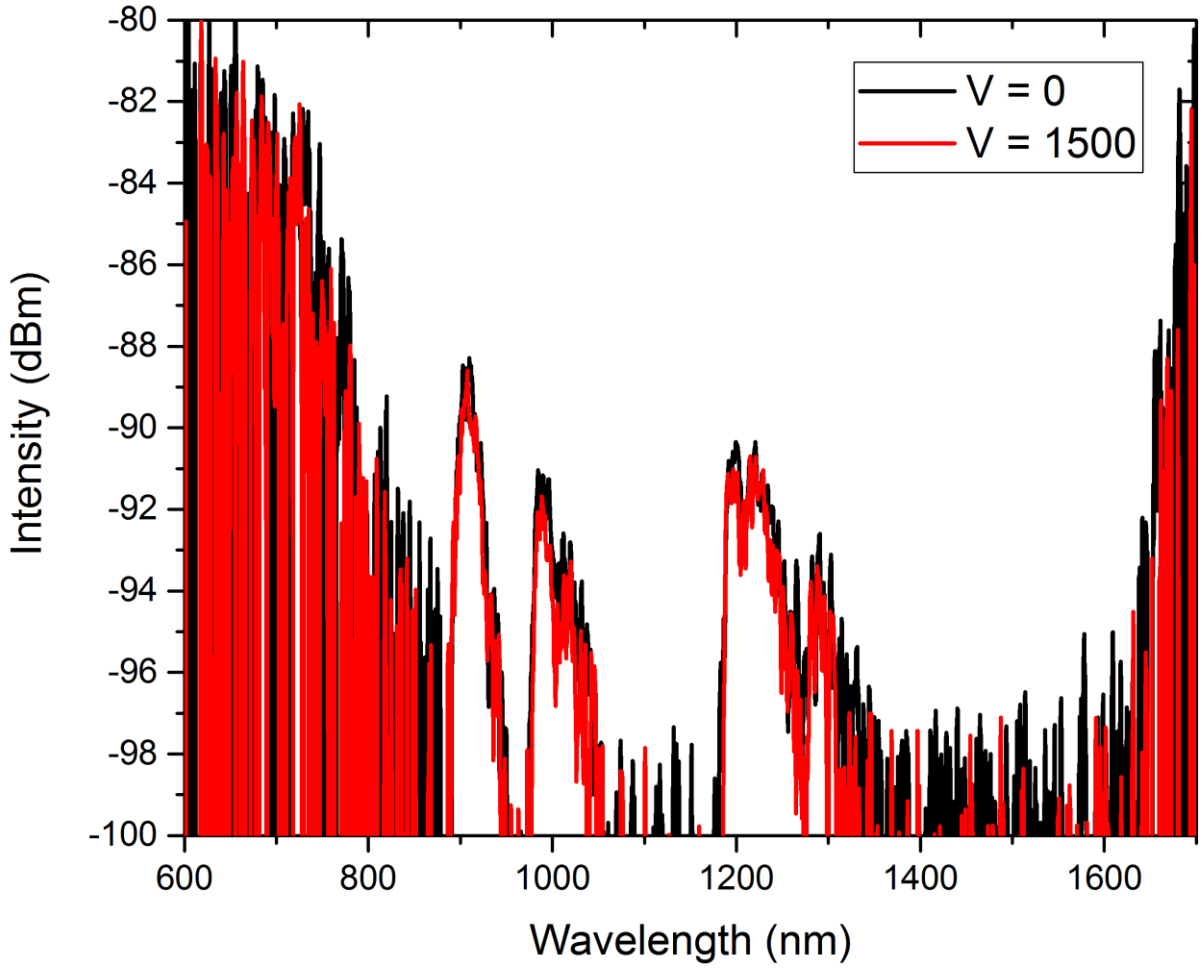

Figure 5.19: The reaction of the ZnSe integrated B0461Y fibre seen in Fig. 5.16 under investigation of a WLS and after the application of a high voltage.

Another likelihood is the that the region of the modulation is in a region of the spectra whereby the ZnSe fibre shows no guidance – or possibly is outside the wavelength range the OSA is able to measure. For the MoS_2 fibre, modulation was found at around the bandgap for the material in it's multi-layer form. For ZnSe – for a bandgap of 500nm in its crystalline form – is outside of our measurement range. However, the likelihood is that the deposited film is polycrystalline, meaning the bandgap is likely to be smaller, nevertheless no modulation was seen.

To learn more about the ZnSe fibre, the output of the fibre was focussed into a camera to perform mode imaging. By analysing the near field mode, hopefully the positioning inside the film of where the light is being propagated should be able to be seen. Due to the thickness of the film, the expected result is that the majority of the light would be guided in the ZnSe region. For this, a 760nm laser was used – which from our WLS results has been seen to guide with relatively strong guidance. The mode images are shown in Figure 5.20. As can be seen the mode images show very little change, suggesting power is not lost due to a change in the E field experienced by the ZnSe. This is reaffirmed by the measured output power, which remained at a constant 0.23mW over all applied voltages.

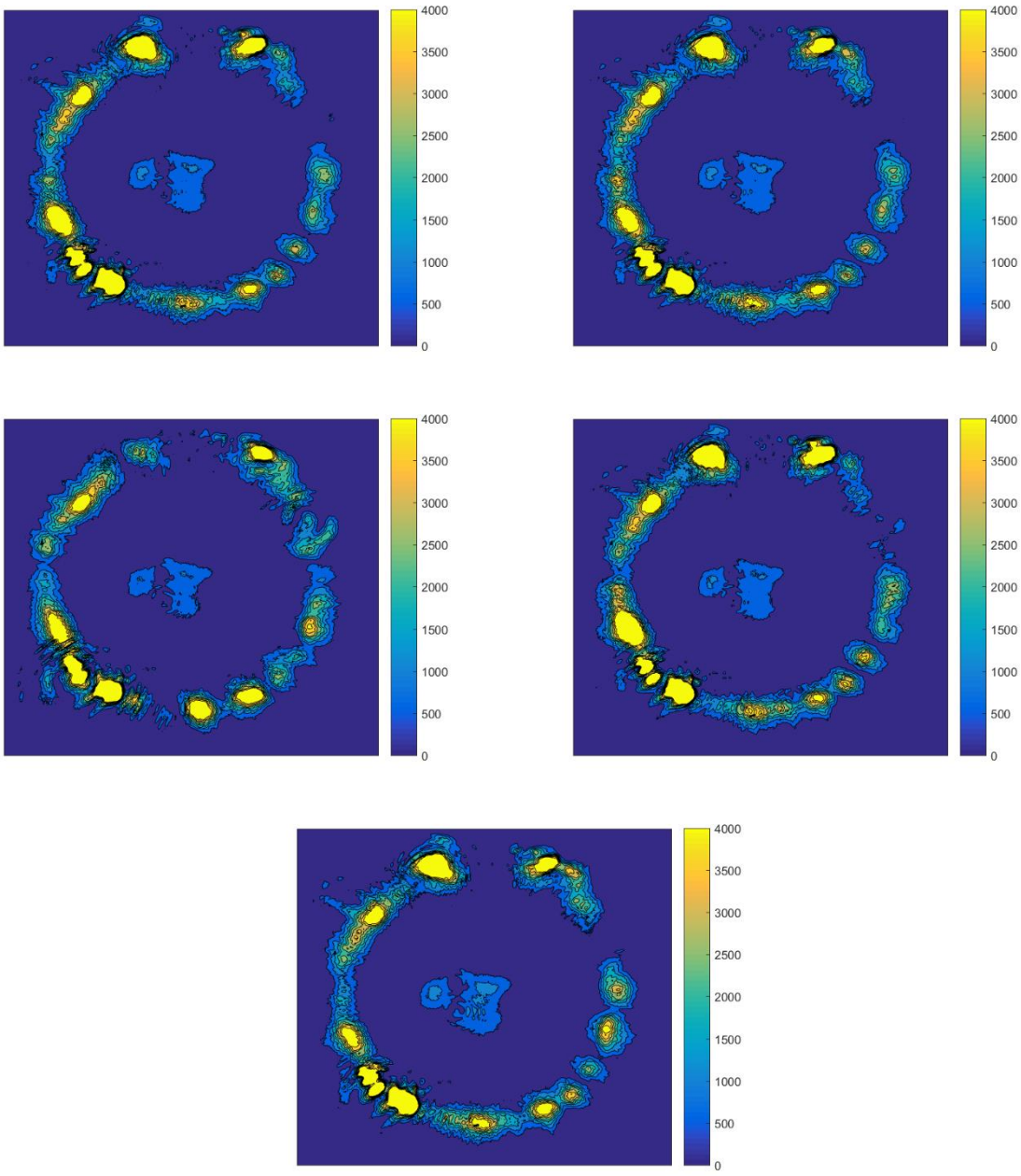

Figure 5.20: Mode images of the ZnSe fibre for increasing applied voltage. As can be seen the guidance in the hollow core region barely fluctuates, implying no modulated film/light interaction occurs.

5.3.2 Zinc Selenide Concluding Remarks

Overall, the ZnSe fibres show poor modulation capability, and their high loss means they would not function well in optical fibres for poling and second order nonlinearity functions. The high thickness of the film causes many problems.

However, if the deposition process could be further refined and a significantly thinner film was created with higher uniformity, theoretically it would still be possible for the film to produce modulation akin to the MoS_2/WS_2 films. It would be possible to raise the voltage placed onto the metallic slab to observe modulation, however the 1.5kV currently being worked at is a potential dangerous – and larger voltages would be harder to transfer to industrial approaches. New applications for a ZnSe films may be sought out, such as doping with Chromium for fabricating mid-IR lasers [158].

5.4 Concluding Remarks on Functionalised Fibres with Additional Films

The template NCF structures offer a great host for the deposition of additional films. The TMDC WS_2 shows potential as a material for gating, but results so far have been less effective as its counterpart MoS_2. This is likely due to the deposition temperature needed to achieve high quality WS_2, which is potentially damaging to the optical fibre, as well as the solution needed for the deposition involving NMP, a potentially toxic solvent. Theoretically, at least, it has been observed that WS_2 has a higher gating potential which hopefully can be exploited in further works.

Looking at different 2D films, such as graphene could also be of interest. The refinement of the deposition technique of graphene is key though, as exfoliation techniques would lead to a non-uniform film.

Focus has also been placed onto the introduction of thicker films into the antiresonant structures. ZnSe has been deposited in the hollow regions, showing severe loss and difficulty in guidance with the presence of the material. SEM images of this have shown irregular deposition, leading to the theory that the loss is mainly due to scattering. With further refinement of the deposition technique, it could be possible to achieve better guidance. Electro-optical modulation techniques were also tested on the ZnSe integrated film. Unfortunately they did not show any form of modulation. The reasoning behind this is currently under investigation, but is likely due to the overall thickness of the film.

Chapter 6 Future Works

Although our integration of 2D films into twin hole fibre structures for the enhancement of the second order nonlinearity in thermal poling has shown positive results, there are aspects of the composite structure that could be improved upon. The same is true of the functionalised optical modulators, as although the 3.5dB modulation is a great result for a novel and unique functional mechanism, the high voltage needed decreases the electro-optic modulators potential for commercialisation of the device. Further analysis of this works shows that there are a few modifications that can be made to both devices to improve them.

There are some changes that can be applied to both fibre devices, as well as some improvements localised to each. This chapter will therefore be split into three sections. We begin by looking at the improvements that could apply to both devices followed by improvements that can be made solely to the functionalised poled fibre and then changes that could improve the novel fibre modulators. As with previously, the chapter will discuss purely MoS_2 films, as this TMDC material has been the main focus of this research thesis.

6.1 Improvements to Both Devices

6.1.1 Film Quality

Both devices can obviously be improved by the increase in quality of the integrated MoS_2 film. Many papers have shown that the deposition of monolayer MoS_2 films in comparison to thicker films leads to better results in their $\chi^{(2)}$ values and their gating modulation capability [110],**Error! Reference ource not found.**,[158]. Furthermore, a thinner film should produce less loss whilst transmitting a signal, due to less film/light interaction and depreciation of the mode shape.

There is also the issue of uniformity. The loss could be further decreased if the quality of the film was such that the film had no irregularities such as cracks in the film and areas of bi-layer or tri-layer deposition. This is a current source of loss in the fibres, and would be removed if the film could be deposited with fewer defects.

There are a few methods that could be used to achieve this. One approach to increase the crystal quality and achieve monolayer thickness could be the increase of the temperature of the anneal, or a second high temperature post-anneal in a sulphurous environment [85]. The literature generally shows that larger temperature depositions show higher film quality – of both the crystallinity and uniformity. However, our deposition process used in the fibres – the liquid phase

deposition process – is limited to a low deposition temperature due to the glass fibres. At higher temperatures, we have seen issues arising with the fibres such as brittleness and bends arising due to heat stress. It would not be possible to increase the quality of the film through this method. Instead, a better approach may be to investigate further into the solvent solution and concentration of the precursor in this process.

As non-expert chemists, the solvents chosen were from the literature. It could be the case that for our fibre designs of circular structures made from amorphous silica, different solvent solutions may perform to a higher standard. Unfortunately, without external help, this problem is unlikely to be resolved. A future aim for the project would be to involve a chemist in the deposition work. In the meantime, focus could be placed on analysing the best concentration of precursor to generate the highest quality film. In previous chapters, anneals were performed on solvent solutions with weight percentages of every 0.5wt%. To enhance our knowledge of the deposition, further investigations could be used to looking into every 0.1wt% instead, to optimise the precursor solution.

6.1.2 Increasing the Deposition Length

Alternatively, the deposition process could also be changed. As can be seen in previous chapters, the length of the deposition is limited to the size of the furnace. To remove this factor as an issue, the idea of laser writing could be used to internally deposit in the fibre and if placed onto a mechanical stage, could potentially write long length fibre depositions on metre scales. It has been shown in recent works that a 532nm laser can be used to anneal the ATTM precursor, which could even allow for in-situ analysis of the deposited film [160]. With optimisation of the writing system, such as the use of a UV laser that has been shown to improve crystal quality of deposition, low power lasers could complete the deposition process with high controllability. Furthermore, this may not require the H_2 gas, allowing high quality film to be created in ambient atmosphere, allowing the process to be undertaken in non-cleanroom locations, saving costs [160]. It would also leave the fibre undamaged as well as offer the capability of laser thinning of the functional material [161]. For longer light/film interaction, the effects of the additional film is likely to be enhanced. However, the introduction of a longer deposition may also cause the fibre to generate more loss, but the benefits of higher $\chi^{(2)}$ and greater modulation may outweigh this. More costly methods such as the use of a longer furnace could be an easier alternative, as the deposition method is already well researched and we know the thermal deposition process allows for conformal film growth in all regions of the fibres.

The use of a laser for annealing could work excellently with the selective filling method for the optical modulators. It has been shown that the depositions with only the cladding of the fibre functionalised show less loss in guidance, but suffer in modulation ability. For longer lengths of film, we predict that the fibres modulation can reach values akin to the samples with deposition in all hollow regions, with lesser loss due to less interaction with film in the core.

6.2 Improvements to Thermally Poled Functionalised Fibres

6.2.1 Optimisation of Quasi-Phase Matching

With the functionalised poled fibres, one key step to increase the efficiency of the enhanced $\chi^{(2)}$ value is in the quasi phase matching of the sample. Currently, the UV erased gratings are the same size as the gratings used for non-functionalised fibres. This means that the gratings are optimised to the second harmonic light generated only by the glass in the core of the fibre. It is expected that the TMDC composite film will also produce SH light. However, due to the difference in refractive index of the MoS_2 and the glass, they will have different QPM conditions. It therefore poses a theoretical argument as to how to optimise the grating.

It would appear that the size of gratings for the glass fibre and the MoS_2 are significantly different. Theoretically, for an input wavelength of 1064nm, the grating needed in the silica glass fibre would be of size 48um, using a value of refractive index of 1.46 at 532nm and a value of 1.449 at 1064nm, with the values taken from Ref [162]. This is considerably larger than a grating using the RI of MoS_2 where the grating would be of 0.44um, using a RI values of 5.9 at 532nm and 4.7 at 1064nm from Ref [8]. These results were calculated using the QPM condition described in Equation 3.5 of the Thermal Poling chapter. It would therefore suggest that the MoS_2 signal interferes with itself much quicker than the silica, and that for a grating written in silica, the MoS_2 signal is not affected much.

It is also worth considering the UV erasure process. The UV erasure removes the nonlinearity of the poled fibre by removing the built-in electrical field in the glass. However, our MoS_2 films may not necessarily be poled, due to the lack of impurity charge in the films. The UV erasure step may therefore be unable to remove the 'poled' $\chi^{(2)}$ of the MoS_2, rendering the grating writing useless. However, this is as yet unclear.

The second option is to do as has been performed with the grating writing – keeping the grating length to be calculated from only the contribution of the glass. Theoretically it makes little sense for a compromise between the two gratings sizes to be made, nor for both gratings to be written in the fibre. To exploit the functional film to be the best of its theoretical ability, it would therefore seem that considerable modelling would need to be performed.

A further test to be performed is to test in which mode the SH and probe beam is propagating in. For the functionalised fibre, this is an experiment that has not been performed, and could give further information as to how well confined the beam is to the core of the fibre. For high quality confinement, it would be expected that little light/film interaction occurs. However, for higher order modes, most likely guiding in the cladding, large interaction is likely. Due to guiding in higher modes, the refractive index changes are likely to be of higher variation.

6.2.2 Removal of the Mercury Contacts

One key step in the treatment of the fibre after the poling step is the removal of the Hg contact. Usually this is performed via gas removal. However, there are two key elements that could be further tested to improve the loss quality of the fibre.

The Hg is flowed into the hole where MoS_2 is present, however, it is yet unclear how the mercury contacts react with the MoS_2. Although mercury is not a particularly reactive material, it is well known that it forms amalgams with many metallic materials. This could potentially have detrimental effects when removing the mercury, as extra pressure may be needed if bonding to the MoS_2 has occurred.

However, this could be a large risk, as the bonding of the MoS_2 to the silica host is particularly weak, and it could be possible for the pressure to also remove the MoS_2. Care must therefore be taken in choosing the correct pressure to apply.

6.3 Improvements to the Functionalised Anti-Resonant Fibre Modulators

6.3.1 Decreasing the Necessary Applied Voltage

To promote the fibre into real-world approaches, it is clear that the voltage applied to the metallic slab is far too high – and potentially dangerous – for industrial approaches. A method to maintain the high applied electrical field as per the work shown in previous sections, but with a smaller voltage must be found. To do this, the electrode must be placed closer to the composite film. An approach to do this has already been considered, with a NCF created with hollow regions placed near the negative curvature hollow structure. A cross section of this is shown in Figure 6.1.

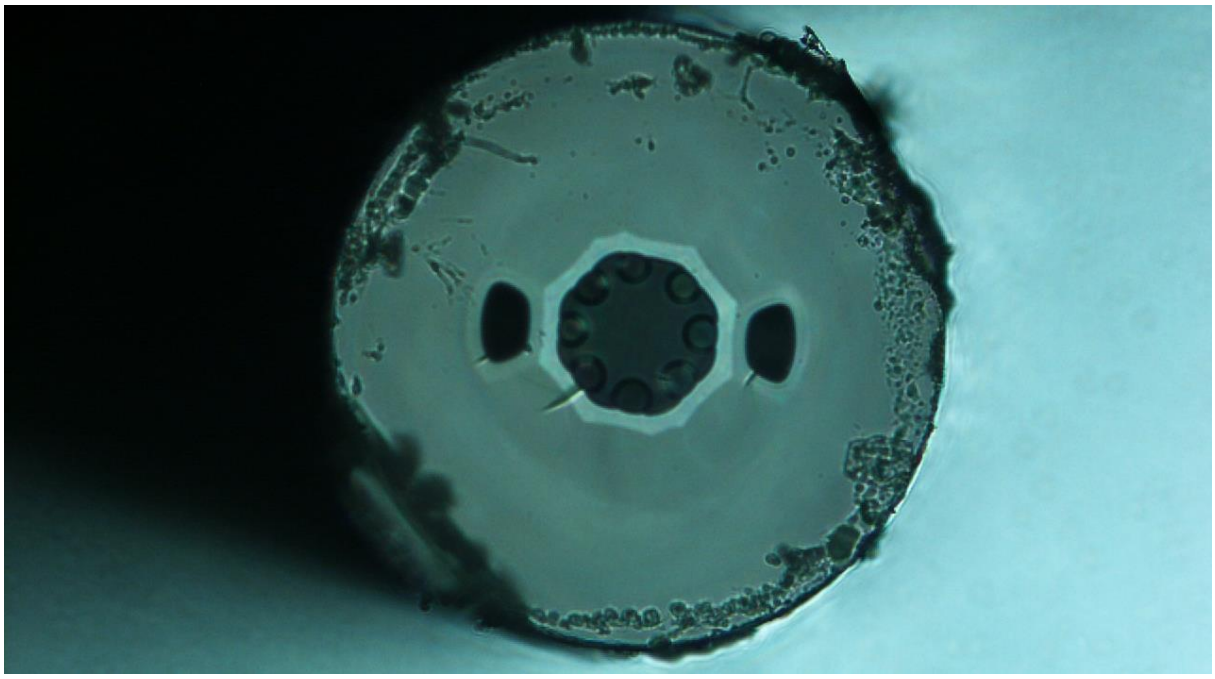

Figure 6.1: A microscope image of a negative curvature fibre fabricated by Walter Belardi with two hollow regions on either side of the core region. It is expected that these holes could be infiltrated with a liquid electrode placed close to the functional films.

It is thought that the selective filling approach would be able to block off the negative curvature hollow region, allowing for liquid metal electrodes such as Hg to be able to penetrate the these additional side hollow regions. As a further thought, it would be difficult to achieve contact with these electrodes without incurring additional loss. If contact were to be made at the endface of the fibre, the core region could potentially become blocked heavily impacting the functionality of the device. This would be especially difficult as the core region could also become blocked, generating huge loss.

It has therefore been suggested that this new fibre configuration could have holes drilled into the side – to open a gap into the hollow regions into which a thin copper/tungsten wire could be placed. To do this, two methods have been suggested. The first is a polishing method much like that used for D-shaped fibres. Essentially, the fibre is placed onto a block and rubbed onto coarse paper. This removes a thickness of the glass, of which the thickness can be determined methods such as the liquid drop technique [163].

A secondary method is the use of a high powered, long wavelength laser to drill into the fibre. This would be able to ablate the glass fibre, penetrating into the hollow region. The laser used as a pulsed CO_2 10.6um laser (Coherent G-100), with a peak effective power of 250W. With control of the length of the pulse, number of pulses and frequency of pulses, the penetrating depth can be controlled.

A capillary core fibre is shown in a before and after image in Figure 6.2a and Figure 6.2b. The penetration into the fibre has caused the channel to become open. We envisage that the metallic liquid could be allowed to flow into this hole with ease. We then tested the 2HNCF in the CO_2 laser, to attempt to penetrate into one of the side regions. This was successfully achieved, with an image showing a tungsten wire of 20um diameter placed into the channel. This is seen in Figure 6.2c. Although this process is not yet refined, as a proof of concept the use of laser drilling show potential for the integration of electrodes into the side holes.

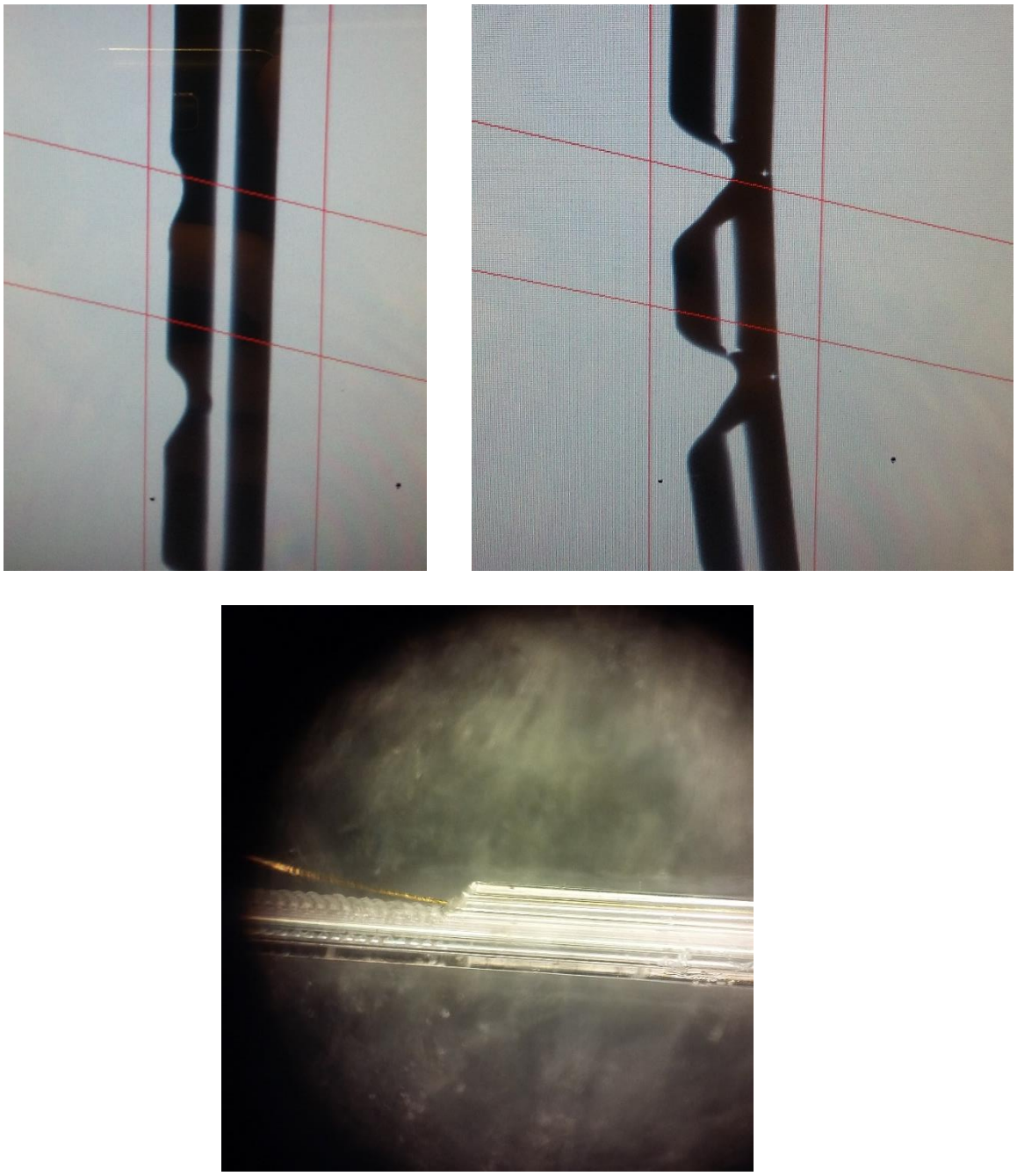

Figure 6.2: Laser drilling of optical fibres. Fig. 6.2a shows a capillary core fibre after a short laser anneal. Fig. 6.2b shows the same capillary core fibre after more laser pulses have been performed.

Fig. 6.2c shows how a 2HNCF has been laser drilled into the hollow side regions. A thin tungsten wire has been inserted into the holes.

However, there are a few issues with this technique. The obvious issue is the quality of the fibre after the drilling process. The fibre, due to missing a large region of the cladding, becomes extremely brittle. Furthermore, when the glass is ablated, the glass reforms with thicker regions at the edges of the hole, the result of this can be seen in Figure 6.2b. This generates an overall bending of the fibre, which could be a potential source of loss when the fibre is used as a device.

6.3.2 Optimisation of the Anti-Resonant Structure

To further exploit the effects of the composite film, the internal structure of the anti-resonant fibre could be altered. To date, only the B0461Y fibre has been functionalised and tested experimentally, however from our results and from a theoretical approach, it is clear this fibre has aspects that could be improved. The touching cladding regions are a major cause of loss, with the fibre showing poor bend loss in our preliminary experiments with it. As an example, a WLS was focussed into the fibre which had been wrapped around a 30cm diameter spool. The guidance of the fibre is seen the black trace of Figure 6.3a with 7 metres of fibre spooled and 1m of fibre kept straight. The fibre was then unwrapped by another metre, producing the red trace, with increased intensity. The difference between the two traces shows around 6dB of loss in the first resonant region, which is likely to arise due to bend loss. The bend loss is likely to be due to the touching cladding regions of the B0461Y fibre. It would therefore seem that for a less lossy device, ringed fibre structures, such as those shown in Figure 6.3b should possibly be used to attempt to decrease the loss.

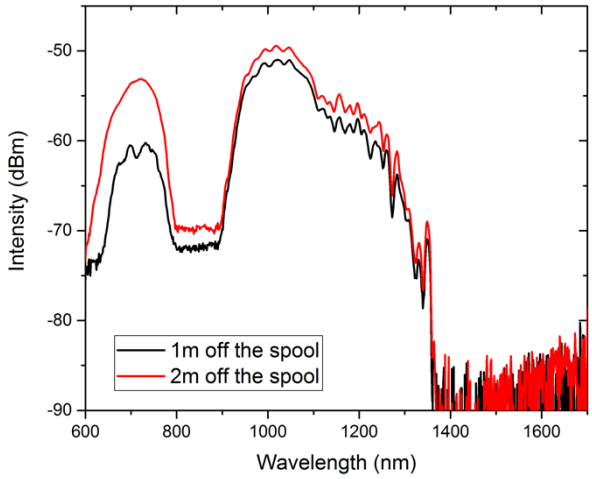

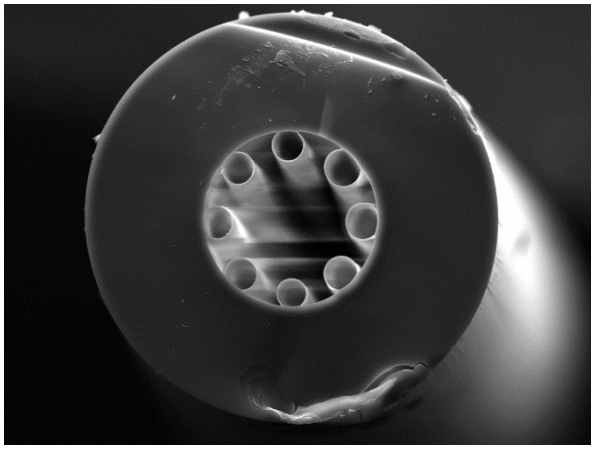

Figure 6.3: The effect of bend loss of the anti-resonant fibre. Fig. 6.3a shows the response of the B0461Y fibre when wrapped around a spool of 30cm. The black trace shows how the fibre reacts with one metre unwrapped, and the red trace shows how the fibre reacts when 2m are unwrapped. The difference between them can be considered to arise due to bend loss. Fig. 6.3b shows a

negative curvature fibre which would offer a different template for deposition, with non-touching cladding regions. This is likely to remove some intrinsic loss.

However, the current B0461Y structure allows for high light/film interaction, as the 'circular' core region allows for deposition all over the inner regions. However, the ringed structures as shown would not have this effect, as only short regions would feel high intensity interaction. It would be expected that such a fibre would show weaker modulation. It therefore needs to be realised as to which aspect of the fibre – the loss or the modulation ability – is most important for industrial approaches.

6.3.3 Further Understanding of the Nature of the Modulation Device

To learn more about the created functionalised modulator, and to know how to fully exploit its potential, its working mechanism must be fully understood, as well as characteristics such as response time and relaxation time optimised. An experiment to understand this has already been undertaken, in the latter stages of chapter 4. This has shown relatively good modulation for a 3Hz input modulation, as well as showing double frequency modulation transitioning to single frequency modulation when the offset voltage is increased.

These results suggest that the optical modulator is working in a way that can be compared to an FET [164]. The response of the modulator acts in a nonlinear fashion for low voltage offsets, which corresponds to the peak/trough region in the FET curve. For larger voltage offsets, the response corresponds to the linear region of the curve, producing single frequency results. It is important to fully understand this effect to learn in which region of the FET curve the modulator is able to respond with the best intensity change, but also with a high repetition rate. It is also important to note the effect the peak-to-peak voltage has on the optical modulator. It has been shown in chapter 4 that for higher $V_{p\text{-}p}$ the intensity response becomes strongly distorted. However, it is as yet unclear as to the limit of this response. By changing the frequency of the voltage change, it has been seen that the intensity fluctuates very little. This suggests the modulator would struggle to handle high frequency signals. However, by altering the $V_{p\text{-}p}$, this effect could be increased. Further experimentation must be undertaken with this approach, to learn more about how the modulator can be optimised.

These previous tests have also been performed at the 633nm wavelength range, however, from our WLS results, we have seen the fibre producing the largest modulation at a working wavelength of 744nm. The previous test has therefore not been optimised to produce the largest modulation result, potentially meaning the fibre is still capable of showing improvements. Key to optimising the

fibre would be to focus in on what wavelength the modulating device performs best at, through fully characterising the fibre with a tuneable source.

6.3.4 Grounding of the Electro-optic Device

The modulation results with a sinusoidal input voltage also seem to show a weak response once a high frequency signal is directed onto the metallic contact. This is likely due to the grounding of the fibre being poor, as the surrounding air – as previously discussed – acts as the ground of the fibre. It is therefore difficult for the fibre to return to a 'normal' state with a high response time. Ideally, electrical contact with the film and the ground should be made to remove this issue. However, it is so far unclear as to how to approach this, as to make contact the core region of the fibre must be interfered with. For example, if the endface of the fibre has contact with the metal, the light is likely to be absorbed or scattered by the metal. Further, this would have poor implications for butt coupling or splicing of the endface of the fibre. Current thought processes to involve a defined ground are currently unclear.

It is also not evident how the grounding effect would work in regards to the grounding of the cladding regions. For a deposition of all hollow regions, we consider film located in the core to be a singular, continuous film, but as the cladding regions are separated by the glass host, each film needs to be considered as a separate entity. It would therefore suggest that each cladding region would therefore need to be grounded separately for each cladding ring. The intricacy of generating such a device, as well as ensuring little loss is produced from it would seem a volume of work beyond the scope of this thesis. We hope this will also remove the charging effect which has been observed in the modulator, leading to a delayed response when the fibre is placed in the set up.

Appendix A List of Publications

Journal Papers

A. H. Lewis, F. De Lucia, W. Belardi, C.-C. Huang, J. R. Hayes, F. Poletti, D. Hewak and P. J. A. Sazio, "Composite material anti-resonant optical fiber electromodulator with 3.5 dB depth", Optics Letters, submitted 08/08/2019

Conference Papers

Morgan, K., Zeimpekis, I., Huang, C-C., Feng, Z., Craig, C., Weatherby, E., Aspiotis, N., Alzaidy, G. A., Ravagli, A., Moog, B. J., Guzman Cruz, F. A., **Lewis, A. H.,** Delaney, M. & Hewak, D., "Chalcogenide materials and applications: from bulk to 2D (Invited Talk)", Electronic Materials and Applications 2019 (EMA 2019), (2019). Abstract: "In this talk, we give an overview of our chalcogenide material and device capabilities and the applications they are driving, scaling from bulk glasses to two-dimensional films. Using a melt-quench technique, we routinely manufacture a family of Ga:La:S semiconducting glasses which offer considerable advantages over commercially available chalcogenides, expanding uses in defense, medical and sensing. We use these glasses to produce optical fibers using extrusion, rod and crucible drawing. We are also developing these materials further, for example by incorporating selenium resulting in improved infrared transmission, enabling both thermal and visible imaging for object recognition. Transition metal dichalcogenides (TMDCs) are promising alternatives to graphene, with bandgaps tunable through composition and number of layers. Today's challenge remains in the fabrication of large area atomically thin TMDCs on desired substrates. We have developed chemical vapor and atomic layer deposition techniques to deposit highly crystalline TMDCs, from nanometers down to a monolayer on up to 6 inch wafers. We recently developed novel patterning techniques that result in defect free devices. Our applications range from 3D photonic crystals to photovoltaics and transistors. Finally we deposit chalcogenide thin films via sputtering and demonstrate applications which exploit their phase change and thermoelectric properties."

Lewis, A. H., Poletti, F., Belardi, W., Huang, C-C., Hewak, D., De Lucia, F. & Sazio, P-J., "Composite material hollow core fibers: functionalization with silicon and 2D materials", SPIE Photonics West, 2017. Abstract: Hollow Core Anti-resonant fibers allow for guidance of mid-infrared light at low

attenuation and allows for a variety of applications, such as high powered laser transmission and gas-based sensing to be achieved. Recent work has seen the integration of silicon [1] into such fibers with linear losses with the potential to be as low as 0.1dB/m. Due to the change in refractive index difference of silicon via for example the free carrier plasma dispersion effect, the prospect of an all optical modulator using such a fiber has been proposed [1]. Here, further work has been undertaken on the integration of functional materials inside hollow core fibers via the deposition of the TMD semiconductor material MoS2, in its few-layered form. Through the use of a liquid precursor, a high quality MoS2 film can be deposited over 30cm length of fiber, as confirmed via Raman spectroscopy. The transmission spectra of these novel composite material hollow core fibers has also been analysed, showing additional loss of around 5bB/m, despite being only around 2nm in thickness. This implies that the refractive index of the integrated material is potentially able to modify the guidance properties of the fiber sample. We will present a comparison of the composite material hollow core fibers we have fabricated to date and discuss the prospects for using these novel waveguides in the active manipulation of light, including optical switching, sensing and frequency generation.

Lewis, A. H., De Lucia, F., Belardi, W., Huang, C-C., Hayes, J., Poletti, F., Hewak, D. & Sazio, P-J., "Composite material hollow core optical fiber electro- modulation", Frontiers In Optics OSA, (2018). Abstract: We demonstrate the integration of the Transition Metal Dichalcogenide (TMDC) materials WS2 and MoS2 into hollow core anti-resonant fibers. We show the potential to use such structures as all fiber electro-optical modulators.

Abbas, O. A., **Lewis, A. H.**, Aspiotis, N., Huang, C., Zeimpekis, I., Hewak, D., Sazio, P., Mailis, S., "Direct laser synthesis of two-dimensional transition metal dichalcogenides", Conference on Lasers and Electro-Optics/Europe – European Quantum Electronics Conference, Munich, Germany (2019). Abstract: We present the spatially selective synthesis, patterning and characterization of two dimensional MoS2 and WS2 layers using laser irradiation of single source precursors under ambient conditions.

Abbas, O. A., **Lewis, A. H.**, Aspiotis, N., Huang, C., Zeimpekis, I., Hewak, D., Sazio, P., Mailis, S. "Direct laser synthesis of two-dimensional transition metal dichalcogenides", Conference on Lasers and Electro-Optics/Europe – European Quantum Electronics Conference, Munich, Germany. (2019) Abstract: We present the spatially selective synthesis, patterning and characterization of two dimensional MoS2 and WS2 layers using laser irradiation of single source precursors under ambient conditions.

Adam H. Lewis, Francesco De Lucia, Walter Belardi, Chung-Che Huang, John R. Hayes, Francesco Poletti, Dan W. Hewak, Pier J.A. Sazio, "Composite Material Antiresonant Fibre Optical Modulator

with >3dB Depth", Conference on Lasers and Electro-Optics/Europe – European Quantum Electronics Conference, Munich, Germany. (2019). Abstract: We demonstrate the integration of the Transition Metal Dichalcogenide (TMDC) materials WS2 and MoS2 into hollow core anti-resonant fibers. Our recent results have seen modulation capabilities measuring more than 3dB.

List of References

[1] K. S. Novoselov, A. K. Geim, S. V. Morozov, D. Jiang, Y. Zhang, S. V. Dubonos, I. V. Grigorieva and A. A. Firsov, “Electric Field Effect in Atomically Thin Carbon Films”, Science, Vol. 306, No. 5696, pp. 666-669 (2004)

[2] D. Li and R. B. Kaner, “Graphene-Based Materials”, Science, Vol. 320, No. 5880, pp. 1170-1171, (2008)

[3] https://www.bbc.co.uk/news/science-environment-39482342

[4] https://www.bbc.co.uk/news/science-environment-30246089

[5] W. Choi, I. Lahiri, R. Seelaboyina and Y. S. Kang, “Synthesis of Graphene and Its Applications: A Review, Critical Reviews”, Solid State and Materials Sciences, Vol. 35, No. 1, pp. 52-71(2010)

[6] V. B. Mohan, K.-T. Lau, D. Hui and D. Bhattacharyya, “Graphene-based materials and their composites: A review on production, applications and product limitations”, Composites Part B: Engineering, Vol. 142, Pages 200-220, (2018)

[7] L. Song, L. Ci, H. Lu, P. B. Sorokin, C. Jin, J. Ni, A. G. Kvashnin, D. G. Kvashnin, J. Lou, B. I. Yakobson and P. M. Ajayan “Large Scale Growth and Characterization of Atomic Hexagonal Boron Nitride Layers”, Nano Lett., Vol. 10, No. 8, pp 3209–3215, (2010)

[8] K. F. Mak, C. Lee, J. Hone, J. Shan, and T. F. Heinz, “Atomically Thin MoS_2: A New Direct-Gap Semiconductor”, Phys. Rev. Lett., Vol. 105, No. 13, 136805 (2010)

[9] H. S. S. Ramakrishna Matte, A. Gomathi, A. K. Manna, D. J. Late, R. Datta, S. K. Pati and C. N. R. Rao, “MoS_2 and WS_2 Analogues of Graphene”, Angew. Chem. Int. Ed., Vol. 49, No. 24, pp 4059-4062, (2010)

[10] A. M. Dimiev and J. M. Tour, “Mechanism of Graphene Oxide Formation”, ACS Nano, Vol. 8, No. 3, pp 3060–3068, (2014)

[11] Q. Wei and X. Peng, “Superior mechanical flexibility of phosphorene and few-layer black phosphorus”, Appl. Phys. Lett., Vol. 104, No. 25, 251915, (2014)

[12] M. E. Dávila, L. Xian, S. Cahangirov, A. Rubio and G. Le Lay, “Germanene: a novel two-dimensional germanium allotrope akin to graphene and silicone”, New J. Phys., Vol. 16, 095002, (2014)

[13] A. G. Cano-Márquez, F. J. Rodríguez-Macías, J. Campos-Delgado, C. G. Espinosa-González, F. Tristán-López, D. Ramírez-González, D. A. Cullen, D. J. Smith, M. Terrones and Y. I. Vega-Cantú, “Ex-MWNTs: Graphene Sheets and Ribbons Produced by Lithium Intercalation and Exfoliation of Carbon Nanotubes” Nano Lett, Vol. 9, No. 4, pp 1527–1533, (2009)

[14] X. Li, X. Wang, L. Zhang, S. Lee and H. Dai “Chemically Derived, Ultrasmooth Graphene Nanoribbon Semiconductors” Science, Vol. 319, No. 5867, pp. 1229-1232, (2008)

[15] W. Zhao, M. Fang, F. Wu, H. Wu, L. Wang and G. Chen, “Preparation of graphene by exfoliation of graphite using wet ball milling”, J. Mater. Chem., Vol .20, pp. 5817-5819, (2010)

[16] X. Chen, L. Zhang and S. Chen, “Large area CVD growth of graphene” Synthetic Metals Vol. 210, Pages 95-108, (2015)

[17] R. Addou, A. Dahal, P. Sutter and M. Batzill, “Monolayer graphene growth on Ni(111) by low temperature chemical vapor deposition”, Appl. Phys. Lett., Vol. 100, No. 2, 021601 (2012)

[18] N. Woehrl, O. Ochedowski, S. Gottlieb, K. Shibasaki and S. Schulz, “Plasma-enhanced chemical vapor deposition of graphene on copper substrates” AIP Advances, Vol. 4, No. 4, 047128 (2014)

[19] R. R. Nair, P. Blake, A. N. Grigorenko, K. S. Novoselov, T. J. Booth, T. Stauber, N. M. R. Peres and A. K. Geim, “Fine Structure Constant Defines Visual Transparency of Graphene” Science, Vol. 320, No. 5881, pp. 1308 (2008)

[20] N. Vermeulen, D. Castelló-Lurbe, M. Khoder, I. Pasternak, A. Krajewska, T. Ciuk, W. Strupinski, J. Cheng, H. Thienpont and J. Van Erps, “Graphene’s nonlinear-optical physics revealed through exponentially growing self-phase modulation”, Nature Communications, Vol. 9, No. 2675 (2018)

[21] E. Hendry, P. J. Hale, J. Moger, A. K. Savchenko, and S. A. Mikhailov, “Coherent Nonlinear Optical Response of Graphene” Phys. Rev. Lett., Vol. 105, No. 9, 097401, (2010)

[22] Q. Bao, H. Zhang, Y. Wang, Z. Ni, Y.i Yan, Z. X. Shen, K. P. Loh and D. Y. Tang, “Atomic-Layer Graphene as a Saturable Absorber for Ultrafast Pulsed Lasers”, Vol. 19, No. 19, Pages 3077-3083 (2009)

[23] Z. Luo, M. Zhou, J. Weng, G. Huang, H. Xu, C. Ye and Z. Cai “Graphene-based passively Q-switched dual-wavelength erbium-doped fiber laser” Vol. 35, No. 21, pp. 3709-3711 (2010)

[24] J. D. Zapata, D. Steinberg, L. A. M. Saito, R. E. P. de Oliveira, A. M. Cárdenas & E. A. Thoroh de Souza, “Efficient graphene saturable absorbers on D-shaped optical fiber for ultrashort pulse generation”, Scientific Reports, Vol. 6, No. 20644 (2016)

[25] B. Yao, Y. Wu, Y. Cheng, A. Zhang, Y. Gong, Y.-J. Rao, Z. Wang and Y. Chen, “All-optical Mach–Zehnder interferometric NH3 gas sensor based on graphene/microfiber hybrid waveguide”, Sensors and Actuators B: Chemical, Vol. 194, Pages 142-148, (2014)

[26] M. Hernaez, C. R. Zamarreño, S. Melendi-Espina, L. R. Bird, A. G. Mayes, and F. J. Arregui, “Optical Fibre Sensors Using Graphene-Based Materials: A Review”, Sensors, Vol. 17, No. 1, (2017)

[27] F. Schwierz, “Graphene transistors”, Nature Nanotechnology, Vol. 5, pp 487–496, (2010)

[28] B. Radisavljevic, A. Radenovic, J. Brivio, V. Giacometti and A. Kis, “Single-layer MoS_2 transistors”, Nature Nanotechnology, Vol. 6, pp 147–150 (2011)

[29] X. Li and H. Zhu, “Two-dimensional MoS_2: Properties, preparation, and applications” Journal of Materiomics, Vol. 1, No. 1, pp 33-44, (2015)

[30] G. Parker , “Introductory Semiconductor device physics” Institute of Physics Publishing (2004); Image from:

https://chem.libretexts.org/Courses/Howard_University/General_Chemistry%3A_An_Atoms_First_Approach/Unit_5%3A_States_of_Matter/Chapter_12%3A_Solids/Chapter_12.06%3A_Metals_and_Semiconductors

[31] C. Yim, M. O'Brien, N. McEvoy, S. Winters, I. Mirza, J. G. Lunney, and G. S. Duesberg, "Investigation of the optical properties of MoS_2 thin films using spectroscopic ellipsometry", Appl. Phys. Lett., Vol. 104, No. 103114 (2014)

[32] R. Wang, H.-C. Chien, J. Kumar, N. Kumar, H.-Y. Chiu and H. Zhao, "Third-Harmonic Generation in Ultrathin Films of MoS_2", ACS Appl. Mater. Interfaces, Vol. 6, No. 1, pp 314–318, (2014)

[33] C. Torres-Torres, N. Perea-López, A. L. Elías, H. R Gutiérrez, D. A Cullen, A. Berkdemir, F. López-Urías, H. Terrones and M. Terrones, "Third order nonlinear optical response exhibited by mono- and few-layers of WS_2", 2D Mater., Vol. 3 No. 021005, (2016)

[34] R. I. Woodward, R. T. Murray, C. F. Phelan, R. E. P. de Oliveira, T. H. Runcorn, E. J. R. Kelleher, S. Li, E. C. de Oliveira, G. J. M. Fechine and G. Eda, "Characterization of the second- and third-order nonlinear optical susceptibilities of monolayer MoS_2 using multiphoton microscopy", 2D Mater., Vol. 4 No. 011006, (2017)

[35] M. Zhao, Z. Ye, R. Suzuki, Y. Ye, H. Zhu, J. Xiao, Y. Wang, Y. Iwasa and X. Zhang, "Atomically phase-matched second-harmonic generation in a 2D crystal", Light: Science & Applications, Vol 5, (2016)

[36] Y. Yu, Y.Yu, L. Huang, H. Peng, L. Xiong, and L. Cao, "Giant Gating Tunability of Optical Refractive Index in Transition Metal Dichalcogenide Monolayers", Nano Lett., Vol. 17, No. 6, pp 3613–3618, (2017)

[37] A. K. M. Newaz, D. Prasai, J. I. Ziegler, D. Caudel, S. Robinson, R. F. Haglund Jr. and K. I. Bolotin "Electrical control of optical properties of monolayer MoS_2", Solid State Communications, Vol. 155, pp. 49-52, (2013)

[38] D. Vella, D. Ovchinnikov, N. Martino, V. Vega-Mayoral, D. Dumcenco, Y-C. Kung, M-R. Antognazza, A. Kis, G. Lanzani, D. Mihailovic and C. Gadermaier, "Unconventional electroabsorption in monolayer MoS_2", 2D Mater., Vol. 4, No. 2, (2017)

[39] K. Wang, J. Wang, J. Fan, M. Lotya, A. O'Neill, D. Fox, Y. Feng, X. Zhang, B. Jiang, Q. Zhao, H. Zhang, J. N. Coleman, L. Zhang, and W. J. Blau, "Ultrafast Saturable Absorption of Two-Dimensional MoS_2 Nanosheets" ACS Nano, Vol. 7, No. 10, pp 9260–9267, (2013)

[40] S. Wang, H. Yu, H. Zhang, A. Wang, M. Zhao, Y. Chen, L. Mei and J. Wang, "Broadband Few-Layer MoS_2 Saturable Absorbers", Vol. 26, No. 21, Pages 3538-3544 (2014)

[41] H. Liu, A.-P. Luo, F.-Z. Wang, R. Tang, M. Liu, Z.-C. Luo, W.-C. Xu, C.-J Zhao and H. Zhang, "Femtosecond pulse erbium-doped fiber laser by a few-layer MoS_2 saturable absorber", Vol. 39, No. 15, pp. 4591-4594 (2014)

[42] P. Joensen, R.F. Frindt and S. Roy Morrison, “Single-layer MoS_2”, Materials Research Bulletin Vol. 21, No. 4, Pages 457-461, (1986)

[43] A. Jawaid, D. Nepal, K. Park, M. Jespersen, A. Qualley, P. Mirau, L. F. Drummy and R. A. Vaia “Mechanism for Liquid Phase Exfoliation of MoS_2”, Chem. Mater., Vol. 28, No. 1, pp 337–348, (2016)

[44] M. Velický and P. S. Toth “From two-dimensional materials to their heterostructures: An electrochemist's perspective”, Applied Materials Today, Vol. 8, Pages 68-103, (2017)

[45] J. Gusakova, X. Wang, L. L. Shiau, A. Krivosheeva, V. Shaposhnikov, V. Borisenko, V. Gusakov and B. K. Tay, “Electronic Properties of Bulk and Monolayer TMDs: Theoretical Study Within DFT Framework (GVJ-2e Method)”, Phys. Status Solidi A, Vol. 214, No. 12, (2017)

[46] H. Li, Q. Zhang, C. C. R. Yap, B. K. Tay, T. H. T. Edwin, A. Olivier and D. Baillargeat “From Bulk to Monolayer MoS_2: Evolution of Raman Scattering”, Advanced Functional materials, Vol. 22, No. 7, pp 1385-1390, (2012)

[47] H. W. Wang, P. Skeldon and G. E. Thompson, “XPS studies of MoS_2 formation from ammonium tetrathiomolybdate solutions” Surface and Coatings Technology, Vol. 91, No. 3, pp 200-207, (1997)

[48] J. Jeon, S. K. Jang, S. M. Jeon, G. Yoo, Y. H. Jang, J.-H. Park and S. Lee, “Layer-controlled CVD growth of large-area two-dimensional MoS_2 films” Nanoscale, Vol. 7, pp 1688-1695, (2015)

[49] J. R. Ferraro, K. Nakamoto and C. W. Brown, “Introductory Raman Spectroscopy”, Elsevier Science & Technology, (2003)

[50] L. Liang and V. Meunier, “First-principles Raman spectra of MoS_2, WS_2 and their heterostructures” Nanoscale, Vol. 6, 5394-5401, (2014)

[51] B. Chakraborty, A. Bera, D. V. S. Muthu, S. Bhowmick, U. V. Waghmare, and A. K. Sood, “Symmetry-dependent phonon renormalization in monolayer MoS_2 transistor”, Phys. Rev. B, Vol. 85, 161403 (2012)

[52] https://www.renishaw.com/en/photoluminescence-explained--25809

[53] A. Splendiani, L. Sun, Y. Zhang, T. Li, J. Kim, C.-Y. Chim, G. Galli and F. Wang “Emerging Photoluminescence in Monolayer MoS_2”, Nano Lett., Vol. 10, No. 4, pp 1271–1275, (2010)

[54] G. Haugstad, “Atomic Force Microscopy : Understanding Basic Modes and Advanced Applications”, John Wiley & Sons, (2012)

[55] C.-I Lu, C. J. Butler, J.-K. Huang, C.-R. Hsing, H.-H. Yang, Y.-H. Chu, C.-H. Luo, Y.-C. Sun, S.-H. Hsu, K.-H. O. Yang, C.-M. Wei, L.-J. Li and M.-T. Lin, “Graphite edge controlled registration of monolayer MoS_2 crystal orientation” Appl. Phys. Lett., Vol. 106, (2015)

[56] J. M. Wagner, “X-Ray Photoelectron Spectroscopy”, Nova Science Publishers Inc, (2010)

[57] J R. Brent, N. Savjani and P. O’Brien, “Synthetic approaches to two-dimensional transition metaldichalcogenide nanosheets”, Progress in Materials Science, Vol. 89, pp. 411–478, (2017)

[58] O. V. Yazyev and Y. P. Chen, “Polycrystalline graphene and other two-dimensional materials”, Nature Nanotechnology, Vol. 9, pp 755–767, (2014)

[59] Y. Huang, E. Sutter, N. N. Shi, J. Zheng, T. Yang, D. Englund, H.-J. Gao and P. Sutter, "Reliable Exfoliation of Large-Area High-Quality Flakes of Graphene and Other Two-Dimensional Materials" ACS Nano, Vol. 9, No. 11, pp 10612–10620, (2015)

[60] M. Mar Bernal, L. Álvarez, E. Giovanelli, A. Arnáiz, L. Ruiz-González, S. Casado, D. Granados, A. M. Pizarro, A. Castellanos-Gomez and E. M. Pérez "Luminescent transition metal dichalcogenide nanosheets through one-step liquid phase exfoliation" 2D Mater., Vol. 3, No. 3, (2016)

[61] G. Zhao, J. Hou, Y. Wu, J. He and X. Hao "Preparation of 2D MoS_2/Graphene Heterostructure through a Monolayer Intercalation Method and its Application as an Optical Modulator in Pulsed Laser Generation", Advanced Optical Materials, Vol. 3, No. 7, pp 937-942, (2015)

[62] S. Zheng, G. Zhong, X. Wu, L. D'Arsiè and J. Robertson, "Metal-catalyst-free growth of graphene on insulating substrates by ammonia-assisted microwave plasma-enhanced chemical vapor deposition" Chem. Soc. Rev, Vol. 46, pp. 6276-6300, (2017)

[63] Y. Yu, C. Li, Y. Liu, L. Su, Y. Zhang and L. Cao, "Controlled Scalable Synthesis of Uniform, High-Quality Monolayer and Few-layer MoS_2 Films" Scientific Reports, Vol. 3, No. 1866 (2013)

[64] Y. Zhao, J.-G. Song, G. H. Ryu, K. Y. Ko, W. J. Woo, Y. Kim, D. Kim, J. H. Lim, S. Lee, Z. Lee, J. Park and H. Kim "Low-temperature synthesis of 2D MoS_2 on a plastic substrate for a flexible gas sensor" Nanoscale, Vol. 10, pp. 9338-9345, (2018)

[65] Y.-H. Lee, X.-Q. Zhang, W. Zhang, M.-T. Chang, C.-T. Lin, K.-D. Chang, Y.-C. Yu, J. T.-W. Wang, C.-S. Chang, L.-J. Li and T.-W. Lin "Synthesis of Large-Area MoS_2 Atomic Layers with Chemical Vapor Deposition" Advanced Materials, Vol. 24, No. 17, pp. 2320-2325 (2012)

[66] B. Liu, L. Chen, G. Liu, A. N. Abbas, M. Fathi, and C. Zhou, "High-Performance Chemical Sensing Using Schottky-Contacted Chemical Vapor Deposition Grown Monolayer MoS_2 Transistors", ACS Nano, Vol. 8, No. 5, pp 5304–5314, (2014)

[67] B. Cho, A. R. Kim, Y. Park, J. Yoon, Y.-J. Lee, S. Lee, T. J. Yoo, C. G. Kang, B. H. Lee, H. C. Ko, D.-H. Kim and M. G. Hahm "Bifunctional Sensing Characteristics of Chemical Vapor Deposition Synthesized Atomic-Layered MoS_2", ACS Appl. Mater. Interfaces, Vol. 7, No. 4, pp 2952–2959, (2015)

[68] J. Park, N. Choudhary, J. Smith, G. Lee, M. Kim and W. Choi, "Thickness modulated MoS_2 grown by chemical vapor deposition for transparent and flexible electronic devices", Appl. Phys. Lett., Vol. 106, No. 012104, (2015)

[69] K. Kang, S. Xie, L. Huang, Y. Han, P. Y. Huang, K. F. Mak, C.-J. Kim, D. Muller and J. Park, "High-mobility three-atom-thick semiconducting films with wafer-scale homogeneity", Nature, Vol. 520, pages 656–660 (2015)

[70] L. Yu, D. El-Damak, U. Radhakrishna, X. Ling, A. Zubair, Y. Lin, Y. Zhang, M.-H. Chuang, Y.-H. Lee, D. Antoniadis, J. Kong, A. Chandrakasan and T. Palacios, "Design, Modeling, and Fabrication of

Chemical Vapor Deposition Grown MoS_2 Circuits with E-Mode FETs for Large-Area Electronics", Nano Lett., Vol. 16, No. 10, pp 6349–6356, (2016)

[71] M.-L. Tsai, S.-H. Su, J.-K. Chang, D.-S. Tsai, C.-H. Chen, C.-I Wu, L.-J. Li, L.-J. Chen and J.-H. He "Monolayer MoS_2 Heterojunction Solar Cells", ACS Nano, Vol. 8, No. 8, pp 8317–8322, (2014)

[72] E. Ponomarev, I. Gutiérrez-Lezama, N. Ubrig and A. F. Morpurgo, "Ambipolar Light-Emitting Transistors on Chemical Vapor Deposited Monolayer MoS_2", Nano Lett., Vol. 15, No. 12, pp 8289–8294, (2015)

[73] Y. Kim, H. Bark, G. H. Ryu, Z. Lee and C. Lee, "Wafer-scale monolayer MoS_2 grown by chemical vapor deposition using a reaction of MoO_3 and H_2S", J. Phys.: Condens. Matter, Vol. 28, No. 184002, (2016)

[74] G. Yang, Y. Gu, P. Yan, J. Wang, J. Xue, X. Zhang, N. Lu and G. Chen, "Chemical Vapor Deposition Growth of Vertical MoS_2 Nanosheets on p-GaN Nanorods for Photodetector Application", ACS Appl. Mater. Interfaces, Vol. 11, No. 8, pp 8453–8460, (2019)

[75] L. K. Tan, B. Liu, J. H. Teng, S. Guo, H. Y. Low and K. P. Loh "Atomic layer deposition of a MoS_2 film" Nanoscale, Vol. 6, No. 18, pp. 10584-10588, (2014).

[76] Y. Jang, S. Yeo, H.-B.-R. Lee, H. Kim and S.-H. Kim "Wafer-scale, conformal and direct growth of MoS_2 thin films by atomic layer deposition", Applied Surface Science Vol. 365, pp. 160-165, (2016)

[77] S. Shin, Z. Jin, D. H. Kwon, R. Bose, and Y.-S. Min, "High Turnover Frequency of Hydrogen Evolution Reaction on Amorphous MoS_2 Thin Film Directly Grown by Atomic Layer Deposition", Langmuir, Vol. 31, No. 3, pp 1196–1202, (2015)

[78] Y. Kim, J.-G. Song, Y. J. Park, G. H. Ryu, S. J. Lee, J. S. Kim, P. J. Jeon, C. W. Lee, W. J. Woo, T. Choi, H. Jung, H.-B.-R. Lee, J.-M. Myoung, S. Im, Z. Lee, J.-H. Ahn, J. Park and H. Kim, "Self-Limiting Layer Synthesis of Transition Metal Dichalcogenides", Scientific Reports, Vol. 6, No. 18754, (2016)

[79] Y. Zhang, W. Ren, Z. Jiang, S. Yang, W. Jing, P. Shi, X. Wu and Z.-G. Ye, "Low-temperature remote plasma-enhanced atomic layer deposition of graphene and characterization of its atomic-level structure" J. Mater. Chem. C, Vol. 2, pp. 7570-7574, (2014)

[80] J.-G. Song, J. Park, W. Lee, T. Choi, H. Jung, C. W. Lee, S.-H. Hwang, J. M. Myoung, J.-H. Jung, S.-H. Kim, C. Lansalot-Matras and H. Kim, "Layer-Controlled, Wafer-Scale, and Conformal Synthesis of Tungsten Disulphide Nanosheets Using Atomic Layer Deposition", ACS Nano, Vol. 7, No. 12, pp 11333–11340, (2013)

[81] M. Mattinen, T. Hatanpää, T. Sarnet, K. Mizohata, K. Meinander, P. J. King, L. Khriachtchev, J. Räisänen, M. Ritala and M. Leskelä "Atomic Layer Deposition of Crystalline MoS_2 Thin Films: New Molybdenum Precursor for Low-Temperature Film Growth" Advanced Materials Interfaces, Vol. 4, No. 18, (2017)

[82] A. U. Mane, S. Letourneau, D. J. Mandia, J. Liu, J. A. Libera, Y. Lei, Q. Peng, E. Graugnard, and J. W. Elam, "Atomic layer deposition of molybdenum disulphide films using MoF_6 and H_2S", Journal of Vacuum Science & Technology A, Vol. 36, (2018)

[83] T. A. Ho, C. Bae, S. Lee, M. Kim, J. M. Montero-Moreno, J. Hyeok Park and H. Shin, "Edge-On MoS_2 Thin Films by Atomic Layer Deposition for Understanding the Interplay between the Active Area and Hydrogen Evolution Reaction", Chem. Mater., Vol. 29, No.17, pp 7604–7614, (2017)

[84] B. Groven, M. Heyne, A. Nalin Mehta, H. Bender, T. Nuytten, J. Meersschaut, T. Conard, P. Verdonck, S. Van Elshocht, W. Vandervorst, S. De Gendt, M. Heyns, I. Radu, M. Caymax and A. Delabie, "Plasma-Enhanced Atomic Layer Deposition of Two-Dimensional WS_2 from WF_6, H_2 Plasma, and H_2S" Chem. Mater., Vol. 29, No. 7, pp 2927–2938, (2017)

[85] K.-K. Liu, W. Zhang, Y.-H. Lee, Y.-C. Lin, M.-T. Chang, C.-Y. Su, C.-S. Chang, H. Li, Y. Shi, H. Zhang, C.-S. Lai and L.-J. Li, "Growth of Large-Area and Highly Crystalline MoS_2 Thin Layers on Insulating Substrates" Nano Lett., Vol. 12, No. 3, pp 1538–1544 (2012)

[86] J. Yang, Y. Gu, E. Lee, H. Lee, S. H. Park, M.-H. Cho, Y. H. Kim, Y.-H. Kimad and H. Kim, "Wafer-scale synthesis of thickness-controllable MoS_2 films via solution-processing using a dimethylformamide/n-butylamine/2-aminoethanol solvent system" Nanoscale, Vol. 7, pp. 9311-9319, (2015)

[87] Y. R. Lim, J. K. Han, S. K. Kim, Y. B. Lee, Y. Yoon, S. J. Kim, B. K. M. Y. Kim, C. Jeon, S. Won, J.-H. Kim, W. Song, S. Myung, S. S. Lee, K.-S. An and J. Lim, "Roll-to-Roll Production of Layer-Controlled Molybdenum Disulphide: A Platform for 2D Semiconductor-Based Industrial Applications" Advanced Materials Vol. 30, No. 5, (2018)

[88] G. Agrawal, "Nonlinear Fiber Optics", Academic Press, (2012)

[89] J. Hecht, "Understanding Fibre Optics", H.W. Sams, (1993); Image from: https://phys.libretexts.org/Bookshelves/University_Physics/Book%3A_Physics_(Boundless)/24%3A_Geometric_Optics/24.2%3A_Reflection%2C_Refraction%2C_and_Dispersion

[90] A. Arie and N. Voloch, "Periodic, quasi-periodic, and random quadratic nonlinear photonic crystals", Laser & Photon Rev., Vol. 4, No. 3, pp. 355-373, (2010)

[91] R. W. Boyd, "Nonlinear Optics", Academic Press, (2003)

[92] D. Cotter, R. J. Manning, K. J. Blow, A. D. Ellis, A. E. Kelly, D. Nesset, I. D. Phillips, A. J. Poustie and D. C. Rogers, "Nonlinear Optics for High-Speed Digital Information Processing" Science, Vol. 286, No. 5444, pp. 1523-1528, (1999)

[93] N. G. R. Broderick, G. W. Ross, H. L. Offerhaus, D. J. Richardson and D. C. Hanna "Hexagonally Poled Lithium Niobate: A Two-Dimensional Nonlinear Photonic Crystal" Phys. Rev. Lett., Vol. 84, No. 4345, (2000)

[94] A. Ashkin, G. Boyd and J. Dziedzic, "Resonant optical second harmonic generation and mixing" IEEE Journal of Quantum Electronics, Vol. 2, No. 6, pp. 109-124, (1966)

[95] M. Han, G. Giese, and J. F. Bille “Second harmonic generation imaging of collagen fibrils in cornea and sclera”, Optics Express, Vol. 13, No. 15, pp. 5791-5797 (2005)

[96] P. G. Kazansky, P. St. J. Russell and H. Takebe “Glass Fiber Poling and Applications”, JOURNAL OF LIGHTWAVE TECHNOLOGY, Vol. 15, No. 8, pp. 1484-1493, (1997)

[97] M. Yamada, N. Nada, M. Saitoh and K. Watanabe, “First-order quasi-phase matched LiNbO3 waveguide periodically poled by applying an external field for efficient blue second-harmonic generation” Appl. Phys. Lett., Vol. 62, No. 5, pp. 435-436, (1993)

[98] H.-Y. Chen, J.-S.. Sue, Y.-H. Lin, C.-S. Tsai, P.-T. Wu, and S. Chao “Thermal poling and ultraviolet erasure characteristics of type-III ultraviolet-grade fused silica and application to periodic poling on planar substrates”, Journal of Applied Physics, Vol. 94, No. 3, pp.1531-1538, (2003)

[99] F. De Lucia, D. Huang, C. Corbari, N. Healy, and P. J. A. Sazio, “Optical fiber poling by induction” Optics Letters Vol. 39, No. 22, pp. 6513-6516 (2014)

[100] P. G. Kazansky and V. Pruneri, “Electric-field poling of quasi-phase-matched optical fibers”, Journal of the Optical Society of America B, Vol. 14, No. 11, pp. 3170-3179 (1997)

[101] L. Li and D. N. Payne, “Permanently-induced linear electro-optic effect in silica optical fibers,” Tech. Dig. Integrated and Guided- Wave Opt., paper TuAA2, 1989, pp. 130-134.

[102] R. A. Myers, N. Mukherjee, and S. R. J. Brueck, “Large second-order nonlinearity in poled fused silica”, Optics Letters, Vol. 16, No. 22, pp. 1732-1734 (1991)

[103] W. Margulis and F. Laurell “Interferometric study of poled glass under etching”, Optics Letters Vol. 21, No. 21, pp. 1786-1788 (1996)

[104] T. Fujiwara, D. Wong and S. Fleming “Large electrooptic modulation in a thermally-poled germanosilicate fiber”, IEEE Photonics Technology Letters, Vol. 7 , No. 10, pp. 1177 – 1179, (1995)

[105] W. Margulis, O .Tarasenko and N. Myrén, “Who needs a cathode? Creating a second-order nonlinearity by charging glass fiber with two anodes”, Opt Express. Vol. 17, No. 18, pp. 15534-40 (2009)

[106] N. Myrén and W. Margulis, “Time evolution of frozen-in field during poling of fiber with alloy electrodes” Optics Express, Vol. 13, No. 9, pp. 3438-3444 (2005)

[107] M. Fokine, L. E. Nilsson, Å. Claesson, D. Berlemont, L. Kjellberg, L. Krummenacher, and W. Margulis, “Integrated fiber Mach–Zehnder interferometer for electro-optic switching”, Optics Letters, Vol. 27, No. 18, pp. 1643-1645 (2002)

[108] F. De Lucia, D. W. Keefer, C. Corbari and P. J. A. Sazio, “Thermal poling of silica optical fibers using liquid electrodes”, Optics Letters, Vol. 42, No. 1, pp. 69-72, (2017)

[109] A. Camara, O. Tarasenko and W. Margulis, “Study of thermally poled fibers with a two-dimensional model”, Optics Express, Vol. 22, No. 15, pp. 17700-17715 (2014)

[110] L. M. Malard, T. V. Alencar, A. Paula M. Barboza, K. F. Mak, and A. M. de Paula "Observation of intense second harmonic generation from MoS_2 atomic crystals" Phys. Rev. B 87, No. 201401(R), (2013)

[111] H. Knape and W. Margulis, "All-fiber polarization switch", Opt. Lett., Vol. 32, pp. 614-616, (2007)

[112] J. R. Sparks, J. L. Esbenshade, R. He, N. Healy, T. D. Day, D. W. Keefer, P. J. A. Sazio, A. C. Peacock and J. V. Badding, "Selective Semiconductor Filling of Microstructured Optical Fibers" Journal of Lightwave Technology, Vol. 29, No. 13, pp. 2005-2008, (2011)

[113] F. De Lucia, R. Bannerman, N. Englebert, M. M. A. N. Velazquez, F. Leo, J. Gates, S.-P. Gorza, J. Sahu and P. J. A. Sazio, "Single is better than double: theoretical and experimental comparison between two thermal poling configurations of optical fibers", Optics Express, *In press*

[114] P. J. Roberts, F. Couny, H. Sabert, B. J. Mangan, D. P. Williams, L. Farr, M. W. Mason, A. Tomlinson, T. A. Birks, J. C. Knight, and P. St.J. Russell, "Ultimate low loss of hollow core photonic crystal fibres", Optics Express, Vol. 13, No. 1, pp. 236-244 (2005)

[115] R. F. Cregan, B. J. Mangan, J. C. Knight, T. A. Birks, P. St. J. Russell, P. J. Roberts and D. C. Allan, "Single mode photonic bandgap guidance of light in air", Science, Vol. 285, No. 5433, pp. 1537-1539, (1999)

[116] F. Benabid, "Hollow-core photonic bandgap fibre: new light guidance for new science and technology", Phil. Trans. R. Soc. A, Vol. 364, pp. 3439–3462, (2006)

[117] F. Benabid, J. C. Knight, G. Antonopoulos and P. St. J. Russell, "Stimulated Raman scattering in hydrogen filled hollow core photonic crystal fiber" Science, Vol. 298, No. 5592, pp. 399-402, (2002)

[118] F. Couny, F. Benabid, P. J. Roberts, P. S. Light and M. G. Raymer, "Generation and Photonic Guidance of Multi-Octave Optical-Frequency Combs" Science, Vol. 318, No. 5853, pp. 1118-1121, (2007)

[119] Y. Y. Wang, N. V. Wheeler, F. Couny, P. J. Roberts, and F. Benabid, "Low loss broadband transmission in hypocycloid-core Kagome hollow-core photonic crystal fiber", Optics Letters, Vol. 36, No. 5, pp. 669-671, (2011)

[120] S.-F. Gao, Y.-Y. Wang, W. Ding and P. Wang, "Hollow core negative-curvature fibre for UV guidance", Optics Letters, Vol. 43, No. 6, pp. 1347-1350, (2018)

[121] W. Belardi and J. C. Knight, "Effect of core boundary curvature on the confinement losses of hollow antiresonant fibers", Optics Express, Vol. 21, No. 19, pp. 21921-21927, (2013)

[122] W. Belardi and J. C. Knight, "Hollow antiresonant fibers with reduced attenuation", Optics Letters, Vol. 39, No. 7, pp. 1853-1856, (2014)

[123] J. C. Knight, T. A. Birks, P. St. J. Russell, and D. M. Atkin, "All-silica single-mode optical fiber with photonic crystal cladding" Optics Letters, Vol. 21, No. 19, pp. 1547-1549 (1996)

[124] F. Yu, and J.C. Knight, “Negative Curvature Hollow-Core Optical Fiber” IEEE Journal of Selected Topics in Quantum Electronics, Vol. 22 , No. 2, (2016)

[125] S. Chaudhuri, L. D. Van Putten, F. Poletti and P. J. A. Sazio “Low Loss Transmission in Negative Curvature Optical Fibers With Elliptical Capillary Tubes” Journal of Lightwave Technology, Vol. 34, No. 18, pp. 4228-4231, (2016)

[126] S.-F. Gao, Y. -Y. Wang, W. Ding, D.-L. Jiang, S. Gu, X. Zhang and P. Wang “Hollow-core conjoined-tube negative-curvature fibre with ultralow loss” Nature Communications, Vol. 9, No. 2828 (2018)

[127] A.F. Kosolapov, G.K. Alagashev, A.N. Kolyadin, A.D. Pryamikov, A.S. Biryukov, I.A. Bufetov and E.M. Dianov “Hollow-core revolver fibre with a double-capillary reflective cladding”, Quantum Electronics, Vol. 46, No. 3, pp. 267-270, (2016)

[128] A. D. Pryamikov, A. S. Biriukov, A. F. Kosolapov, V. G. Plotnichenko, S. L. Semjonov and E. M. Dianov, “Demonstration of a waveguide regime for a silica hollow - core microstructured optical fiber with a negative curvature of the core boundary in the spectral region > 3.5 μm”, Optics Express, Vol. 19, No. 2, pp. 1441-1448, (2011)

[129] F. Yu, W.J. Wadsworth and J.C. Knight, “Low loss silica hollow core fibers for 3–4 μm spectral region”, Optics Express, Vol. 20, No. 10, pp. 11153-11158 (2012)

[130] Y. Yang, and D. Wei, “Confinement loss in hollow-core negative curvature fiber: A multi-layered model”, Optics Express, Vol. 25, No. 26, pp. 33122-33133 (2017)

[131] A. N. Kolyadin, A. F. Kosolapov, A. D. Pryamikov, A. S. Biriukov, V. G. Plotnichenko, and E. M. Dianov, “Light transmission in negative curvature hollow core fiber in extremely high material loss region”, Optics Express, Vol. 21, No. 8, pp. 9514-9519 (2013)

[132] C. Wei, J. T. Young, C. R. Menyuk, and J. Hu, “Temperature Sensor Using Fluid-Filled Negative Curvature Fibers”, Conference on Lasers and Electro-Optics (CLEO), paper JW2A.179 (2018)

[133] B.Gu, Y. Chen and Z. Wang, “Characteristics of 1.9-μm laser emission from hydrogen-filled hollow-core fiber by vibrational stimulated Raman scattering” Optical Engineering, Vol. 55, No.12, (2016)

[134] W. Belardi, F. De Lucia, F. Poletti, and P. J. Sazio “Composite material hollow antiresonant fibers”, Optics Letters, Vol. 42, No. 13, pp. 2535-2538 (2017)

[135] C. Wei, J. Hu, and C. Menyuk, “Comparison of Loss in Silica and Chalcogenide Negative Curvature Fibers as the Wavelength Varies”, Front. Phys., Vol. 4, No. 30 (2016)

[136] G. T. Forcherio, J. Riporto, J. R. Dunklin, Y. Mugnier, R. Le Dantec, L. Bonacina, and D. K. Roper, “Nonlinear optical susceptibility of two-dimensional WS_2 measured by hyper Rayleigh scattering”, Optics Letters, Vol. 42, No. 23, pp. 5018-5021, (2017)

[137] H. H. Yudar, S. Pat, Ş. Korkmaz, S. Özen and V. Şenay, "Zn/ZnSe thin films deposition by RF magnetron sputtering", Journal of Materials Science: Materials in Electronics, Vol. 28, No. 3, pp 2833–2837, (2017)

[138] J. R. Sparks, R. He, N. Healy, M. Krishnamurthi, A. C. Peacock, P. J. A. Sazio, V. Gopalan and J. V. Badding, "Zinc Selenide Optical Fibers", Advanced Materials, Vol. 23, No. 14, pp. 1647-1651, (2011)

[139] H. R. Gutiérrez, N. Perea-López, A. L. Elías, A. Berkdemir, B. Wang, R. Lv, F. López-Urías, V. H. Crespi, H. Terrones and M. Terrones, "Extraordinary Room-Temperature Photoluminescence in Triangular WS_2 Monolayers", Nano Lett. Vol. 13, No. 8, pp. 3447-3454 (2013)

[140] Y. Cui, R. Xin, Z. Yu, Y. Pan, Z.-Y. Ong, X. Wei, J. Wang, H. N. Z. Ni, Y. Wu, T. Chen, Y. Shi, B. Wang, G. Zhang, Y.-W. Zhang and X. Wang, "High-Performance Monolayer WS_2 Field-Effect Transistors on High-κ Dielectrics" Advanced Materials, Vol. 27, No. 35, pp. 5230-5234, (2015)

[141] H.-L. Liu, C.-C. Shen, S.-H. Su, C.-L. Hsu, M.-Y. Li, and L.-J. Li, "Optical properties of monolayer transition metal dichalcogenides probed by spectroscopic ellipsometry", Appl. Phys. Lett., Vol. 105, No. 201905 (2014)

[142] J. Kumar, M. A. Kuroda, M. Z. Bellus, S.-J. Han, and H.-Y. Chiu, "Full-range electrical characteristics of WS_2 transistors", Appl. Phys. Lett., Vol. 106, No. 123508 (2015)

[143] B. Mahler, V. Hoepfner, K. Liao and G. A. Ozin, "Colloidal Synthesis of 1T-WS_2 and 2H-WS_2 Nanosheets: Applications for Photocatalytic Hydrogen Evolution", J. Am. Chem. Soc., Vol. 136, No. 40, pp. 14121-14127, (2014)

[144] K. Wu, X. Zhang, J. Wang, X. Li and J. Chen, "WS_2 as a saturable absorber for ultrafast photonic applications of mode-locked and Q-switched lasers", Optics Express, Vol. 23, No. 9, pp. 11453-11461 (2015)

[145] D. Yang and R. F. Frindt, "Li-intercalation and exfoliation of WS_2", Journal of Physics and Chemistry of Solids, Vol. 57, No. 6–8, pp. 1113-1116, (1996)

[146] M. Okada, T. Sawazaki, K. Watanabe, T. Taniguch, H. Hibino, H. Shinohara and R. Kitaura, "Direct Chemical Vapor Deposition Growth of WS_2 Atomic Layers on Hexagonal Boron Nitride", ACS Nano, Vol. 8, No. 8, pp. 8273-8277, (2014)

[147] K. M. McCreary, A. T. Hanbicki, G. G. Jernigan, J. C. Culbertson and B. T. Jonker, "Synthesis of Large-Area WS_2 monolayers with Exceptional Photoluminescence" Scientific Reports, Vol. 6, No. 19159, (2016)

[148] S. Cadot, O. Renault, D. Rouchon, D. Mariolle, E. Nolot, C. Thieuleux, L. Veyre, H. Okuno, F. Martin and E. A. Quadrelli, "Low-temperature and scalable CVD route to WS_2 monolayers on SiO_2/Si substrates", Journal of Vacuum Science & Technology A, Vol. 35, No. 061502, (2017)

[149] B. Yorulmaz, A. Özden, H. Şar, F. Ay, C. Sevik and N. K. Perkgöz "CVD growth of monolayer WS_2 through controlled seed formation and vapor density" Materials Science in Semiconductor Processing, Vol. 93, Pages 158-163, (2019)

[150] B. Shi, D. Zhou, S. Fang, K. Djebbi, S. Feng, H. Zhao, C. Tlili, and D. Wang, "Facile and Controllable Synthesis of Large-Area Monolayer WS_2 Flakes Based on WO_3 Precursor Drop-Casted Substrates by Chemical Vapor Deposition" Nanomaterials, Vol. 9, No. 4, (2019)

[151] A. Berkdemir, H. R. Gutiérrez, A. R. Botello-Méndez, N. Perea-López, A. L. Elías, C.-I. Chia, B. Wang, V. H. Crespi, F. López-Urías, J.-C. Charlier, H. Terrones, and M. Terrones "Identification of individual and few layers of WS_2 using Raman Spectroscopy", Sci Rep., Vol. 3, No. 1755, (2013)

[152] S. Wang, J. You , B. Geng and Z. Cheng "Fabrication of ZnSe hexagonal prism with pyramid end through the chemical vapour deposition route" CrystEngComm, Vol. 13, pp. 668-673, (2011)

[153] S. Adachi and T. Taguchi, "Optical properties of ZnSe", Phys. Rev. B, Vol. 43, No. 12, pp. 9569-9577, (1991)

[154] H. P. Wagner, M. Kühnelt, W. W. Langbein and J. M. Hvam, "Dispersion of the second-order nonlinear susceptibility in ZnTe, ZnSe, and ZnS" Physical Review B Condensed Matter, Vol. 58, No. 16, pp. 10494-10501, (1998)

[155] T. D. Chinh, W. Seibt, and K. Siegbahn, "Dot patterns from second-harmonic and sum-frequency generation in polycrystalline ZnSe", Journal of Applied Physics, Vol. 90, No. 5, pp. 2612-2614, (2001)

[156] A. Goudarz, G. M. Aval, R. Sahraei and H. Ahmadpoor, "Ammonia-free chemical bath deposition of nanocrystalline ZnS thin film buffer layer for solar cells", Thin Solid Films, Vol. 516, No. 15, Pages 4953-4957, (2008)

[157] M. H. Jupina, Elsa M. Garmire, N. Shibata, and S. Zembutsu, "Electroabsorption and Electrooptic Modulation in Single Crystal ZnSe-ZnSSe Waveguides Grown by OMPVE on GaAs", IEEE JOURNAL OF QUANTUM ELECTRONICS, Vol. 28, No. 3, (1992)

[158] S. C. Aro, J. R. Sparks, S. A. McDaniel, M. G. Coco, A. T. Hendrickson, V. Gopalan, G. Cook, and J. V. Badding, "Cr^{2+}:ZnSe Fiber Lasers", Lasers Congress (ASSL, LSC, LAC), paper AW3A.4, (2016)

[159] Y. Li, Y. Rao, K. F. Mak, Y. You, S. Wang, C. R. Dean and T. F. Heinz, "Probing Symmetry Properties of Few-Layer MoS_2 and h-BN by Optical Second-Harmonic Generation", Nano Lett., Vol. 13, No.7, pp. 3329-3333, (2013)

[160] J. Jung, J. Lee, Y. Kim, H. Bark and C. Lee, "Ultrafast and low-temperature synthesis of patternable MoS_2 using laser irradiation", Journal of Physics D: Applied Physics, Vol. 52, No. 18, (2019)

[161] A. Castellanos-Gomez, M. Barkelid, A. M. Goossens, V. E. Calado, H. S. J. van der Zant and G. A. Steele, “Laser-Thinning of MoS_2: On Demand Generation of a Single-Layer Semiconductor” Nano Lett., Vol. 12, No. 6, pp. 3187-3192, (2012)

[162] I. H. Malitson “Interspecimen Comparison of the Refractive Index of Fused Silica”, Journal of the Optical Society of America, Vol. 55, No. 10, pp. 1205-1209 (1965)

[163] M. J. F. Digonnet, J. R. Feth, L. F. Stokes, and H. J. Shaw “Measurement of the core proximity in polished fiber substrates and couplers” Optics Letters, Vol. 10, No. 9, pp. 463-465, (1985)

[164] M. Grundmann, “The Physics of Semiconductors”, Springer Verlay, (2010)